

Thèse

Pour obtenir le grade de Docteur de l'Université de Lille

Spécialité : **Micro- et Nanotechnologies, Acoustique et Télécommunications**

Préparée au sein de l'**Institut d'Électronique, de Micro- et de Nanotechnologies**

dans le cadre de l'école doctorale **Sciences Pour l'Ingénieur**

Soutenue le 15 Juillet 2020 par

Salim Alhajj Assaf

Innovative nanostructured textiles for thermal comfort

Textiles innovants nanostructurés pour le confort thermique

Soutenue devant le jury composé de :

Rapporteurs :

Frédérique Gadot

Professeur

Université Paris Nanterre

Bjorn Maes

Professeur

Université de Mons

Examineurs :

Christian Seassal

Directeur de recherche CNRS

Ecole Centrale de Lyon

Eric Lheurette

Professeur

Université de Lille

Directeur de thèse

Yan Pennec

Professeur

Université de Lille

Co-Directeur de thèse

Vincent Thomy

Maître de conférences

Université de Lille

Membres invités

Michèle Carette

Maître de conférences

Université de Lille

Guillaume Boussaroque

Responsable Innovation,

Damart France

The world ain't all sunshine and rainbows. It's a very mean and nasty place and I don't care how tough you are it will beat you to your knees and keep you there permanently if you let it. You, me, or nobody is gonna hit as hard as life. But it ain't about how hard ya hit. It's about how hard you can get hit and keep moving forward. How much you can take and keep moving forward. That's how winning is done!

Rocky balboa

Acknowledgements

First of all, I would like to thank my thesis supervisor Yan Pennec, as well as my co-thesis supervisor Vincent Thomy, for having supervised me during my research and for helping me acquire new scientific knowledge and skills. I greatly appreciate their readiness to offer advice, support and guidance whenever needed. They were always available, attentive to my many questions, and were always interested in the progress of my work. The many discussions we have had and their advice have a lot to do with the end result of this work. Finally, their numerous rereadings and corrections of this thesis were very significant.

I would also like to warmly thank Michèle Carette for devoting her time and expertise to teach me about clean room processing and she took the time to re-read my thesis report.

I thank the members of my thesis committee, Dr. Frédérique Gadot, Dr. Bjorn Maes, Dr. Christian Seassal and Dr. Eric Lheurette for devoting their time to read the manuscript and for their insightful comments and remarks.

My sincere and warm gratitude goes to Mr Abdellatif Akjouj and Mr Bahram Djafari Rouhani, who have been a great advisor, always generous with his ideas and advice, both on the scientific and personal level, which I truly appreciated.

I would like to cordially thank all the people and collaborations who have participated in the advancements of my Ph.D. project, such as Hayriye Dgidik (Laboratoire GemTex, HEI Lille), who has allowed me to use their FT-IR spectroscopy. I also acknowledge the help of Anthony Treizebre to teach me about clean room processing and for preparing my samples many times.

I thank the company DAMART for partial PhD financial support especially Mrs Cecile LECLAND innovative project manager in Damart and Mr Guillaume BOUSSAROQU head of Damartsport for the interest in our thesis subject and their future perspectives.

I would also like to thank all the members of the EPhONI team for their welcome and kindness, and for making these years of thesis, a period as pleasant as it was instructive.

Special thanks go to my amazing friends in France and Lebanon, Roudy, Charbel, Reda, Joelle and Arthur. I am truly and deeply thankful for your moral support.

I also thank, with great affection, my heart and soulmate Rim who has been by my sides these last years. Words cannot describe how dear you are to me; you have been there during my ups and downs, my best moments and my darkest moments, and you were always an amazing support in all times. I am truly grateful for having you by my side and in my life.

My warmest gratitude goes to my beloved parents and sister, Nohad, Elie, Charbel and Laure, to whom I dedicate this Ph.D. Your unconditional and unlimited love and support, not to mention your endless sacrifices have made all this possible and got me where I am today. Thank you!

Finally, this list would not be complete and I would not be sincere if I leave out my dear Savior Jesus Christ. Thank You for the good and the bad moments, and for carrying me through the most stressful situations I have ever faced in my life so far. I would not have done it without You and without my faith in You.

Salim Assaf

26/05/2020

Table of Contents

List of abbreviations.....	12
Introduction.....	15
Chapter I:.....	24
Technical solutions for thermal comfort in textile.....	24
I.1 The impact of technology in the textile and application to thermal comfort.....	25
I.1.1 Concept of thermal comfort and thermoregulation.....	25
I.1.2 Heat and moisture transfer within the microclimate.....	30
I.1.2.1 Conductive heat transfer.....	32
I.1.2.2 Convective heat transfer.....	32
I.1.2.3 Evaporative heat transfer.....	33
I.1.2.4 Radiative heat transfer.....	34
I.1.3 Smart textiles for thermal comfort.....	39
I.1.3.1 Definition and classification.....	39
I.1.3.2 Smart textile structures.....	39
I.1.3.2.a) Waterproof-breathable textiles.....	39
I.1.3.2.b) Phase change materials.....	41
I.1.3.2.c) Shape memory materials.....	42
I.1.3.2.d) Conductive materials.....	45
I.2 Introduction on photonic crystals and Fano resonances.....	46
I.2.1 Introduction.....	46
I.2.2 Photonic crystals.....	46
I.2.2.1 One-dimensional photonic crystals (1D): The Bragg mirror.....	47
I.2.2.2 Two-dimensional photonic crystals (2D).....	48
I.2.2.3 Three-dimensional photonic crystals (3D).....	49
I.2.3 Maxwell equations in periodic dielectric structures.....	52
I.2.4 Brillouin zone and band diagram.....	53
I.2.4.1 Irreducible Brillouin zone.....	53
I.2.4.2 Band diagram.....	55
I.2.5 Fano resonance.....	56
I.3 Thermoregulatory clothing for personal thermal management.....	59
Conclusion.....	66

References.....	69
Chapter II:.....	78
Numerical and experimental study of a silicon membrane in the mid-infrared range.....	78
Introduction.....	79
II.1 Finite element method.....	80
II.1.1 Definition and principle.....	80
II.1.2 Boundary conditions.....	82
II.1.2.1 Periodic boundary condition.....	82
II.1.2.2 Perfectly matched layer.....	83
II.2 Description of the electromagnetic properties of dielectric materials: adaptation of the Lorentz-Drude model.....	83
II.2.1 Description of the Drude model.....	84
II.2.2 Description of the Lorentz-Drude model.....	86
II.3 Ridges photonic crystal membrane made of polycrystalline silicon.....	90
II.3.1 Structure Si/Air/Si wafer.....	90
II.3.1.1 Variation of the silicon substrate thickness.....	91
II.3.1.2 Variation of the air thickness.....	92
II.3.2 Structure Si/Air.....	93
II.3.2.1 Origin of modes.....	93
II.3.2.2 Influence of the thickness h , width L and period P of the ridges on the reflection spectrum.....	95
II.3.3 Structure Si/SiO ₂ /Si wafer.....	98
II.3.3.1 Influence of the width of the ridge.....	100
II.3.3.2 Origin of modes.....	101
II.4 Holes photonic crystal membrane made of polycrystalline silicon.....	103
II.4.1 Influence of the polarization (TE and TM).....	104
II.4.2 Influence of hole diameter.....	105
II.4.3 Influence of the periodic lattice.....	106
II.5 Manufacturing method of ridges and holes grating.....	108
II.6 Fourier Transform-Infrared analysis method.....	111
II.7 Comparison between experimental and simulated spectra.....	114
Conclusion.....	115
References.....	117

Chapter III:	119
Optical and thermal analysis of the Benzocyclobutene (BCB) polymer photonic membrane	119
Introduction	120
III.1 Choice of the polymer	120
III.2 Model and method	121
III.3 Spectral analysis in the mid-infrared	123
III.3.1 Unstructured Benzocyclobutene membrane	123
III.3.2 Structured benzocyclobutene membrane	125
III.3.3 Modulation of the spectral coefficients in the mid-infrared	128
III.3.3.1 Influence of the scaling factor	128
III.3.3.2 Variation of the diameter	133
III.3.3.3 Variation of the thickness	135
III.3.3.4 Influence of incident angle	138
III.3.3.5 Variation of the refractive index of the microclimate	139
III.3.4 Conclusion on the impact of the optical properties	141
III.4 Heat transfer analysis	142
III.4.1 Thermal balance model	142
III.4.2 Non-thermally conductive Benzocyclobutene membrane	145
III.4.2.1 Temperature of the non-thermally conductive unstructured membrane	146
III.4.2.2 Effect of the structuration of the non-thermally conductive membrane	147
III.4.2.3 Effect of the hole diameter of the non-thermally conductive membrane	150
III.4.2.4 Effect of the membrane thickness of the non-thermally conductive membrane	152
III.4.2.5 Effect of the moisture of the non-thermally conductive membrane	153
III.4.3 Thermally conductive membrane	154
III.4.3.1 Temperatures evolution using a thermally conductive non-structured membrane	154
III.4.3.2 Effect of the structuration of the thermally conductive membrane	156
III.4.3.2 Effect of the thickness on the thermally conductive structured membrane	158
III.4.3.4 Effect of holes diameter for the thermally conductive BCB membrane	159
III.4.3 Effect of moisture on the thermally conductive BCB membrane	160
III.5 First experimental demonstration	161

Conclusion.....	162
References.....	164
Chapter IV:.....	165
Ideal polymer for personal thermoregulation.....	165
Introduction:.....	166
IV.1 Optical analysis of usual polymers in textile.....	166
IV.1.1 Choice of polymers.....	167
IV.1.1.1 Polydimethylsiloxane (PDMS).....	167
IV.1.1.2 Polyimide (PI).....	167
IV.1.1.3 Polyethylene (PE).....	168
IV.1.1.4 Polyethylene terephthalate (PET).....	168
IV.1.2 Refractive index of polymers.....	168
IV.1.3 Study of polymer membranes.....	171
IV.1.3.1 Optical spectra.....	171
IV.1.3.2 Efficiency coefficient.....	175
IV.2 Thermal response of the polymers.....	175
IV.3 Fabrication of PDMS polymer membrane.....	180
IV.3.1 Method of manufacturing a thin PDMS membrane.....	181
IV.3.2 Comparaison of the FT-IR measurement and the simulation.....	183
IV.4 Conclusion about the ideal polymer.....	184
Conclusion.....	185
References.....	187
Conclusion.....	189
Perspectives.....	194
Abstract.....	197
Résumé.....	198

List of abbreviations

A : Absorption

ASHRAE: American Society of Heating, Refrigerating and Air Conditioning Engineers

BC: Boundary Condition

BCB: Benzocyclobutene

C: Heat flux exchanged by convection

D: Hole diameter

E: Electric fields

E_{ev} : Evaporative flow

e_{SiO_2} : Silica layer of thickness

e_{SiW} : Thickness of silicon substrate

FEM: Finite Element Method

FT-IR: Fourier Transform InfraRed

H: Magnetic fields

h: Thickness of silicon ridges/silicon membranes/polymer membrane

h_c : Convection coefficient

k_{air} : Thermal conductivity of air

$k_{\text{BCB}}/k_{\text{PE}}/k_{\text{PI}}/k_{\text{PET}}/k_{\text{PDMS}}$: Extinction coefficient of BCB/PE/PI/PET/PDMS

k_{BCB} : Thermal conductivity of BCB

L: Width of silicon ridges

M: Metabolic power

MC: Microclimate

MIR: Mid-infrared

n_{air} : Refractive index of air

$n_{\text{BCB}}/n_{\text{PE}}/n_{\text{PI}}/n_{\text{PET}}/n_{\text{PDMS}}$: Refractive index of BCB/PE/PI/PET/PDMS

n_{eff} : Effective refractive index

$n_{\text{Si}}/n_{\text{PolySi}}$: Refractive index of silicon and polysilicon materials

n_{SiO_2} : Refractive index of silica

n_{water} : Refractive index of water

P: Periodic lattice

PBC: Periodic Boundary Condition

PBG: Photonic band gap

PC: Photonic Crystal

PCM: Phase change materials

PDMS: Polydimethylsiloxane

PE: Polyethelene

PET: Polyethylene terephthalate

PI: Polyimide

PML: Perfectly Matched Layers

PolySi: Polycrystalline silicon

$q_{\text{cond,air}}$: Conductive heat flux in the air gap between the skin and the textile

$q_{\text{cond,m}}$: Conductive heat flux into the membrane

q_{conv} : Convective heat flux from the membrane to the ambient air.

q_{gen} : Metabolic body heat production

$q_{\text{rad,mi}}$: Radiative heat flux from the polymer membrane inner surface

$q_{\text{rad,a}}$: Radiative heat flux from the ambient air

$q_{\text{rad,mo}}$: Radiative heat flux from the polymer membrane outer surface

$q_{\text{rad,s}}$: Radiative heat flux from the skin

R: Reflection

RIE: Reactive ion etching

SEM: Scanning electron microscopy

SMM: Shape memory materials

T: Transmission

T_1 : Temperatures of the inner surfaces of the membrane

T_2 : Temperatures of the outer surfaces of the membrane

T_a : Temperature of the ambient air,

T_{BCB} : Temperature of BCB membrane

TE: Transverse electric

TM: Transverse magnetic

T_{PDMS} : Temperature of PDMS membrane

T_{PE} : Temperature of PE membrane

T_{PET} : Temperature of PET membrane

T_{PI} : Temperature of PI membrane

T_s : Temperature of the skin

α_i : Scaling factors

η : The efficiency factor

Introduction

The building sector in the European Union is considered to be the largest consumer of energy with up to 40% of total energy consumption [1]. 37% of this energy is attributed to the temperature control, using Heating, Ventilation and Air Conditioning (HVAC) systems [2]. A reduction in this consumption will definitively contribute to both environmental protection and costs saving. One way is to support building insulation; another way is to control the energy consumption by personal thermoregulation. Nevertheless, in this second issue, conventional textiles made from natural and synthetic polymers are not designed for infrared radiation control and have an emissivity of about 0.8 [3]. Thus, a new generation of textiles, capable of controlling the emissivity of the body in order to achieve thermal comfort has recently emerged. Indeed, infrared radiation (from 5 to 15 μm) represents, for the human body, 50 % of heat losses with a maximum of the emissive peak at the wavelength of 9.5 μm [4].

To control thermal radiations, photonic nanostructures have represented a paradigm, offering a panel of exciting properties for energy applications during the past ten years [5,6]. Photonic nanostructures demonstrate their ability to manage thermal radiations properties in a way drastically different from conventional thermal emitters due to their abilities to control and manage electromagnetic waves at the mid-Infrared (MIR) wavelength scale. Indeed, photonic crystals performances allowed the overtaking of usual thermal emitters constraints [7] toward narrowband emission, directionality, polarization, coherence.... Photonic band gap materials dealing with the modification of Planck blackbody radiations have been discussed on simple photonic multilayered structures [8] or more complex 1D [9,10], 2D [11,12] and 3D [13] ones. In those papers, the enhancement, suppression and selectivity of thermal emissions was demonstrated, based on the photonic crystals properties. Such control of the thermal radiations has led to different applications in the energy domain, as thermophotovoltaic devices, where hot absorber-emitters [14] convert sunlight into thermal emission. The concept of daytime radiative cooling with the objective to cool passively terrestrial structures is another example. In this latter case, the broad band photonic mirror in the MIR was used to reflect sunlight in the atmosphere [15,16].

More recently, another field of application has appeared in the thermal radiation control, with the introduction of photonic nanostructures in textiles for personal thermoregulation. For personal heating textiles, integration of metallic nanowires or particles embedded in polyethylene or cotton matrices has been proposed [17,18]. The heating production is then generated both by the radiation

reflected from the human body and by the Joule effect generated by the current flowing through the metallic wires.

For cooling purpose, recent papers proposed different fibers [19,20,21,22] or membranes [23,24,25] fabrics in order to increase IR transparency. In the fiber configuration, Tong *et al.* [19] proposed an infrared-transparent-visible-opaque-fabric (ITVOF), made of synthetic polymer structured fibers presenting high IR transparency and visible opaqueness. For membranes fabrics, Hsu *et al.* [23] proposed an experimental development of a textile that promotes effective radiative cooling composed of nanoporous polyethylene (PE), also transparent to MIR human body radiations. The dual functionalities (cooling and heating) within a same textile has been proposed in two different ways. Hsu *et al.* investigated a textile made of a passive bilayer thermal emitter embedded inside an IR-transparent nano-PE [26]. They proposed the same non-symmetric piece of textile to perform both radiative heating and cooling. Zhong *et al.* [27], proposed reversible humidity sensitive clothing using shape memory polymer. This smart textile has been designed to reversibly adapt the thermal insulation functionality, thus permitting the reduction of the humidity, the apparent temperature and the air flow at the same time. Recently, Zhang *et al.* have proposed a dynamic control in the mid-infrared in reaction of the relative humidity of the underlying skin by coating triacetate-cellulose bimorph fibers with a thin layer of carbon nanotubes [28].

The personal thermoregulation, especially in the energy efficiency context, appears as an exciting scientific challenge to investigate. Many subjective parameters are attached to the thermoregulation of the human body linked to the apparent temperature and personal resentment [29]. However, to meet user demand for better thermal comfort, a tremendous effort is still necessary to develop smart wearable thermoregulating textiles. Until now, the previous papers have reported on the introduction of metallic particles for heating effects or on transparent polymers (as PE) for cooling. In addition, complex geometries presenting heating and / or cooling properties have been detailed. In the present work, we aim to propose a simple micro-structured photonic membrane for the thermoregulation functionality. Our purpose is to take advantage of the modulation of the electromagnetic waves at the mid-Infrared (MIR) to modulate the human body thermal comfort.

This thesis manuscript is divided into four chapters:

- In the first chapter, we will define the concept of thermal comfort and the influence of the physiological and environmental parameters. Then, we will present the different mechanisms of thermal and moisture transfer that affect the thermoregulation of the human body. To do this, we will describe the three heat transfer mechanisms: convection, conduction and radiation, then define and classify the technological development achieved in the field of textiles for thermal comfort so far (waterproof-breathable textile, phase change materials, shape memory materials). The remainder of this chapter will be devoted to the definition of photonic crystals which have desirable properties for the control of thermal radiation. Depending on the chosen crystal geometry, they may have desirable optical properties either in the visible, near infrared, medium infrared or far infrared domains. In addition, we will provide an overview of existing research related to personal heating and cooling textiles. Finally, we will define our project in relation to the context of thermoregulatory clothing for personal thermal management.
- In the second chapter, we first will present the finite element method. These numerical methods allow to solve the Maxwell frequency equations and are used to simulate the behavior of photonic crystals. Afterwards, we will define the Drude-Lorentz model describing the dielectric permittivity of materials, which will be implemented in the simulation calculations. Subsequently, we will present the different results on the study of ridges and holes in photonic crystal membranes made of polycrystalline silicon in the mid-infrared range (5-15 μm). The influence of different parameters (such as membrane thickness, ridge width, hole diameter, grating period and incident wave polarization) on the reflection spectra will be considered. The numerical calculations performed in this chapter were done in relation to the experimental silicon structure fabrication carried out by another PhD student of the Bio-MEMS group (IEMN), Maude Viallon. To conclude the chapter, we will describe the Fourier Transform-Infrared analysis method and then compare the experimental and simulation results obtained.

- In the third chapter, we will focus on membranes composed of polymer materials instead of silicon to better suit the field of textile applications. First, we will justify the choice of the polymer used. Then we will define the model used and study the influence of Benzocyclobutene (BCB) membrane structuration on the transmission, reflection and absorption spectra in the mid-infrared domain. Next, we will define and analyze the thermal balance between the human body and the indoor environment through the photonic membrane, taking into consideration the radiation, convection and conduction mechanisms. We will work on two cases: non-thermally conductive and thermally conductive membranes. Finally, we will present the results of the first experimental demonstration that was carried out by Maude Viallon during her thesis.
- Finally, in the last chapter, we will focus on studying a set of different polymers (PDMS, PE, PI and PET). We will start by justifying the choice of these polymers, then will present their refraction indices in the infrared medium and investigate their optical properties considering the effects of structuration. By doing so, we will couple the optical properties with the thermal balance analysis applied between the human body and the surrounding environment. Then, to facilitate textile application, we will describe our method for manufacturing a thin PDMS membrane. Finally, we will compare our experimental and simulation results. Thanks to this research, studies, we hope to demonstrate the optimal properties of an ideal polymer for our proposed application.

The research presented in this manuscript is the result of a collaboration between the Institute of Electronics, Microelectronics and Nanotechnologies (IEMN) and DAMART Company (who partially funded this PhD). This PhD work was also part of, and benefited from, the European Commission project PHOTONITEX under the INTERREG program France - Wallonia - Vlaanderen, started in 2018. This thesis was carried out at IEMN within the Ephoni and BioMEMS group. This collaboration made it possible to share the expertise of each of the partners (micro-

nano simulation and technologies for the IEMN, technical textiles and thermal comfort in hot and cold atmosphere for the European Commission project PHOTONITEX and DAMART).

References

1. Recast, E. P. B. D. (2010). Directive 2010/31/EU of the European Parliament and of the Council of 19 May 2010 on the energy performance of buildings (recast). Official Journal of the European Union, 18(06), 2010.
2. Balaras CA, Gaglia AG, Georgopoulou E, Mirasgedis S, Sarafidis Y, Lalas DP. European residential buildings and empirical assessment of the Hellenic building stock, energy consumption, emissions and potential energy savings. *Build Environ*. 2007;42:1298–314.
3. Mason, M. T., & Coleman, I. (1967). Study of the Surface Emissivity of Textile Fabrics and Materials in the 1 to 15MU Range. BLOCK ENGINEERING INC CAMBRIDGE MA.
4. Hardy JD, DuBois EF. Regulation of Heat Loss from the Human Body. *Proc Natl Acad Sci*. 1937;23:624–31.
5. Sawhney APS, Condon B, Singh KV, Pang SS, Li G, Hui D. Modern Applications of Nanotechnology in Textiles. *Text Res J*. 2008;78:731–9.
6. Li W, Fan S. Nanophotonic control of thermal radiation for energy applications [Invited]. *Opt Express*. 2018;26:15995.
7. Kittel C, Kroemer H. Thermal physics. 2d ed. San Francisco: W. H. Freeman; 1980.
8. Cornelius CM, Dowling JP. Modification of Planck blackbody radiation by photonic band-gap structures. *Phys Rev A*. 1999;59:4736–46.
9. Foley JM, Itsuno AM, Das T, Velicu S, Phillips JD. Broadband long-wavelength infrared Si/SiO₂ subwavelength grating reflector. *Opt Lett*. 2012;37:1523.
10. Foley JM, Young SM, Phillips JD. Narrowband mid-infrared transmission filtering of a single layer dielectric grating. *Appl Phys Lett*. 2013;103:071107.
11. Liu X, Tyler T, Starr T, Starr AF, Jokerst NM, Padilla WJ. Taming the Blackbody with Infrared Metamaterials as Selective Thermal Emitters. *Phys Rev Lett* [Internet]. 2011 [cited 2020 Feb 28];107. Available from: <https://link.aps.org/doi/10.1103/PhysRevLett.107.045901>

12. Viallon M, Assaf S, Treizebré A, Gidik H, Dupont D, Bedek G, et al. Modulation of the refractive properties of 1D and 2D photonic crystal polycrystalline silicon-based membranes in the MIR frequency range. *J Phys Appl Phys.* 2019;52:205101.
13. Lin S-Y, Fleming JG, Chow E, Bur J, Choi KK, Goldberg A. Enhancement and suppression of thermal emission by a three-dimensional photonic crystal. *Phys Rev B.* 2000;62:R2243–6.
14. Lenert A, Bierman DM, Nam Y, Chan WR, Celanović I, Soljačić M, et al. A nanophotonic solar thermophotovoltaic device. *Nat Nanotechnol.* 2014;9:126–30.
15. Rephaeli E, Raman A, Fan S. Ultrabroadband Photonic Structures To Achieve High-Performance Daytime Radiative Cooling. *Nano Lett.* 2013;13:1457–61.
16. Raman AP, Anoma MA, Zhu L, Rephaeli E, Fan S. Passive radiative cooling below ambient air temperature under direct sunlight. *Nature.* 2014;515:540–4.
17. Hsu P-C, Liu X, Liu C, Xie X, Lee HR, Welch AJ, et al. Personal Thermal Management by Metallic Nanowire-Coated Textile. *Nano Lett.* 2015;15:365–71.
18. Yu Z, Gao Y, Di X, Luo H. Cotton modified with silver-nanowires/polydopamine for a wearable thermal management device. *RSC Adv.* 2016;6:67771–7.
19. Tong JK, Huang X, Boriskina SV, Loomis J, Xu Y, Chen G. Infrared-Transparent Visible-Opaque Fabrics for Wearable Personal Thermal Management. *ACS Photonics.* 2015;2:769–78.
20. Catrysse PB, Song AY, Fan S. Photonic Structure Textile Design for Localized Thermal Cooling Based on a Fiber Blending Scheme. *ACS Photonics.* 2016;3:2420–6.
21. Jafar-Zanjani S, Salary MM, Mosallaei H. Metafabrics for Thermoregulation and Energy-Harvesting Applications. *ACS Photonics.* 2017;4:915–27.
22. Gao T, Yang Z, Chen C, Li Y, Fu K, Dai J, et al. Three-Dimensional Printed Thermal Regulation Textiles. *ACS Nano.* 2017;11:11513–20.
23. Hsu P-C, Song AY, Catrysse PB, Liu C, Peng Y, Xie J, et al. Radiative human body cooling by nanoporous polyethylene textile. *Science.* 2016;353:1019–23.

24. Song Y-N, Ma R-J, Xu L, Huang H-D, Yan D-X, Xu J-Z, et al. Wearable Polyethylene/Polyamide Composite Fabric for Passive Human Body Cooling. *ACS Appl Mater Interfaces*. 2018;10:41637–44.
25. Cai L, Song AY, Li W, Hsu P-C, Lin D, Catrysse PB, et al. Spectrally Selective Nanocomposite Textile for Outdoor Personal Cooling. *Adv Mater*. 2018;30:1802152.
26. Hsu P-C, Liu C, Song AY, Zhang Z, Peng Y, Xie J, et al. A dual-mode textile for human body radiative heating and cooling. *Sci Adv*. 2017;3:e1700895.
27. Zhong Y, Zhang F, Wang M, Gardner CJ, Kim G, Liu Y, et al. Reversible Humidity Sensitive Clothing for Personal Thermoregulation. *Sci Rep [Internet]*. 2017 [cited 2020 Feb 28];7. Available from: <http://www.nature.com/articles/srep44208>
28. Zhang XA, Yu S, Xu B, Li M, Peng Z, Wang Y, et al. Dynamic gating of infrared radiation in a textile. *Science*. 2019; 363:619–23.
29. Steadman RG. The assessment of sultriness. Part I: A temperature-humidity index based on human physiology and clothing science. *Journal of applied meteorology*. 1979 Jul;18(7):861-73.

Chapter I:

Technical solutions for thermal comfort in textile

I.1 The impact of technology in the textile and application to thermal comfort

I.1.1 Concept of thermal comfort and thermoregulation.

Human beings live constantly in a changing thermal environment and this, of course, with the wish to feel comfortable. Thermal comfort is a concept of satisfaction with the external environment. A person who is in a state of thermal neutrality does not want to be warmer or colder. This physiological reaction is determined by the amount of heat produced by the body and transmitted to the external environment. This concept is now a key issue in the textile industry (clothing, sports, personal protective equipment, construction ...) because of the increasing demand for improvements and efficiency, in terms of comfort of today's consumers. However, the concept of thermal comfort is specific to each individual and depends both on the physical activity carried out by the person and on several environmental parameter (temperature and humidity among others detailed afterwards) [1,2].

One of the most important properties of the human body is the homeothermy: human must maintain constant internal body temperature (around 37 °C) regardless of external influences. This property is obtained by thermoregulation mechanisms.

The temperature is not homogeneous over the whole body. We can distinguish two temperatures: the internal one, corresponding to the one of the organs of the individual, and the skin one, measured at the surface of the skin.

In the context of a resting state, the human body skin and the surface temperature is strongly affected by various external conditions. They may include changes in ambient temperature, vapor pressure, air velocity, and clothing isolation, among other factors that affect the skin temperature [3]. It produces heat in case of low temperature (chills, peripheral vasoconstriction ...) and releases heat to the outside in case of too high temperature (perspiration, conduction, convection, thermal radiation) [4]. The body converts the chemical energy of its food into work and heat. These metabolic processes produce a large amount of heat depending on the degree of activity [5].

The internal temperature depends on the heat produced by the body. Heat is a byproduct of basic metabolism and physical activity. Most of the heat produced by the body comes from the viscera

(heart, brain, liver mainly) and muscles during exercise. To maintain a constant internal temperature, heat production, heat gains and heat losses must balance.

The heat produced by the organs and muscles is then transferred through the network of blood vessels and tissues to the skin where it is released into the environment to prevent any increase in the internal temperature. If the production of heat generated by the muscles is not dissipated quickly enough, it accumulates. The thermal core extends. This situation can lead to an increase in the internal temperature. In this case, there is a risk of hyperthermia.

Conversely, if the thermal losses are higher or faster than the production, the internal temperature of the body decreases leading to a risk of hypothermia. These losses occur in the skin through changes in blood flow.

To feel comfortable, the individual must be able to maintain a stable body temperature close to 37 °C. For this, the human body is endowed with physiological mechanisms that will allow it to maintain this temperature. All these mechanisms constitute the phenomenon of thermoregulation [6,7]. Thermoregulation is the regulation of thermal exchanges of thermogenesis and thermolysis – therefore it is necessary to maintain this thermal equilibrium and the internal temperature. This regulation occurs due to the many responses that the human body can provide, depending on the thermal environment in which he is immersed [8]. Mechanisms of thermoregulation can be passive, active unconscious or active conscious. The interest and principle of each of these mechanisms is briefly described below.

Passive/Active unconscious mechanisms: Passive mechanisms allow heat exchange between the human body and the environment, similar to a home that loses or gains heat. They occur naturally as soon as a difference in temperature or pressure exists between a human being and his environment. Unlike passive mechanisms, these modes of heat transfer are activated by the body according to the ambient conditions. These thermoregulatory mechanisms are triggered unconsciously and contribute to the maintenance of thermal equilibrium. There are three of them, detailed in the followings [9,10]:

- **Vasodilation and vasoconstriction:** The human body can be represented as a central nucleus (consisting of the skeletal muscles, viscera and central nervous system) in which most body heat production takes place, surrounded by an envelope (the skin) that produces only a

small part of the heat [11]. Human vasomotor response allows variation in blood flow to the skin, which causes a change in cutaneous thermal resistance and therefore helps to modulate thermal losses from the skin. Within certain limits, vasoconstriction and vasodilatation are sufficient to maintain thermal equilibrium by controlling the heat exchange occurring in the skin. Depending on the ambient conditions, the thermal core is extended to a varying degree, making it possible to regulate thermal losses. In a "cold" environment, the lower limit of the thermal comfort zone, the peripheral limbs are sacrificed from a thermal point of view in order to keep the heat in the center, in the nucleus (state of vasoconstriction). In a "hot" environment, the upper limit of the thermal neutrality zone, the thermal core extends in order to increase the thermal losses (state of vasodilatation) [12].

- Sweating: In a hot environment, vasomotor mechanisms are no longer sufficient to maintain thermal equilibrium. Sweating becomes an important way to evacuate heat. Moreover, Hardy and DuBois have shown that sweating becomes also the only way to regulate when skin temperature and ambient temperature are equal [12]. Sweat evaporates from skin by absorbing latent heat, taking some heat body with it and resulting in a local temperature decrease [13]. When the sweat is just flowing on the skin, heat loss is less important because there is no evaporation. The evacuated heat comes from the skin and thus, from the inside of the body, which makes it possible to maintain the internal temperature or to limit its increase. When wearing clothes, the evaporation of sweat is absorbed by the clothes, it is carried out on the surface of clothing.
- Chills are a succession of uncoordinated contractions of the skeletal muscles to produce heat. In a cold environment, the thrill becomes the most important means of producing heat. Hardy and DuBois showed that the succession of chills was the only method of regulating central temperature in a cold environment in absence of physical exercise [12].

Active conscious mechanisms: The conscious active mechanisms of regulation constitute the behavioral part of thermoregulation. These are voluntary actions on the part of the subject which allow him to modify heat losses, for example:

- Adding or removing clothes, to modify the insulation between the subject and the environment.
- Changing the level of physical activity which makes possible to modify the production of heat: intense physical activity will result in increasing heat output as a result of muscle activity.

Furthermore, the human body is designed to live in a moderate or warm environment where it can maintain its vital functionalities, particularly thermoregulation, without artifice. Below 20°C, we cannot maintain our constant internal temperature without behavioral adjustments such as wearing clothes or using heated dwellings. The clothes thus allowed Human to be established everywhere in the world [14]. These are the main thermal insulators of everyday life. They act as a barrier to heat and vapor transfer between the skin and the environment, reducing the metabolic cost of thermoregulation [15].

The textile structure appears essential in maintaining the thermal equilibrium between the heat produced by the body and the thermal transfer to the external environment. When properly adapted, it protects the human body against possible hyperthermia or hypothermia. It is characterized by its resistance to heat and moisture transfer and also by its protection from environmental radiation (solar radiation...). The textile will therefore act on heat and water transfers to ensure a balance between production and heat loss and maintain a constant internal temperature [16,17,18]. It is an intermediary between the body and the environment, crucial in the thermal balance analysis. Since a long time, the individual uses the layer of air confined between the textile and the skin to preserve its thermal comfort. This layer of air establishes a microclimate (MC) which is of great importance since it plays a very active role in the management of heat and water transfers. This microclimate is dependent on the temperature of the confined air, its relative humidity, the time of confinement and its renewal [19,20].

The study of all these parameters made it possible to establish a scale of thermal comfort and indices of comfort which remain purely qualitative and peculiar to an individual. The thermal comfort scale offers a way to correlate the optimal physiological parameters with the psychological sensation of comfort. The most commonly thermal comfort scales used are reported in figure 1.1.

Bedford scale		ASHRAE scale	
Much too warm	3	Hot	3
Too warm	2	Warm	2
Comfortably warm	1	Slightly warm	1
Comfortable	0	Neutral	0
Comfortably cool	-1	Slightly cool	-1
Too cool	-2	Cool	-2
Much too cool	-3	Cold	-3

Figure 1.1: Most commonly used thermal comfort scales (Bedford and ASHRAE scale) [21].

The thermal comfort of a person is defined by the ‘standard 55’ of ASHRAE scale (1966) as the state of mind of satisfaction with respect to the thermal environment for which the person does not know if she/he would prefer a warmer or cooler environment [22]. This notion is subjective as each individual is different from a thermal point of view. It is not possible to satisfy all the members of a group subjected to the same climatic atmosphere at the same time [22]. Thus the thermal comfort and personal resentment can be analyzed in terms of the apparent temperature. This is a function not only of the air temperature, but also of the humidity, radiation, and local wind simulated for each scenario. A variation of $\pm 1\text{ }^{\circ}\text{C}$ or $\pm 2\text{ }^{\circ}\text{C}$ could act on the individual feeling.

So, thermal comfort is influenced by both environmental and physiological parameters.

Six primary factors that directly affect the human perception of thermal comfort, which can be divided into four basic environmental variables and two physiological parameters. These are defined and described as follows [23]:

The four environmental parameters are:

- air temperature: is the most important environmental parameter. It refers to the temperature of the air that a person is in contact with.
- mean radiant temperature: is a weighted average of the temperature of the surfaces surrounding a person.
- air velocity: affects the exchange of heat between the person and the air, the faster the air is moving, the greater the heat exchange (convection).
- relative humidity: The humidity of the air affects evaporative cooling. The higher the relative humidity, the more difficult it is to lose heat through the evaporation of sweat.

The two physiological parameters are:

- Activity level or metabolic rate M : Metabolism is a biological process performed by the human body to obtain the energy needed from food and store it as chemical energy. This process generates energy for human activities. If work or physical activity are performed, most of the energy released is in the form of heat and mechanical work. The rate of this transformation per unit of skin surface area is called the 'metabolic rate' which increases in order to produce the energy needed for the various physical activities. The energy required for mechanical work will vary from about zero for many activities to no more than 25% of the total metabolic rate. The metabolic rate depends on the activity level, age, and sex, and is proportionate to the weight and size of the body.
- Clothing insulation: is a property of the clothing itself, representing the resistance to heat transfer between the skin and the clothing surface. The rate of heat transfer through clothing is affected by conduction

We have established in this section that comfort, in the broad sense, is a complex and subjective notion that cannot be evaluated quantitatively. In fact, thermal comfort is very sensitive to the environmental conditions in which the individual is located but also to the person physiology through his metabolism. Its maintenance results in the balance between the gains (thermogenesis) and the heat loss (thermolysis) experienced by the individual. The subject is so vast that we will focus on the study of the microclimate and heat exchanges considering only the influence of ambient temperature in the context of a resting state.

I.1.2 Heat and moisture transfer within the microclimate

A large part of building energy consumption is attributed to room temperature control using Heating, Ventilation and Air Conditioning (HVAC) systems. Decreasing this consumption, even slightly, will contribute to both environmental protection and costs saving. One way is to support building insulation; another way is to control the energy consumption by personal thermoregulation. This latter point has justified the emergence of technical textiles and, in particular, the so-called "smart" textiles (some examples will be detailed in section I.1.3), adapted to the surrounding conditions. Due to the increased desire of performance and living's standard, new textile technologies are emerging in clothing by improving the wearer's comfort, and thus promoting exchanges between humans and their environment. It will act on heat and hydric

transfers at the skin-textile interface (microclimate), in order to maintain the equilibrium of the thermal balance [24].

The garment acts as a barrier between the skin and the environment. One of the required functions for clothing is to keep the heat and humidity of the human body to a certain level depending on environmental conditions and physical activity. One can consider three areas where these exchanges occur (Figure. 1.2). The first one takes into consideration the transfers between the skin and the clothing, in the air gap, which we have already defined as the microclimate (MC). The second one considers the transfers inside the garments and the last one the transfers between the outer surface of the garment and the environment [25,26].

The moisture transfer mechanism includes wetting and capillary diffusion. The transmission of water vapor is due to the difference in its concentrations. The fibers absorb water vapor thanks to their compositions and structure. These water transfers are dynamically coupled with heat transfer [27].

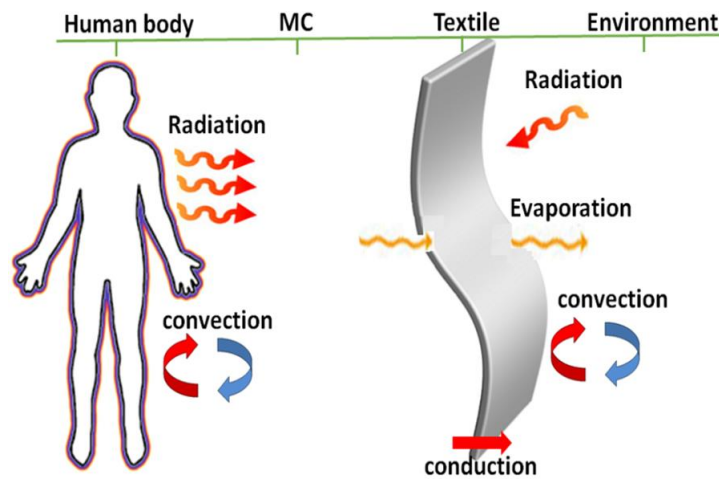


Figure. 1.2: Thermal and moisture exchanges within MC, textiles and the environment.

Heat transfer mechanisms in textiles include conduction, radiation and convection. The various mechanisms of conduction, convection and evaporation transfer are briefly presented below.

I.1.2.1 Conductive heat transfer

Conduction is the phenomenon by which heat is transmitted from a high to a low temperature region within a solid medium (liquid or gaseous under certain conditions) or between different media in contact with each other. It is based on the transmission of the kinetic energy of thermal agitation of the particles from the higher temperature regions to the lower one [28,29]. The conductive heat flux is expressed using Fourier's law:

$$\vec{\phi}_{\text{cond}} = -\lambda \cdot \overrightarrow{\text{grad}}(T) \quad \text{I.1}$$

Where $\vec{\phi}_{\text{cond}} \left(\frac{W}{m^2} \right)$ is the conductive heat flux, $\lambda \left(\frac{W}{m.K} \right)$ is the thermal conductivity of the material and $\overrightarrow{\text{grad}}(T)$ is the temperature gradient, expressed in $\left(\frac{K}{m} \right)$.

The majority of conductive exchanges takes place between the garment and the solids on contact (shoes / floor, seat / buttocks...) or between the hands and objects that are cold or hot.

I.1.2.2 Convective heat transfer

When heat transfer is accompanied by mass transfer, it corresponds to a convective transfer. This mode of heat exchange exists within fluid media or when a fluid circulates around a solid. The amount of heat exchanged depends on the speed of the air flow (or liquid if the body is in the water) that passes around the body. The higher the speed, the more important is the heat exchange [30]. For example, the amounts of heat exchanged during a running is 6 to 7 times higher than during a walk [31]. As another example, when the room temperature exceeds the skin one (more than 34 °C), the body gains heat by convection [30]. This mode transfer occurs at the respiratory and cutaneous level.

At the respiratory level, the exchanges are a function of the ventilation rate and the temperature difference between the inspired air and the exhaled air [32], as seen in equation (I.2):

$$C_{\text{res}} = \frac{V_p C_p (T_{\text{ex}} - T_{\text{ins}})}{A_D} \quad \text{I.2}$$

Where C_{res} is the convection respiratory flow $\left(\frac{W}{m^2}\right)$, V is the ventilator flow $\left(\frac{l}{s}\right)$, ρ is the density of expired gases $\left(\frac{kg}{l}\right)$, C_p is the specific heat of gases $\left(\frac{J}{Kg.K}\right)$, and A_D is the body surface calculated (m^2) . T_{ex} and T_{ins} are respectively the temperatures of the exhaled and inspired air (K) . In 1972, *Fanger* proposed a simplified expression described in equation (I.3):

$$C_{res} = 0.0014 \cdot M(34 - T_{ins}) \quad I.3$$

With M the metabolic power expressed in $\left(\frac{W}{m^2.K}\right)$.

At the level of the cutaneous surface, the convective exchanges are established between the skin and the ambient air in contact, or in the microclimate (MC) of clothing created by the air trapped between the skin and the first layer of the garment. The heat flux exchanged by convection (C) is then calculated according to the equation (I.4):

$$C = h_c \cdot f_{cl.C}(T_{sk} - T_{ins}) \quad I.4$$

Where h_c is the convection coefficient $\left(\frac{W}{m^2.K}\right)$ that varies with the air velocity, $f_{cl.C}$ is the clothing area factor (unitless) and T_{sk} is the skin temperature. These exchanges increase when the air is renewed quicker, due to the movement of the wearer. It is the "pump" effect of the underwear climate (air gap between the skin and the garment).

I.1.2.3 Evaporative heat transfer

Evaporative heat exchange occurs at the skin (sweat) and pulmonary levels. At the respiratory level (E_{res}), the heat flux is estimated by the expression (eq. I.5) proposed by *Fanger* [33],

$$E_{res} = 0.0173 \cdot M \cdot (P_{ins} - 5.87) \quad I.5$$

which represents a multiple function of the vapor partial pressure in the inspired air (P_{ins} in kPa), the exhaled air (P_{ex} in kPa) and the ventilatory flow $\left(\frac{l}{s}\right)$.

At the skin level, the phenomenon of sweating allows an important evaporative heat loss. Indeed, the evaporation of the liquid film placed on the surface of the skin occurs by taking most of the heat necessary from the body, is evaluated by considering the law of *Kerslake* defined as follows:

$$E_{ev} = h_E \cdot w \cdot f_{cl.E} \cdot (P_{sk,sat} - P_{ins}) \quad I.6$$

Where E_{ev} is the overall evaporative flow of the skin $\left(\frac{W}{m^2}\right)$, P_{ins} is the partial pressure of ambient water vapor (kPa), $P_{sk,sat}$ (kPa) is the saturating pressure of water vapor at the skin temperature T_{sk} , w is the cutaneous wetting (unit less), $f_{cl.E}$ is the reduction factor of evaporative exchanges by the garment, and h_E represents the evaporation coefficient.

I.1.2.4 Radiative heat transfer

Heat emission and heat absorption occur in the form of electromagnetic (EM) radiation. Therefore everybody constantly exchanges heat with its environment in the form of EM waves [34]. Electromagnetic radiation can be classified according to the measured wavelength (Figure 1.3).

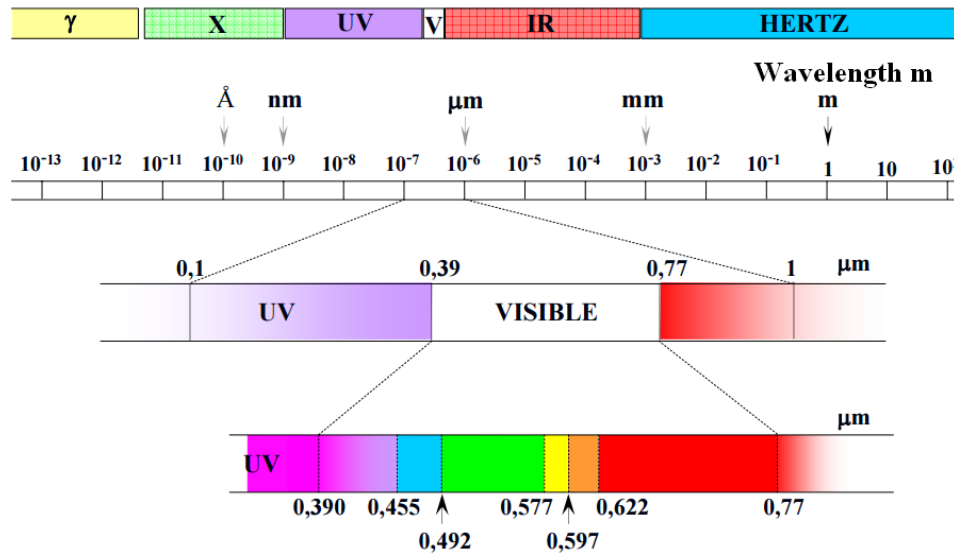


Figure 1.3: Classification of the electromagnetic waves spectrum [34].

Electromagnetic waves, such as light for example, traveling in a non-attenuating isotropic homogeneous medium, are described as transverse waves, which means that the electric field E

and the magnetic field H are perpendicular to the direction of wave propagation and that E and H are also perpendicular to each other [35] (Figure 1.4).

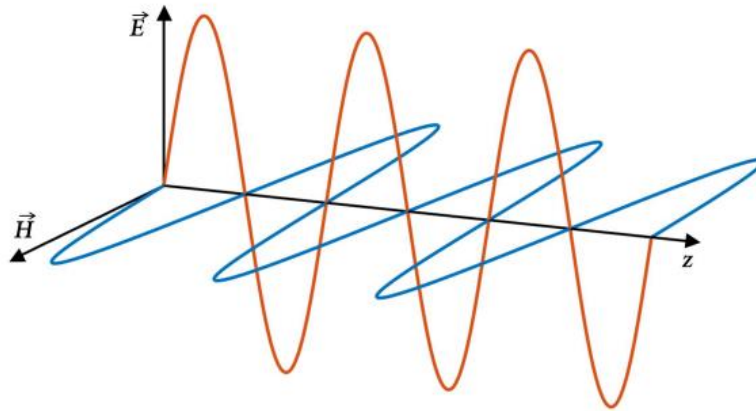


Figure 1.4: Propagation of an electromagnetic wave along the z axis [35].

The polarization of light incident upon a grating is defined by the orientation of its electric and magnetic fields relative to the plane of incidence, where the plane of incidence is defined by the two vectors being the propagation vector of the illumination and the grating normal.

Light is called unpolarized if the direction of this electric field fluctuates randomly in time. If the direction of the electric field of light is well defined, it is called polarized light.

TE (Transverse Electric) polarized light is characterized by its electric field being perpendicular to the plane of incidence. TM (Transverse Magnetic) polarized light is characterized by its magnetic field being perpendicular to the plane of incidence.

These two orthogonal (mutually perpendicular) polarizations are shown in figure 1.5. Note that the short arrows (TM polarization) in figure 1.5 (a) represent an electric field vibrating in the plane of the page, perpendicular to the beam direction. The dots (TE polarization) in figure 1.5 (b) represent an electric field vibrating in and out, perpendicular to the plane of the page. These vibrations are also perpendicular to the beam direction.

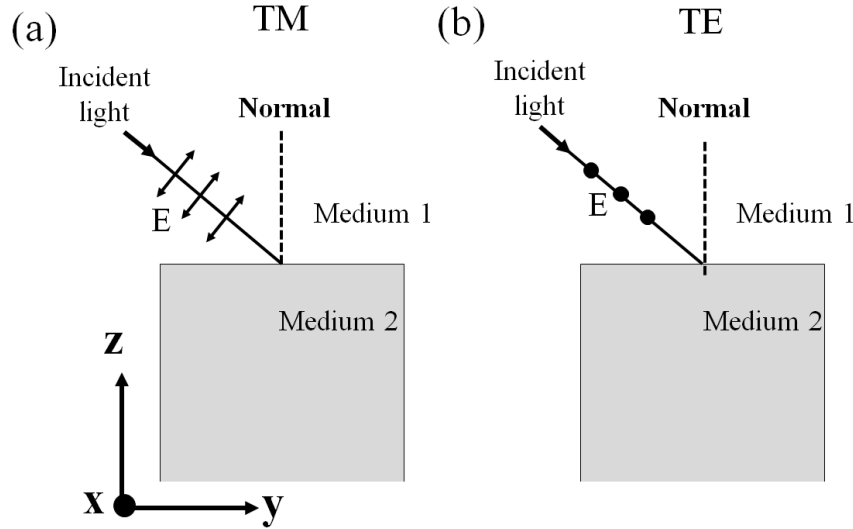


Figure 1.5: Illustration of the TE and TM polarizations of the incident light.

High temperature objects emit thermal radiations (infrared radiations) that transport energy. Higher temperature materials emit infrared radiations and heat transfers occur to cooler ones without direct contact between the two objects. In the case of the human body, heat radiation occurs between the human body and surrounding objects, such as clothing, objects and other equipments. The importance of radiation exchanges depends on the differences in temperature between the human body and the hot source, the distance between them and their respective absorptive power. The ability of a body to exchange heat in this form depends on its emissivity [34,36,37]. The emissivity of a material depends on its nature, surface condition and temperature. It corresponds to the ratio between the energy radiated by a body and the one a black body would radiate at the same temperature. A black body absorbs and sends back all the energy, which corresponds to an emissivity equal to 1. All other bodies have an emissivity less than 1. The spectral radiance, B_{λ}^0 , of the black body at the wavelength of the radiation is expressed by Planck's law (eq. I.7):

$$B_{\lambda}^0 = \frac{2hc^2}{\lambda^5} \frac{1}{e^{\frac{hc}{\lambda k_B T}} - 1} \text{ (W. m}^{-3}\text{)} \quad \text{I.7}$$

Where $\lambda = \frac{\lambda_0}{n}$, with λ_0 the wavelength of the radiation of the black body in vacuum and n the refractive index of the medium, λ is the wavelength of the radiation of the black body in the

medium in (m) , h is the Planck's constant ($h = 6.626.10^{-34}J.s$), c (m/s) is the propagation speed of the black body radiation in the medium, k_B is the Boltzmann constant ($k_B = 1.38.10^{-23}J/K$) and T is the black body temperature (K).

With an emissivity very close to 1, the skin is currently assimilated to a black body. Eq. I.7 allows to plot the normal EM emission spectrum of the human body skin at a temperature of 34 °C in the mid-infrared spectra (MIR) with the maximum of emission at 9.5 μm (Figure 1.6).

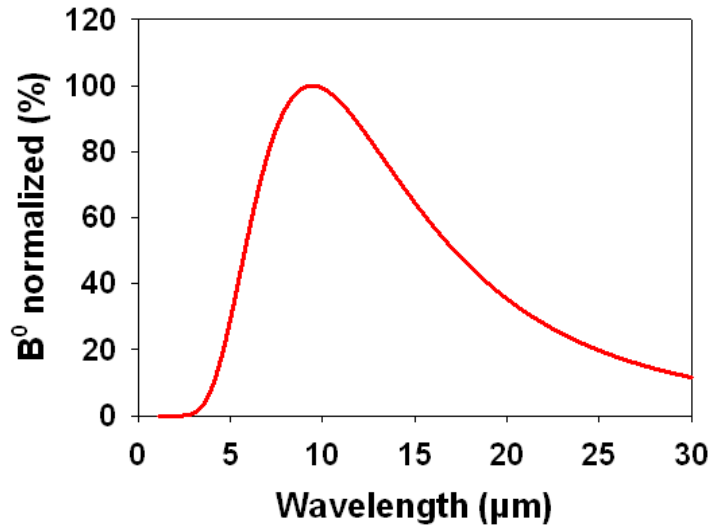


Figure 1.6: Electromagnetic emission spectrum of the human skin (assimilated to a black body) at the temperature of 34 °C.

The value of the wavelength λ_{max} (μm), which corresponds to the maximum of the spectral emittance peak of the black body, varies as a function of the temperature. It moves towards shorter wavelengths as the temperature increases. Wien's law of displacement is deduced from Planck's law in order to define the relation linking the wavelength λ_{max} and the temperature equation I.8.

$$\lambda_{max} = \frac{2897.8}{T} \quad I.8$$

The integration of the Planck formula for all wavelengths gives the total emittance of the black body which is no longer a function of temperature. We thus obtain the well-known Stefan-Boltzmann law as:

$$B_T^0 = \sigma T_{em}^4 \text{ (W. m}^{-2}\text{)} \quad \text{I.9}$$

Where σ is the Stefan-Boltzmann constant $\left(\sigma = 5.67 \cdot 10^{-8} \frac{W}{m^2 K^4}\right)$ and T_{em} is the emitter body temperature (K).

One can note that the emittance of a gray body is expressed by the equation I.10:

$$B_T = \varepsilon \sigma T_{em}^4 \text{ (W. m}^{-2}\text{)} \quad \text{I.10}$$

Where ε is the emissivity of the material (unitless), with value between 0 and 1.

The mechanisms of heat transfer (conduction, convection, radiation and evaporation) do not matter in equal proportions according to the state of the individual. Figure 1.7 presents the participation of the different modes of heat transfer within the microclimate in the case of an individual in standard conditions (rest or moderate activity, ambient temperature of 25 °C, standard clothing) [38]. In most cases, radiative transfers predominate and are responsible of about 50% of the heat losses produced by the human body. As a counter-example, in case of intense activity or when the ambient temperature exceeds 35 °C, the transfers by evaporation will become the main source of heat losses.

Heat exchange within the microclimate

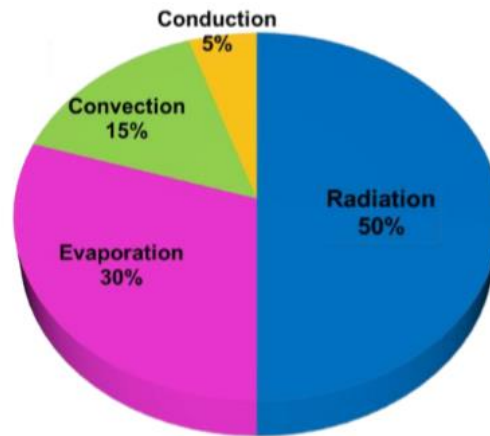


Figure 1.7: Distribution of the different modes of heat loss under standard conditions (rest or moderate activity, ambient temperature of 25 °C, standard clothing) [38].

I.1.3 Smart textiles for thermal comfort

I.1.3.1 Definition and classification

Smart textiles are defined as textiles that can detect and react to environmental conditions thanks to mechanical, thermal, chemical, electrical or magnetic stimuli. Depending on the functional activity of smart textiles, they can be classified into three categories [39]:

- Passive smart textiles, which constitute the first generation, can detect environmental conditions or stimuli.
- Active smart textiles belong to the second generation of intelligent textiles, acting both as actuator and sensors, by detecting signals, either directly, or from a control unit.
- Smart "interactive" textiles, the third generation of smart textiles, can feel, react and adapt to environmental conditions or stimuli. This class of textiles is a combination of traditional textiles and clothing technologies based on materials science, structural mechanics, sensors and actuators, signal processing technology, communication, artificial intelligence, biology ...

I.1.3.2 Smart textile structures

I.1.3.2.a) Waterproof-breathable textiles

When considering potential textile applications for thermal management, it is useful to review existing textile technology. Innovations in the field of waterproof-breathable fabrics can be categorized into four main types [40] (Figure 1.8) :

- High-density textiles : a microfiber fabric is very tightly woven such that no gaps appear between the threads [39,40]. The resulting textile is flexible with a very high breathability, especially with water vapor. Water transfers are made by diffusion [42] (Figure 1.8 (a)).
- Textiles laminated and coated with a microporous film: is generally made from the polymers polytetrafluoroethylene (PTFE), polyurethane (PU), polyolefins, polyamides, polyester, polyether and polyether-based copolymers. In most cases they can be cast directly onto the fabric (i.e. coated) or formed into a membrane and then laminated to the

fabric. This microporous film is classified as waterproof breathable because of its permanent porous structure (Figure 1.8 (b)). The membrane is built in such a way that the pores allow the transfer of water in vapor form but not as a liquid. The pore size ranges from 0.1 to 50 μm [43].

- Textiles made of film with hydrophilic treatment: The transmission of water vapor is provided by a molecular mechanism of adsorption, diffusion, and desorption. Hydrophilic groups embedded in the polymer chains of the material absorb, diffuse and desorb the water vapor molecules through the film to the outside [44, 45].
- A combination of microporous coating with a hydrophilic top coat: A microporous coating or film can be further coated with hydrophilic layer in order to increase waterproofness and to seal the surface pores, reducing the possibility of contamination of the microporous layer by dust particles, detergent, etc (Figure 1.8 (c)) [45].

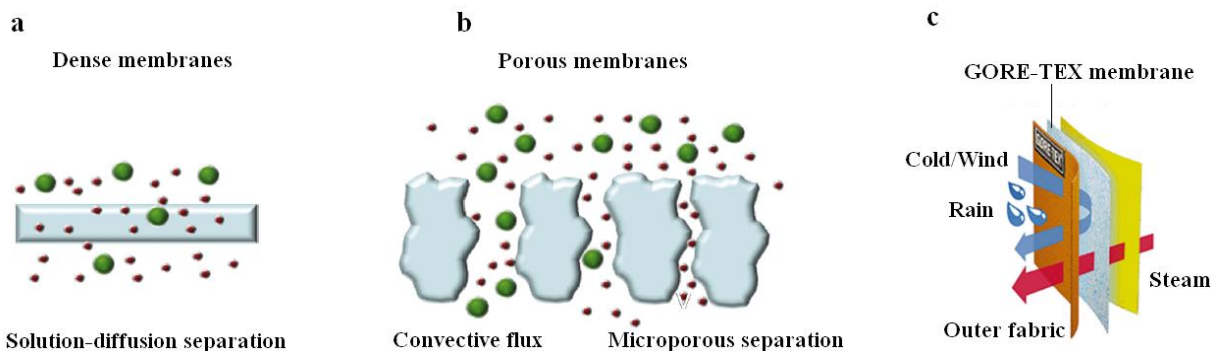


Figure 1.8: Mechanisms of transport through (a) dense and (b) porous membranes [44], and (c) representation of a waterproof and breathable membrane (GORE-TEX) [45].

As an example, one of the most used polymers in the textile industry is polytetrafluoroethylene (PTFE), which is a hydrophobic and chemically inert polymer. It is the key component of microporous membranes marketed under the name of GORETEX® (membranes capable of diffusing water vapor towards the outside without allowing liquid water to pass due to the size of its pores, by making a membrane both breathable and water repellent on its external face) (Figure 1.8 (c)).

I.1.3.2.b) Phase change materials

For thirty years, a new type of insulation material appeared on the textile market, named as phase change materials (PCMs), to improve the thermal behavior of fabrics (air permeability, conductivity and thermal resistance). This type of thermoregulated material interacts directly with the human / environment interface by modifying the characteristics of the microclimate.

When a material goes from one state to another, we talk about a phase change. PCMs have the particularity of being able to store energy in the form of latent heat. The heat being absorbed or restored during the transition from the solid state to the liquid state (and vice versa) [46]. Phase change materials absorb or release thermal energy, thus suddenly limiting the heat transfer over a temperature range of 2 to 3 °C for pure materials, and wider for some mixtures [47].

PCMs are based on the application of a simple physical principle. Beyond a certain temperature of transition, the material liquefies by absorbing the heat from the ambient atmosphere (endothermic transformation). When the temperature drops, they deliver the heat by solidifying (exothermic transformation). This material property is related to its important melting energy per unit of volume: the larger it is, the more interesting are the properties of heat storage / return. For energy storage, other phase changes can theoretically be feasible as solid-solid, solid-gas, liquid-gas, but in practice the solid-liquid represents the most efficient transition. Phase change process of PCM from solid to liquid and vice versa is schematically shown in figure. 1.9.

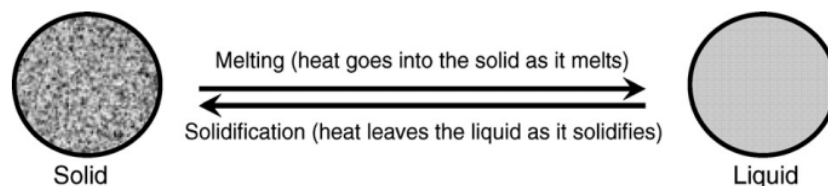


Figure 1.9: Schematic representation of the phase transformation process [48].

PCMs can be classified into three categories:

- Organic compounds, found in organic compounds as mainly paraffins, sugar alcohols, fatty acids and others less used compounds such as ketones or esters.
- Inorganic compounds, classified into three categories: salts, salt hydrates and metals.

- Organic and inorganic eutectics: eutectic PCMs are mixtures of two or more organic and inorganic substances that behave like a pure body with unique transition temperature.

With the development of this new PCM concept, the most recent reviews have focused on improving their properties and their integration in the field of building. Liu *et al.* reported on the enhancement of the thermal conductivity in building for better indoor thermal by increasing the charging/discharging rate of the PCM [49]. Akeiber *et al.* summarized different types of PCMs, changing their melting points within the thermal comfort zone. They reviewed thoroughly the integration of PCMs into building components i.e., walls, roofs, windows and floors [50].

PCM are also used in textile industry, in the form of microcapsules placed in the heart of the fibers, which can absorb, store and release the energy in a reactive way to warm when it is cold or cool when it is cold. PCMs regulate the heat transfer between the human body and the outside world.

The commercial textile structures contain microencapsulated paraffins and PEGs (polyethylene glycols) whose phase transformation takes place over a temperature range very close to the skin temperature [51,52]. These PCMs are microencapsulated in the form of small spheres, a few microns in diameter, resistant to abrasion, pressure, having good stability and chemical compatibility [53]. Whatever the physical state of the material, it remains trapped inside, which allows to consider the incorporation of microcapsules in the textile media either by spinning, by coating or in foam [54]. However, the implementation of the PCMs on textile is not satisfactory. Incorporation of microcapsules requires a compromise with the usual properties of the fabric. Their integration causes considerable decrease in the breathability of the clothing and modifies the moisture transfer [55]. Thus, a compromise between carriage rate and breathability is required for this type of product. Recently, a new type of process has emerged to integrate microcapsules PCMs within a fabric, called grafting. This technique corresponds to the durable fixation by covalent bonds of the membrane of the capsule on the textile fiber [56].

I.1.3.2.c) Shape memory materials

The shape memory materials (SMM) are likely to change shape from one transitional state to another, depending on an external stimulus. The shape transformation is most often activated by temperature, but also by a mechanical stress, electromagnetic, electrical, pH [57,58]. For several

years, interesting applications in the field of comfort have emerged with the development of shape memory Polymers or Gels (respectively SMP and SMG).

Figure 1.10 shows the shape memory effect of a polymer responding to a thermal stimulus, this is the most common activation to date. The polymer is heated to its vitreous transition temperature to be put into its temporary form (by extension or compression or torsion) and then cooled below its glass temperature (T_g) to fix it. When the polymer reaches its T_g again, it returns to its permanent shape.

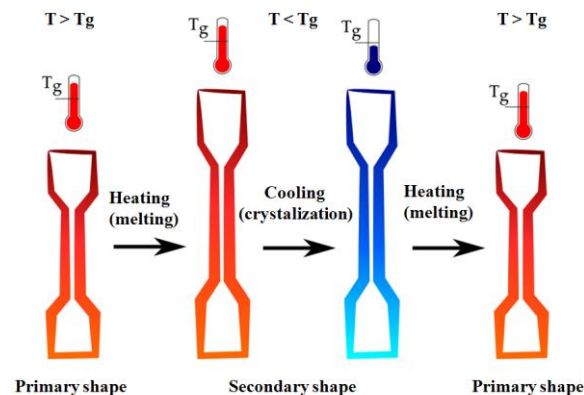


Figure 1.10: Schematic representation of the shape memory transformation by thermal activation [59].

The main shape memory polymers (SMP) studied are thermosetting polymers [60,61,62].

Ji F *et al.* reviewed that fibers based on SMPs can be implemented to develop smart textiles that respond to thermal stimulus. SMP can then be used for clothing, textile based on yarn, fabric or fiber [63]. These textile structures aim to improve the feeling of comfort in order to maintain the microclimate (MC) in the comfort zone of the individual [63].

Figure 1.11 explains the different transformation steps of a thermosetting shape memory polymer. In its permanent state at room temperature, in phase (1), the stiffness of the polymer is ensured by Van der Waals bonds. By heating (2), these bonds are broken allowing to the mobility of the molecular chains in the limit of the crosslinking nodes. Indeed, the elongation of the material will be higher as the length of the chains between crosslinking nodes will be large. The polymer can therefore be deformed (3). Internal stresses can then appear because of the conformation of the molecules which no longer corresponds to their stable state. By maintaining the deformation and

cooling (4), Van der Waals bonds reform and maintain the polymer in the secondary shape. By heating, Van der Waals bonds break again, and the polymer resumes its permanent form under the effect of internal stresses (5) [64,65].

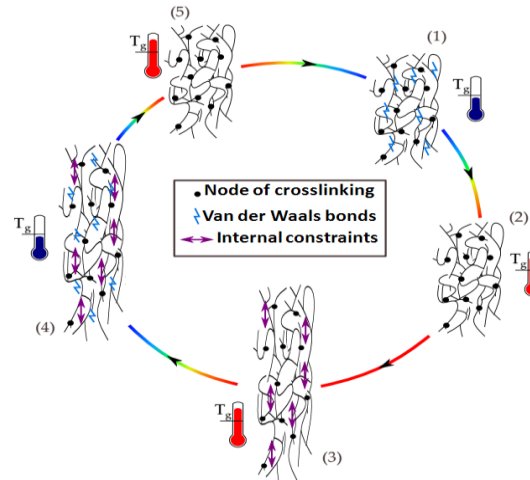


Figure 1.11: Working steps of a shape memory polymer [65].

This shape memory of polymers has been known for many years, but over the past two decades it has attracted a certain interest in the academic as well in industrial world because many innovative applications are envisaged.

Shape Memory Gels (SMGs) have the ability to respond to infinitesimal changes in their environment through volume changes. Volume changes can be triggered by temperature, variation of the pH value, ... [52,66] .

Gels made from poly (N-isopropyl acrylamide) (PNIPAAm) have attracted considerable interest because of their potentiality to be activated by the temperature or LCST ("Lower Critical Solution Temperature"), in an aqueous medium of about 34 °C, close to skin temperature [67]. Most of the developments concern the pharmaceutical field with the controlled release of active ingredients in organs such as the liver [68]. However, the potential of these biomaterials has shifted recently to textile applications.

I.1.3.2.d) Conductive materials

During thermophysical exchanges with the fabric, part of the transfers is done by conduction. Thus, conductive materials enhancing conductive exchange can be inserted. The addition of nickel, copper, silver or carbon in clothing offers a combination of thermal and electrical properties for a variety of applications [69]. The use of electrically conductive materials makes possible to design clothes heated by the Joule effect in extreme winter conditions or diving suits for very cold water. In these cases, a source of electrical power is needed [70].

The materials listed above deal on heat and moisture transfers by conduction, convection and evaporation but not on radiative transfers. However, we have seen (5% conduction, 15% convection, 30% evaporation and 50% radiation [36]) that in MC, these radiative transfers represent the majority of heat losses in many situations, especially under standard conditions, which are the subject of our study.

With the increasing amount of research dedicated to wearable technology nowadays, there is a new opportunity to integrate thermal management capabilities into textiles for everyday use. This would target one of the major domains in energy consumption, cooling and heating systems. Our approach to thermal management involves using smart textiles to adjust, control and even modulate EM radiation to improve the heat balance of the microclimate. We can cite the nanoporous polyethylene membrane of P.C. Hsu *et al* [71], which allows dynamic warming in a cold atmosphere in order to keep the microclimate temperature stable and a body temperature around 37 °C.

During my thesis, we rely on the properties of photonic crystals which have remarkable properties very well known for the control of thermal radiation. Depending on the chosen geometry, they may have desirable optical properties either in the visible, near infrared, medium infrared or far infrared domains. Photonic crystal structures induce interesting physical phenomena depending on the absolute band gap properties of the structure, which results in particular optical behavior.

I.2 Introduction on photonic crystals and Fano resonances

I.2.1 Introduction

Since the early works of Yablonovitch and John in 1987 [72,73], the concept of "Photonic Crystals" has aroused a great interest in many research fields, particularly nanophotonics. Photonic crystals have special properties that arise from their regular arrangement along one or more directions of space. What makes the use of photonic crystals advantageous compared to other structures, is the fact that they are one of the only materials able to control the light. In fact, these structures allow to overcome certain obstacles to scientific development in areas such as wave optics or electromagnetism, thus offering the possibility to fabricate photonic devices capable of confining, filtering and guiding light.

I.2.2 Photonic crystals

The photonic crystals are artificially structured dielectric or metal materials whose dielectric constant varies periodically at the wavelength scale along several directions of space (1D, 2D, 3D) with a sufficiently high index contrast. Figure 1.12 shows the 3 main types of photonic structures [74, 75].

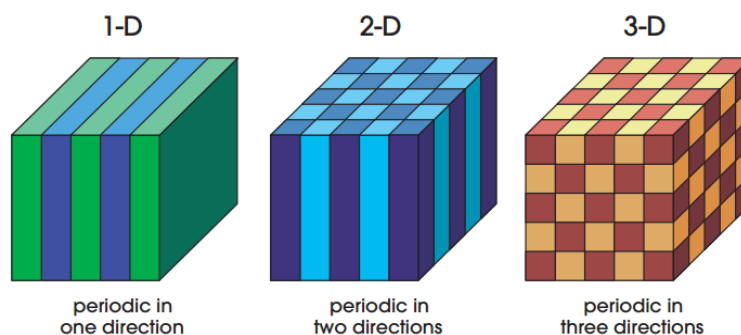


Figure 1.12: Schematic representation of one-dimensional (1D), two-dimensional (2D) and three-dimensional (3D) photonic crystals. The different colors represent materials with different dielectric constants [75].

These periodic structures have the ability to inhibit the propagation of light in certain directions in a frequency range called photonic band gap (PBG) [76]. To better understand the functionalities

of such material, it is possible to make the analogy with the electronic energy band gap characterizing atomic crystal lattices: the photonic structures thus have one (or more) band gap frequencies for which no electromagnetic wave can propagate, whatever the polarization and the direction of propagation of this wave.

Photonic crystal is obtained when the lattice parameter of the periodic crystal is of the same order of magnitude than the wavelength of light in the medium [77]. The photonic bandgap property was originally shown by Lord Rayleigh in 1887 in Bragg mirror structures, and then, in 1987, Yablonovitch and John were able to extend photonic band gaps (PBGs) to two and three dimensions [72,73].

I.2.2.1 One-dimensional photonic crystals (1D): The Bragg mirror

One-dimensional structures have been extensively studied and used as dielectric mirrors, optical filters or anti-reflective coatings. It is characterized by alternating, in a single direction of space, two dielectric media whose dielectric constants ε_1 and ε_2 are different. This structure is also called Bragg mirror (Figure 1.13 (a)) [75,78]. Thus, when an incident wave propagates within one of these two medium and arrives at the interface between them, part of this light is reflected. This reflection is accompanied by a phase change of π if the wave goes from a low index medium to a high index medium. The other part is transmitted to the second medium in which it will spread. The operation we have just described is repeated for each constituent layer of the Bragg mirror as shown in figure 1.13 (b). This is a very simple description of the phenomenon. We must still pay attention to the value of the phase shifts, which themselves depend on the wavelength. Depending on their values, constructive or destructive interference will lead to complete or zero reflection.

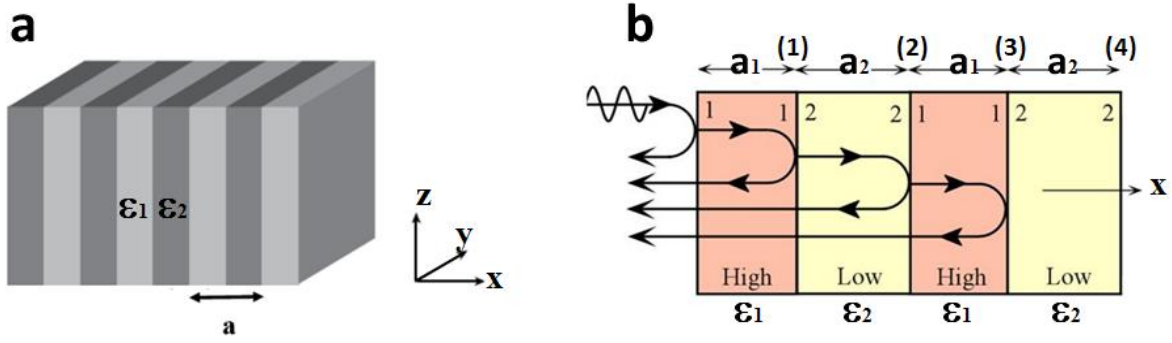


Figure 1.13: (a) Schematic of a Bragg mirror made of stacked layers of thicknesses a_1 and a_2 of different permittivity ϵ_1 and ϵ_2 ($\epsilon_1 > \epsilon_2$), (b) Principle of multiple interferences phenomenon within a Bragg mirror. For an incident wave propagating within a first medium is partly reflected at the interface (1) while the other part is transmitted in the second medium. This phenomenon is repeated at all interfaces [75].

To obtain a perfectly reflective structure (Figure 1.13 (b)) over a defined wavelength range, the thickness of the layer has to be chosen judiciously. When the total optical thickness $a_1 \cdot n_1 + a_2 \cdot n_2$ of the alternations is $\lambda/2$ where λ is the wavelength, the wave reflected at the interface (1) is in phase with those reflected at the interfaces (3), (5), etc. Following this constructive interference, a total reflection is obtained, which means that the wave may not spread, thus dealing with a photonic band gap. In the particular case where the two layers of each alternation have the same optical thickness $a_1 \cdot n_1 = a_2 \cdot n_2 = \lambda/4$, it is observed that the waves reflected by all interfaces (1), (2), (3), etc. are in phase. This corresponds to the largest band gap and allows to make dielectric mirrors with very high reflection coefficients (close to 1). Without going into the calculations details, when the optical thicknesses of the different layers are equal, the width of this band gap $\Delta\omega$ depends only on the index contrast [79].

$$\Delta\omega = \frac{4}{\pi} \omega_0 \sin^{-1} \left| \frac{n_1 - n_2}{n_1 + n_2} \right| \quad \text{I.11}$$

Where $n_1 = \sqrt{\epsilon_1}$ and $n_2 = \sqrt{\epsilon_2}$ are the refractive index of the two dielectric materials and ω_0 the central frequency.

One-dimensional photonic crystals are the oldest structures that have been studied. They are mainly used as dielectric mirrors (for example for lasers) or optical fiber. During the year 1972, V.P. Bykov conducted a detailed theoretical study of one-dimensional optical structures. More specifically, he was the first to examine the effect of band gaps on spontaneous emission from

atoms and molecules integrated into the structure [80]. He also formulated hypotheses on the use of two-dimensional and three-dimensional structures discussed in the following section.

I.2.2.2 Two-dimensional photonic crystals (2D)

A two-dimensional photonic crystal is a structure which presents a periodic modulation of the dielectric permittivity in two spatial dimensions, while the effect in the third dimension is homogeneous. There are several ways to achieve two-dimensional structures. For example, we can place disconnected (isolated) dielectric micro-pillars in the air medium (Figure 1.14 (a)) or air cylinders in a dielectric platform (Figure 1.14 (b)). In order to open wide bands of low permittivity, a sufficiently large index contrast (i.e. difference between the indices of the medium and the micro-pillars) is required.

2D photonic crystals in membranes of finite heights (2D PC) are a special class of photonic crystals, which consists of a two-dimensional periodic network introduced into a guide layer (usually a dielectric) with a high refractive index (Figure 1.14 (c)). These crystals are quasi-3D structures that have a large and more or less complete photonic band gap for any electromagnetic wave propagating in the membrane. Due to their finite structure and the variety of possible functionalities which they offer, these 2D PCs can be easily integrated with other photonic components for the design of photonic integrated circuits by means of micro- and nano-manufacturing.

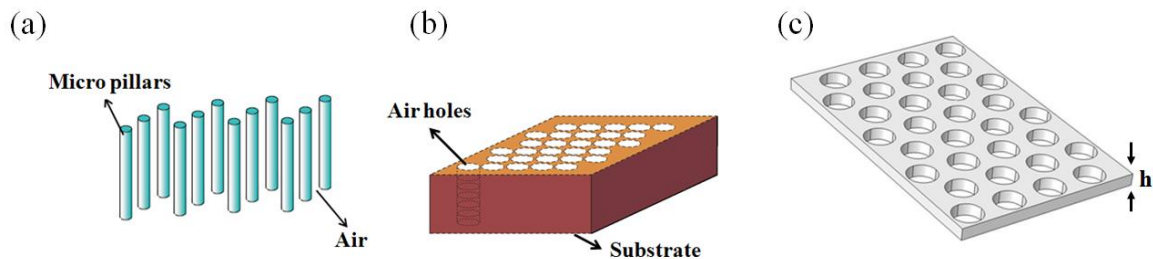


Figure 1.14: Example of infinite two-dimensional photonic crystal of (a) micro-pillar networks, (b) air columns in a dielectric substrate [75]. (c) 2D photonic crystals in membranes of finite heights.

I.2.2.3 Three-dimensional photonic crystals (3D)

Three-dimensional photonic crystals are structures with a dielectric constant arranged periodically along the three directions of space. Then, we have the possibility to obtain a complete band gap in all directions of space.

There are several types of structures that have been constructed [75]:

- The woodpile structure: is obtained thanks to a stack of rectangular or circular dielectric rods. The two consecutive levels are perpendicular and the two consecutive planes of parallel rods are offset by half a period. In the field of microwaves wavelenghts, such structures have been made either with alumina rods or with silicon. In this case, etched grids are stacked on top of each other by rotating them 90° on each floor while preserving the alignment of the entire structure [81]. The example of Figure 1.15 (a) is obtained by depositing polycrystalline silicon ribbons in silica trenches in successive layers. Once this structure is achieved, the silica is removed in order to obtain a 3D Si/air photonic crystal whose index contrast is sufficient to open an omnidirectional energy band gap [82].
- Yablonovite: In the objective of improving the laser efficiency, E. Yablonovitch interested in how he could prevent spontaneous emission in semiconductor lasers [83]. To do this, he designed a structure with a spatial periodicity with period exactly half the wavelength in all directions of space. The story usually retains from him his famous "Yablonovite" shown in Figure 1.15 (b), one of the first structures with a 3D photonic band gap in the field of microwaves wavelenghts he proposed in 1993 [84]. It is obtained by drilling holes in Plexiglas at three azimuthal angles separated by 120° and making an angle of 35° to the normal.
- Inverse opals or Inverse Colloidal Crystals-Spheres: are three dimensionally ordered macroporous materials formed through the infiltration of an artificial opal or from a native material from which we removed the spheres (Figure 1.15 (c)).

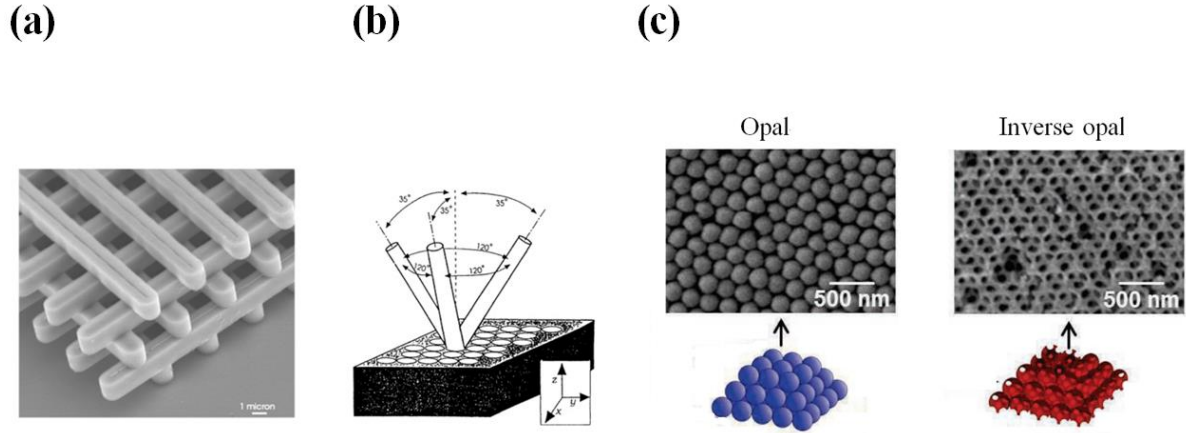


Figure 1.15: Three famous examples of three-dimensional photonic crystals, (a) schematic representation of the woodpile structure [83], (b) Yablonovite structure [82] and (c) Opale and inverse opals structure [75].

I.2.3 Maxwell equations in periodic dielectric structures

In this part, photonic crystal will be assumed to extend infinitely along all directions of space, characterized by a relative dielectric permittivity $\epsilon_r(x,y,z)$ assuming to be real and periodic along N directions (with $N = 1, 2$ or 3) and invariant along the other $3 - N$ orthogonal directions. The elementary cell of a photonic crystal can be obtained from the vector r which defines the position of any direct lattice of the crystal:

$$r = \sum_{i=1,N} \rho_i a_i \text{ with } \rho_i \in [0, 1] \quad \text{I.12}$$

Where a_i are the vectors describing the elementary cell of the lattice and $i \in \{1, \dots, N\}$.

We assumed that the electric and magnetic fields E and H satisfy the time-harmonic Maxwell's equations and the fields can be written:

$$E(r, t) = E_0 e^{-i\omega t} \quad \text{I.13 a}$$

$$H(r, t) = H_0 e^{-i\omega t} \quad \text{I.13 b}$$

We can write the Maxwell equations in the following form:

$$\nabla \times E - i\omega\mu_0 H = 0 \quad \text{I.14 a}$$

$$\nabla \times H + i\omega\epsilon_0\epsilon_r(x, y, z)E = 0 \quad \text{I.14 b}$$

$$\nabla \cdot [\varepsilon_r(x, y, z)E] = 0 \quad \text{I.14 c}$$

$$\nabla \cdot H = 0 \quad \text{I.14 d}$$

According to (I.16 a) and (I.16 b) equations, the following two equations of propagation are obtained for the electric and magnetic fields:

$$\frac{1}{\varepsilon_r(x, y, z)} \nabla \times [\nabla \times E] - \frac{\omega^2}{c^2} E = 0 \quad \text{I.15 a}$$

$$\nabla \times \left[\frac{1}{\varepsilon_r(x, y, z)} \nabla \times H \right] - \frac{\omega^2}{c^2} H = 0 \quad \text{I.15 b}$$

Where ε_r is a dielectric function and c is the speed of light. We deduce that E and H are eigenfunctions with eigenvalues $k^2 = \frac{\omega^2}{c^2}$.

This equation can be rewritten as an eigenvalue equation:

$$\widehat{O}_1 E = \frac{\omega^2}{c^2} E \quad \text{I.16 a}$$

$$\widehat{O}_2 H = \frac{\omega^2}{c^2} H \quad \text{I.16 b}$$

Where \widehat{O}_1 and \widehat{O}_2 are an operator such as $\widehat{O}_1 = \left(\frac{1}{\varepsilon_r(x, y, z)} \nabla \times \nabla \times \right)$ and $\widehat{O}_2 = \left(\nabla \times \frac{1}{\varepsilon_r(x, y, z)} \nabla \times \right)$.

The periodicity of the dielectric function $\varepsilon(r)$ is given by:

$$\varepsilon(r + R) = \varepsilon(r) \quad \text{I.17}$$

Where R is the direct lattice vector.

The solutions of the equation of propagation assume the form of Bloch modes. These modes satisfy Maxwell's equations for crystals formed from any type of material.

Recall that for crystals, the modes of Bloch u are the eigenfunctions of the translation operators T , and they are written in the following mathematical form:

$$u = v \cdot e^{ik \cdot r} \quad \text{I.18}$$

Hence $v = \sum_G V(G) e^{iG \cdot r}$ and G belongs to the reciprocal lattice. So, the Bloch modes are the product of a plane wave $e^{ik \cdot r}$ by a function v which has the periodicity of the crystalline lattice. The equation I.20 becomes:

$$u = e^{ik \cdot r} \sum_G V(G) e^{iG \cdot r} \quad \text{I.19}$$

For photonic crystals, Bloch's functions can be written as follows:

$$E = e^{ik \cdot r} \sum_G E(G) e^{iG \cdot r} \quad \text{I.20 a}$$

$$H = e^{ik \cdot r} \sum_G H(G) e^{iG \cdot r} \quad \text{I.20 b}$$

The modes which can propagate in the photonic crystal will be given by calculating the u_k and ω_k for each wave vector k of the first Brillouin zone. The set of discrete solutions of ω thus constitutes the band structure or the dispersion diagram of the periodic structure.

I.2.4 Brillouin zone and band diagram

I.2.4.1 Irreducible Brillouin zone

The first Brillouin zone is the elementary cell of reciprocal space where the points are closer to the origin than all the other nodes of the periodic lattice. Figures 1.16 and 1.17 show different examples of photonic crystals as well as the corresponding irreducible Brillouin zone.

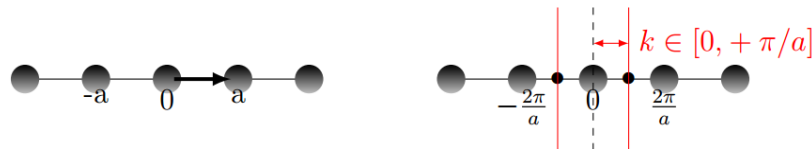


Figure 1.16: Example of a one-dimensional photonic crystal (left) and the corresponding Brillouin zone (right).

The interval $[-\frac{\pi}{a}; +\frac{\pi}{a}]$ is the first Brillouin zone and $[0; +\frac{\pi}{a}]$ is the irreducible Brillouin one.

In the 1D and 2D cases, the first Brillouin zone is obtained by tracing the mediators of the segments joining the origin to the nodes closest to the reciprocal lattice. From the domain thus delimited, one can cover all the reciprocal space thanks to the translations of vectors G . In other words, it is enough to make evolve k in this domain to represent the set of the dispersion curves of the crystal. The k domain can be further reduced by taking advantage of the symmetries of the crystal. In the case of 1D, the symmetry of the crystal with respect to the origin has the consequence that, if a wave of vector k and frequency ω is the solution of the problem, the wave of vector $-k$ also propagates in the opposite direction. We can thus restrict the study interval to $[0; +\frac{\pi}{a}]$ instead of $[-\frac{\pi}{a}; +\frac{\pi}{a}]$ where a is the step of the lattice.

Let us now consider the two-dimensional crystal with square symmetry (Figure 1.17 (1)). This structure made from dielectric or metal rods supposed to be infinite, has 4 axes of symmetry which are deduced from each other by symmetries of $\frac{\pi}{4}$. The reciprocal lattice is also a square lattice and the first Brillouin zone is defined by:

$$k_x \in [-\frac{\pi}{a}; +\frac{\pi}{a}] \text{ and } k_y \in [-\frac{\pi}{a}; +\frac{\pi}{a}]$$

It has been shown that the studied interval of k can be further reduced by using the different symmetries of the structure. Finally, the k values are reduced to an isosceles right triangle whose two equal sides have length $\frac{\pi}{a}$. The points Γ (0, 0), X ($\frac{\pi}{a}$, 0) and M ($\frac{\pi}{a}$, $\frac{\pi}{a}$) designate the three vertices of the triangle that constitutes the irreducible Brillouin zone of the square lattice. In the study of dispersion diagram, we generally limit ourselves to the three sides of the triangle.

In the case of a two-dimensional crystal with rectangular symmetry of length a and width b (Figure 1.17 (2)), the reciprocal lattice is also a rectangular lattice and the first Brillouin zone is a rectangle whose length is $\frac{\pi}{a}$ and the width $\frac{\pi}{b}$ [85]. The vertices are usually designated by Γ (0, 0), X ($\frac{\pi}{a}$, 0), M ($\frac{\pi}{a}$, $\frac{\pi}{b}$) and P (0, $\frac{\pi}{b}$). Here again, in the study of dispersion diagram, we limit ourselves to the four sides of the rectangle [86].

In the case of a two-dimensional crystal with hexagonal symmetry (Figure 1.17 (3)), the reciprocal lattice is also a hexagonal lattice and the first Brillouin zone is a hexagon. In this case, we have six axes of symmetry which are deduced from each other by rotations of $\frac{\pi}{6}$ with a rotation invariance

of $\frac{\pi}{3}$. We show that the irreducible Brillouin zone is a half-triangle equilateral whose vertices are usually designated by Γ (0, 0), K ($\frac{4\pi}{3a}$, 0) and M ($\frac{\pi}{a}$, $\frac{\pi}{\sqrt{3}a}$). As for the first case, note that in the study of the dispersion diagram, we limit ourselves to the three sides of the triangle.

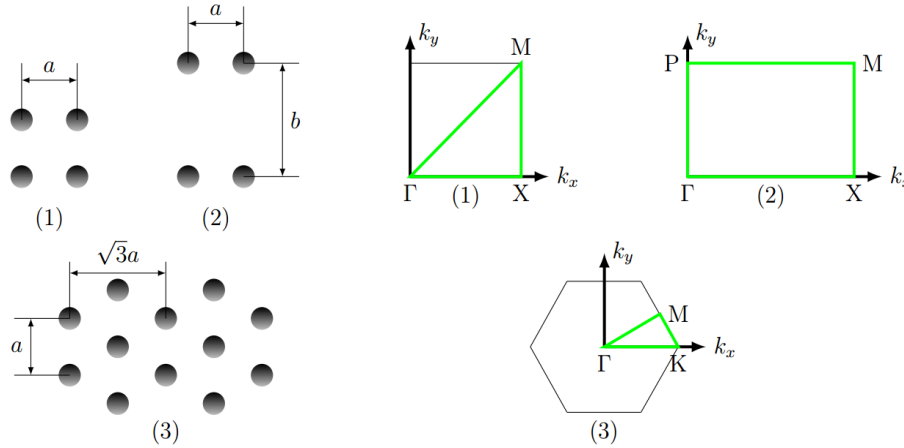


Figure 1.17: Two-dimensional photonic crystals with (1) square, (2) rectangular and (3) triangular symmetries with their corresponding irreducible Brillouin zones (in green line) [87].

1.2.4.2 Band diagram

The relationship between the pulsation and its wave vector, $\omega(k) = k$, is called the dispersion relation whose representation is the dispersion curve. The graphical representation of the set of dispersion curves for the values of the wave vector belonging to the first Brillouin zone is called the scatter plot, or band diagram. The different bands of energy and the band gaps appear clearly on this diagram.

As an illustration, we present below a band diagram for the 1D case (Figure 1.18) and another for the 2D case (Figure 1.19). The dispersion curves of the modes are represented in solid black line. It may be noted that certain frequency bands $\Delta\omega$, underlined by the gray background on the dispersion diagram, are free of modes: these bands correspond to the complete band gaps.

Band diagram of one-dimensional photonic crystals: The 1D crystal consists here of a period of two successive layers of a material of high index n_h and another of low index n_b ; the period is noted a . The dispersion curves of the eigenmodes are displayed in figure 1.18 and present the evolution of the reduced pulsation as a function of the wave vector k varying from $-\frac{\pi}{a}$ to $\frac{\pi}{a}$ in

order to describe the first Brillouin zone. The gray regions represent the complete band gaps of the crystal. We note that the structure taken as an example has 5 band gaps for reduced pulsations ranging from 0 to 2 [88].

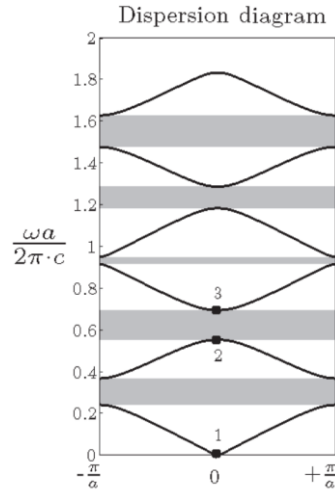


Figure 1.18: Example of band diagram of one-dimensional photonic crystals representing the evolution of the reduced pulsation as a function of the wave vector k varying from $-\frac{\pi}{a}$ to $+\frac{\pi}{a}$.

Band diagram of two-dimensional photonic crystals: Structures with a two-dimensional periodicity are a generalization of the concept of Bragg reflector. In the two-dimensional case, the wave vector k can take all the directions of propagation in the plane of the periodicity, according to the first Brillouin zone.

Figure 1.19 shows the dispersion diagram of a photonic crystal having a square lattice and a periodicity a , composed of silicon and circular air inclusions of normalized radius $r/a = 0.43$ [89]. Thus, in this example, starting from the origin (Γ) the wave vector will follow the direction X, then the direction M, then returns to the origin Γ . It has two complete band gaps near the reduced pulsations of 0.3 and 0.45.

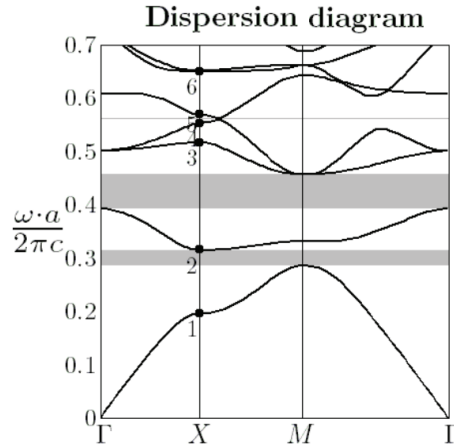


Figure 1.19: Example of dispersion diagram of a 2D crystal linking the reduced pulsation versus the direction of the wave vector for the first six modes.

I.2.5 Fano resonance

The Fano resonances were introduced for the first time by Ugo Fano in 1961, who also proposed a theoretical description in his famous article published in 1961 [90]. The unusual presence of sharp peaks in the absorption spectrum of a noble gas, observed by Beutler in 1935, caught his attention. One of the main features of Fano resonance is to have a distinct asymmetrical line profile. This dissymmetry comes from the coupling between a discrete state and a continuum. This type of resonance can be observed in many fields of physics, such as quantum physics [91], plasmonic [92], but also photonics [93,94].

Fano effect is not limited to quantum systems, but is a very general wave interference phenomenon that has also been encountered in optical transmission and reflection spectra for a wide variety of structures such as photonic crystals [95]. Actually the shape of the asymmetric profile depends on the interaction between the discrete state and the continuum state (Figure 1.20). This interaction is quantified by a phenomenological parameter q . In the case of a discrete state of energy E_d and width Γ_d , the profile of the cross-section of the observed physical phenomenon is shown in:

$$\sigma(k) = \frac{(k + q)^2}{k^2 + 1} \quad \text{I.24}$$

Where k is the reduced energy defined by $\frac{2(E - E_d)}{\Gamma_d}$.

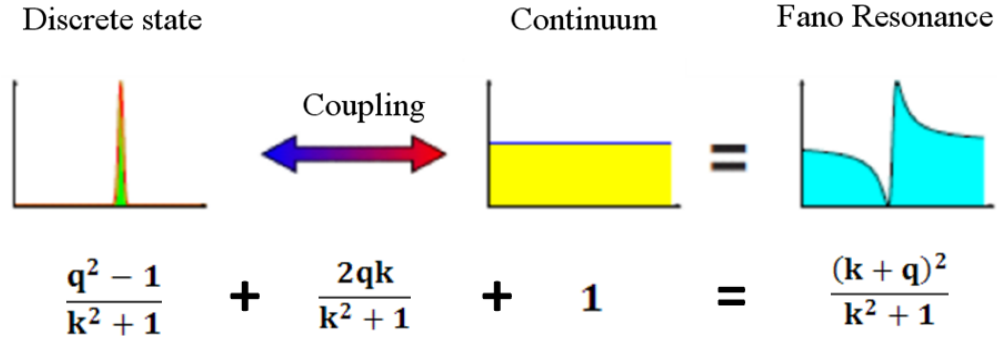


Figure 1.20: Definition of the Fano formula as the superposition of a discrete state of Lorentzian profile and a flat continuum [95].

The parameter q characterizes the ratio of the probabilities of transition between the discrete state and the continuum, describing the degree of asymmetry of the resonance. It can take any values between 0 and infinity and thus gives rise to many different asymmetrical profiles (Figure 1.21), making the richness of the Fano resonances. In the case of $q = \infty$, the probability of an interaction between the discrete state and the continuum is weak and we obtain a Lorentzian profile. On the other hand, when $q = 0$, a symmetrical anti-resonance is observed. In the case of $q = 1$, we obtain an asymmetric profile called "perfect" (continuous and discrete transitions of the same force) with a maxima $E_{max} = E_d + \frac{\Gamma_d}{2q}$ and a minima $E_{min} = E_d - \frac{\Gamma_d}{2q}$

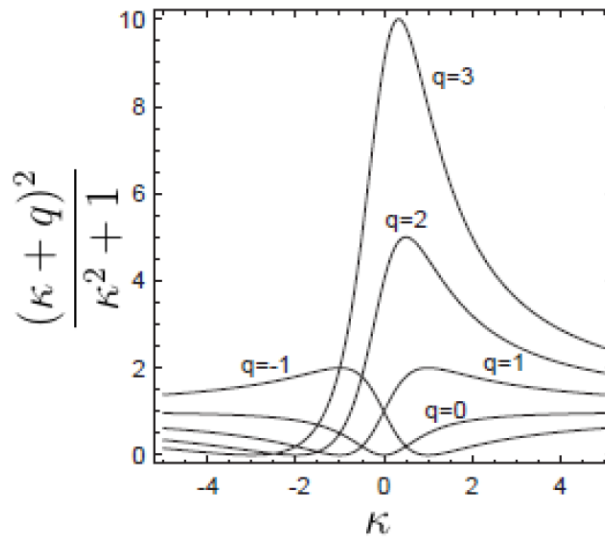


Figure 1.21: Fano resonances shapes for different values of q .

Fano resonances can appear in different physical media and their profiles can be deduced from the Fano formula I.24. Many profiles can be obtained by adjusting the asymmetric parameter q , thereby obtaining various quality factors making these physical systems interesting for different applications such as photonic devices and quantum systems. The asymmetrical shape and the abrupt transition from a maximum to a minimum of the Fano resonance profile have opened the door to new perspectives for many applications in photonic devices such as optical filters, switches, sensors, reflectors broadband, lasers, detectors.... In the rest of this chapter, we will look at the cases of 2D photonic crystal plates that can be easily integrated in many photonic devices [94].

Let us take a square lattice of period a , with air holes of radius $r = 0.2.a$ formed in a dielectric plate of dielectric constant $\epsilon_h = 12$ and thickness $t_h = 0.5a$ as presented in figure 1.22 (a). The transmission spectrum obtained for this structure for an incident wave perpendicular to the network is presented in figure 1.22 (b). It shows the presence of Fano resonances with strong asymmetric profiles. One can see in the neighborhood of the resonance that the intensity of transmission undergoes a sudden variation between 0 and 100% indicating the existence of constructive and destructive interferences very close to each other. This phenomenon comes from the rapid change of the local mode phase resonant compared to the continued mode.

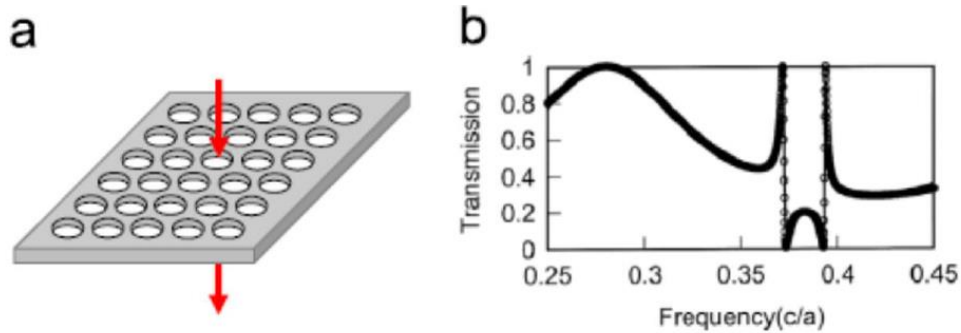


Figure 1.22: (a) 3D representation of a square lattice of air holes of given period and diameter; the red arrows represent the direction of propagation of the incident wave; (b) Corresponding transmission spectrum with Fano resonances [94].

In this part, we have seen that the Fano resonances observed in the 2D photonic crystals are the result of the coupling of the discrete guided resonance modes localized in the lattice with the continuous mode of the incident radiation, thus allowing the manipulation of the light in privileged

directions, thus offering particular optical properties and additional application possibilities for a wide range of photonic devices and structures. The asymmetric shapes associated with steep transitions in amplitude and phase between peaks and dips in the transmission / reflection spectra characteristic of Fano resonances, allows the control over a defined spectral range of bandwidth in order to obtain broadband mirrors with high quality factors.

By choosing appropriate structural parameters, it is possible to design ultra-thin 2D PC membranes having a band of transmission, reflection, or absorption in a defined spectral range. In addition, a wide range of planar dielectric structures may be used to create a different type of optical beam control functions, such as coupling, focusing, collimation, isolation, and beam direction.

I.3 Thermoregulatory clothing for personal thermal management

As indicated above in section I.1.3, thermoregulating textiles currently developed act mainly on evaporation and convection transfers. For a typical indoor scenario, IR radiative heat dissipation contributes to more than 50% of the total body heat loss [96,97]. The term "personal thermal management" has been introduced to describe the radiative heat transfers. The expression is still weakly explored, although some technologies and materials began to appear in recent years. The objective of personal thermal management is to enhance the radiative dissipation by promoting the transmission of IR to the outside, leading to a cooling effect, or to suppress radiative dissipation and return the IR radiation to the skin, which leads to a heating process.

For personal heating textiles [98,99], the authors currently proposed the integration of metallic nanowires or particles embedded in cotton matrices. The heating production is generated from the supplementary reflection of the human body radiation that can even be increased by adding Joule heating to complement the passive insulation.

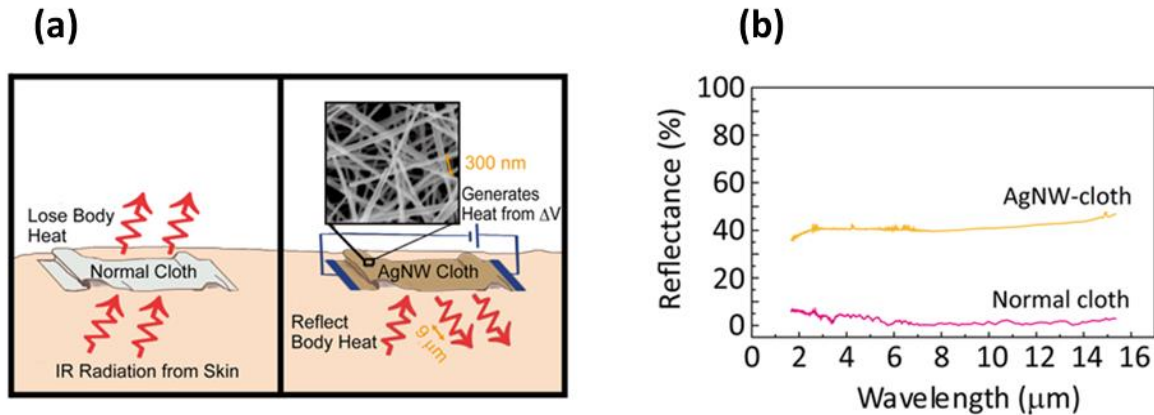


Figure 1.23: (a) Schematic of nanowire cloth with thermal radiation insulation and active heating. (b) FT-IR reflection spectra of normal cloth and Ag nanowires cloth [98] .

P.C. Hsu *et al.* [98], from Stanford University, have, for their part, functionalized cotton fibers with silver nanowires thus making the fabric both capable of reflecting the infrared radiation emitted by the human body towards itself and also authorizing Joule heating to improve thermal comfort. After forming the silver nanowires by nucleation, they are dispersed in isopropanol and deposited by dip-coating on a cotton fabric.

Figure 1.23 (a) and (b) shows that a non-coated tissue transmits infrared radiation coming from the skin of the human body. After coating the cloth with metallic nanowires, the reflection was increased from 1.3% to 40.8% reducing the radiative losses. The arrangement of the nanowires makes it possible to have a continuous electrical conductivity and the spaces between neighboring nanowires make the textile transparent to visible light. They form a porous conductive network on the fabric that has, in the same time, good water vapor permeability, infrared reflection and a Joule heat source (from 20 °C to 55 °C in 5 min at 16V). This paper is directly related to our study because it shows the possibility, by reflecting the infrared radiation with a wavelength of 9 μm (wavelength mainly emitted by the body), to drastically reduce radiative heat losses from the human body.

Z. Yu *et al.* [99] deposited, on a cotton, nanocomposites nanowires of silver / polydopamine by intramolecular crosslinking (Figure 1.24 (a)). Firstly, the surface of the cotton is functionalized with dopamine by soaking. Then, it undergoes a second functionalization via dip-coating in a solution containing the silver nanowires (AgNW) and polydopamine in order to obtain an AgNW composite / polydopamine on the surface of the cotton. Figure 1.24 (b) shows that the average

reflectance of the human body radiation (86%) for the AgNW/polydopamine cloth (ADNC) is significantly higher than that of the normal cloth (1.8%).

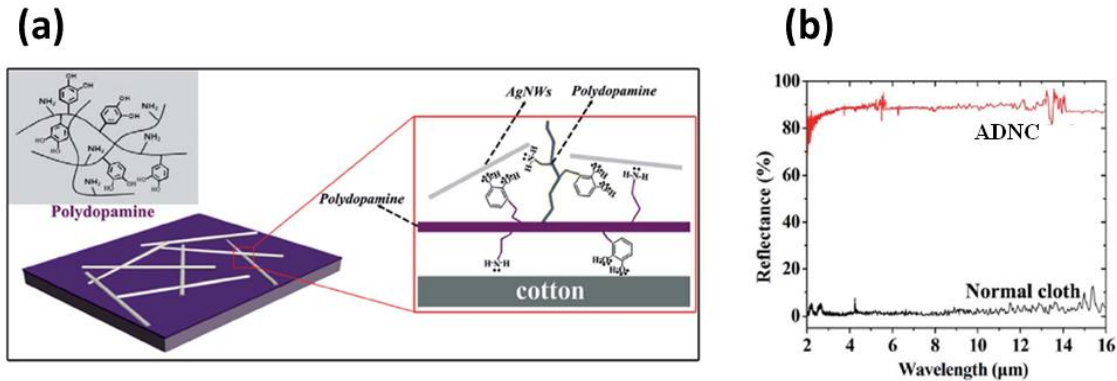


Figure 1.24: (a) schematic description of interactions between polydopamine and AgNWs/cotton surface. (b) FT-IR reflection spectra of normal cloth and ADNC [99].

The textile thus obtained has excellent radiative thermal insulation, without alteration of its performance in terms of flexibility and resistance to washing. Moreover, like the material developed by P.C. Hsu *et al.*, it can generate a Joules effect with a fast thermal response (1 min, from 22 °C to 40 °C).

For personal cooling textiles, recent papers have proposed different fibers [100,101, 102,103] or membranes [71,104,105] fabrics to increase light transmittance.

Among the research groups that explored the cooling path using the fiber configuration, we can cite in particular the team of J.K. Tong *et al.* [100], from Massachusetts Institute of Technology (MIT), who developed, in 2015, an opaque fabric to visible radiation but totally transparent to infrared emitted by the human body. This fabric allows, by a passive cooling mechanism, to directly transmit the thermal radiation emitted by the body to the external environment. By choosing the diameter and the arrangement of synthetic fibers based on polyethylene as well as the diameter and the arrangement of the yarns obtained from these fibers, the authors have highlighted two different light diffraction regimes. Significant Mie diffractions are obtained on visible wavelengths [106] while low Rayleigh diffractions occur in the IR range, making the final textile opaque to visible radiation and transparent to IR.

For membranes fabrics, P.C. Hsu *et al.* [71] have published in Science in 2016, results dealing with a textile based on a nano-porous polyethylene membrane (nano PE) deposited on a cotton. Because of its high porosity and the size of the nano-pores, the membrane is transparent to the radiation of the human body but opaque in the visible spectral range. With pore diameters of the order of visible wavelengths, the nano-porous membrane diffracts visible light while appears transparent in the IR. In order to improve the mechanical and fluidic properties of the textile, polydopamine (PDA) coating is grafted onto the nanoporous membrane and a membrane is deposited on each side of the cotton (cotton mesh) (Figure 1.25 (a)). The textile obtained has an average transmittance of 77.8% for IR and an opacity of over 99% for visible radiation (Figure 1.25 (b)) and c)). In addition to its cooling radiative effect, this textile has air permeability, water absorption capacity and a sufficient mechanical strength to be worn.

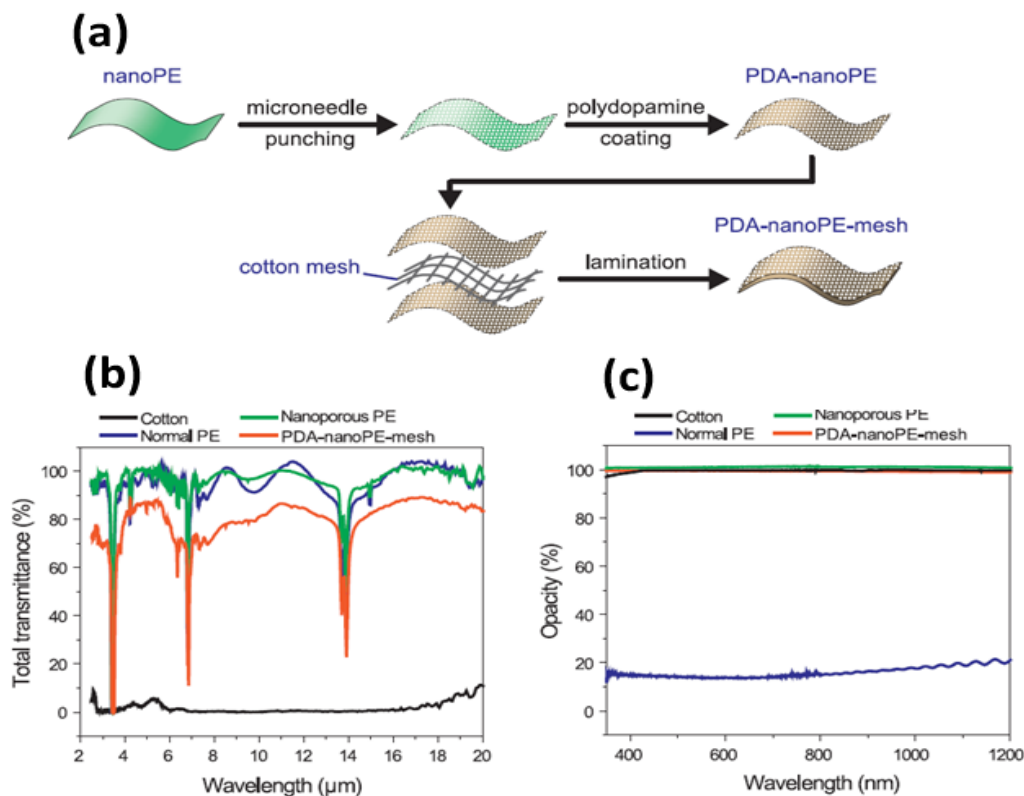


Figure 1.25: (a) Fabrication of the nanoporous PE membrane and (b) transmittance and (c) opacity obtained for this membrane in the infrared and visible domains respectively [71].

Ying-Nan Song *et al.* [104] designed a bilayer structure fabric with high thermal comfort by increasing the dissipation of human thermal radiation and reducing solar energy absorption simultaneously. The fabric consists in two layers, including a polyethylene film with nanopores (100-1000 nm in pore size) and a film made of nylon 6 nanofibers (100 nm in diameter) with beads (230 nm in diameter), with the aim to increase the visible light reflectance and simultaneously not affect the infrared wave radiation. Therefore, the designed fabric showed a high heat dissipation power, which was 17.93 W/m^2 higher than that of the selected traditional textiles of cotton, linen and odile, respectively, suggesting a good cooling capability (Figure 1.26).

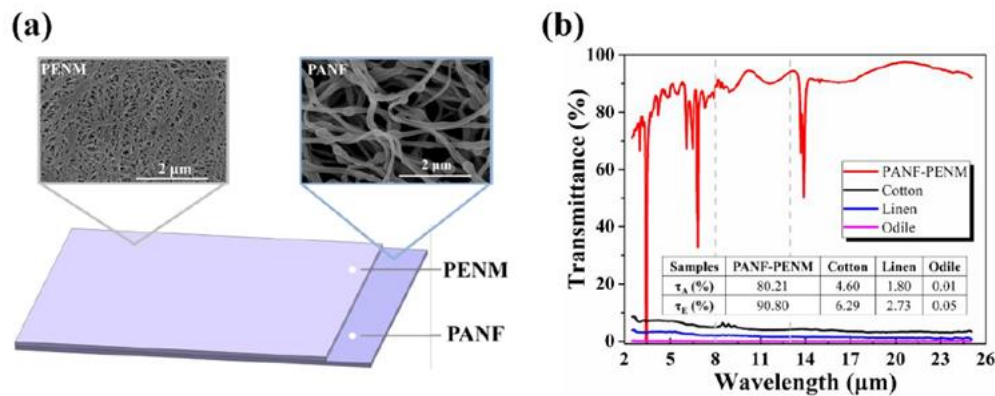


Figure 1.26: (a) Structural design of PANF-PENM (PA6 nanofibres -nanoporous PE membrane) fabric. The inner layer was non-woven fabric made of PANFs and the outer layer was PENM with many nanopores. PANF-PENM has high IR transmittance and visible reflectance, and thus was good in cooling. PENM was stacked by PE fibers, thus forming a polyporous structure. (b) IR transmittance curves of PANF-PENM, cotton, linen and odile. PANF-PENM had the highest IR transmittance, above 90%, while traditional textiles are usually below 10% [104].

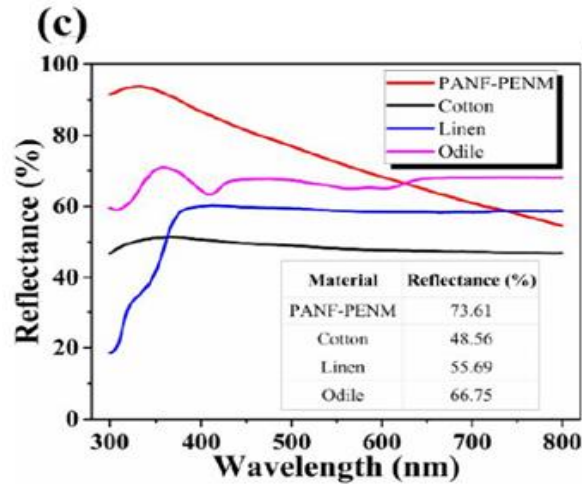


Figure 1.27: Visible reflectance curves of PANF-PENM (PA6 nanofibres -nanoporous PE membrane), cotton, linen and odile. PANF-PENM had the highest visible reflectance with a value of 73.61%, and the traditional textiles were lower, with values of 48.56%, 55.69%, and 66.75% for cotton, linen, and odile, respectively [104].

The dual functionalities (cooling and heating) within a same textile is a real challenge that need tremendous efforts. Such mechanisms have been proposed in two different ways. Hsu *et al.* [107] investigated a textile for human body radiative using a bilayer thermal emitter embedded inside an IR-transparent nanoPE that can perform both passive radiative heating and cooling using the same non-symmetric piece of textile. Reversible humidity sensitive clothing for personal thermoregulation was also proposed using shape memory polymer [108]. The smart textile has been designed to reversibly adapt the thermal insulation functionality, thus permitting the air flow and reducing the humidity level and the apparent temperature.

Recently, Zhang *et al.* have proposed a dynamic control in the mid-infrared in reaction of the relative humidity of the underlying skin by coating triacetate-cellulose bimorph fibers with a thin layer of carbon nanotubes [109]. The figure 1.28 represents the design principles of an infrared gating textile.

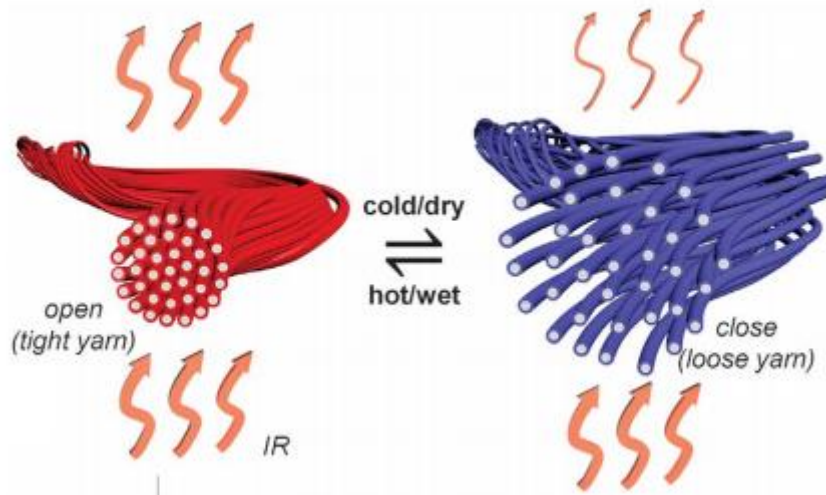


Figure 1.28: Principle of an IR gating textile [109].

Each yarn knitted into the textile is composed of multiple metafibers that contain infrared-active nanostructures. The yarn is fluffy with large distances between the fibers. When hot and wet, the yarn collapses into a tight bundle, bringing the neighboring metafibers into resonant electromagnetic coupling that shifts the infrared emissivity to spectrally overlap with that of the skin. This effectively “opens” the cloth to promote radiative cooling of the human body. When cold and dry, the reverse effect occurs. In this way, the coupled temperature–sweating response of humans to thermal discomfort is directly used to allow adaptive gating of radiation through the textile. The infrared “open” state here corresponds at the yarn level to a collapsed (i.e., smaller interfiber spacing) structure but larger pores between yarns at the fabric level. This design allows this new adaptive infrared gating mechanism to synergistically occur with conventional heat exchange channels, including convection and evaporation (not shown), to maximize personal cooling (when hot and sweating) and heating (when cold and dry).

The materials presented above have highly interesting reflective properties in infrared offering a new opportunity for the thermal management of textile.

In the present manuscript, we are interested in a new generation of photonic polymer membranes able to modify the optical response of an incident electromagnetic wave by varying its physical nature and geometrical structure in the mid-infrared. These membranes were proposed with the objective to control thermal radiation, which, as a reminder, represents 50% of the heat losses of

the human body under standard temperature and relative humidity conditions. We aim to propose a simple micro-structured photonic membrane that provides thermoregulation functionality. We limit ourselves to a functional membrane for everyday use, with the assumption that the human body is in a sedentary state, inside a room. Consequently, uniform skin temperature at 34 °C and heat generation from the human body are considered. The air between the skin and the polymer membrane is assumed to be stationary, meaning that convective heat transfer in this region will be ignored. In addition, moisture transfer will not be taken into consideration in our study.

Conclusion

In this first chapter, the thermoregulation and the thermal comfort were introduced. We have detailed how it affects the human body. Different types of mechanisms of thermoregulation were presented that can be passive/active unconscious and active conscious. Since both environmental and physiological parameters influence thermal comfort, it appears essential to find a textile that can maintain the thermal equilibrium between the heat produced by the body and that transferred to the external environment. In addition, we introduced the mechanisms of heat and humidity transfer between the human body and the textile with the environment. We limited our study to improving the thermal comfort of a person resting indoors. We described the three heat transfer mechanisms: convection, conduction and radiation. From the current literature, we found that radiative transfers predominate and are responsible of about 50% of the heat loss produced by the human body. We will focus our work on the radiative transfer mechanism. The evolution of the textile from traditional to smart textile was further introduced. Moreover, by introducing a structuration, we aim to change their optical properties according to the spectral range. These specific objects, called photonic crystals, have been formerly defined. Finally, papers related to the personal heating and cooling textile were described. Personal cooling textile has been developed to enhance the radiative dissipation by nano-porous polyethylene film while personal heating textiles have been controlled by the integration of metallic nanowires embedded in the textile. The originality of this work is to use the photonic crystals properties to control thermal radiation for personal thermoregulation. The referred papers are at the state of the art, some of them published in high impact journals and coming from renowned universities, published during this

PhD work, showing that this subject is attracting and represents a great deal of interest from both the scientific community and the industry.

The originality of our project lies both on the thermoregulation management and on the use of the designed photonic crystals. The objective is to propose an efficient thermo-regulating membrane in the mid-infrared. Indeed, our goal is to produce micro-structured polymer-based membranes whose microstructure dimensions allow the modulation of the reflection and transmission waves emitted by the human body.

The work presented in this manuscript is an upstream research work aimed at showing theoretically and experimentally the link between the structural properties of a polymer membrane and its optical properties in the MIR.

This work is based on two aspects:

- First, simulation of membrane performance:
 - to investigate the optical properties of various polymer membranes, considering the effect of membrane structuration on the reflection, transmission, and absorption coefficients in the MIR range, and to analyze the origin of the specific features that occur.
 - to define and to analyze the thermal balance between the human body and the indoor environment through a photonic membrane, considering radiation, convection and conduction mechanisms.
 - to understand the relationship between the optical properties of the polymer and its thermal response.
- Second, the technological fabrication of designed membranes which is done in the IEMN cleaning room and their characterization by Fourier Transform Infrared spectroscopy (FT-IR).

In the next chapter, we will describe the finite element method used to modelize the proposed structures. We will first investigate the effect of the grating parameters on the reflective properties of ridges and holes photonic crystal membrane made of polycrystalline silicon in the mid-infrared (MIR) range (5–15 μm).

References

1. Steadman RG. The assessment of sultriness. Part I: A temperature-humidity index based on human physiology and clothing science. *Journal of applied meteorology*. 1979 ;18(7):861-73.
2. Steadman RG. The assessment of sultriness. Part II: effects of wind, extra radiation and barometric pressure on apparent temperature. *Journal of Applied Meteorology*. 1979 ;18(7):874-85.
3. Threlkeld JL. *Thermal environmental engineering*. Prentice Hall; 1970.
4. Teodoreanu E. Thermal Comfort Index. *Present Environ Sustain Dev*. 2016 ;10:105–18.
5. Harris NC. *Modern air conditioning practice*.
6. Mattila H, editor. *Intelligent textiles and clothing*. Woodhead Publishing; 2006 Jul 28.
7. Mangat MM. *Clothing comfort—A combination of objective and subjective evaluation*. Technical University Liberec. 2010.
8. Mokhtari Yazdi M, Sheikhzadeh M. Personal cooling garments: a review. *J Text Inst*. 2014; 105:1231–50.
9. Pan N, Gibson P, editors. *Thermal and moisture transport in fibrous materials*. Woodhead Publishing; 2006.
10. Brocas J, Fromageot C. *Transferts et régulations (les échanges d'énergie entre l'environnement, l'homme et l'animal)*.
11. Sommet A. *La thermorégulation*. 2013
12. Hardy JD, DuBois EF. Regulation of Heat Loss from the Human Body. *Proc Natl Acad Sci*. 1937; 23:624–31.
13. Johnson AT. *Biomechanics and exercise physiology: quantitative modeling*. CRC Press; 2007.
14. Havenith G. Interaction of Clothing and Thermoregulation. *Exog Dermatol*. 2002; 1:221–30.
15. Arens EA, Zhang H. The Skin's Role in Human Thermoregulation and Comfort. :51.

16. Bishop PA. Ergonomics and Comfort in Protective and Sport Clothing: A Brief Review. J Ergon [Internet]. 2014 [cited 2020 Mar 6]; S2. Available from: <http://www.omicsgroup.org/journals/ergonomics-and-comfort-in-protective-and-sport-clothing-a-brief-review-2165-7556.S2-005.php?aid=21518>
17. Haslam RA, Parsons KC. Quantifying the effects of clothing for models of human response to the thermal environment. Ergonomics. 1988; 31:1787–806.
18. McCullough EA. Factors affecting the resistance to heat transfer provided by clothing. J Therm Biol. 1993; 18:405–7.
19. Levin J, Maibach H. The correlation between transepidermal water loss and percutaneous absorption: an overview. J Controlled Release. 2005; 103:291–9.
20. Elsner P, Maibach HI, Berardesca E, Fluhr JW. Bioengineering of the skin: water and the stratum corneum. CRC press; 2004.
21. Deb C, Ramachandraiah A. Evaluation of thermal comfort in a rail terminal location in India. Build Environ. 2010; 45:2571–80.
22. Fanger PO. Assessment of Man's Thermal Comfort in Practice. Br J Ind Med. 1973;30:313–24.
23. Parsons K. Human thermal environments: the effects of hot, moderate, and cold environments on human health, comfort, and performance. CRC press, 2014.
24. Eckert ERG, Goldstein RJ, Ibele WE, Patankar SV, Simon TW, Decker NA, et al. Heat transfer-a review of 1990 literature. :80.
25. Morozumi Y, Akaki K, Tanabe N. Heat and moisture transfer in gaps between sweating imitation skin and nonwoven cloth: effect of gap space and alignment of skin and clothing on the moisture transfer. Heat Mass Transf. 2012; 48:1235–45.
26. Gibson PW, Charmchi M. Coupled heat and mass transfer through hygroscopic porous materials- Application to clothing layers. Sen'i Gakkaishi. 1997;53(5):183-94.
27. Li Y, Zhu Q, Yeung KW. Influence of Thickness and Porosity on Coupled Heat and Liquid Moisture Transfer in Porous Textiles. Text Res J. 2002 ;72 :435–46.
28. Bakr MH, Cours : transfert de chaleur, Université de technologie Compiègne.

29. Brau J, Cours : conduction, Département génie civil et urbanisme, INSA de Lyon, 2006 ; 53-92.
30. Brotherhood JR. Heat stress and strain in exercise and sport. *J Sci Med Sport*. 2008; 11:6–19.
31. Nadel ER, Wenger CB, Roberts MF, Stolwijk JAJ, Cafarelli E. PHYSIOLOGICAL DEFENSES AGAINST HYPERTHERMIA OF EXERCISE. *Ann N'Y Acad Sci*. 1977 ;301:98–109.
32. Mairiaux P, Malchaire J. Le travail en ambiance chaude. Paris: Masson. 1990.
33. Fanger PO. Thermal comfort. Analysis and applications in environmental engineering. Thermal comfort. Analysis and applications in environmental engineering. 1970.
34. Jannot Y. Transferts thermiques. Ecole des mines Nancy. 2012 :161.
35. Bruce H. Billings. Selected papers on applications of polarized light. SPIE Optical Engineering Press, 1992.
36. TP L3 physique, CESIRE, Université Joseph Fourier, Grenoble.
37. Bianchi AM, Fautrelle Y, Etay J. Transferts thermiques. PPUR presses polytechniques ; 2004.
38. Vanggaard L, Paulev PE, Zubietta-Calleja G. Thermo-regulation temperature and radiation. *Medical Physiology and Pathophysiology: Essentials and Clinical Problems*. Editors: Zubietta-Calleja, G., and Paulev, PE. 2011.
39. Van Langenhove L, Hertleer C. Smart clothing: a new life. *International journal of clothing science and technology*. 2004;16(1-2):63-72.
40. Sen AK. Coated Textiles Principles and Applications, tech editor Damewood Journal, Technomic Publishing Co., USA, 2001, pp. 133-154.
41. Gottwald L. Water Vapor Permeable PUR Membranes for Weatherproof Laminates. *J Coat Fabr*. 1996;25:168–75.
42. Van Roey M. Water-Resistant Breathable Fabrics. *J Coat Fabr*. 1992; 22:20–31.
43. Gugliuzza A, Drioli E. A review on membrane engineering for innovation in wearable fabrics and protective textiles. *J Membr Sci*. 2013; 446:350–75.

44. Kramar L. Recent and future trends for high performance fabrics providing breathability and waterproofness. *Journal of coated fabrics*. 1998;28(2):106-15.
45. Mattila H. *Intelligent textiles and clothing*. Woodhead Publishing, 2006.
46. Reinertsen RE, Færevik H, Holbø K, Nesbakken R, Reitan J, Røyset A, et al. Optimizing the Performance of Phase-Change Materials in Personal Protective Clothing Systems. *Int J Occup Saf Ergon*. 2008 ;14:43–53.
47. Salaün F. *Conception-élaboration de textiles réactifs: application à la thermorégulation (Doctoral dissertation, Lille 1)*.
48. Mondal S. Phase change materials for smart textiles – An overview. *Appl Therm Eng*. 2008;28:1536–50.
49. Pereira da Cunha J, Eames P. Thermal energy storage for low and medium temperature applications using phase change materials – A review. *Appl Energy*. 2016; 177:227–38.
50. Akeiber H, Nejat P, Majid MZAbd, Wahid MA, Jomehzadeh F, Zeynali Famileh I, et al. A review on phase change material (PCM) for sustainable passive cooling in building envelopes. *Renew Sustain Energy Rev*. 2016;60:1470–97.
51. Kuklane K, Nordisk Koordinationsgruppe om Beskyttelseklaeder som Teknisk Forebyggelsemiddel, European Conference on Protective Clothing, editors. *Ergonomics of protective clothing: proceedings of NOKOBETEF 6 and 1st European Conference on Protective Clothing held in Stockholm, Sweden, May 7 - 10, 2000*. Stockholm: Arbetslivsinstitutet; 2000.
52. Leitch P, Tassinari TH. Interactive Textiles: New Materials in the New Millennium. Part 1. *J Ind Text*. 2000;29:173–90.
53. Bryant YG. Fibers with enhanced, reversible thermal energy storage properties. *InTechtextil-Symposium 1992*:1-8.
54. Neuwald J., EP 1703033A2, Interior building panel with PCM, Corus Technology BV, 2006.
55. Chung H, Cho G. Thermal Properties and Physiological Responses of Vapor-Permeable Water-Repellent Fabrics Treated with Microcapsule-Containing PCMs. *Text Res J*. 2004; 74:571–5.

56. Torsten K. WO 2006/117702 A (UNIV DO MINHO [PT]; NAYLOR ROCHA GOMES JAIME ISIDO [PT]; MAGALHAES VAZ) 9 November 2006 (2006-11-09) cited in the application the whole document. :4.
57. Shape-memory materials and hybrid composites for smart systems: Part I Shape-memory materials. :20.
58. Lendlein A, Jiang H, Jünger O, Langer R. Light-induced shape-memory polymers. *Nature*. 2005; 434:879–82.
59. Ota S. Current status of irradiated heat-shrinkable tubing in Japan. *Radiat Phys Chem* 1977. 1981; 18:81–7.
60. Lin JR, Chen LW. Shape-memorized crosslinked ester-type polyurethane and its mechanical viscoelastic model. *J Appl Polym Sci*. 1999; 73:1305–19.
61. McClung AJW, Tandon GP, Baur JW. Strain rate- and temperature-dependent tensile properties of an epoxy-based, thermosetting, shape memory polymer (Veriflex-E). *Mech Time-Depend Mater*. 2012; 16:205–21.
62. Gall K, Yakacki CM, Liu Y, Shandas R, Willett N, Anseth KS. Thermomechanics of the shape memory effect in polymers for biomedical applications. *J Biomed Mater Res A*. 2005;73A:339–48.
63. Ji F, Zhu Y, Hu J, Liu Y, Yeung L-Y, Ye G. Smart polymer fibers with shape memory effect. *Smart Mater Struct*. 2006; 15:1547–54.
64. Lendlein A, Kelch S. Shape-Memory Polymers. *Angew Chem Int Ed*. 2002; 41:2034.
65. Hu J, Zhu Y, Huang H, Lu J. Recent advances in shape–memory polymers: Structure, mechanism, functionality, modeling and applications. *Prog Polym Sci*. 2012; 37:1720–63.
66. Pause B. Phase change materials show potential for medical applications. *Technical Textiles International*. 1999 Sep; 9:23-6.
67. Hayashi S, Tasaka Y, Hayashi N, Akita Y. Development of Smart Polymer Materials and its Various Applications. 2004;3.

68. Wang Z-C, Xu X-D, Chen C-S, Wang G-R, Wang B, Zhang X-Z, et al. Study on novel hydrogels based on thermosensitive PNIPAAm with pH sensitive PDMAEMA grafts. *Colloids Surf B Biointerfaces*. 2008; 67:245–52.
69. Liu B, Hu J. The application of temperature-sensitive hydrogels to textiles: A review of Chinese and Japanese investigations. *Fibres & Textiles in Eastern Europe*, 2005;13: 45-49.
70. Voelk M. (76) Inventors: Martin Krobok, Aichach (DE); 2006;6.
71. Hsu P-C, Song AY, Catrysse PB, Liu C, Peng Y, Xie J, et al. Radiative human body cooling by nanoporous polyethylene textile. *Science*. 2016; 353:1019–23.
72. Yablonovitch E. Inhibited Spontaneous Emission in Solid-State Physics and Electronics. *Phys Rev Lett*. 1987; 58:2059–62.
73. John S. Strong localization of photons in certain disordered dielectric superlattices. *Phys Rev Lett*. 1987; 58:2486–9.
74. Yablonovitch E. Photonic band-gap crystals. *J Phys Condens Matter*. 1993; 5:2443–60.
75. Joannopoulos JD, Johnson SG, Winn JN, Meade RD. Photonic crystals: molding the flow of light. 2nd edition. Princeton Oxford: Princeton University Press; 2008.
76. Yablonovitch E, Gmitter TJ. Photonic band structure: The face-centered-cubic case. *Phys Rev Lett*. 1989;63:1950–3.
77. Gascon A. Fabrication et caractérisation de cristaux photoniques pour exaltation de fluorescence (Doctoral dissertation, École Polytechnique de Montréal).2010.
78. Rigneault H, Lourtioz JM, Delalande C, Levenson A, editors. Nanophotonics. John Wiley & Sons; 2010 Jan 5.
79. Sale TE, Roberts JS, Woodhead J, David JP, Robson PN. Room temperature visible (683-713 nm) all-AlGaAs vertical-cavity surface-emitting lasers (VCSELs). *IEEE Photonics Technology Letters*. 1996; 8:473-5.
80. Zengerle R. Light Propagation in Singly and Doubly Periodic Planar Waveguides. *J Mod Opt*. 1987; 34:1589–617.

81. Kiriakidis G, Katsarakis N. FABRICATION OF 2-D AND 3-D PHOTONIC BAND-GAP CRYSTALS IN THE GHz AND THz REGIONS. :7.
82. Lin SY, Fleming JG, Hetherington DL, Smith BK, Biswas R, Ho KM, et al. A three-dimensional photonic crystal operating at infrared wavelengths. *Nature*. 1998; 394:251–3.
83. Yablonovitch E, Gmitter T, Leung K. Photonic band structure: The face-centered-cubic case employing nonspherical atoms. *Phys Rev Lett*. 1991; 67:2295–8.
84. Yablonovitch E, Gmitter TJ, Meade RD, Rappe AM, Brommer KD, Joannopoulos JD. Donor and acceptor modes in photonic band structure. *Phys Rev Lett*. 1991; 67:3380–3.
85. Căbuz AI, Centeno E, Cassagne D. Superprism effect in bidimensional rectangular photonic crystals. *Appl Phys Lett*. 2004; 84:2031–3.
86. Qiu G, Lin F, Li YP. Complete two-dimensional bandgap of photonic crystals of a rectangular Bravais lattice. *Opt Commun*. 2003 ;219 :285–8.
87. Gauffillet F. Cristaux photoniques à gradient : dispositifs et applications. :168.
88. Lourtioz JM, Benisty H. Les cristaux photoniques ou la lumière en cage. Hermes-Science; 2003.
89. Lourtioz JM, Benisty H, Berger V, Gerard JM, Maystre D, Tcheltnokov A. Photonic crystals. Towards Nanoscale Photonic Devices. 2005.
- .90. Fano U. Effects of configuration interaction on intensities and phase shifts. *Physical Review*. 1961;124(6):1866.
91. Ueda A, Eto M. Resonant tunneling and Fano resonance in quantum dots with electron-phonon interaction. *Phys Rev B* [Internet]. 2006 [cited 2020 Mar 7];73. Available from: <https://link.aps.org/doi/10.1103/PhysRevB.73.235353>
92. Miroshnichenko AE, Flach S, Kivshar YS. Fano resonances in nanoscale structures. *Rev Mod Phys*. 2010; 82:2257–98.
93. Rybin MV, Khanikaev AB, Inoue M, Samusev KB, Steel MJ, Yushin G, et al. Fano Resonance Between Mie and Bragg Scattering in Photonic Crystals. *ArXiv09024053 Cond-Mat Physicsphysics* [Internet]. 2009 [cited 2020 Mar 7]; Available from: <http://arxiv.org/abs/0902.4053>

94. Zhou W, Zhao D, Shuai Y-C, Yang H, Chuwongin S, Chadha A, et al. Progress in 2D photonic crystal Fano resonance photonics. *Prog Quantum Electron*. 2014; 38:1–74.
95. Gallinet B. Fano Resonances in Plasmonic Nanostructures. PhD thesis, STI, Lausanne, 2012.
96. Hardy J D, Muschenheim C. The radiation of heat from the human body. IV. The emission, reflection, and transmission of infra-red radiation by the human skin. *The Journal of clinical investigation*, 1934;13, 817-831.
97. Winslow C-EA, Gagge AP, Herrington LP. THE INFLUENCE OF AIR MOVEMENT UPON HEAT LOSSES FROM THE CLOTHED HUMAN BODY. *Am J Physiol-Leg Content*. 1939; 127:505–18.
98. Hsu P-C, Liu X, Liu C, Xie X, Lee HR, Welch AJ, et al. Personal Thermal Management by Metallic Nanowire-Coated Textile. *Nano Lett*. 2015; 15:365–71.
99. Yu Z, Gao Y, Di X, Luo H. Cotton modified with silver-nanowires/polydopamine for a wearable thermal management device. *RSC Adv*. 2016; 6:67771–7.
100. Tong JK, Huang X, Boriskina SV, Loomis J, Xu Y, Chen G. Infrared-Transparent Visible-Opaque Fabrics for Wearable Personal Thermal Management. *ACS Photonics*. 2015; 2:769–78.
101. Catrysse PB, Song AY, Fan S. Photonic Structure Textile Design for Localized Thermal Cooling Based on a Fiber Blending Scheme. *ACS Photonics*. 2016; 3:2420–6.
102. Jafar-Zanjani S, Salary MM, Mosallaei H. Metafabrics for Thermoregulation and Energy-Harvesting Applications. *ACS Photonics*. 2017 ;4 :915–27.
103. Gao T, Yang Z, Chen C, Li Y, Fu K, Dai J, et al. Three-Dimensional Printed Thermal Regulation Textiles. *ACS Nano*. 2017 ;11 :11513–20.
104. Song Y-N, Ma R-J, Xu L, Huang H-D, Yan D-X, Xu J-Z, et al. Wearable Polyethylene/Polyamide Composite Fabric for Passive Human Body Cooling. *ACS Appl Mater Interfaces*. 2018;10:41637–44.
105. Cai L, Song AY, Li W, Hsu P-C, Lin D, Catrysse PB, et al. Spectrally Selective Nanocomposite Textile for Outdoor Personal Cooling. *Adv Mater*. 2018; 30:1802152.
106. Hergert W, Wriedt T. The Mie theory: basics and applications. Springer. 2012

107. Hsu P-C, Liu C, Song AY, Zhang Z, Peng Y, Xie J, et al. A dual-mode textile for human body radiative heating and cooling. *Sci Adv.* 2017;3:e1700895.
108. Zhong Y, Zhang F, Wang M, Gardner CJ, Kim G, Liu Y, et al. Reversible Humidity Sensitive Clothing for Personal Thermoregulation. *Sci Rep* [Internet]. 2017 [cited 2020 Mar 7];7. Available from: <http://www.nature.com/articles/srep44208>
109. Zhang XA, Yu S, Xu B, Li M, Peng Z, Wang Y, et al. Dynamic gating of infrared radiation in a textile. *Science.* 2019 ;363:619–23.

Chapter II:

Numerical and experimental study of a silicon membrane in the mid-infrared range

Introduction

In the previous chapter, photonic crystals were proposed as a solution to modulate the optical properties of a material in the mid-infrared (MIR) domain. We have also shown that the optical properties of the photonic crystals are dependent of the lattice parameters. Indeed, when these parameters are well chosen, its period in particular, scattering phenomena emerge. It results in the appearance of characteristic peaks in the electromagnetic spectrum at the wavelengths range where the emissivity of the human body is the most important.

To define the optimal characteristic of the photonic crystals to predict their optical properties in the mid-infrared, and in the perspective of their fabrication, we used numerical computation methods. There are different methods for modeling the electromagnetic properties of structures composed of several materials with different dielectric properties associated with complex geometries.

A number of numerical methods are used to simulate the behavior of photonic crystals, the most notables being the Plane Wave method (PWE) [1], the method of Guided Modes expansion (GME) [2], the Finite Element Method (FEM) [3,4,5], the Fourier modal method, and the Finite Difference Time Domain (FDTD) [6]. In the framework of this thesis, we used the FEM through the commercial software COMSOL.

Indeed, among all the methods mentioned above, the FEM stands out by its versatility design for the geometry that can be simulated. Thus, this method allows to treat a wide range of periodic structures in three dimensions without geometrical shape limitation.

In this chapter II, we investigate numerically, by Finite Element Method (FEM), the effect of grating parameters on the reflective properties of ridges and holes photonic crystal (PC) membrane made of polycrystalline silicon (PolySi) in the mid-infrared (MIR) range (5-15 μm).

The numerical calculations performed in this thesis were done in relation with the experimental silicon structures fabrication, carried out previously by another PhD student of the Bio-MEMS group (IEMN), Maud Viallon. In addition to the structure simulation, I also participated to the Fourier Transform InfraRed (FT-IR) optical characterization at the engineering school HEI in Lille.

The silicon was chosen in order to ensure a high refractive-index contrast with air. Moreover, the silicon microfabrication is well mastered in the clean room at IEMN and silicon structures have already been widely studied in the literature. For example, Wang *et al.* have fabricated a 1D Bragg

mirror showing modular and reversible reflective properties in the visible range depending on air humidity [7]. Foley *et al.* have shown that silicon / SiO₂ ridges grating exhibited high reflectivity (70%) in the 13-16 μm band [8]. Lai and co-authors have designed 2D germanium / SiO₂ holes triangular grating showing very high reflectivity (95%) at 8 μm .

II.1 Finite element method

II.1.1 Definition and principle

The finite element method, initially used to numerically solve partial differential equations, is a well-known method [9] that allows, among other things, to solve the Maxwell frequency equations. FEM has the advantage of being able to describe the physical behavior of objects having a very complex geometry by the use of unstructured meshes of space. Thus, it allows the modeling of structures difficult to access by other methods of calculation. This method is suitable for solving spectral and modal problems.

The computational domain is discretized into a number of elements called "finite elements". In each element, the sought solutions are developed on a set of basic functions. The choice of these basic functions depends on the studied system and the type of boundary conditions required the continuity of the function and / or its derivatives. The wave function solutions of the problem are thus interpolated in terms of values they themselves, or their derivatives, take at the nodes of the mesh. This facilitates the integration of boundary conditions into the formulation. From a numerical point of view, the choice of the basic functions is also governed by the necessary compromise between the degree of approximation of the solution and the number of freedom degrees related to the total cost of calculation [10]. The projection of the differential equations on the basic functions, in each of the finite elements, brings the problem back to a system of linear equations. Regarding the heterogeneous interfaces, the boundary conditions ensure the assembly of the elementary matrices into a global matrix of the complete system [11]. The finite element method has several advantages. On one hand, the method uses a mesh directly adapted to the studied geometry, contrariwise to the FDTD method (Finite Differences Time Domain) whose mesh is strictly parallelepipedic and generates discontinuities at the interfaces. On the other hand, it is possible to optimize the mesh while avoiding the use of an excessively fine mesh. This mesh, according to the domain studied and the involved equations, can be triangular or quadrangular.

The size of the system to be solved is related to the number of tetrahedral modules present within the mesh of the structure.

We used the commercial COMSOL software that not only gives a friendly interface for the modeling aspect but authorizes also to solve multiphysics problems. We first start from the design of the 1D and 2D geometry (Figure 2.1 (a)). Then, we define the elementary unit cell used in the calculation (Figure 2.1 (b)) and add the boundary conditions. The geometry is meshed in elements (here triangular, Figure 2.1 (c)) before solving the optical equations in this discretized domain.

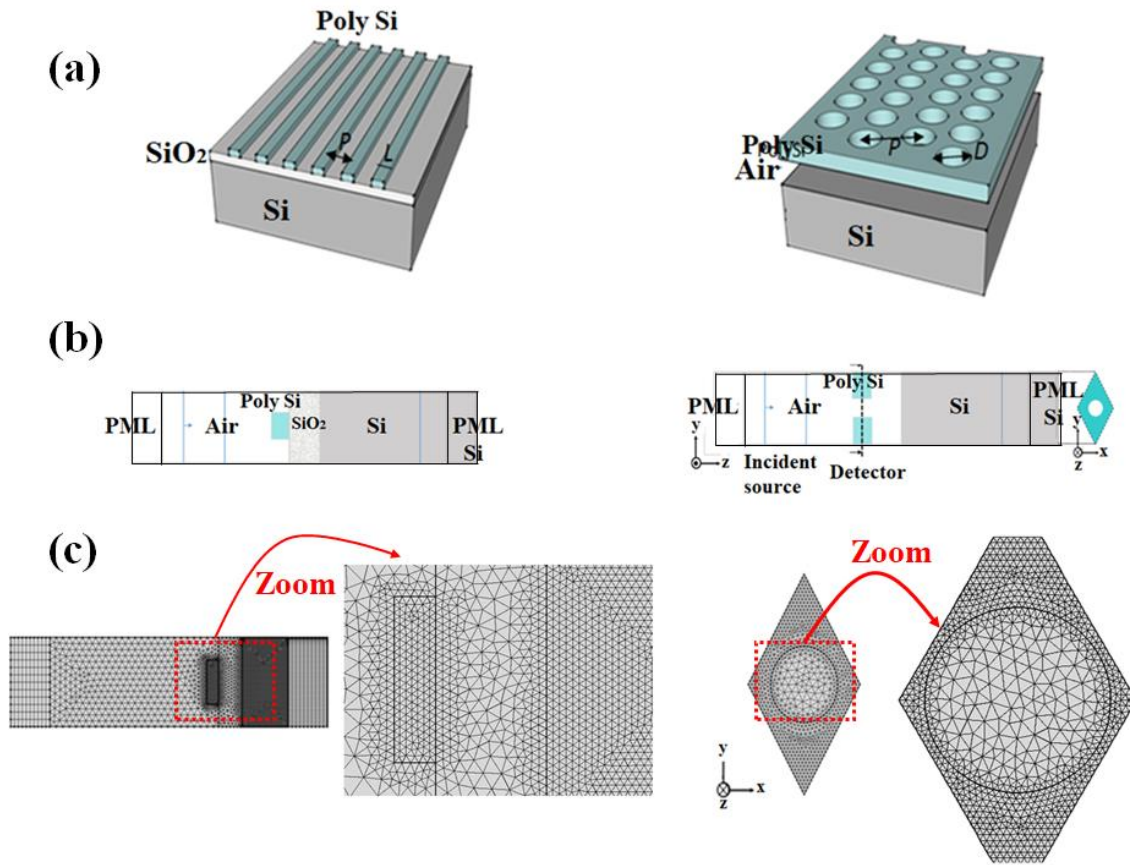


Figure 2.1: (a) 3D schematic representation of the photonic crystal (PC) films made of ridges of width L (left) and holes of diameter D (right). (b) Projection of the unit cell used for the FEM calculation of PC film made of ridges (left) and holes (right) in (y, z) and (x, y) planes. (c) Meshing of the unit cell of PC film made of ridges (left) and holes (right).

II.1.2 Boundary conditions

II.1.2.1 Periodic boundary condition

One of the most powerful methods for describing the electromagnetic fields in a periodic structure is based on the Floquet-Bloch theorem, which enables the wave inside a structure to be decomposed into a set of Floquet-Bloch modes. The Floquet-Bloch modes of a periodic layered structure can be found by imposing translational invariance of the wave over a period within a multiplicative exponential factor [12].

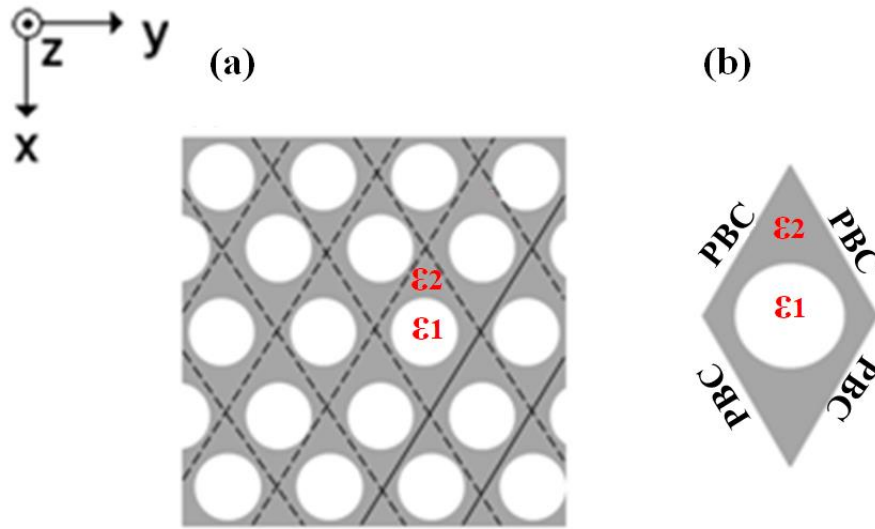


Figure 2.2: Representation of a (a) finite and (b) infinite periodic lattice with periodic boundary condition (PBC)

We consider a periodic linear lattice following the axis (Oy) (see figure 2.2 (b)). The periodic Boundary Condition (PBC) applied to the electric field $\vec{E}(x, y, z, t) = \vec{E}_0 e^{j(\omega t - k_x x - k_y y - k_z z)}$ gives:

$$\vec{E}(x, y + P, z, t) = \vec{E}(x, y, z, t) e^{-jk_y P} \quad \text{II.1a}$$

$$\vec{E}(x, y, z, t) = \vec{E}(x, y + P, z, t) e^{+jk_y P} \quad \text{II.1b}$$

The Floquet-Bloch theorem therefore makes it possible to calculate the fields in a spatial period of the lattice (i.e. within the elementary cell).

II.1.2.2 Perfectly matched layer

The use of electromagnetic field in photonic problems (such as photonic crystal modeling) faces a major problem of truncation of unbounded domains. Perfectly Matched Layers (PML) were introduced by Bérenger in 1994 [13] in order to deal with this unbounded problem. PMLs are layers of finite thickness that encompass the region of interest of the modeled structure. These layers are non-reflective and totally absorb all the waves propagating inside them. Since the formalization of Transformation Optics, the most natural way to understand a PML is to consider it as a complex geometric transformation of space that result in equivalent material properties (permittivity (ϵ) and permeability (μ)) [14]. Thus, even if the materials constituting the unbounded domains of space have transparent, isotropic and homogeneous material properties, those of the corresponding PMLs are lossy, anisotropic and possibly inhomogeneous. These transformations lead to equivalent materials that have the same impedance as the initial medium (by the fact that ϵ_r and μ_r are transformed in the same way). This property ensures that PMLs are non-reflective. The unbounded domains can thus be truncated under the condition that the external artificial boundary of the PML is located in a region where the field is sufficiently absorbed.

II.2 Description of the electromagnetic properties of dielectric materials: adaptation of the Lorentz-Drude model.

Dielectric permittivity and magnetic permeability describe the electrical and magnetic properties of materials respectively. The dielectric permittivity leads to polarization phenomena induced in matter during the propagation of an electromagnetic wave [15]. Dielectric materials, unlike metals, do not have electric charges that can move over long distances (macroscopically). They cannot drive the current. However, they are not totally electrically inert. Indeed, they can have, on the atomic scale, electrostatic dipoles that will interact with the applied external electric field. Under the application of an electric field, the dipoles reorganize, creating a polarization. These displacements of small amplitudes often correspond to a deformation of the electronic cloud of the atoms which compose the material thus creating an electrostatic dipole. Dielectrics are also dispersive materials, so they have a complex permittivity that depends on the frequency of the incident electromagnetic wave. The phenomenon of dispersion in these materials can be formulated through phenomenological microscopic models such as the Drude [16] or the Lorentz-

Drude models. The choice of one or the other depends on the material and the spectral range studied.

II.2.1 Description of the Drude model.

The Drude model is a kinetic model of transport in metals. It dates from 1900, that is to say, it closely follows the discovery of electrons by J.J. Thomson (1897). The Drude model considers metal as a lattice of fixed ions bathed in a gas of free electrons. The electrons, of mass m and charge $-e$, form a conventional gas of density n (\vec{r}). Electric transport and thermal transport are due to the presence and motion of those electrons in the metal. The ions of the structure are fixed and do not participate to the transport.

With regard to collisions, the Drude model assumptions are as follows:

- Electron-ion or electron-electron interactions are limited to collisions. As in a perfect gas, the collisions heat the electron gas.
- After each collision, an electron emerges with a speed distributed randomly according to the (local) distribution law of velocities.
- The collision probability per unit of time is $\frac{1}{\tau}$, where τ is the collision time. In other words, the probability that an electron undergoes a collision between t and $t + dt$ is independent of t (the electron has no memory) and is equal to $\frac{dt}{\tau}$. This collision time depends on the temperature.

The Drude model makes it possible to calculate the kinetic coefficients of the transport as a function of the collision time.

The motion of conduction electrons in the presence of an electromagnetic field is typically described by neglecting additional fields created by other electrons and ions. According to the fundamental principle of Newton's dynamics, an electronic equation of motion is written as follows:

$$m_e \frac{d^2 \vec{r}_c}{dt^2} = -e\vec{E} - e \frac{d\vec{r}_c}{dt} \times \vec{B} - m_e \Gamma_D \frac{d\vec{r}_c}{dt} \quad \text{II.2}$$

Where, m_e is the mass of the electron and \vec{r}_c is its vector position. The conduction electron is subjected to two forces, the Lorentz force and a viscous friction force which is due to the collisions that it undergoes. Drude attributed these collisions to shocks with the ions of the lattice. In fact,

they correspond to the electron-phonon interaction and the presence of impurities in the network [15]. The term Γ_D is a damping term equal to the inverse of the mean time between two collisions, or relaxation times.

Since the velocity of the electrons is much less than the speed of light, the Laplace force can be neglected with respect to the electric force [17]. In steady state, the solution of equation (II.2) will be a harmonic solution of same shape than the electric field:

$$\vec{r}_c = \frac{e}{m_e} \frac{1}{\omega^2 - i\omega\Gamma_D} \vec{E} \quad \text{II.3}$$

If N_c is the number of conduction electrons per unit volume, then the polarization induced in the material by the propagation of the electromagnetic wave is written as follows:

$$\vec{P} = -N_c e \vec{r}_c = N_c \vec{p}_c \quad \text{II.4}$$

Where \vec{P} is the polarization vector or volume density of electric dipole moment and \vec{p}_c is the dipolar moment of the conduction electron.

Replacing \vec{r}_c by its expression in equation (II.3) yields to:

$$\vec{P} = -\frac{N_c e^2}{m_e} \frac{1}{\omega^2 - i\omega\Gamma_D} \vec{E} \quad \text{II.5}$$

In linear mode, the macroscopic polarization is proportional to the applied electric field:

$$\vec{P} = \epsilon_0 \chi \vec{E} \quad \text{II.6}$$

Where the coefficient of proportionality χ is the dielectric susceptibility of the material.

The relative permittivity and susceptibility are related to each other by the following relation:

$$\epsilon_r(\omega) = 1 + \chi(\omega) \quad \text{II.7}$$

The relative permittivity, as part of the Drude model, is therefore expressed as follows:

$$\epsilon_{r,D}(\omega) = 1 - \frac{\omega_p^2}{\omega^2 - i\omega\Gamma_D} \quad \text{II.8}$$

Where the term ω_p is a pulsation characterizing the collective oscillation of the conduction electrons, called plasma pulsation:

$$\omega_p = \sqrt{\frac{N_c e^2}{\epsilon_0 m_e}} \quad \text{II.9}$$

After several approximations and introduction of variables representing the physical phenomena generated, we obtain the final expression of the dielectric constant, derived from the Drude model, following:

$$\epsilon_{r,D}(\omega) = \epsilon_\infty - \frac{\omega_p^2}{\omega^2 - i\omega\Gamma_D} \quad \text{II.10}$$

With ϵ_∞ the dielectric constant at infinite frequencies.

In the case of dielectric materials and in the spectral range investigated, the Drude model is not sufficient to describe alone all the phenomena resulting from the propagation of the electromagnetic wave in the dielectric material. Indeed, the dielectric materials have several variations of their real and complex refractive index resulting in several absorption peaks. It is therefore necessary to increase the number of oscillators in order to better represent their dielectric properties. For this reason, we used the Lorentz-Drude model.

II.2.2 Description of the Lorentz-Drude model

The Lorentz-Drude model allows us to take into account the real and complex variation of the refractive index of a dielectric. In our study, the silicon and polysilicon materials have constant refractive index in the mid-infrared range ($n_{Si} = n_{PolySi} = 3.47$) while silica exhibits absorption phenomena in the [5-15] μm range that can be predicted by a Lorentz-Drude (LD) model.

In order to correctly describe the properties of a dielectric materials for wavelengths below the threshold marking the beginning of inter-band transitions, the formula of the permittivity obtained with the Drude model must be completed. This can be done using the elastically bound electron model introduced by H. Lorentz at the end of the 19th century [17,18].

In the presence of an electromagnetic field, each valence electron is treated as a damped harmonic oscillator, in forced sinusoidal mode. The fundamental principle of the dynamic applied to the electron gives the equation of motion:

$$m_e \frac{d^2 \vec{r}_v}{dt^2} = -e\vec{E} - m_e \Gamma_L \frac{d\vec{r}_v}{dt} - K_L \vec{r}_v \quad \text{II.11}$$

The valence electron is subjected to three forces: the electric force, a fluid damping force reflecting the energy dissipation, and an elastic restoring force having a spring constant equal to:

$$K_L = m_e \omega_L^2 \quad \text{II.12}$$

Where ω_L is the proper pulsation of the atomic valence-atomic electron system.

In steady state, the solution of equation (II.12) is written as follows:

$$\vec{r}_v = \frac{e}{m_e} \frac{1}{(\omega^2 - \omega_L^2) - i\omega\Gamma_L} \vec{E} \quad \text{II.13}$$

If N_v is the volume density of valence electrons, then the polarization induced by the valence electrons during the propagation of an electromagnetic wave is:

$$\vec{P}_v = -N_v e \vec{r}_v = N_v \vec{p}_v \quad \text{II.14}$$

Where \vec{p}_v is the dipole moment of a valence electron.

The total polarization induced is the sum of the polarization due to the core-electrons and the polarization due to the conduction electrons:

$$\vec{P} = \vec{P}_v + \vec{P}_c = N_c \vec{p}_c + N_v \vec{p}_v \quad \text{II.14}$$

By introducing the expressions of the position vectors of conduction electrons \vec{r}_c (Equation (II.3)) and valence electrons \vec{r}_v , (Equation (II.13)) in equation (II.14), we obtain the following relation for the total polarization:

$$\vec{P} = \left(-\frac{N_c e^2}{m_e} \frac{1}{\omega^2 - i\omega\Gamma_D} - \frac{N_v e^2}{m_e} \frac{1}{(\omega^2 - \omega_L^2) - i\omega\Gamma_L} \right) \vec{E} \quad \text{II.15}$$

According to equation (II.6), we deduce that:

$$\chi(\omega) = -\frac{N_c e^2}{\epsilon_0 m_e} \frac{1}{\omega^2 - i\omega\Gamma_D} - \frac{N_v e^2}{\epsilon_0 m_e m_e} \frac{1}{(\omega^2 - \omega_L^2) - i\omega\Gamma_L} \quad \text{II.16}$$

The dielectric susceptibility thus contains two contributions. The first one is due to intra-band transitions and is described by the Drude model. The second one is due to inter-band transitions and is described by the Lorentz model.

Relative permittivity, as part of the Lorentz-Drude model, is written as follows:

$$\epsilon_{r,LD}(\omega) = 1 - \frac{\omega_p^2}{\omega^2 - i\omega\Gamma_D} - \frac{\Omega_L^2}{(\omega^2 - \omega_L^2) - i\omega\Gamma_L} \quad \text{II.17}$$

$$\text{With } \Omega_L = \sqrt{\frac{N_v e^2}{\epsilon_0 m_e}} \quad \text{II.18}$$

It is possible to improve the description of the inter-band transitions by complementing the classical Lorentz approach with a simple quantum approach [19,20]. The electronic structure of atoms and molecules is organized in discrete energy levels. The interaction between matter and radiation is done by absorption and photon emission processes associated with transitions between two energy levels such as:

$$E_2 - E_1 = h_p \nu_{12} \quad \text{II.19}$$

Where h_p is the Plank constant and ν_{12} the frequency associated with the transition between the two energy levels 1 and 2.

Atoms and molecules have a discrete set of possible excited energy levels. As a result, they will only pick up and emit specific values of the frequency. Metals, on the other hand, have a continuum of excited energy levels above the Fermi level. This set of permissible transitions, from the valence band to the conduction band, may be described by a set of harmonic oscillators damped in a forced sinusoidal regime.

Each oscillator has its own damping coefficient Γ_m and its own resonance frequency ν_m . Each resonant frequency characterizes an inter-band transition allowed by the Planck relation.

And finally, relative permittivity is written according to the following relation:

$$\epsilon_{r,LD}(\nu) = \epsilon_\infty + \sum_{j=1}^m \chi_j(\nu) \quad \text{II.20}$$

$$\text{With } \chi_j(\nu) = \frac{\nu_{pj}^2}{\nu_{0j}^2 - \nu^2 - i\nu\Gamma_j} \quad \text{II.21}$$

With m the total numbers of oscillators, j an integer designating the oscillator, ν_{0j} the j oscillator frequency (in Hertz), Γ_j the damping of the oscillator j (in Hertz) and ν_{pj} the plasma frequency of the oscillator j (in Hertz).

This model makes it possible to show that the dielectric constant takes into account the contribution of both free and bound charges.

The values of ε_∞ , ν_{pj} , ν_{0j} and Γ_j , used to calculate the real part and the imaginary part of the SiO₂ refractive index over the (700 – 2000) cm⁻¹ frequency range, are listed in the table 2.1 (for a number of oscillators $m = 5$) [21]:

$\varepsilon_\infty = 2.09$			
i^{th} oscillator	$\nu_{pi} (cm^{-1})$	$\nu_{0i} (cm^{-1})$	$\Gamma_i (cm^{-1})$
1	544	1046	15.53
2	309	1167	4.43
3	466	1058	0.42
4	427	443	54.14
5	223	799	12.94

Table 2.1: Physical parameters of the SiO₂ substrate

The numerical tools presented in the previous parts, are used in the followings to study the geometrical effects on the reflection properties of two different structures: a polysilicon / SiO₂ grating ridges and a polysilicon / air holes triangular grating (Figure 2.1).

We have investigated the effect of several parameters on the grating reflection properties:

- the width of the ridges,
- the hole diameters,
- the grating period,
- the incident wave polarization,
- the polycrystalline silicon thickness
- and the SiO₂ or air layer.

II.3 Ridges photonic crystal membrane made of polycrystalline silicon

II.3.1 Structure Si/Air/Si wafer

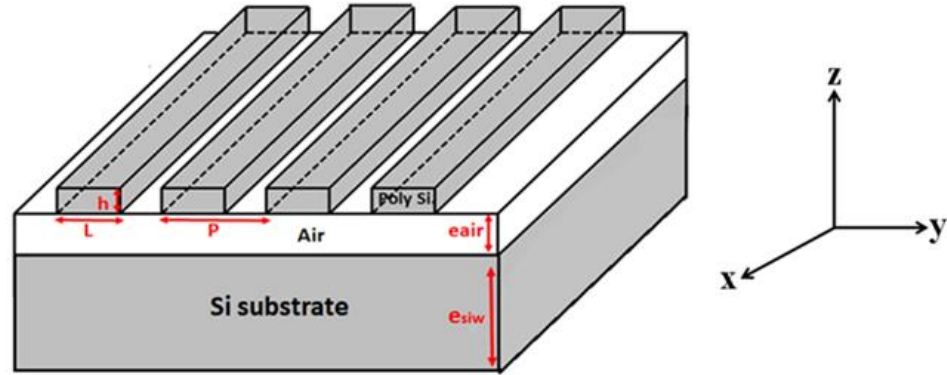
In this part, we consider an incident non-polarized electromagnetic wave radiating in air from the human body skin and interacting with a photonic crystal (PC) membrane made of polycrystalline silicon (PolySi) ridges in the mid-infrared (MIR) range (5-15 μm). To simulate a non-polarized incident wave, we first present the spectra considering the average of the transverse-electric (TE) and transverse-magnetic (TM) polarization of the reflective light. We will first study the effect of the geometry on the reflection spectrum and then we will determine the origin of the modes.

The investigated structure is composed of silicon ridges arranged on a silicon wafer substrate, separated by a layer of air (Figure 2.3 (a)). The model consists of silicon beams of infinite length along the x axis, characterized by their height h and width L . These silicon beams are periodically arranged on a silicon wafer substrate of thickness e_{siw} separated by an air layer of thickness $e_{air} = 2 \mu\text{m}$ and with respectively the refractive indices $n_{Si} = 3.47$ and $n_{air} = 1$ in the MIR (Figure 2.3 (a)). We consider P the period, applied along the axis Oy . On the unit cell of the ridges structure (Figure 2.3 (b)), Perfect Matching Layer (PML) are applied at the left and right sides to avoid reflections of outgoing waves. Periodic Boundary Conditions (PBC) are applied at all other boundaries to induce the periodicity. The incident electromagnetic waves propagate perpendicularly to the grating structures. The reflection detector is placed in the air medium, between the source and the periodic structure.

Since silicon is non-absorbent in the infrared spectrum, we can deduce the response of the transmission by calculating the reflection and then following the equation $T = 1 - R$.

Throughout this chapter we will simply present the reflection spectrum.

(a)



(b)



Figure 2.3: (a) 3D schematic representation of the PC films (Si/Air/Si structure) made of ridges of width L and height h . (b) Projection of the unit cell used for the FEM calculation.

II.3.1.1 Variation of the silicon substrate thickness

The structure of reference consists of the polysilicon ridges having a thickness $h = 750$ nm, a width $L = 4$ μm and a periodic lattice $P = 5$ μm . They are separated by a layer of air having a thickness $e_{air} = 2$ μm .

We first study the influence of the silicon substrate thickness e_{siw} on the reflection spectrum. Two thicknesses were chosen ($e_{siw} = 20$ μm and $e_{siw} = 80$ μm) to calculate the reflective behavior under normal incidence for a non-polarized source (Figure 2.4). One can see that the silicon substrate thickness has no effect on the reflection spectrum. Moreover, the reflection spectrum presents one peak and two dips (red arrows) due to the structuration at the wavelength $\lambda = 5.46$ μm , $\lambda = 6$ μm and $\lambda = 8.8$ μm respectively.

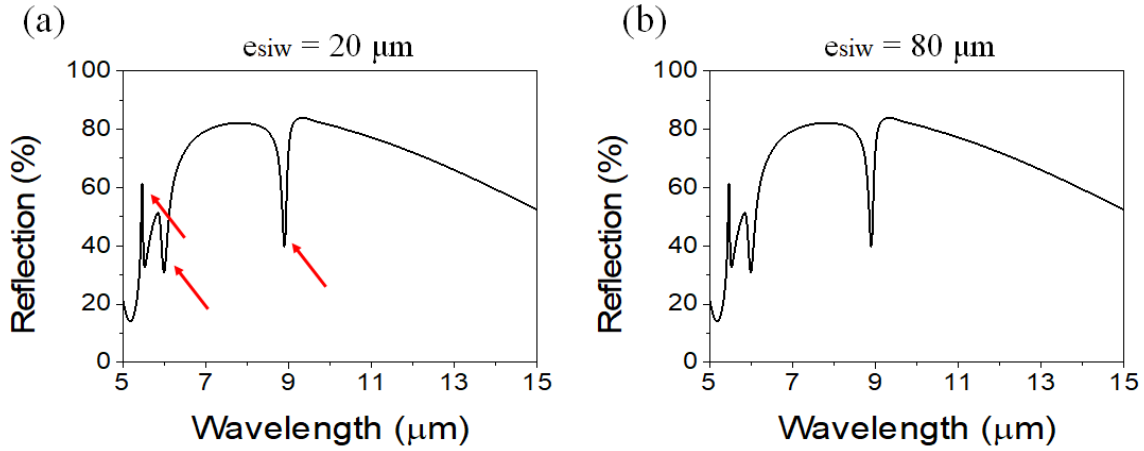


Figure 2.4: Reflection spectra of PolySi / Air / Si structure ($h = 750$ nm, $L = 4$ μ m, $P = 5$ μ m, $e_{air} = 2$ μ m) for a non-polarized incident for a substrate silicon thickness (a) $e_{siw} = 20$ μ m, and (b) $e_{siw} = 80$ μ m.

II.3.1.2 Variation of the air thickness

Now, we study the influence of the air thickness between the silicon beam and the silicon substrate, using the same dimensions as before for the system of periodic beams ($h = 750$ nm, $L = 4$ μ m, $P = 5$ μ m, $e_{siw} = 20$ μ m). Similarly, we have calculated the reflection behavior for a non-polarized source for an air thickness $e_{air} = 42$ μ m (Figure 2.5).

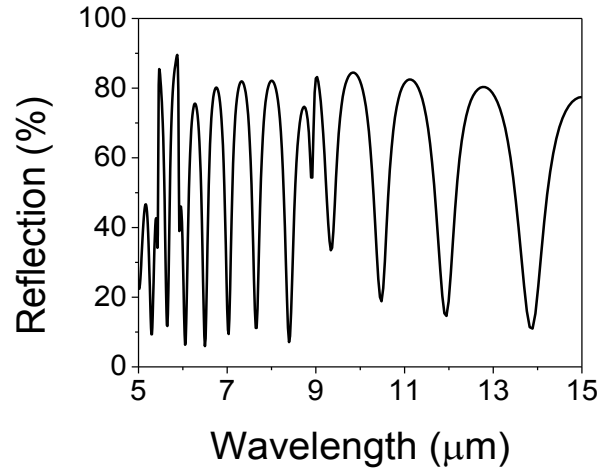


Figure 2.5: Reflection spectrum of a normally incident non-polarized light for the reference system of PolySi / Air / Si structure ($h = 750$ nm, $L = 4$ μ m, $P = 5$ μ m, $e_{siw} = 20$ μ m) with $e_{air} = 42$ μ m.

Series of oscillations can be seen in the reflection spectra due to waves trapped in the air gap between the ridge and the silicon substrate. These are known as Fabry-Perot oscillations. In

addition, the peaks described above are always present and they disturb the regularity of Fabry-Perot oscillations.

II.3.2 Structure Si/Air

II.3.2.1 Origin of modes

To identify the origin of the peaks/dips, the silicon substrate was removed, so the cavity between the ridge and the substrate does not exist anymore, and the Fabry-Perot oscillation disappears as expected (Figure 2.6).

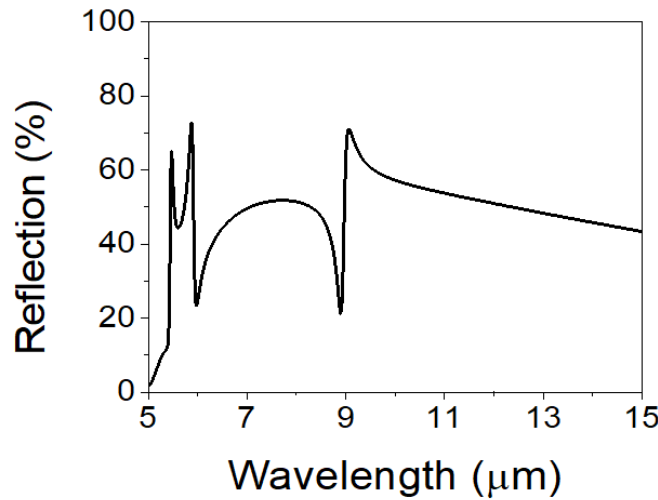


Figure 2.6: Reflection spectrum of the normally incident non-polarized light of a structure PolySi / Air (for $L = 4 \mu\text{m}$, $P = 5 \mu\text{m}$, $h = 750 \text{ nm}$).

One can see clearly a peak at the wavelength $\lambda = 5.46 \mu\text{m}$ and two asymmetric peaks. For the first asymmetric peak, it exists at a wavelength of $\lambda = 5.8 \mu\text{m}$ (maximum) and $\lambda = 6 \mu\text{m}$ (minimum). For the second one, it exists at a wavelength of $\lambda = 8.9 \mu\text{m}$ (maximum) and $\lambda = 9 \mu\text{m}$ (minimum). In order to understand the origin of the peaks and dips described in the previous paragraph and the effect of the light polarization on the reflection spectrum, we have dissociated the TE and TM polarizations.

In figure 2.7, two different spectra were found for the TE and TM incident wave polarizations.

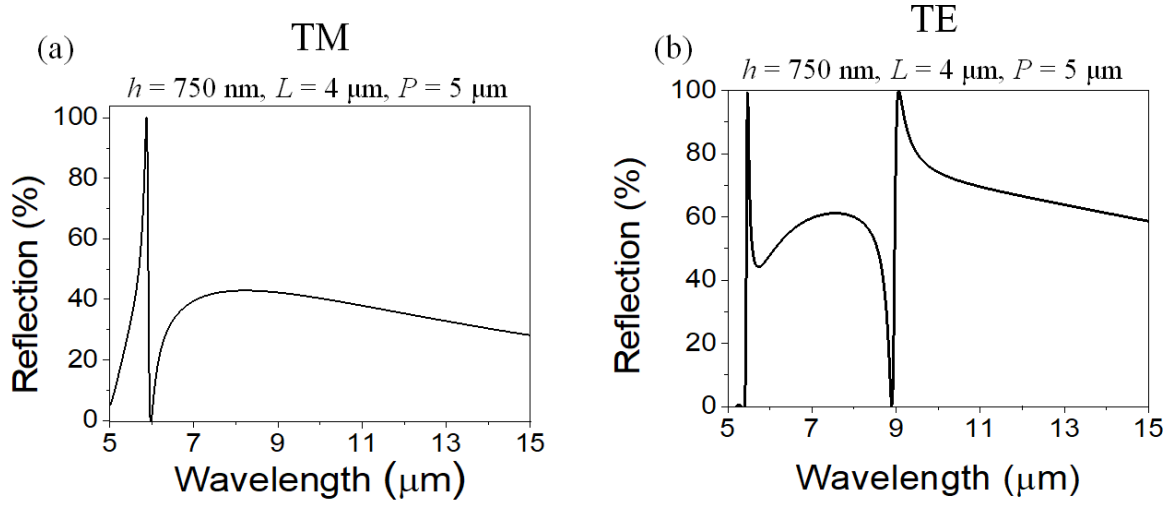


Figure 2.7: Reflection spectra of a PolySi / Air structure for (a) the TM and (b) TE polarizations for $L = 4 \mu\text{m}$, $P = 5 \mu\text{m}$ and $h = 750 \text{ nm}$.

The comparison of these two spectra with the one observed for non-polarized wave allows to attribute, in figure 2.6, the peaks at $\lambda = 5.46 \mu\text{m}$ and the asymmetric peak around $9 \mu\text{m}$, to the TE polarization. The asymmetric peak around $6 \mu\text{m}$ comes from the TM polarization. Then we have calculated the distribution of the electric field for all these peaks.

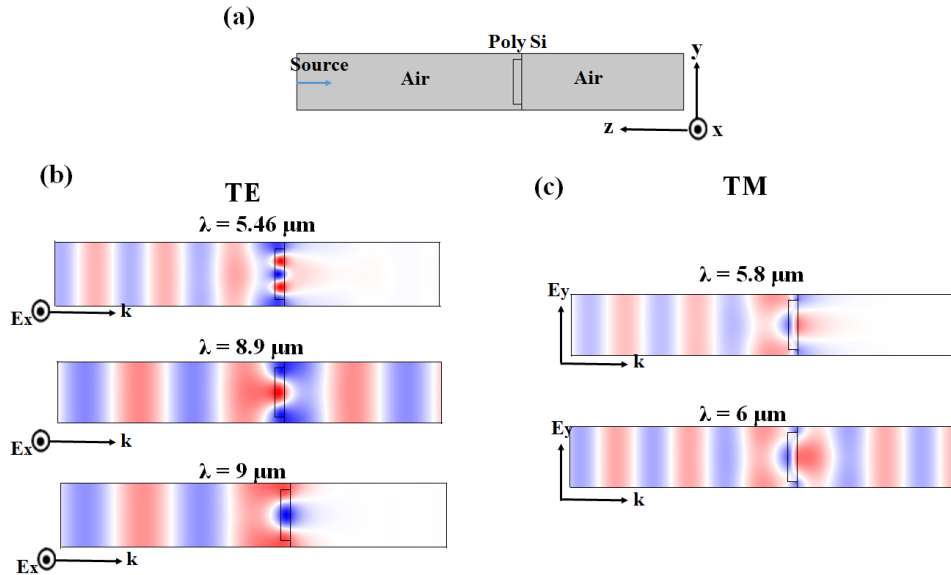


Figure 2.8: (a) Scheme of the unit cell of a PolySi/Air structure. (b) Field maps calculations for TE polarization at the wavelengths $\lambda = 5.46 \mu\text{m}$, $\lambda = 8.9 \mu\text{m}$ and $\lambda = 9 \mu\text{m}$. (c) Field maps calculations for TM polarization at the wavelengths $\lambda = 5.8 \mu\text{m}$ and $\lambda = 6 \mu\text{m}$.

Figure 2.8 (a) recalls the elementary cell used for the computation of electric field maps. Figure 2.8 (b) represents the calculation of the electric field in TE polarization (E_x) at the wavelengths 5.46 μm , 8.6 μm and 9 μm .

For the field map which corresponds to the peak at the wavelength $\lambda = 5.46 \mu\text{m}$, the incident wave propagating from left to right interacts with the silicon ridge. At this wavelength, we observe a zero transmission as shown by the absence of field to the right of the membrane.

Then, for the asymmetric peak associated respectively with the wavelengths 8.9 and 9 μm , the field map shows that the wave is transmitted through the first membrane while the second membrane leads to total reflection of the wave.

Also, in the figure 2.8 (c), we represent the calculation of the electric field in TM polarization (E_y) at the wavelengths 5.8 μm and 6 μm . The same observation can be made: the wave interacts with the membrane and leads to a total reflection at the wavelength 5.8 μm and to a total transmission at 6 μm . This time we note that, contrary to the previous case, the reflection occurs at low wavelengths, reversing the asymmetrical shape of the peak.

In both cases, TE and TM, the origin of the interaction can be described as follows:

The propagative incident wave interacts with a stationary mode of the photonic ridge, leading to a destructive or constructive interference. This phenomenon is known as Fano resonance, defined by the interaction between a continuous (propagative) mode and a stationary (localized) mode (see section I.2.5). The two waves are superimposed and interfere, giving rise to transmission or reflection depending on whether they are in phase or out of phase.

II.3.2.2 Influence of the thickness h , width L and period P of the ridges on the reflection spectrum.

In this section, we varied the geometric parameters so that the reflective modulations observed in the previous spectrum could be active in the wavelength range between [5-15] μm .

Figure 2.9 illustrates the reflection spectra of an incident non-polarized light transmitted normally to the PolySi / air structure ($L = 4 \mu\text{m}$, $P = 5 \mu\text{m}$) for a variety of thicknesses, h , of the ridges, ranging from 750 nm to 1200 nm.

One can see clearly that the asymmetric peak described above approximately $9 \mu\text{m}$ for TE polarization (black solid line) moves towards longer wavelengths as the thickness of the silicon ridges is increased.

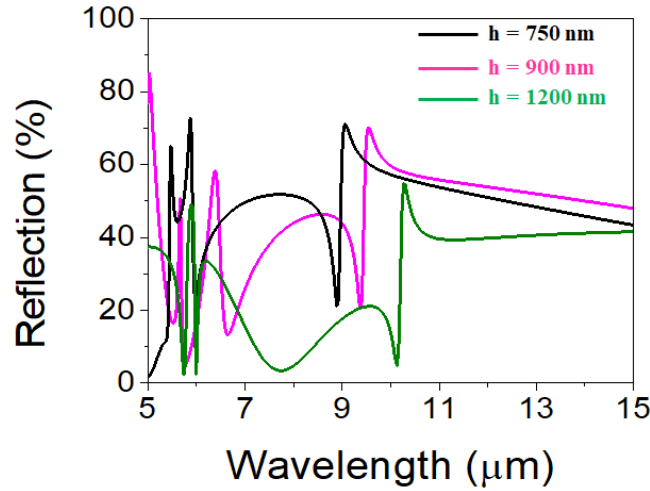


Figure 2.9: Evolution of the reflection spectra as a function of the thickness of the membrane, $h = 750 \text{ nm}$, $h = 900 \text{ nm}$ and $h = 1200 \text{ nm}$, for ($L = 4 \mu\text{m}$, $P = 5 \mu\text{m}$).

For a more detailed interpretation of the effect of the material thickness, the figure 2.10 below represents the same calculation by differentiating the TE and TM polarizations, specifically for a ridge thickness of $h = 1200 \text{ nm}$.

For TM polarization, when the thickness becomes large ($h = 1200 \text{ nm}$) two large peaks appear at low wavelengths. The calculations of the distribution of the electric field at $\lambda = 5.4$ and $7.5 \mu\text{m}$ shows us that its peaks correspond to the resonance modes of the membrane (Figure 2.10 (a)).

For the TE mode (Figure 2.10 (b)), we find the asymmetric peak at $10 \mu\text{m}$ which corresponds to the Fano resonance. We also obtain an additional mode at $\lambda = 5.74 \mu\text{m}$ compared to the $5.46 \mu\text{m}$ mode obtained previously for the membrane of thickness $h = 750 \text{ nm}$. The field map is represented in figure 2.10 (b) at $\lambda = 5.74 \mu\text{m}$ in which we see that the mode is located in the membrane. Unlike the previous mode, it is asymmetrical with respect to the plane of symmetry which passes through the middle of the membrane.

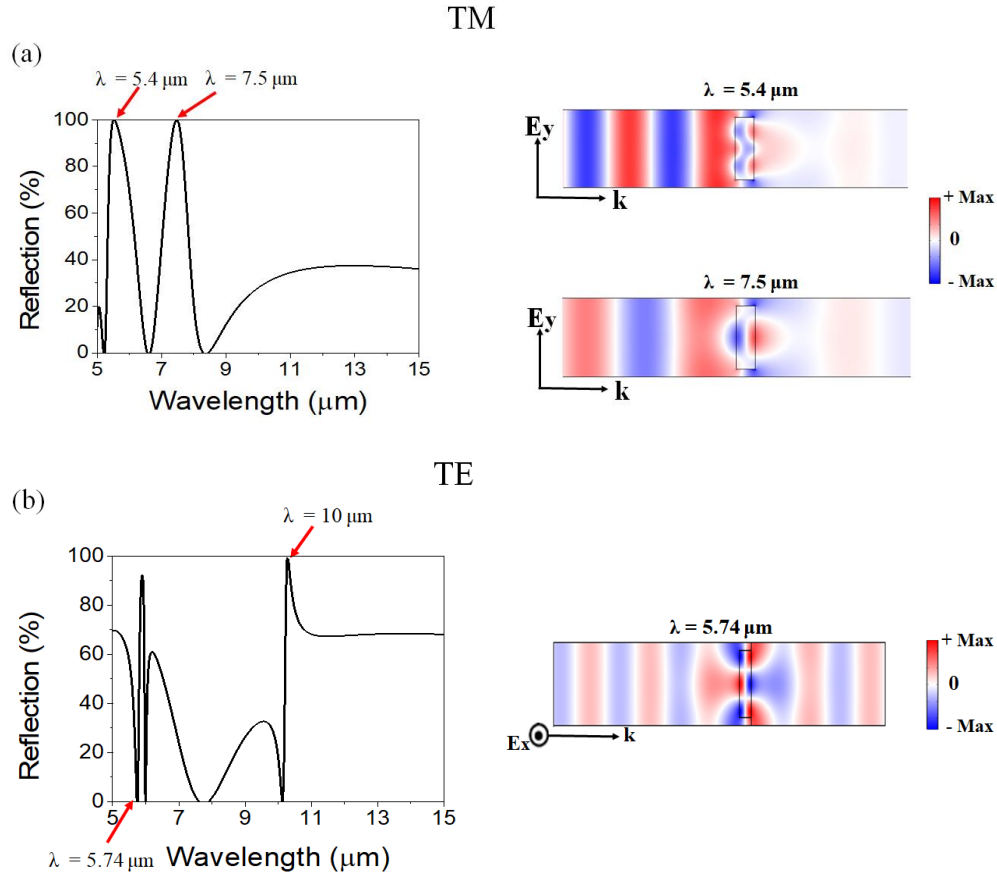


Figure 2.10: (a) Reflection spectrum (Left) and distribution of the electric field (Right) at the wavelength $\lambda = 5.4 \mu\text{m}$ and $7.5 \mu\text{m}$ for the TE polarization of a Si / air structure for $L = 4 \mu\text{m}$, $P = 5 \mu\text{m}$ and $h = 1200 \text{ nm}$. (b) Reflection spectrum (Left) and distribution of the electric field (Right) at the wavelength $\lambda = 5.74 \mu\text{m}$ for the TM polarization.

The increase in thickness would therefore have the same consequence for the two polarizations, TE and TM, which reveals additional resonance modes of the membrane.

Finally, we applied a scale law on the geometrical parameters to shift the specific dips and peaks at higher wavelength. Indeed, by increasing all dimensions of the structure homothetically, all features of the wavelength spectrum shift towards the higher wavelengths (Figure 2.11).

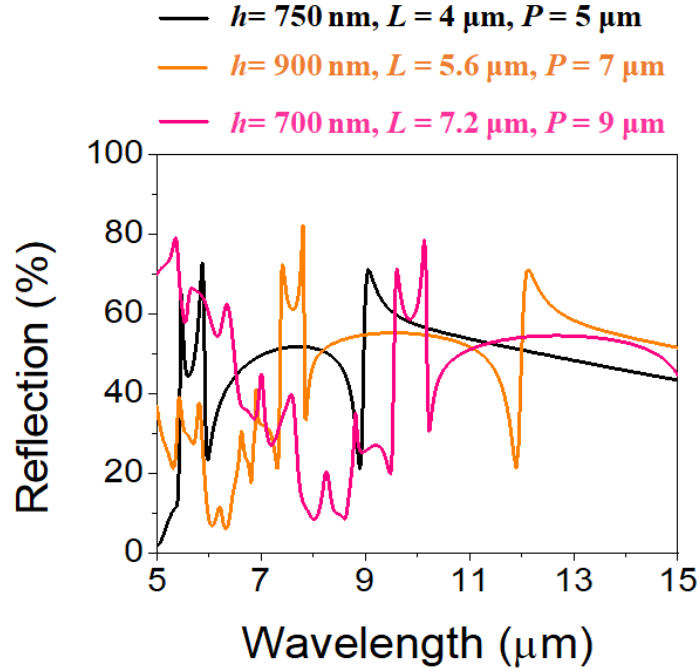


Figure 2.11: Evolution of the reflection spectra for an incident non-polarized wave launched perpendicularly to the membrane for a homothetic variation of the parameters P , h and L , with $L/P = 0.8$.

In summary, the progression of the reflective properties of a photonic crystal membrane made up of polycrystalline silicon ridges and separated from a silicon wafer substrate by a layer of air was studied in the mid-infrared range (5-15 μm). This structure made it possible to identify two physical effects. The first one comes from the existence of membrane resonance modes which depend on the thicknesses of the membrane. The second one is the occurrence of sharp asymmetric peaks and dips which depend on the geometrical parameters of the membranes (h , L and P). The origin of these asymmetric peaks is known as Fano resonance, which is characterized by the interaction between a continuous (propagative) mode and a stationary mode located in the structured silicon membrane.

Due to experimental constraints, PolySi/air/Si wafer structure could not be achieved. Therefore, the air layer has been replaced by a SiO_2 layer in order to support the ridges. The corresponding Si/ SiO_2 /Si structure will be presented in the upcoming section.

II.3.3 Structure Si/ SiO_2 /Si wafer

Although the previous structure is efficient (polysilicon ridges in air) in the objective of interaction in the 9 μm range, the structured polysilicon membranes were impossible to release.

To overcome the experimental difficulties, the system under consideration consists of the same periodically spaced polysilicon beams (infinite length along the x axis, height h and width L) but now arranged on a silica layer of thickness $e_{\text{SiO}_2} = 2 \mu\text{m}$, this latter based on a thick silicon substrate of thickness e_{Siw} (Figure 2.12 (a)). We consider, as before, the non-polarized electromagnetic waves coming from the human body skin radiating and interacting with the photonic crystal (PC) membrane of polycrystalline silicon (PolySi) ridge.

The constitutive materials were chosen in order to ensure a high refractive-index contrast and because their optical properties and microfabrication process are well mastered. The silicon and polysilicon materials have constant refractive index in the mid-infrared range ($n_{\text{Si}} = n_{\text{PolySi}} = 3.47$ in MIR) while silica exhibits absorption phenomena in the 5-15 μm range its real refractive index is low compared to Si and therefore it is possible to have an index contrast.

Perfect Matching Layer (PML) are applied at the left and right sides of the unit cell of the ridges structure (Figure 2.12 (b)) to avoid any reflections of outgoing waves, while Periodic Boundary Conditions (PBC) are applied at all other boundaries along x and y to induce the periodicity. The incident electromagnetic wave propagates perpendicularly to the grating structures, along the z direction. The reflection detector is placed in the air medium, between the source and the periodic structure.

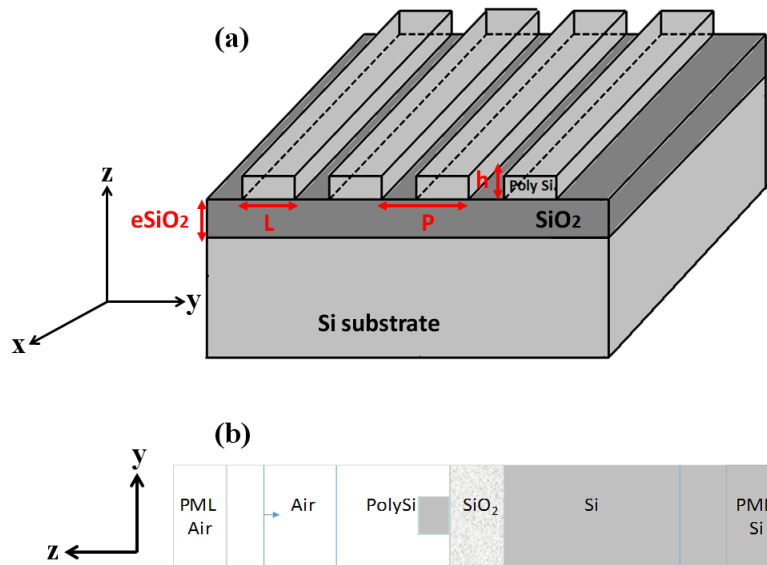


Figure 2.12: (a) 3D schematic representation of the PC films (Si/SiO₂/Si structure) made of ridges of width L (b) Projection of the unit cell used for the FEM calculation.

II.3.3.1 Influence of the width of the ridge

We have studied the influence of the width of the beam (denoted L) of a PolySi / SiO₂ / Si beam network on the optical response. We have calculated the evolution of the reflection under normal incidence for a non-polarized light as a function of the wavelength when the width (L) of the PolySi ridges decreases from 5 μm to 0 μm with a constant pitch, $P = 5 \mu\text{m}$. The results obtained are presented in Figure 2.13 (a). The thicknesses of the PolySi and SiO₂ membranes are $h = 750 \text{ nm}$ and $e_{\text{SiO}_2} = 2 \mu\text{m}$ respectively. A larger thickness of SiO₂ cannot be experimentally used (max 2 μm) due to the constraints of the deposition process (deposition rate: 3 nm/min).

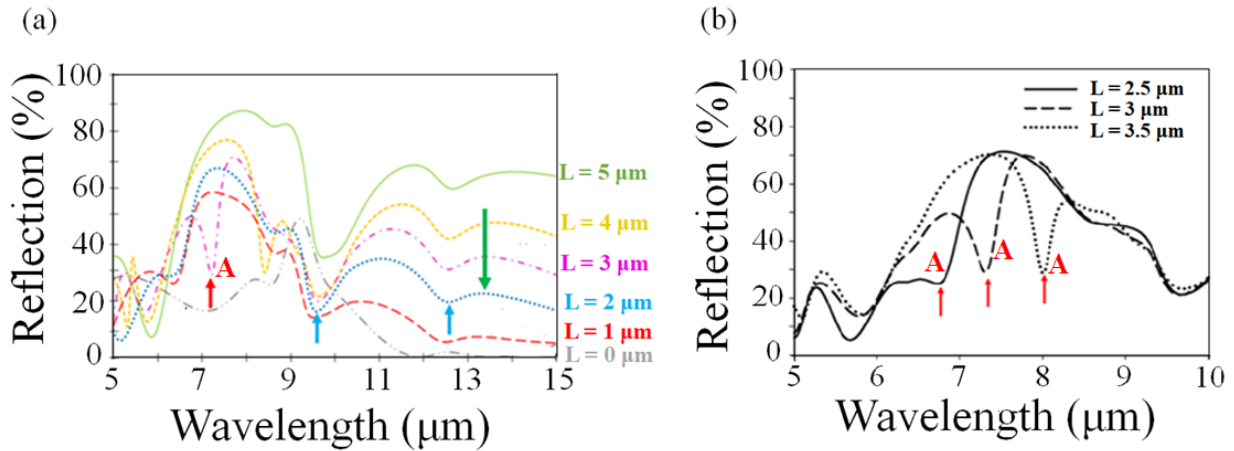


Figure 2.13: Evolution of the reflection spectrum of a Si/SiO₂/Si structure in the mid-infrared range versus the width of the ridges (L), for the ridges structure having a periodic lattice $P = 5 \mu\text{m}$ and thicknesses of PolySi and SiO₂, $h = 750 \text{ nm}$ and $e_{\text{SiO}_2} = 2 \mu\text{m}$ respectively (a) [5, 15] μm and (b) [5, 10] μm .

From figure 2.13 (a), we observe, for $L = 5 \mu\text{m}$ (PolySi plane surface, unstructured), two large dips in the reflection spectra in the vicinity of 9.5 μm and 12.5 μm corresponding to the absorption property of silica. This behavior increases with the porosity, thus discovering the SiO₂ surface (blue arrows). Besides, one can also see that the average level of reflection decreases when the filling factor decreases (green arrow). Finally, a third valley is also present at $\lambda = 7.36 \mu\text{m}$ for $L = 3 \mu\text{m}$ (red arrow). Looking deeply in details in the [5 – 10] μm range (Figure 2.13 (b)), one can clearly see that this wavelength strongly depends on the ridge width, meaning this reflective dip A is due to a resonant mode of the membrane which couples to the incident wave. In figure 2.13, I performed the calculations during Maude Villon thesis using the FDTD method.

II.3.3.2 Origin of modes

In order to understand the origin of the dips described in the previous paragraph and the effect of light polarization on the reflection spectrum, we have dissociated in this part the TE and TM (Transverse Electric and Transverse Magnetic respectively) polarization.

TE and TM incident wave polarizations (Figure 2.14) induce very different spectra. Indeed, when the wave is TE polarized (the electric field is along the x axis) the reflectance reaches an intensity greater than 90% for the reflection band ranging from 7.5 to 9.5 μm for $L = 3 \mu\text{m}$. The average reflection intensity for the TM polarization (magnetic field along the x axis) is much lower than TE in the wavelength range of interest.

Moreover, the dip A observed in (Figure 2.10 (a)) at 7.2 μm , for $L = 3 \mu\text{m}$, comes from the TE polarization and was partially attenuated by the spectrum of polarization TM.

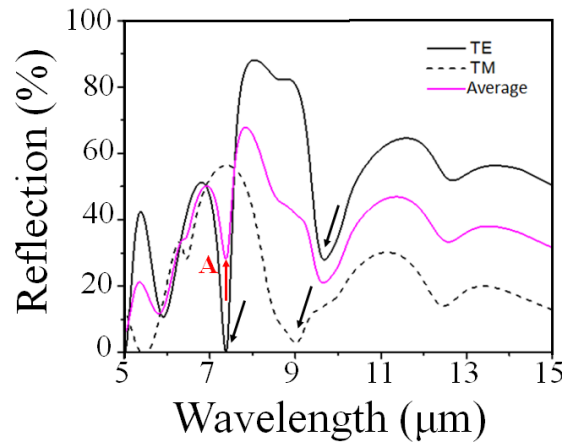


Figure 2.14: Reflection spectra of a Si/SiO₂/Si structure for the TE, TM polarizations and the average of TE and TM polarized for a ridge width of $L = 3 \mu\text{m}$ and period $P = 5 \mu\text{m}$.

To determine the origin of the reflection peaks occurring in the spectra of figure 2.14(a) (black arrows), we calculated the field maps at the wavelengths 7.3 μm and 9.7 μm for TE and 9.1 μm for TM. The results are shown in figures 2.15 (TE) and 2.16 (TM). These allow us to verify that the intensity variation, and the shift towards the longest wavelengths, are due to the presence of the polysilicon ridges grating since one can see that the electric and magnetic fields are localized in the ridge.

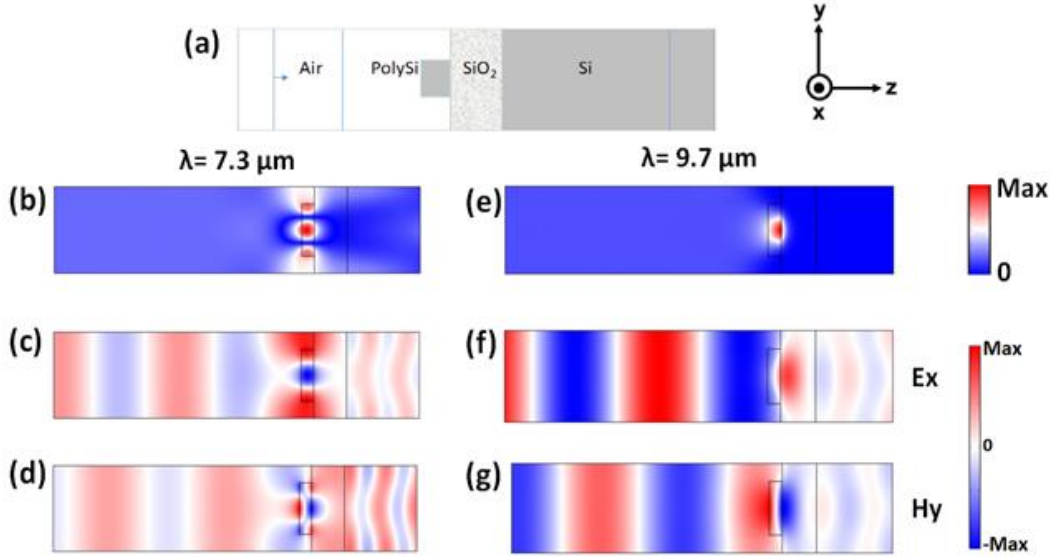


Figure 2.15: Field maps calculations for TE polarization of a Si/SiO₂/Si structure ($L = 3 \mu\text{m}$, $P = 5 \mu\text{m}$) at the wavelengths $7.3 \mu\text{m}$ (left) and $9.7 \mu\text{m}$ (right): (a) Scheme of the unit cell, (b, e) Pointing vector, (c, f) E_x components, and (d, g) H_y components.

Figure 2.15 (a) recalls the elementary cell used for the computation of the field maps. The figure 2.15 (b) corresponds to the calculation of the Pointing vector at the wavelength $7.36 \mu\text{m}$. This represents the energy in the different media crossed by the incident EM wave. Looking at the components of the electric fields E_x and magnetic H_y in polarization TE at this same wavelength (Figure 2.15 (c)) and (d) respectively), one can see that the dip at the wavelength $7.36 \mu\text{m}$ corresponds to a symmetric mode strongly localized in the silicon ridges. The dip at $9.72 \mu\text{m}$ wavelength in TE polarization corresponds to an antisymmetric mode strongly localized in the ridges silicon (Figures 2.15 (f) and (g)). Similarly, the calculation of the distribution of the electric field for the dip at the $9.1 \mu\text{m}$ wavelength in TM polarization, for ridges grating of width $L = 3 \mu\text{m}$ and period $P = 5 \mu\text{m}$, reveals an antisymmetric mode strongly localized in the ridges silicon (Figure 2.16).

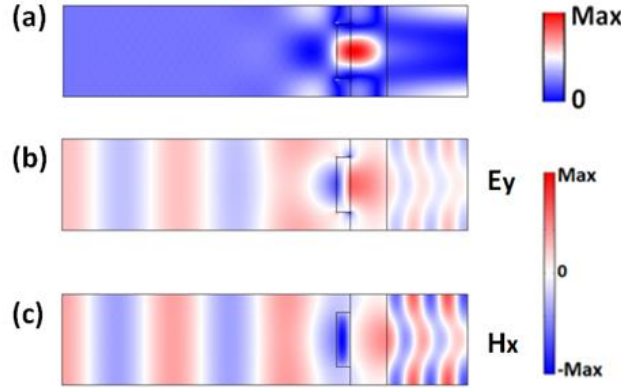


Figure 2.16: Field maps of a Si/SiO₂/Si structure for ridges grating of width $L = 3 \mu\text{m}$ and period $P = 5 \mu\text{m}$ at a wavelength of $9.1 \mu\text{m}$ for TM polarization: (a) Poynting vector and field components (b) E_y and (c) H_x .

II.4 Holes photonic crystal membrane made of polycrystalline silicon

As for the periodic polysilicon ridges grating, we studied the influence of the various geometrical parameters of a polysilicon / air triangular holes grating of refractive index ($n_{\text{Si}} = n_{\text{PolySi}} = 3.47$) (Figure 2.17 (a)).

We defined a 3D unit cell to represent the full 2D periodic structure. Figures 2.17 (b) and (c) shows a 3D representation of the elementary unit cell used for the calculation and the involved geometrical parameters.

We consider an incident non-polarized electromagnetic waves radiating in air from the human body skin and interacting with the photonic silicon membrane. The reflection spectra presented in this study correspond to an average of the two polarizations (TE and TM). In the calculation, the incident wave is launched perpendicularly to the membrane and the reflection (R) of the outgoing signal is recorded. The source and the detector are placed in air before the membrane. The incident source is a plane wave generated in the air medium which propagates along the z -direction, perpendicularly to the periodic structure.

Along the x and y direction, periodic boundary conditions (PBC) are applied on each side of the unit cell to build the periodic structure. As the structure is supposed to be infinite along the z direction, perfect matching layers (PMLs) are applied at the finite boundaries of the box, along z , in order to avoid any reflections of outgoing waves. All calculations have been performed on a periodic triangular array of holes drilled in the membrane.

We have studied the influence of the geometrical parameters (the hole diameter D , the period of the crystal lattice P and the thickness of the membrane, h) of the PolySi / Air / Si triangular holes

grating on their optical properties in reflection. In this section, all the reflection spectra calculations were done by the FDTD method during my first year of Phd for Maud Viallon thesis.

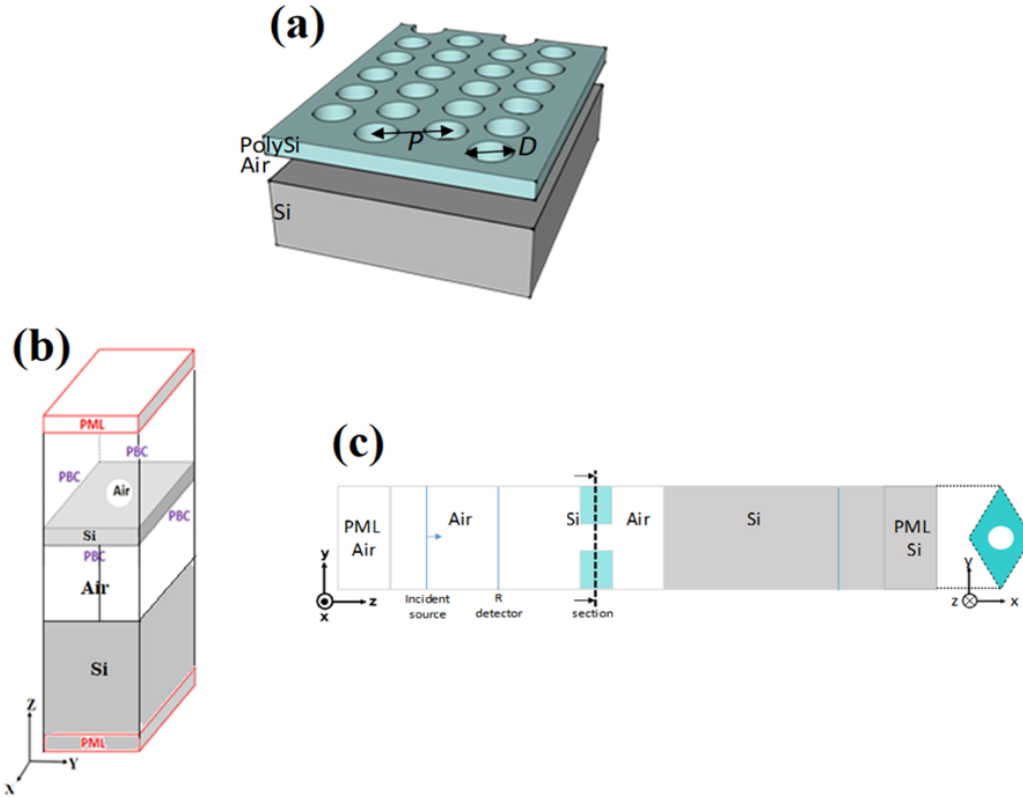


Figure 2.17: (a) 3D schematic representation of the PC of the silicon membrane (Si/Air/Si structure) of thickness h , drilled with a triangular array of air holes with period P and diameter D a). (b) 3D Schematic representation of the 3D elementary unit cell for the FEM calculation of PC film made of triangular holes grating (Si/Air/Si structure). (c) Section of the unit cell according to the planes (y, z) and (x, y) .

II.4.1 Influence of the polarization (TE and TM)

In this section we have calculated the reflection spectra of a Si/Air/Si structure for TE (solid line) and TM (dotted line) polarizations of the incident light, for the hole diameter $D = 2 \mu\text{m}$, the period of the lattice $P = 5 \mu\text{m}$ and the thickness of the membrane $h = 750 \text{ nm}$ (Figure 2.18). One can see that the two spectra are the same. This result indicates that for a triangular hole lattice, the reflection at $7.3 \mu\text{m}$ is not dependent on the polarization of the incident EM wave. The lattice will therefore have the same optical properties whatever the polarization of the EM wave. This result will make the calculation simpler, since we can make simulation for only one polarization.

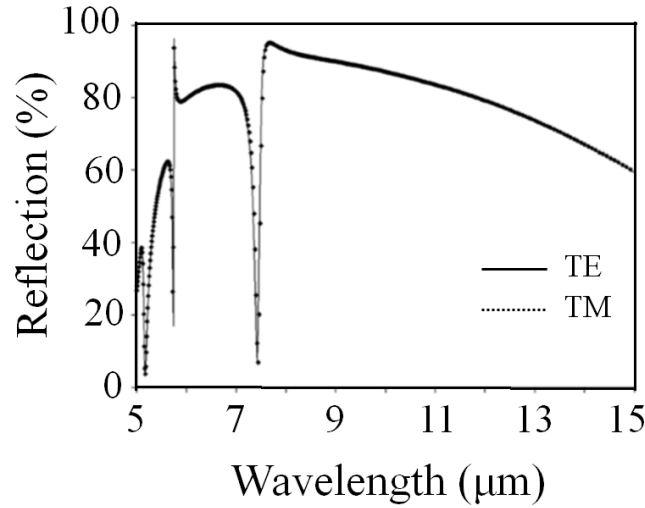


Figure 2.18: Reflection spectra of a Si/Air/Si structure for TE (solid line) and TM (dotted line) polarizations of the incident light, for $D = 2 \mu\text{m}$, $h = 750 \text{ nm}$ and $P = 5 \mu\text{m}$.

II.4.2 Influence of the hole diameters

Similarly, to the ridge structure, we have calculated the reflective behavior of the perforated membrane under normal incidence, considering a variation of the hole diameter (D), keeping the period $P = 5 \mu\text{m}$. Figure 2.19 (a) gives the evolution of the reflective spectrum versus D , in the range $[5, 15] \mu\text{m}$. For wavelength higher than $9 \mu\text{m}$, the reflectivity decreases when D increases (green arrow). As previously, the variation of the effective refractive index of the membrane leads to a variation of the reflection coefficients according to Fabry-Perot general behaviors. At wavelength lower than $9 \mu\text{m}$, one can see the occurrence of a narrow dip (**B**) at $\lambda = 7.4 \mu\text{m}$ for $D = 2 \mu\text{m}$ (red circle). This dip is strongly dependent of the diameter of the holes, suggesting that the contribution comes from the structuration of the membrane. This dip is shifted towards shorter wavelength as the diameter of holes increases (upward direction arrows).

This result is strengthened by the representation of the electric field component E_x (TE polarization) at the wavelength $\lambda = 7.4 \mu\text{m}$ (Figure 2.19 (b)). Again, this dip corresponds to a resonant mode which belongs to the membrane and couple to the incident wave. Contrariwise to the ridges structure, the energy is spread over the whole membrane, i.e. both inside and between the holes, meaning that it corresponds to a guided mode of the membrane. Its asymmetric shape suggests that the mechanisms behind this feature is attributed to Fano resonances.

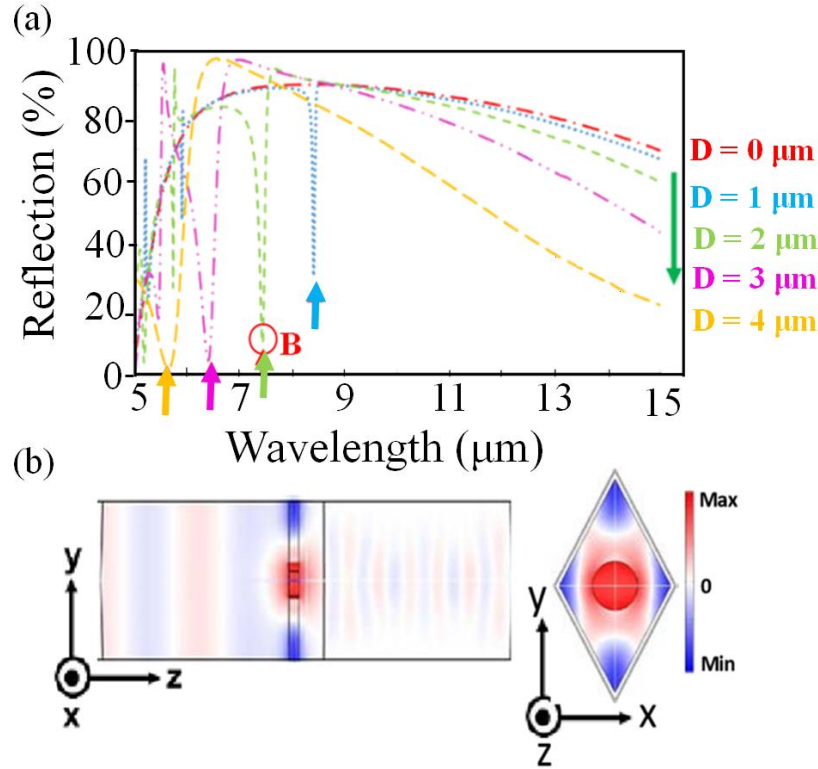


Figure 2.19: (a) Evolution of the reflection spectrum of a Si/Air/Si structure for the perforated membrane versus the diameter (D) of the holes in the range $[5, 15] \mu\text{m}$. (b) Representation of the electric field component E_x at the wavelength $7.4 \mu\text{m}$ (dip **B**) for $D = 2 \mu\text{m}$ in the plane (y, z) (left) and (x, y) (right).

II.4.3 Influence of the periodic lattice

The period is a crucial parameter of the photonic crystal structure, in close relation with the wavelength range. By scaling the period and all parameters of the photonic crystal, we will be able to operate a translation of the reflective dips in the wavelength of interest. We studied the influence of the period on the spectrum patterns and the reflection intensities by comparing different lattice of holes of different diameters and periods. For this study, we fixed the thickness of Polysilicon and air at 750 nm and $2 \mu\text{m}$ respectively and we kept a fixed filling factor of 0.72 . The periods of the triangular lattice vary from 5 to $12.6 \mu\text{m}$. The results are shown in figure 2.20.

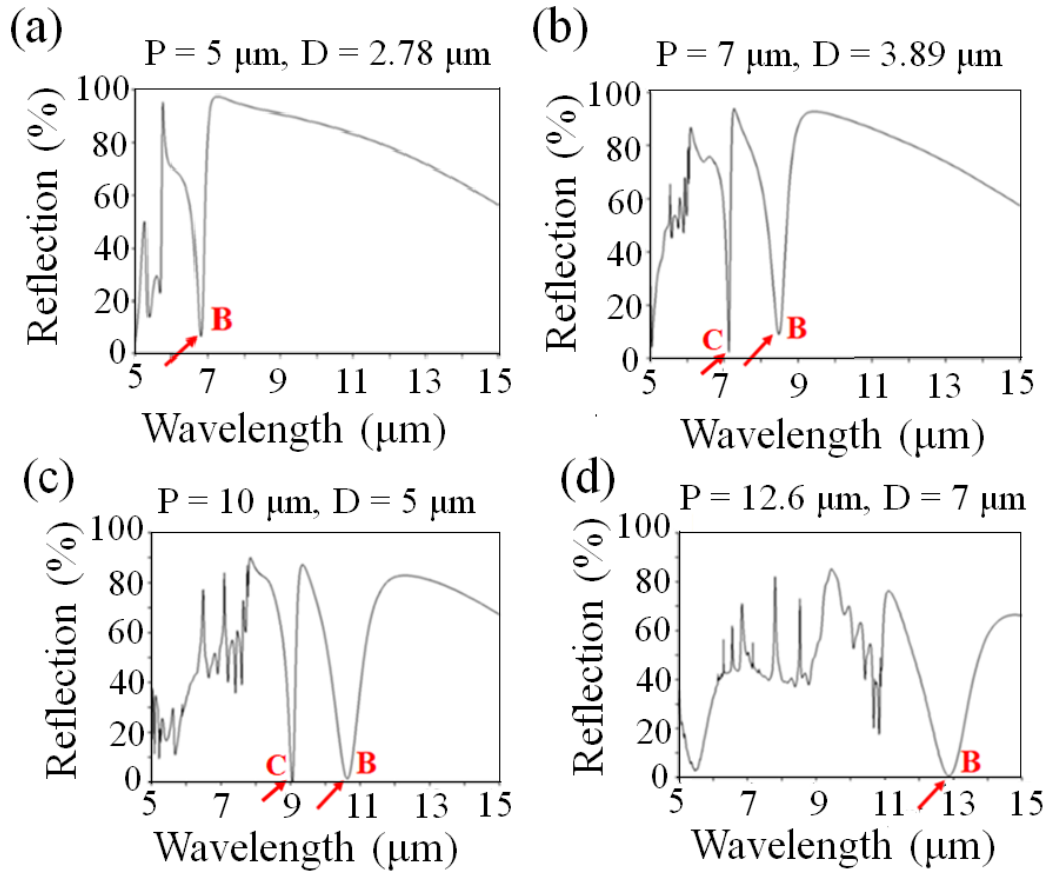


Figure 2.20: Reflection spectra of the triangular hole grating (Si/Air/Si structure) for different diameters D and periods P , a constant filling factor of 0.72 and for Polysilicon and air thicknesses of 750 nm and 2 μm respectively. The main reflection dips are indicated by red arrows.

When increasing the period of the triangular lattice, one can note a shift of the whole spectrum towards the longer wavelengths. The general shape of spectrum patterns and peak/dips intensities are similar regardless of the period. Also, one can see the dip **B** in the vicinity of respectively $\lambda = 6.8 \mu\text{m}$, $\lambda = 8.8 \mu\text{m}$, $\lambda = 10.8 \mu\text{m}$ and $\lambda = 12.9 \mu\text{m}$, in correspondence with the period P of the lattice. It clearly appears a second dip (**C**) at $\lambda = 7.2 \mu\text{m}$ and $\lambda = 9.02 \mu\text{m}$ in figure 2.18 (b) and (c) respectively.

The distribution of the electric field (Figure 2.19) for the second dip (**C**) in figure 2.18 (c) corresponds to a guided mode in the silicon membrane that presents, compared to the mode **B**, a higher order of distribution of the electromagnetic field along the x axis.

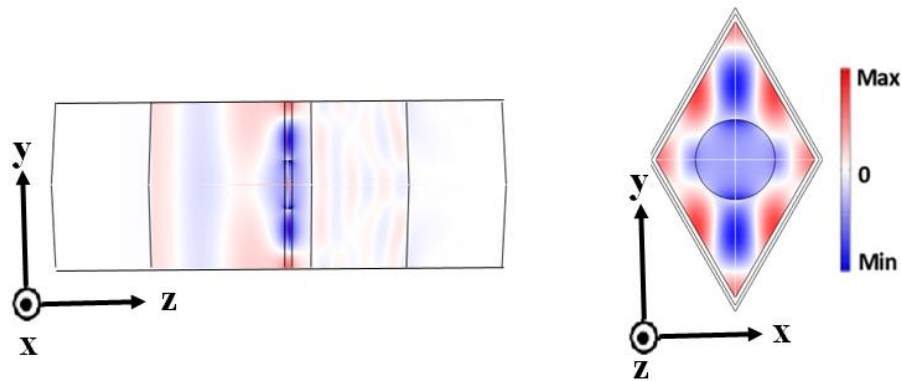


Figure 2.21: Representation of the electric field component E_x at the wavelength $7.2 \mu\text{m}$ (second dip C), for $D = 5 \mu\text{m}$, $h = 750 \text{ nm}$ and $P = 10 \mu\text{m}$, in the planes (y, z) (left) and (x, y) (right) .

We made the demonstration that it was possible to tune the specific features of the reflective spectrum with the geometrical parameters and to display them more specifically around the $9 \mu\text{m}$, the wavelength corresponding to the maximum of the human body emission.

II.5 Manufacturing method of ridges and holes grating

In this part, we described the experimental work done, in the clean room, by a former PhD of the Bio-MEMS group (IEMN), Maud Viallon [22]. We present her main results dealing with the filing of the silicon dioxide (SiO_2) and polycrystalline silicon (PolySi) layers, as well as the manufacturing process of both types of gratings in the layer of PolySi.

The FT-IR optical characterization of the obtained structures thereafter presented was made in collaboration between Maud Viallon and myself.

Figure 2.22 shows the global scheme of the manufacturing process of these gratings. Firstly, a SiO_2 layer, of about $2 \mu\text{m}$, is formed on a silicon substrate by a wet thermal oxidation and then a layer of polycrystalline silicon (PolySi) of about 750 nm is deposited on this layer by chemical vapor deposition (CVD). In a second time, ridges and holes grating are structured in the PolySi layer using photolithography and reactive ion etching (RIE) methods.

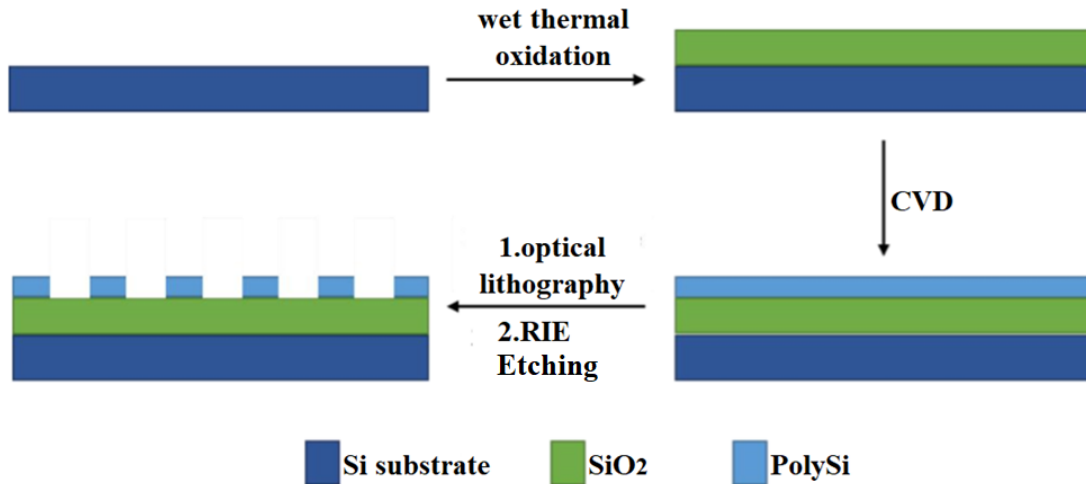


Figure 2.22: Global scheme of the manufacturing process of silicon polycrystalline ridges and holes periodic gratings [22].

Three chrome masks, with various period and hole diameter or beam width, were specially manufactured to fabricate the two types of networks. The ridges or holes grating patterns were periodically reproduced on a square surface of 2.3 cm x 2.3 cm to obtained structured surfaces compatible with the mid-infrared characterization facilities we used.

An example of the mask is presented in the figure, that might give two structures depending of the mask. The first structure is the ridge gratings ($P = 10\mu\text{m}$, $L = 5.5\mu\text{m}$), while the second structure is the hole gratings ($P = 10\mu\text{m}$, $L = 5.5\mu\text{m}$) (Figure 2.23).

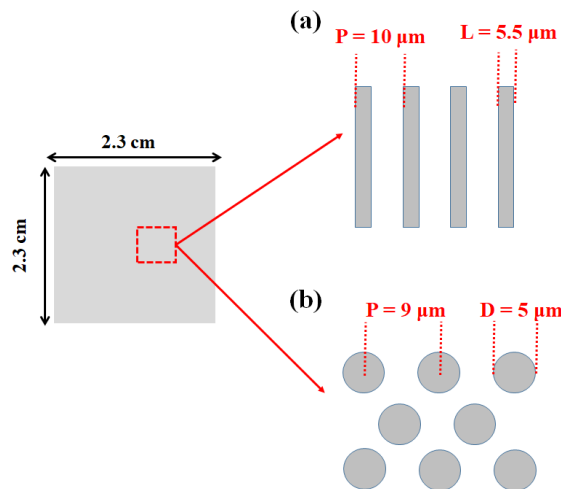


Figure2.23: An example of optical mask, used for the UV exposure of a 3'' substrates, gives (a) ridge gratings with $P = 10\mu\text{m}$ and $L = 5.5\mu\text{m}$ and (b) hole gratings with $P = 10\mu\text{m}$, $L = 5.5\mu\text{m}$) [22].

This manufacturing process allowed us to obtain 8 different dimensions, 4 corresponding to the ridge structure $[(P=5\text{ }\mu\text{m}, L=2\text{ }\mu\text{m}), (P=5\text{ }\mu\text{m}, L=3\text{ }\mu\text{m}), (P=10\text{ }\mu\text{m}, L=5.5\text{ }\mu\text{m}), (P=15\text{ }\mu\text{m}, L=8.25\text{ }\mu\text{m})]$ and 4 corresponding to the hole structure $[(P=5\text{ }\mu\text{m}, D=2\text{ }\mu\text{m}), (P=5\text{ }\mu\text{m}, D=3\text{ }\mu\text{m}), (P=9\text{ }\mu\text{m}, D=5\text{ }\mu\text{m}) \text{ and } (P=12.6\text{ }\mu\text{m}, D=7\text{ }\mu\text{m})]$.

An example of a scanning electron microscopy (SEM) images is represented in the figure 2.24 for one of the ridges gratings with a period and beam width equal to 10.2 and 5.5 μm respectively. In addition, this example gives the result of the fabrication of a triangular hole grating after SiO_2 etching with a period equal to 9.1 and a hole diameter equal to 5.1 μm .

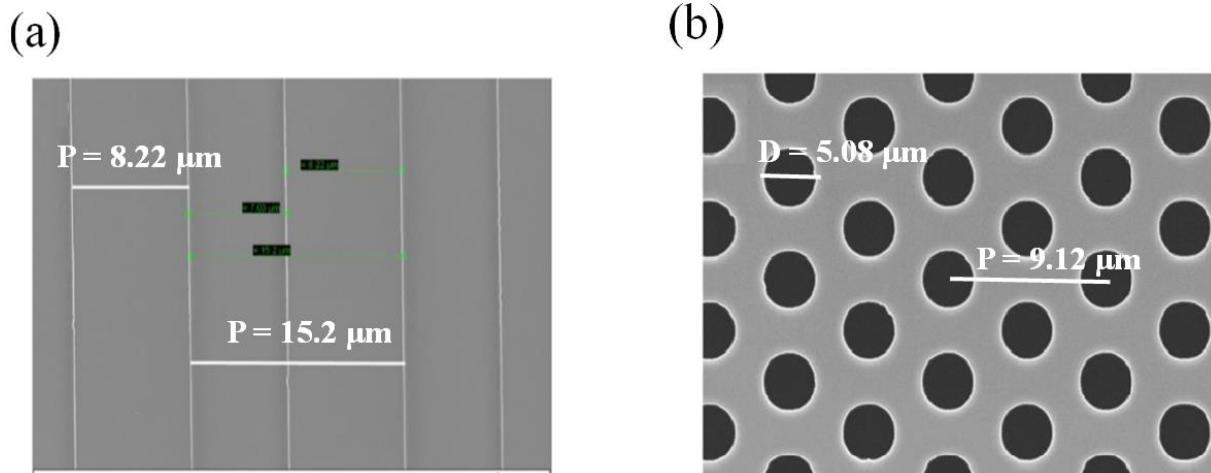


Figure 2.24: Scanning electron microscopy images of the: (a) ridges structure ($L = 8.22\text{ }\mu\text{m}$ and $P = 15.2\text{ }\mu\text{m}$) and (b) hole structure ($D = 5.08\text{ }\mu\text{m}$ and $P = 9.12\text{ }\mu\text{m}$) after PolySi etching [22].

The measured geometrical features of all the micro-fabricated ridges and holes structures are given in table 2.2 showing the fabrication process is well calibrated and kept the dimensions initially drawn on the chromium mask.

Number of sample	<i>Ridges structures</i>		<i>Holes structures</i>	
	Measured Width (μm) (target value)	Measured Periodicity (μm) (target value)	Measured Diameter (μm) (target value)	Measured Periodicity (μm) (target value)
4	1.83 (2.00)	5.00 ± 0.10 (5.00)	1.85 ± 0.20 (2.00)	4.99 ± 0.15 (5.00)
4	2.76 ± 0.10 (3.00)	5.00 (5.00)	2.91 ± 0.15 (3.00)	5.01 ± 0.17 (5.00)
2	5.52 (5.50)	10.20 (10.00)		
2	8.21 (8.25)	15.2 (15.00)		
4			5.08 (5.00)	9.12 (9.00)
4			7.01 ± 0.10 (7.00)	12.70 ± 0.10 (12.60)

Table 2.2: Geometrical features of the micro-fabricated ridges and holes structures measured by scanning electron microscopy and targeted values as reported on the quartz/chromium mask used for the photolithography [22]

II.6 Fourier Transform-Infrared analysis method

Ridge and hole gratings have been characterized with the help of Fourier Transform Infrared Spectroscopy (FT-IR). This method allows us to obtain a measurement of the optical properties, through the measurement of the reflection and the transmission coefficient of a sample in the wavelength range [5 - 15 μm]. The reflected and transmitted radiation by the sample is measured at HEI Lille's GEMTEX laboratory using a FT-IR spectrometer attached to an integrating sphere. The FT-IR spectrometer IR Prestige 21 (from Shimadzu) integrating a sphere system (from PIKE Technologies) is used. The sphere diameter is coated by a high reflectance diffuse gold coating. The entrance port, with a diameter of 2.3 cm, is situated on the side of the sphere. A detector records reflected and transmitted radiation by the sample in the spectral range from 2 μm to 20 μm . The proportion measurement of specular and diffuse components of reflectance and transmittance of analyzed samples can be performed as well. The schematic view of integrating

sphere design is shown in figure 2.25. In order to ensure that the incident beam impacts the structured surface, the surface area has to be of 4.15 cm² minimum, which corresponds to the top or the opening window of the entrance port side of the integrating sphere.

In the reflectance measurement, the samples are placed directly onto the sample port diameter = 2.3 cm) located on the top of the sphere. The radiation from an internal source of the spectrometer enters into the integrating sphere through the entrance port and is reflected by the rotary mirror to the sample port under the angle of 12°. The radiation reflected by the sample is repeatedly reflected inside the integrating sphere until it leaks through the detector port onto the detector.

In the transmittance mode (used in the next chapters), the radiation from the internal source of the spectrometer passes through the sample placed in front of the entrance port. Subsequently, the radiation enters the integrating sphere system, where it is repeatedly reflected until it leaks through the detector port onto the detector.

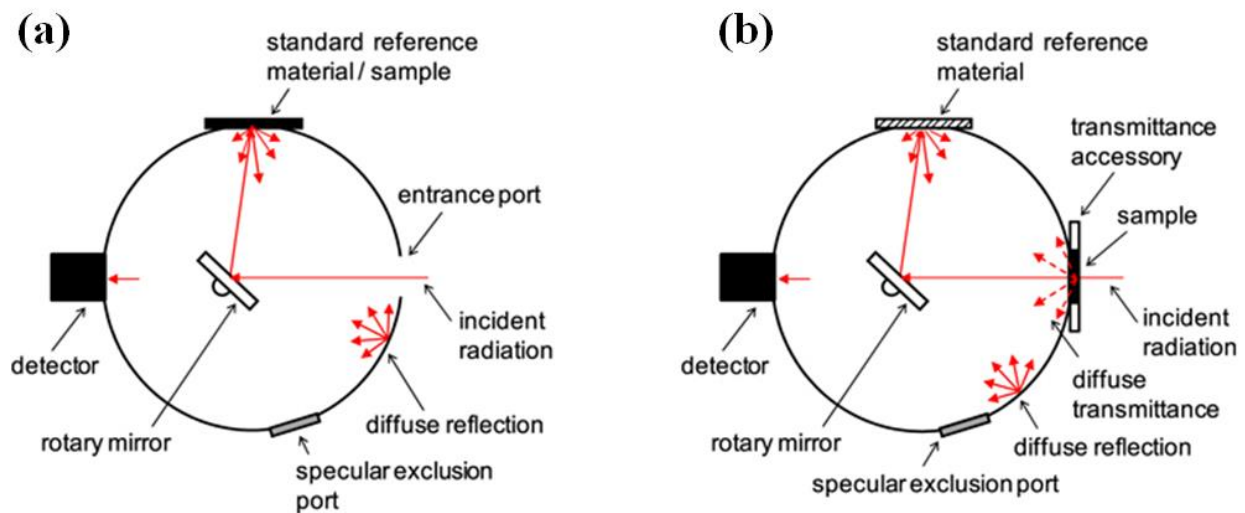


Figure 2.25: Schematic view of integrating sphere system for a normal hemispherical (a) reflectance and (b) transmittance measurement mode [23].

The main technical characteristics are listed in table 2.3.

FT-IR Spectrophotometer – IR Prestige-21	
Interferometer type: Michelson interferometer	Optical system: single beam optics
Beam splitter: KBr/Germanium	Light source: Ceramic (MIR & FIR)
Detector: DLATGS	Wavelength range: 1.2-28.5 μm
Resolution: 0.5; 1; 2; 4; 8 & 16 cm^{-1}	Signal/Noise ratio: $\geq 40\ 000:1$
Mirror speed: 2.8;5 or 9 mm.s^{-1}	Gain: automatic or manual ($\times 1$ - $\times 128$)
Integral sphere Pike	
Size / Area: 3 inch/Gold	Diameter of the sample holder: 2.35cm
Detector: DTGS or MCT	Wavelength range: 2-15.38 μm

Table 2.3: Technical characteristics of the IR Prestige 21 and the Pike sphere

Measurements are controlled via the IR Solution software provided by the manufacturer. The spectrum obtained corresponds to the reflection or transmission intensities of the sample normalized by the reference in the chosen spectral range. The collected data can be processed either via the IR Solution software directly or exported in text format to be used in an Excel spreadsheet. This last option was chosen for the operating results.

The spectral acquisition parameters were optimized to limit noise and get the most accurate and readable spectra possible. The optimal acquisition parameters to get well-defined peaks and reproducible spectra are summarized in table 2.4.

FT-IR acquisition parameters	
Measuring mode : % Reflectance,transmittance	Number of repetitions: 80
Spectral range: 2-28.57 μm	Resolution: 8 cm^{-1}
Apodization: App-Genzel	Detector: Standard or option 2
Infrared range: MIR (2.5-25 μm)	Light source: Infrared (Laser)
Gain: 2	Opening: Automatic

Table 2.4: Optimal acquisition parameters used for the FT-IR characterization of the PC membranes

II.7 Comparison between experimental and simulated spectra

The results have been compared with the FEM calculations. Figure 2.26 reports the spectra obtained experimentally (solid lines) and numerically (dashed lines) for the ridges and holes structuration of the PolySi membrane. The calculations have been made with an incidence of 12° in agreement with the experimental conditions. For the ridge structure (Figure 2.26(a)), the period is equal to $15.2\ \mu\text{m}$ and the width of the ridges is equal to $8.22\ \mu\text{m}$. For the hole gratings (Figure 2.26 (b)), the period is equal to $9.12\ \mu\text{m}$ and the hole diameter is equal to $5.08\ \mu\text{m}$. In both cases, we obtain a good general agreement between the experimental and the numerical curves. The positions between the peaks/dips are similar but there is a weak decrement in the amplitude.

The difference in amplitude between the experimental and numerical spectra might be explained following two hypotheses. In the first one, the index of refraction of SiO_2 , used in the simulation and obtained from the literature might not be the real index of the material used in the experiments. In the second one, the measurements were not normalized properly with respect to the reference. Nevertheless, the numerical model is able to predict the different dips and peaks observed in the experimental spectra.

For the ridge grating, the calculation of the electric field component E_x (TE polarization) is presented Figure 2.26 (c) at the wavelength $\lambda_A = 8.66\ \mu\text{m}$ (dip **A**), with the incident angle of 12° . One can see that the reflective dip is due to the resonant mode of the membrane whose couple to the incident wave. Due to a wider period/length of the ridge in the experimental part, we get a higher order of the ridge mode compared to the one defined in the theoretical section (see for instance 2.10).

For the hole grating, we calculated the distribution of the electric field component E_x (TE polarization) at the wavelength $\lambda_B = 10.67\ \mu\text{m}$ (dip **B**) (Figure 2.26 (d)). As already defined in the theoretical section, the energy of the excited mode is spread over the whole membrane, i.e. both inside and between the holes, and corresponds to a guided mode of the membrane.

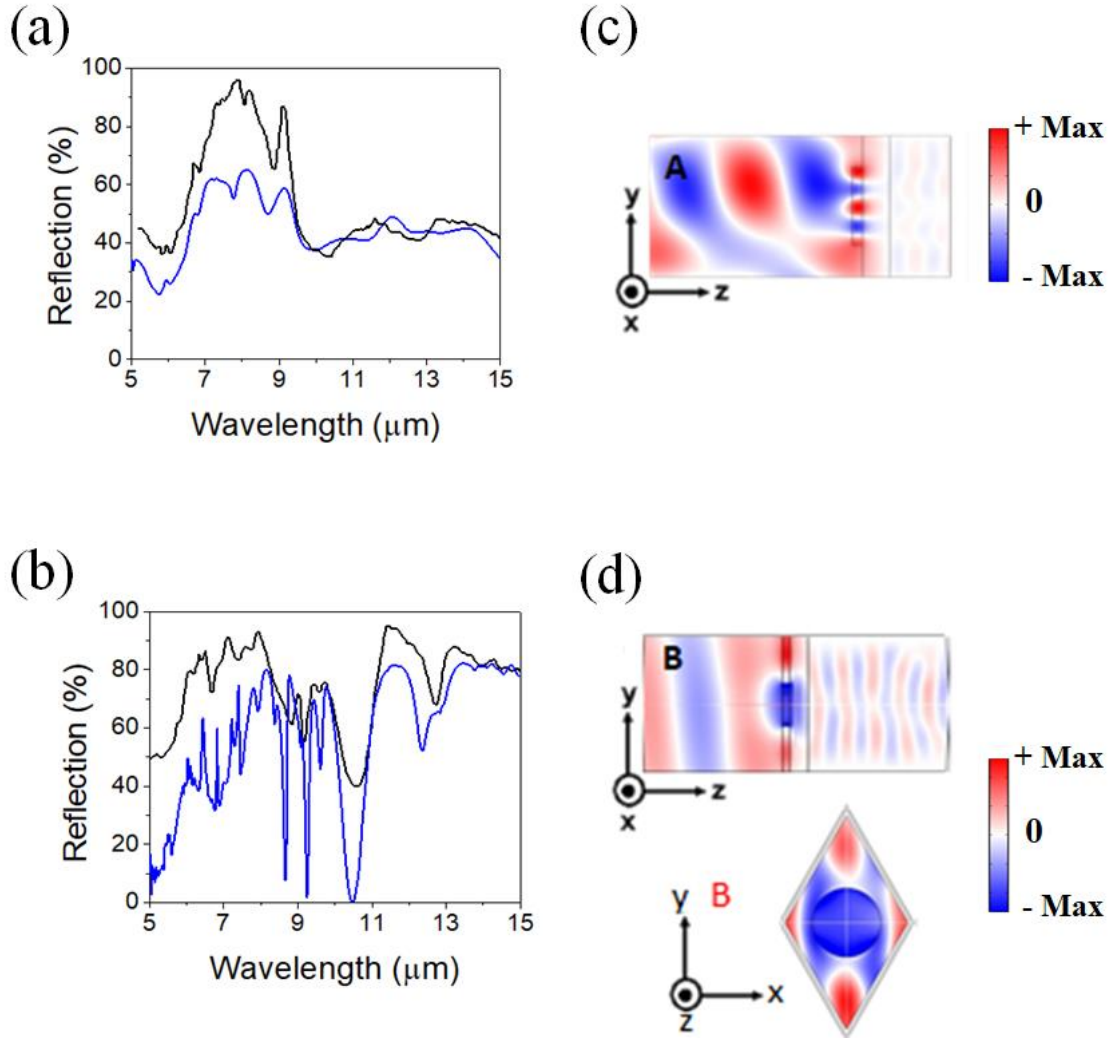


Figure 2.26: FT-IR (black solid line) and FEM (blue solid line) reflection spectra under an incidence of 12° for (a) ridges grating of width $L = 8.25 \mu\text{m}$ and period $P = 15 \mu\text{m}$ and (b) holes grating of diameter $D = 5 \mu\text{m}$ and period $P = 9 \mu\text{m}$. Representation of the electric component E_x of the EM field at the wavelength (c) $\lambda_A = 8.66 \mu\text{m}$ and (d) $\lambda_B = 10.67 \mu\text{m}$.

Conclusion

In this chapter, we have studied the evolution of the reflective properties of two photonic crystal membranes, with 1D or 2D periodicity, in the mid-infrared range (5-15 μm) versus their geometrical parameters. We were interested in the interaction of a normal incident wave with the photonic membrane and its response in reflection.

We first described the FEM method used to simulate the structures. The principle and the requirements of the method were stated and completed by adding in the code the Lorentz-Drude

model to take into account the SiO_2 absorption. We found that the interactions of an incident wave with the ridges or holes slabs modify the reflection spectrum. In both cases, we demonstrated the existence of at least one specific dip in the reflection spectrum due to the structuration of the membrane. We show that, in the ridge grating, the mode is confined inside the ridges while in the holes one, the mode is spread over the whole membrane.

In order to support our model, we have experimentally characterized the two types of periodic lattices based on polycrystalline silicon (PolySi) and SiO_2 , fabricated formerly by Maud Viallon: a lattice of PolySi ridges and a triangular lattice of air holes in a PolySi layer. For each type of network, several samples of different dimensions were characterized by FT-IR spectroscopy during this thesis. We compared the spectra obtained by numerical simulation with the one obtained by FT-IR measurement and obtained a good agreement between the experimental and the numerical curves. This demonstrates the photonic crystal membranes interest in the mid-infrared highlighted with specific dips of the reflection spectra.

Nevertheless, to target our final application, we now turn to membranes for the field of textile composed of polymer instead of silicon. It should be noted that most polymers are absorbent materials in the mid-infrared, so transmission modulation may result either in reflection or in absorption, causing very significant consequences on the thermal performance of the material. Considering this, we will study the reflection, transmission and absorption properties of the polymer membrane in the mid-infrared domain. Then, we will investigate the optical effects on the thermal balance analysis, applied between the human body and the surrounding environment, through the structured membrane. This work is the subject of the chapters III and IV of this manuscript. Since the structure of triangular arrays of silicon membrane shows robust results regarding polarization, we will now only study the effects of a network of holes in the rest of the thesis.

References

1. Leung KM, Liu YF. Photon band structures: The plane-wave method. *Phys Rev B*. 1990; 41:10188–90.
2. Andreani LC, Gerace D. Photonic-crystal slabs with a triangular lattice of triangular holes investigated using a guided-mode expansion method. *Phys Rev B*. 2006; 73:235114.
3. Delort T, Maystre D. Finite-element method for gratings. *J Opt Soc Am A*. 1993; 10:2592.
4. Ohkawa Y, Tsuji Y, Koshiba M. Analysis of anisotropic dielectric grating diffraction using the finite-element method. *J Opt Soc Am A*. 1996; 13:1006.
5. Bao G, Chen Z, Wu H. Adaptive finite-element method for diffraction gratings. *J Opt Soc Am A*. 2005; 22:1106.
6. Kane Yee. Numerical solution of initial boundary value problems involving maxwell's equations in isotropic media. *IEEE Trans Antennas Propag*. 1966 ;14:302–7.
7. Wang Z, Zhang J, Xie J, Li C, Li Y, Liang S, et al. Bioinspired Water-Vapor-Responsive Organic/Inorganic Hybrid One-Dimensional Photonic Crystals with Tunable Full-Color Stop Band. *Adv Funct Mater*. 2010; 20:3784–90.
8. Foley JM, Young SM, Phillips JD. Narrowband mid-infrared transmission filtering of a single layer dielectric grating. *Appl Phys Lett*. 2013; 103:071107.
9. Volakis JL, Chatterjee A, Kempel LC. Finite element method for electromagnetics: antennas, microwave circuits, and scattering applications. New York: IEEE Press; 1998.
10. Li X, Liu Z. Coupling of cavity modes and guiding modes in two-dimensional phononic crystals. *Solid State Commun*. 2005; 133:397–402.
11. Dobrzyński L, Akjouj A, Pennec Y, Al-Wahsh H, Lévêque G, Djafari-Rouhani B. Phononics: interface transmission tutorial book series. Elsevier. 2017.
12. Ashcroft NW, Mermin ND. *Physique des solides*. EDP sciences.2012.
13. Berenger JP. A perfectly matched layer for the absorption of electromagnetic waves. *Journal of computational physics*,1994; 114:185-200.

14. Nicolet A, Zolla F, Agha YO, Guenneau S. Leaky modes in twisted microstructured optical fibers. *Waves Random Complex Media*. 2007 ;17 :559–70.
15. Kittel C, McEuen P, Dion J, McEuen P. *Physique de l'état solide : cours et problèmes*. Dunod. 2007.
16. Taflove A, Hagness SC. *Computational Electrodynamics: The Finite-Difference Time-Domain Method*», 3e éd., Norwood, MA: Artech House, Inc., 2005.
17. Hulot JC, Venturi M. *Ondes*, Nathan, 2009.
18. Taillet R, Villain L, Febvre P. *Dictionnaire de Physique*, 2e éd., Bruxelles: De Boeck Université, 2009.
19. Slater JC, Frank NH. *Electromagnetism*, New York: Dover Publications, Inc, 1969.
20. Rakic AD. Algorithm for the determination of intrinsic optical constants of metal films: application to aluminium. *Applied Optics*.1995;34:4755-4767.
21. Kischkat J, Peters S, Gruska B, Semtsiv M, Chashnikova M, Klinkmüller M, et al. Mid-infrared optical properties of thin films of aluminum oxide, titanium dioxide, silicon dioxide, aluminum nitride, and silicon nitride. *Appl Opt*. 2012 ; 51:6789.
22. Viallon M. *Réalisation et caractérisation de membranes polymères microstructurées capables de moduler leurs propriétés de réflexion dans le domaine du moyen infrarouge : application aux textiles pour le confort thermique (Doctoral dissertation, Lille 1)*. 2017.
23. Honnerová P, Martan J, Veselý Z, Honner M. Method for emissivity measurement of semitransparent coatings at ambient temperature. *Sci Rep [Internet]*. 2017 [cited 2020 Apr 9];7. Available from: <http://www.nature.com/articles/s41598-017-01574-x>.

Chapter III:

Optical and thermal analysis of the Benzocyclobutene (BCB) polymer photonic membrane

Introduction

Based on the electromagnetic simulation tools developed and validated on silicon in the previous chapter, and in view of the intended application, we report in this chapter the optical and thermal properties of a periodically structured polymer membrane.

We investigate the effect of the geometrical parameters and their efficiency on the spectral coefficients in the mid-infrared. We will define and analyze the thermal balance between the human body and the indoor environment through the Benzocyclobutene (BCB) photonic membrane considering the radiation, convection and conduction mechanisms. We aim to demonstrate that a simple photonic membrane, under specific geometric and physical parameters, can act as a thermoregulating fabric depending on the indoor temperature of the room.

The study is carried out on analytical calculations and numerical simulations with the help of the finite element method (FEM) using COMSOL software. It is also necessary to note that, at the beginning of my PhD, technological developments were underway as part of Maud Viallon's thesis, with fabrication of BCB membranes and optically characterization in the mid-infrared.

III.1 Choice of the polymer

The silicon structures studied in the previous chapter allow to demonstrate the use of photonic crystal properties for the management of the optical waves in the mid-infrared. Although the technological processes for silicon are well known, such a material is not compatible with textile application.

So, we focus in this chapter on a polymer that meets the requirement of both cleanroom fabrication processes and textile application. For physical reasons, the polymer needs first to have high refractive index in infrared, thus offering significant contrast with air. Second, to be compatible with technological stresses, it must be able to be dissolved in usual solvent used in IEMN clean room in order to be spin-coated on the fabrication support. Furthermore, this polymer has to fulfill a well-known manufacturing process to be easily structured and to obtain an experimental demonstration.

We propose to study the Benzocyclobutene (BCB) as the constitutive material of the membrane, which is a polymer currently used in micro-technical manufacturing processes. It was chosen because of its low sensitivity to moisture, its good thermal stability, its ease of implementation in

the form of film, its very small variation of thickness during the polymerization process and the possibility of structuring it by photolithography and dry etching.

III.2 Model and method

In chapter II, we studied the geometrical effects of two different structures on the reflection properties: a polysilicon / SiO₂ grating ridges and a polysilicon / air holes triangular grating. Now, due to the absorption properties of the polymers, we focused in this chapter on the three optical coefficients (reflection (R), transmission (T) and absorption (A)) of the BCB polymer membrane in the mid-infrared domain. Since the structure of triangular arrays of silicon membrane shows robust results regarding polarization, we will take the same structure and condition as the polysilicon / air holes triangular grating structure, considering the non-polarized incident source (radiation of the human body) while applying periodic boundary conditions (PBC) and perfect matching layers (PMLs).

The source and the detector are placed in air, respectively before and after the membrane. We record the reflection (R) and transmission (T) coefficients and then deduce the absorption coefficient following the equation $A = 1 - R - T$ (Figure 3.1 (a)). The structure of the elementary 3D unit cell used for the FE calculation is shown in figure 3.1 (b) and (c).

All calculations have been performed on a periodic triangular array of holes drilled in the membrane. The geometrical parameters involved in the study are the lattice parameter P , the hole diameter D , and the thickness of the membrane, h .

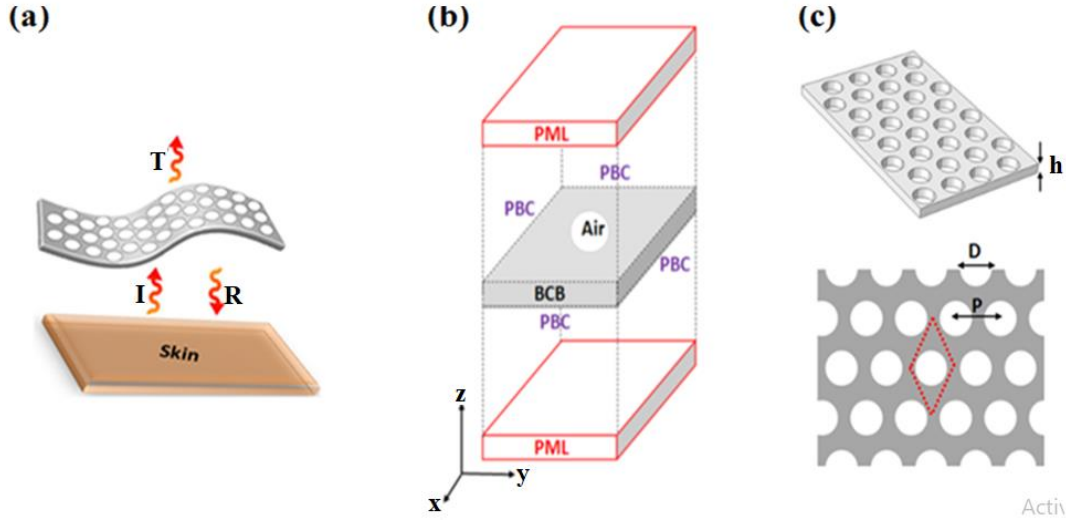


Figure 3.1: (a) Schematic representation of the polymer membrane textile under human body radiation from the skin where (I), (R) and (T) represent respectively the incident, reflection and transmission coefficients of the electromagnetic waves. (b) Elementary unit cell used for the FE calculations with perfect matching layers (PML) and periodic boundary conditions (PBC). (c) 3D and in-plane view of the polymer membrane of thickness h , drilled with triangular array of period P with air holes of diameter D .

In the calculations, the frequency-dependent complex permittivity of BCB, with real (n_{BCB}) and imaginary (k_{BCB}) components, obtained from ellipsometry measurements (data obtained in collaboration with the Semilab company ©), has been described by the Drude-Lorentz oscillator model with the help of the software PeakFitTM.

We used the Drude-Lorentz model, described in Chapter II (eq. II.20), to fit the real and complex variations of the refractive index of the BCB in the mid-infrared from the ellipsometry data.

The coefficients of the oscillators are reported in Table 3.1, which allowed us to plot the curve of complex refractive index as a function of the wavelength, represented figure 3.2.

$\epsilon_{\infty} = 2.3447$			
i^{th} oscillator	$n_{pi} \text{ (cm}^{-1}\text{)}$	$n_{oi} \text{ (cm}^{-1}\text{)}$	$\Gamma_i \text{ (cm}^{-1}\text{)}$
1	63	794	25
2	101	834	65
3	46	1028	37
4	120	1060	58
5	65	1256	20

Table 3.1: Physical parameters of the BCB photonic membrane

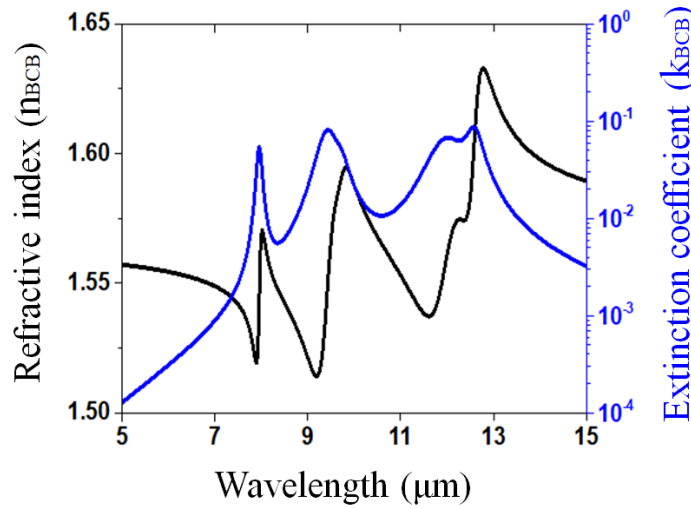


Figure 3.2: Representation of the refractive index components with respect to the real (n , black) and imaginary part (k , blue) in the mid-infrared range [5-15] μm .

The real average part of the refractive index is around $n_{\text{BCB}} \sim 1.56$, which makes it a good candidate to ensure a sufficient refractive-index contrast with air. It is to be noted that this polymer has a low extinction coefficient $k_{\text{BCB}} \sim 0.01$.

The investigation of the properties of the BCB-based photonic membrane in the mid-infrared has been done numerically with the help of the Finite Element (FE) method.

III.3 Spectral analysis in the mid-infrared

For a better understanding of the impact of the polymer membrane structuration, we first study, for a non-polarized incident light, the influence of the unstructured BCB polymer membrane thickness on the reflection, transmission and absorption spectra. Then, we study the influence of the geometrical parameter of the hole grating.

III.3.1 Unstructured Benzocyclobutene membrane

We first studied the influence of the thickness h of the unstructured polymer membrane (BCB) without introducing the absorption in the calculation (extinction coefficient $k_{\text{BCB}} = 0$). The effect of the thickness of the polymer layer on the reflectivity of the membrane is evaluated by varying h from 1 to 10 μm . Figure 3.3 shows the reflection (black line) and transmission (blue line) spectra,

taking the thickness of the membrane $h = 1 \mu\text{m}$, $4 \mu\text{m}$, $7 \mu\text{m}$ and $10 \mu\text{m}$. In these spectra (see for instance figure 3.4 (d)), a succession of oscillations appears. These oscillations are known as Fabry-Perot type. As the thickness of the membrane increases, oscillations tighten and their number increases consequently. We also find defects in the regularity of oscillations. As we have considered the imaginary part of the refractive index equal to zero in this part (no absorption), these defects therefore come from the variation of the real part of the index as a function of the wavelength (compared with figure 3.2, black curve).

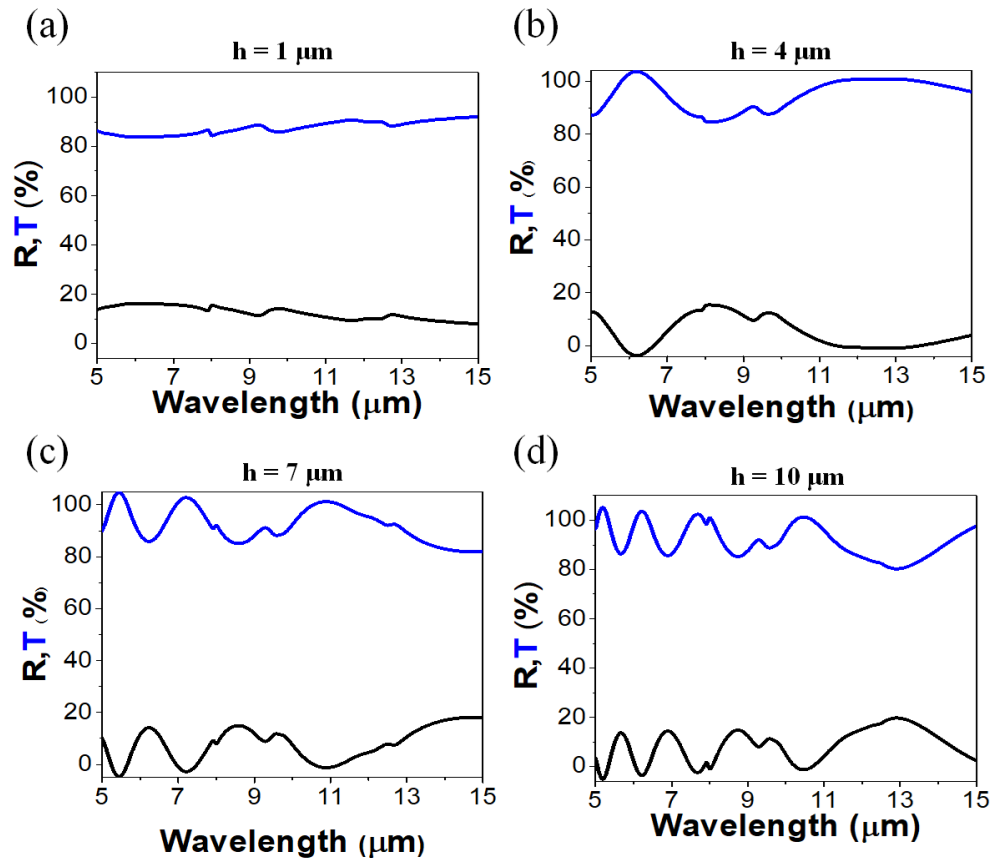


Figure 3.3: Reflection and transmission spectra of unstructured BCB polymer membrane without absorption for (a) $h = 1 \mu\text{m}$, (b) $h = 4 \mu\text{m}$, (c) $h = 7 \mu\text{m}$ and (d) $h = 10 \mu\text{m}$.

Then, we added the imaginary part of the refractive index in the calculation. Figure 3.4 presents the reflection, transmission and absorption coefficient spectra of a non-structured BCB membrane, having a thickness of $h = 4.0 \mu\text{m}$. This will be the reference spectrum for the structuration study of the next part. At wavelengths close to $8.0 \mu\text{m}$, $9.5 \mu\text{m}$ and $12.0 \mu\text{m}$, several dips appear in the transmission spectrum (blue line), corresponding to peaks in the absorption spectrum (vertical

dotted lines). These peaks are directly linked to the extinction coefficient of the refractive index of the BCB (Figure 3.2) and can thus be affected to the absorption of the polymer. One can note that all peaks impact the human body emittance, calculated from the Planck law at $T = 34\text{ }^{\circ}\text{C}$, represented within the grey hatched area. A low reflection (black curve), less than 20%, is recorded with a maximum at $8.5\text{ }\mu\text{m}$ and a zero at $6.0\text{ }\mu\text{m}$. This modulation corresponds to Fabry-Perot oscillations through the BCB membrane as observed in the membrane of same thickness in figure 3.3 (b). It means that the reflection is almost not affected by the structuration.

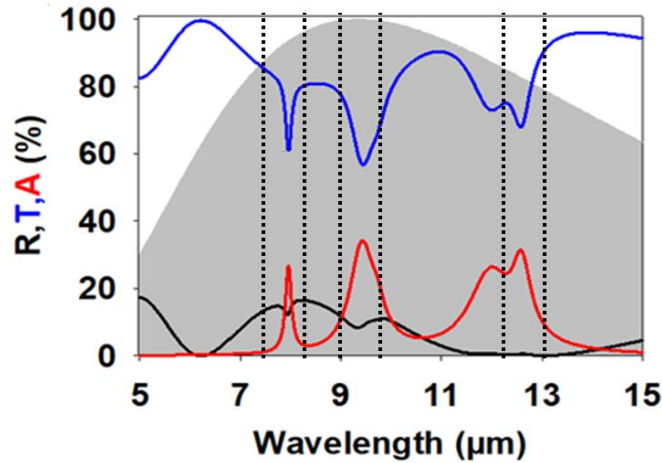


Figure 3.4: Reflection (black), transmission (blue) and absorption (red) spectra for the non-structured membrane of BCB with thickness $h = 4\text{ }\mu\text{m}$.

III.3.2 Structured benzocyclobutene membrane

We now proceed to the structuration of the membrane, following a triangular array of air holes, with the geometrical parameters $P = 7.0\text{ }\mu\text{m}$, $D = 5.5\text{ }\mu\text{m}$, and $h = 4.0\text{ }\mu\text{m}$. Figure 3.5 (a) shows the corresponding calculation of the reflection (black), transmission (blue) and absorption (red) spectra with the TM polarization (E_y, H_x). Figure 3.5 (b) shows the calculation obtained under the same conditions but with a TE polarization (E_x, H_y). As in the previous chapter dealing with the silicon membrane, we showed here that the polarization has no influence on the result of the transmission and reflection calculations. Therefore, due to the triangular structuration of the photonic crystal array, the results can be extended to the TM polarization (E_y, H_x) of the normal incident light in the following sections.

First, we find the peaks of absorption of the BCB, described previously and closed to $8.0\ \mu\text{m}$, $9.5\ \mu\text{m}$ and $12.0\ \mu\text{m}$. Then, one can see the occurrence of new features appearing at low wavelengths, between $6.0\ \mu\text{m}$ and $7.5\ \mu\text{m}$. For clarity, the reflection, transmission and absorption spectra are magnified in figure 3.5 (c). One can see that the reflection can be described as two main peaks (**a** and **b**), at $6.08\ \mu\text{m}$ and $6.88\ \mu\text{m}$, and a narrow one (**c**) at $6.41\ \mu\text{m}$ in between. This latter decreases the reflection for the main benefit of the absorption. On the other hand, the two larger peaks (**a** and **b**), decrease the transmission for the benefit of the reflection. They present the most important contribution in the variation of the transmitted and reflective spectra.

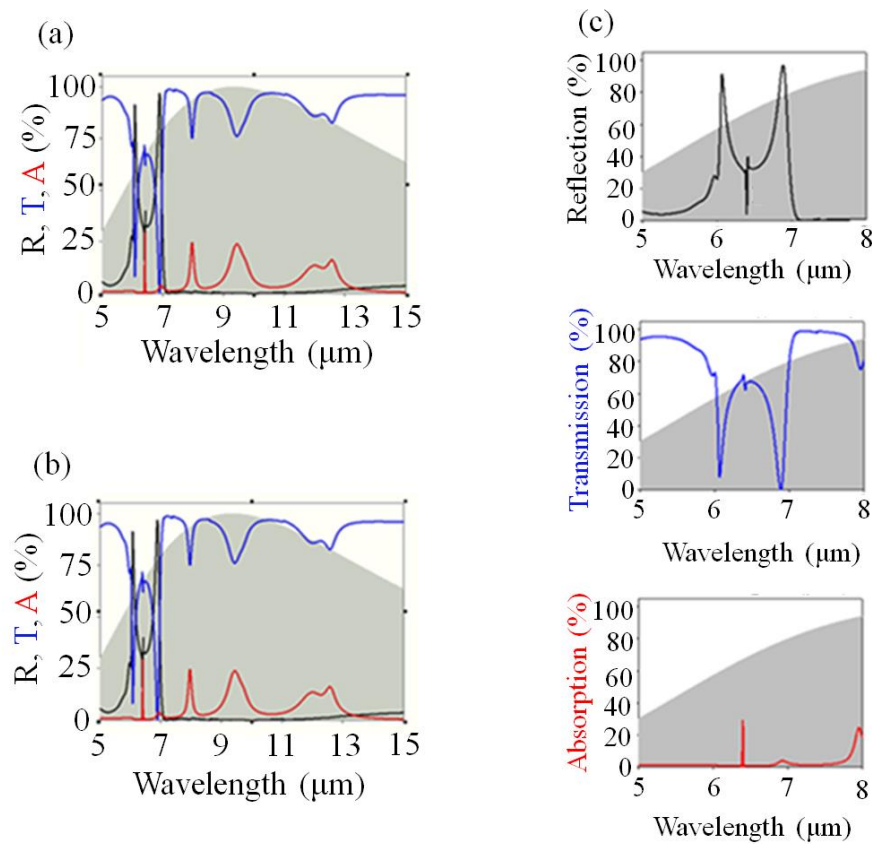
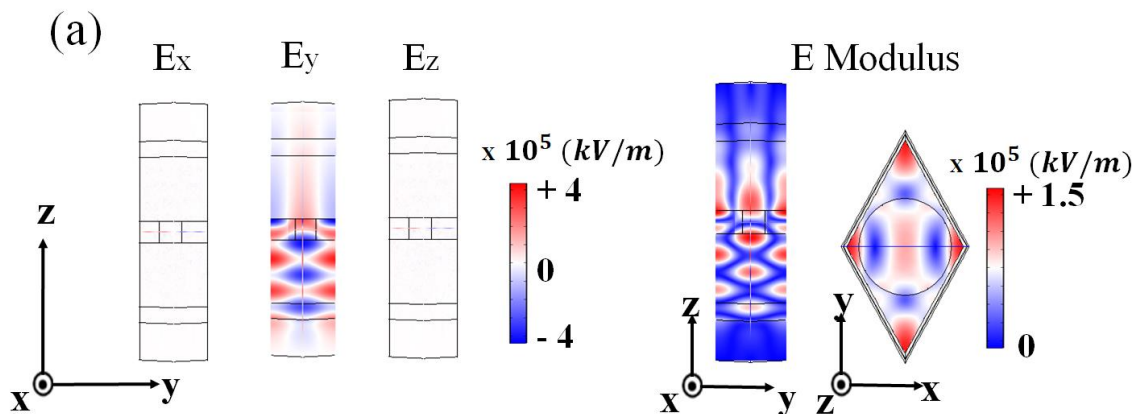


Figure 3.5: (a) Reflection (black), transmission (blue) and absorption for a structured BCB membrane with the geometrical parameters: $P = 7.0\ \mu\text{m}$, $D = 5.5\ \mu\text{m}$, $h = 4.0\ \mu\text{m}$ for (a) TM polarization (E_y , H_x) and (b) TE polarization (E_x , H_y). (c) Detail of the reflection, transmission and absorption curves in the wavelength range $[5, 8]\ \mu\text{m}$. The grey hatched area represents the black body emissivity of the human body, calculated from the Planck law at $34\ ^\circ\text{C}$.

To understand their origin, we performed the calculations of the EM field distribution for TM polarization at the wavelengths of the three peaks (**a**, **b** and **c**). We present figure 3.6 the maps of the electric field for the three components E_x , E_y , E_z and their modulus E .

Concerning the peaks (**a** and **b**), one can see that E_y is the main component. In both axes, the input signal, launched from the bottom, is weakly transmitted through the membrane. This behavior comes from the excitation of a stationary mode which belongs to the BCB membrane. The two high reflective peaks (**a** and **b**) correspond to modes spreading over the BCB membrane. They are attributed to guided modes of the plate: one is antisymmetric ($\lambda_a = 6.08 \mu\text{m}$) and the other ($\lambda_b = 6.88 \mu\text{m}$) is symmetric with respect to the mid-plane of the membrane (Figure 3.6 (a) and (b)).

Concerning the peak **c**, one can see that the component E_z represents the main contribution to the modulus E of the electric field. This peak corresponds to an antisymmetric mode of component E_z , strongly confined inside the air hole. This supposes that the structured membrane, by scattering effect, has resulted in a redistribution of the incident electric field (initially with an E_y component) thus allowing the excitation of a mode confined in the air hole. One can note that this localized mode, in interaction with the incident wave as a continuum, gives rise to a peak of asymmetric shape in the reflection spectrum. This type of wave interaction phenomenon, known as Fano resonance has been already detailed section I.1.2.5 for the theoretical aspects and section II.3.2.1 for the silicone membrane.



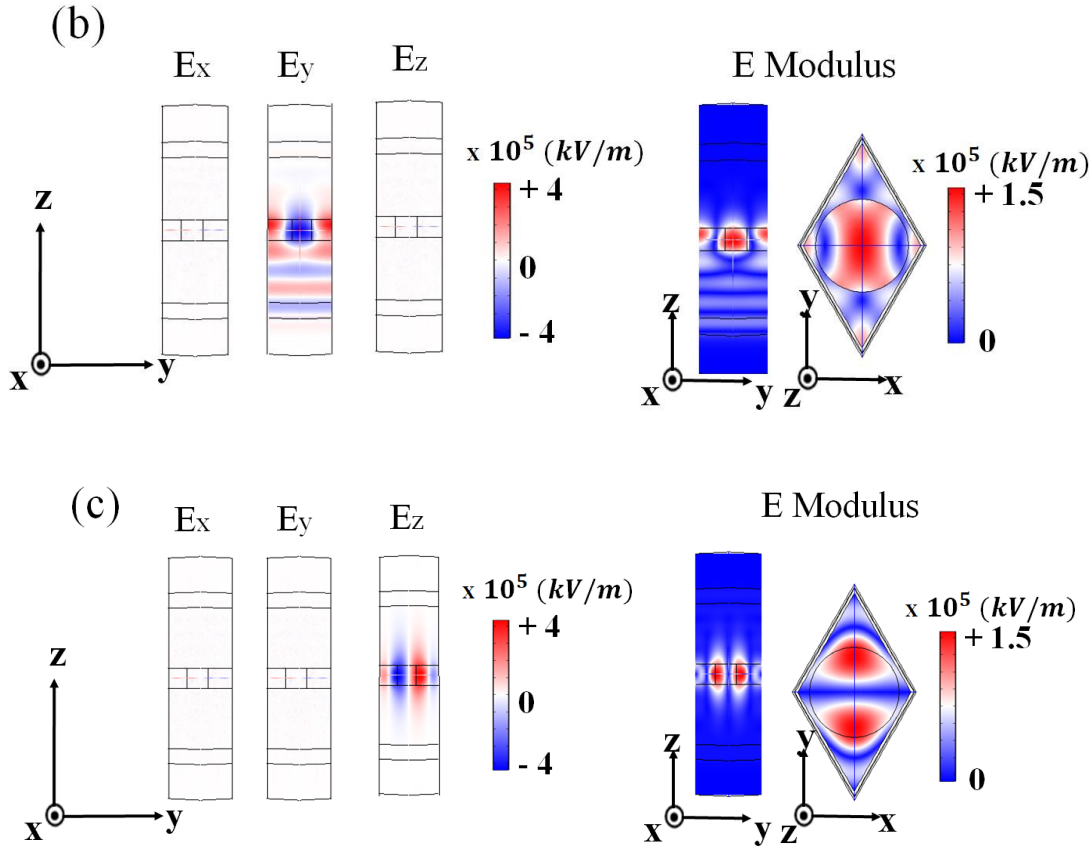


Figure 3.6: (a, b, c) Snapshots of the components E_x , E_y , E_z and E modulus of the electric field for TM polarization at the wavelength $\lambda_a = 6.08 \mu\text{m}$, $\lambda_b = 6.88 \mu\text{m}$ and $\lambda_c = 6.41 \mu\text{m}$ respectively.

As a conclusion, the structuration of the photonic membrane has induced scattering effect inside the membrane of the incoming wave. With the set of geometrical parameters chosen here the scattering effects have impacted both the transmission and the reflection in the low part of the MIR range, i.e. closed to $6 \mu\text{m}$.

III.3.3 Modulation of the spectral coefficients in the mid-infrared

III.3.3.1 Influence of the scaling factor

The objective is now to modulate the spectral coefficients over the MIR range. To reach this objective, we proceeded to a systematic calculation of the R , T and A coefficients as a function of the geometrical parameters of the photonic membrane.

To see the impact of the geometric parameters on the emissivity of the human body, we multiplied all dimensions of the membrane by a scaling factor α_i in the same way than in the previous chapter

(section II.3.2.2). The structure of the previous section ($P = 7.0 \mu\text{m}$, $D = 5.5 \mu\text{m}$, $h = 4.0 \mu\text{m}$) will be set as the reference structure for the following study (Figure 3.5 (a)). Table 3.2 reports the set of parameters associated to the scaling factors α_i .

Scaling factor α_i	Period P (μm)	Diameter D (μm)	Thickness h (μm)
$\alpha_{-1} = 0.72$	5.0	3.9	2.9
$\alpha_0 = 0.86$	6.0	4.7	3.4
$\alpha_1 = 1.0$	7.0	5.5	4.0
$\alpha_2 = 1.14$	8.0	6.3	4.6
$\alpha_3 = 1.28$	9.0	7.1	5.1
$\alpha_4 = 1.42$	10.0	7.9	5.7
$\alpha_5 = 1.56$	11.0	8.6	6.3
$\alpha_6 = 1.7$	12.0	9.4	6.9
$\alpha_7 = 1.84$	13.0	10.2	7.4
$\alpha_8 = 1.98$	14.0	11.0	8.0
$\alpha_9 = 2.12$	15.0	11.8	8.6

Table 3.2: Set of parameters of the BCB photonic membrane following a scaling law indexed by α_i .

The calculated reflection, transmission and absorption coefficients are shown in figure 3.7 for four scaling factors α_1 , α_4 , α_7 and α_9 . In the reflection spectrum, we found that, increasing the size of the geometrical parameters the three reflective features (**a**, **b** and **c**) shift toward higher wavelengths (Figure 3.7 (a)).

In the transmission spectrum (Figure 3.7 (b)), one can follow the signature of the corresponding dips modes. The double transmission dips fully cross the human body emissivity toward the high wavelength when α_i increases, thus altering deeply the transmission of the incident wave. From the point of view of the absorption, one can observe a variation of the coefficient which depends of α_i . It means that the scattering effects, characterized in the previous section, impact now all optical spectra in the mid-infrared.

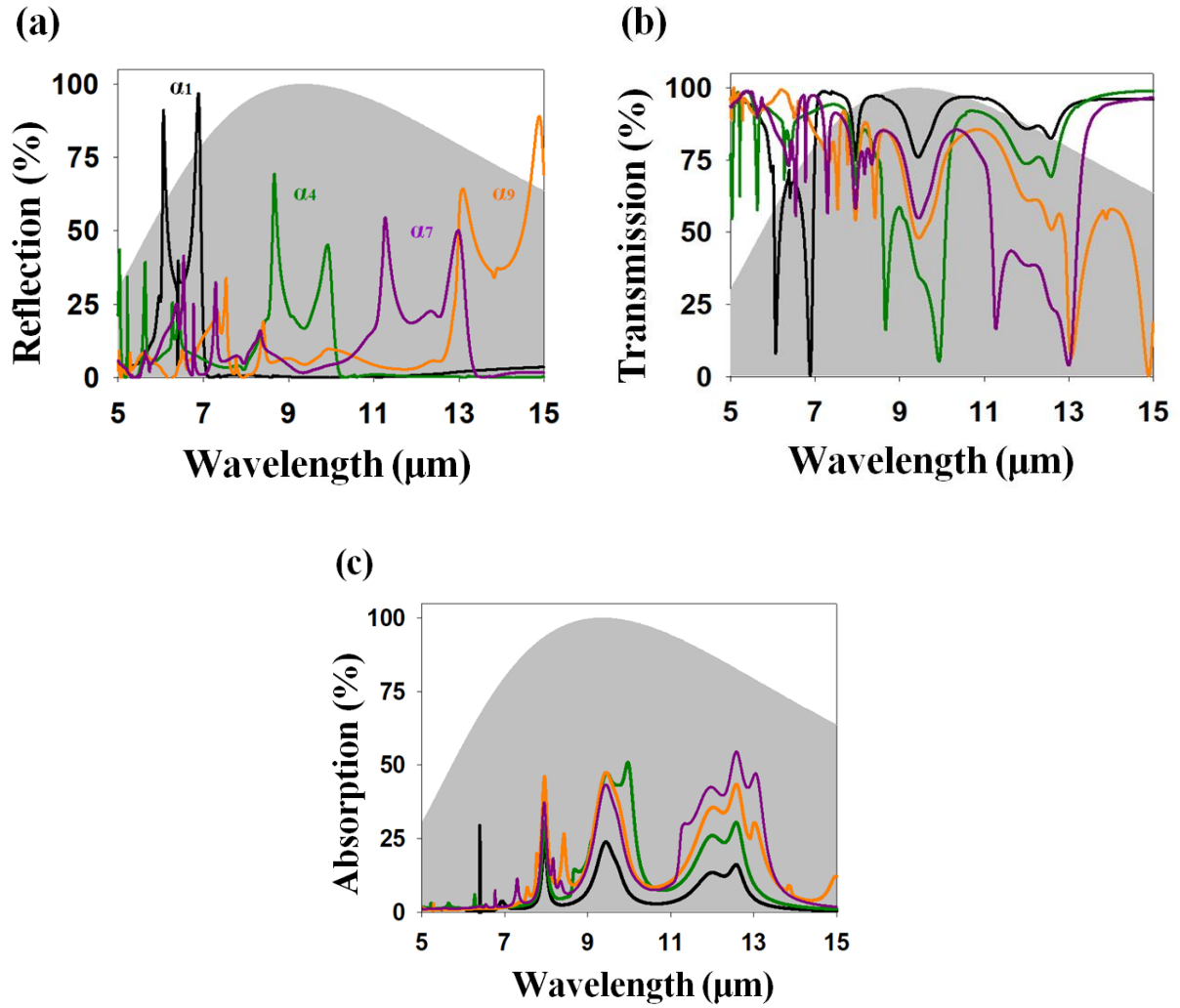


Figure 3.7: (a) Evolution of the reflection (R), (b) transmission (T) and (c) absorption (A) coefficients as a function of the wavelength in the mid-infrared for four photonic membranes, designed following the scaling factors α_1 , α_4 , α_7 and α_9 .

To get a quantitative estimation of these behaviors, we defined an efficiency coefficient η , corresponding to a numerical integration of the R , T and A coefficients over a defined wavelength range. This coefficient is calculated and normalized with respect to the emissivity of the human body. Such a coefficient is currently used for the estimation of photovoltaic solar cells efficiency. In the case of photovoltaic cells, the efficiency factor is used to evaluate the ability of cells to absorb wavelengths corresponding to the solar emission spectrum. The efficiency factor η for photovoltaic cells is defined by the following relation (eq. III. 1) [1]:

$$\eta = \frac{\int_0^{\lambda_g} I(\lambda) \cdot A(\lambda) \cdot \frac{\lambda_g}{\lambda} \cdot d\lambda}{\int_0^{\infty} I(\lambda) \cdot d\lambda} \quad \text{III.1}$$

where $I(\lambda)$ is the solar irradiance spectrum, $A(\lambda)$ is the silicon absorption, and λ_g is the wavelength corresponding to the energy band gap of the silicon.

For the purpose of the human body in the mid-infrared, we replace $A(\lambda)$ by χ_λ which then represents the R , T or A coefficients at the wavelength λ . $I(\lambda)$ is replaced by E_λ which characterizes the human body emissivity.

The integration will be done over the wavelength interval $[\lambda_{min} = 7.5 \mu\text{m}, \lambda_{max} = 11.5 \mu\text{m}]$ that cover 70% of the human body emissivity with a maximum at $\lambda = 9 \mu\text{m}$.

The efficiency factor η is thus explained through the following formula (eq. III.2):

$$\eta = \frac{\int_{\lambda_{min}}^{\lambda_{max}} E_\lambda \cdot \chi_\lambda \cdot d\lambda}{\int_{\lambda_{min}}^{\lambda_{max}} E_\lambda \cdot d\lambda} \quad \text{III.2}$$

The figure 3.8 (a) reports the evolution of η for the reflection (black solid line), transmission (blue solid line) and absorption (red solid line) as a function of the scaling factors α_i .

One can see that, increasing α_0 to α_3 , the transmission drops by 28%, *i.e.* from 94% to 66% for the benefit of the reflection and the absorption which increase respectively by 16% (from 0.5% to 16%) and 12% (from 5.5% to 17.5%). The efficient coefficient is then almost constant until the geometrical parameters reach α_6 where the transmission increases again. As demonstrated previously, such modulation of the efficiency coefficients is directly associated with the crossing of the reflective peaks (**a**, **b** and **c**) over the wavelength interval. The modulation has been compared with the one of a non-structured membrane with an equivalent thickness (dashed lines). We clearly see that the structural configuration of the membrane can modulate the transmission coefficient, from transparent to opaque in the mid-infrared, by increasing the geometrical factor α_i . Then, one can choose to have either a more transparent ($\alpha_i \leq \alpha_1$) or more opaque ($\alpha_i > \alpha_2$) photonic membrane, with higher transmission coefficient by respectively $\approx 14\%$ and $\approx 13\%$ than an unstructured membrane.

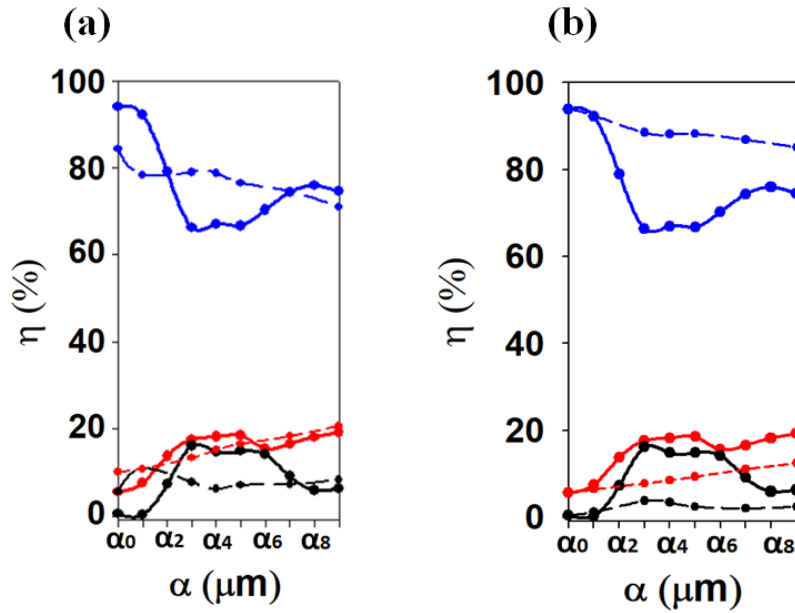


Figure 3.8: Evolution of the efficiency coefficient η , associated to the reflection (black), transmission (blue), absorption (red) responses of the structured (solid lines) BCB membrane. The comparison is done with respect to (a) a non-structured (dashed lines) and (b) an effective membrane, considering the incremental porosity.

To decouple the effect of the structuration from the index variation coming from the introduction of air holes, we calculated the effective index n_{eff} using the following expression (eq. III.3):

$$n_{eff} = (1 - f) \cdot \tilde{n}_{BCB} + f \cdot n_{air} \quad \text{III.3}$$

Where n_{eff} is the effective refractive index, \tilde{n}_{BCB} is the complex refractive index of BCB, n_{air} is the refractive index of air and f is the filling factor.

$$f = \frac{\frac{\pi D^2}{4}}{\frac{\sqrt{3}P^2}{2}} \quad \text{III.4}$$

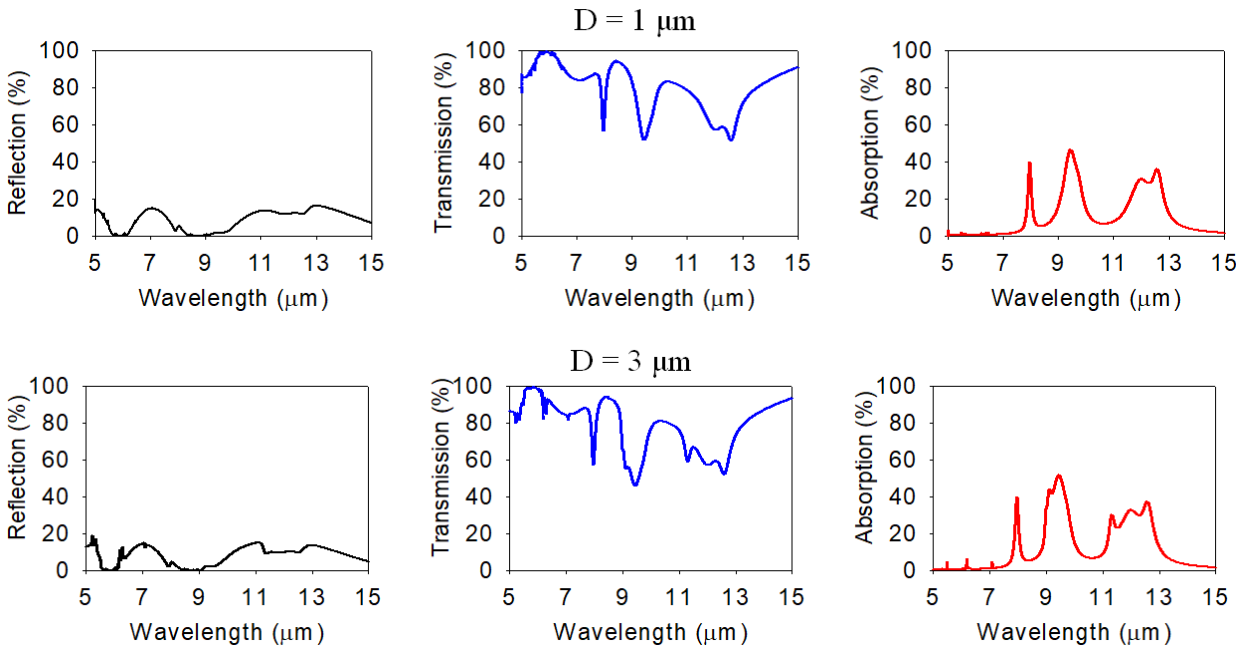
The figure 3.8 (b) compares the R , T and A efficiency coefficients for the structured photonic crystal (solid line) with the effective membrane (n_{eff}) of equivalent thickness (dashed line).

With this reference, we show that the modulations of the R , T and A spectra come mainly from the structural configuration and not from the effective index variation especially for $\alpha_i > \alpha_2$.

III.3.3.2 Variation of the diameter

In the previous paragraph, we applied an overall variation of the different parameters involved in the photonic structure through the scaling coefficient α_i . We now try to dissociate the different effects and to discuss them through an independent variation of the different geometrical parameters of the membrane (D , P , h).

Thus, we have calculated the reflection, transmission and absorption behavior of the perforated membrane under normal incidence, considering a variation of the hole diameter (D), keeping the period $P = 10 \mu\text{m}$ and the thickness $h = 5.7 \mu\text{m}$. Figure 3.9 gives the evolution of R , T , and A spectra versus D , in the range $[5, 15] \mu\text{m}$. When the hole diameters are small, we reproduced the behavior of a non-structured membrane which is 80 % transparent to the human body radiation. As the hole diameter increases, the features described in the previous section, as peaks **a**, **b**, and **c** (black arrows), progressively affect the different spectra. As reported previously, these peaks correspond to guided and localized resonant modes of the membrane which couple to the incident wave (see for instance figure 3.6).



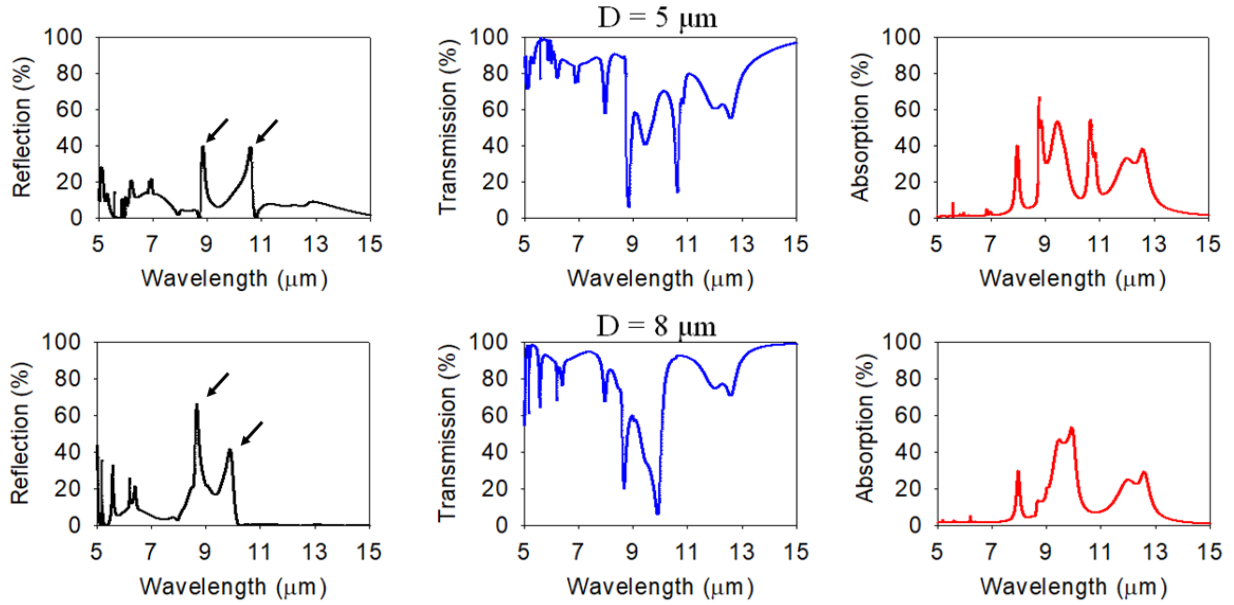


Figure 3.9: Evolution of the reflection, transmission and absorption spectra for the structured membrane versus the diameter (D) of the holes in the range $[5, 15]$ μm , keeping constant the period $P = 10$ μm and the thickness $h = 5.7$ μm for $D = 1$ μm , $D = 3$ μm , $D = 5$ μm , and $D = 8$ μm .

The figure 3.10 shows the evolution of the efficiency coefficient η for the reflection (black solid line), the transmission (blue solid line) and absorption (red solid line) as a function of the hole diameters in which the period $P = 10$ μm and thickness $h = 5.7$ μm are kept constant while we investigate the variation of the diameter. All spectra are drastically affected for diameters higher than 5 μm in the wavelength range $[7.5, 11.5]$ μm with an increasing opacity of the membrane for the benefit of both the reflection and the absorption. This perturbation is strongly dependent of the diameter of the holes, confirming the strong contribution coming from the membrane structuration. For a diameter $D = 8$ μm , we recover a decrease of the transmission down to 66%. In between, the spectral coefficients can still be tuned, for instance we obtain an increased opacity of 15% for $D = 7$ μm .

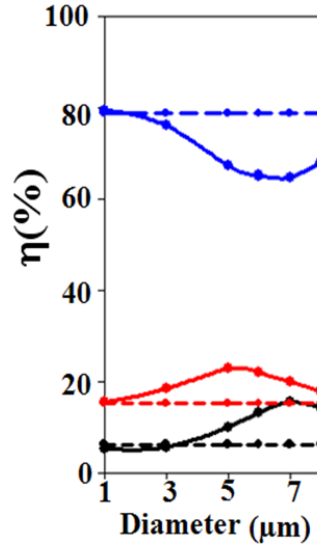
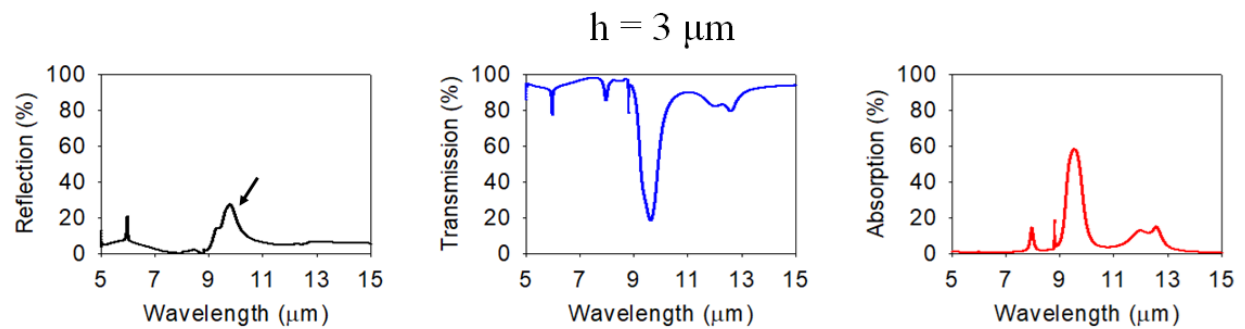


Figure 3.10: Evolution of the reflection (black), transmission (blue), and absorption (red) efficiency coefficients η in the range $[7.5 - 11.5] \mu\text{m}$, as a function of the diameter of air holes, keeping constant the period $P = 10 \mu\text{m}$ and the thickness $h = 5.71 \mu\text{m}$. The solid (resp. dashed) lines correspond to the structured (resp. non-structured) responses.

III.3.3.3 Variation of the thickness

We now study the influence of the membrane thickness h on the optical properties. The calculation of the reflection, transmission and absorption spectra are performed for the BCB hole's grating, with a hole diameter $D = 7.9 \mu\text{m}$, period $P = 10 \mu\text{m}$ and a thickness ranging from 3 to 11 μm . These parameters, based on the scaling factor α_4 , were selected to allow the appearance of peaks in an area corresponding to the maximum emission of the human body, i.e. $9\mu\text{m}$. The obtained results have been reported in figure 3.11.



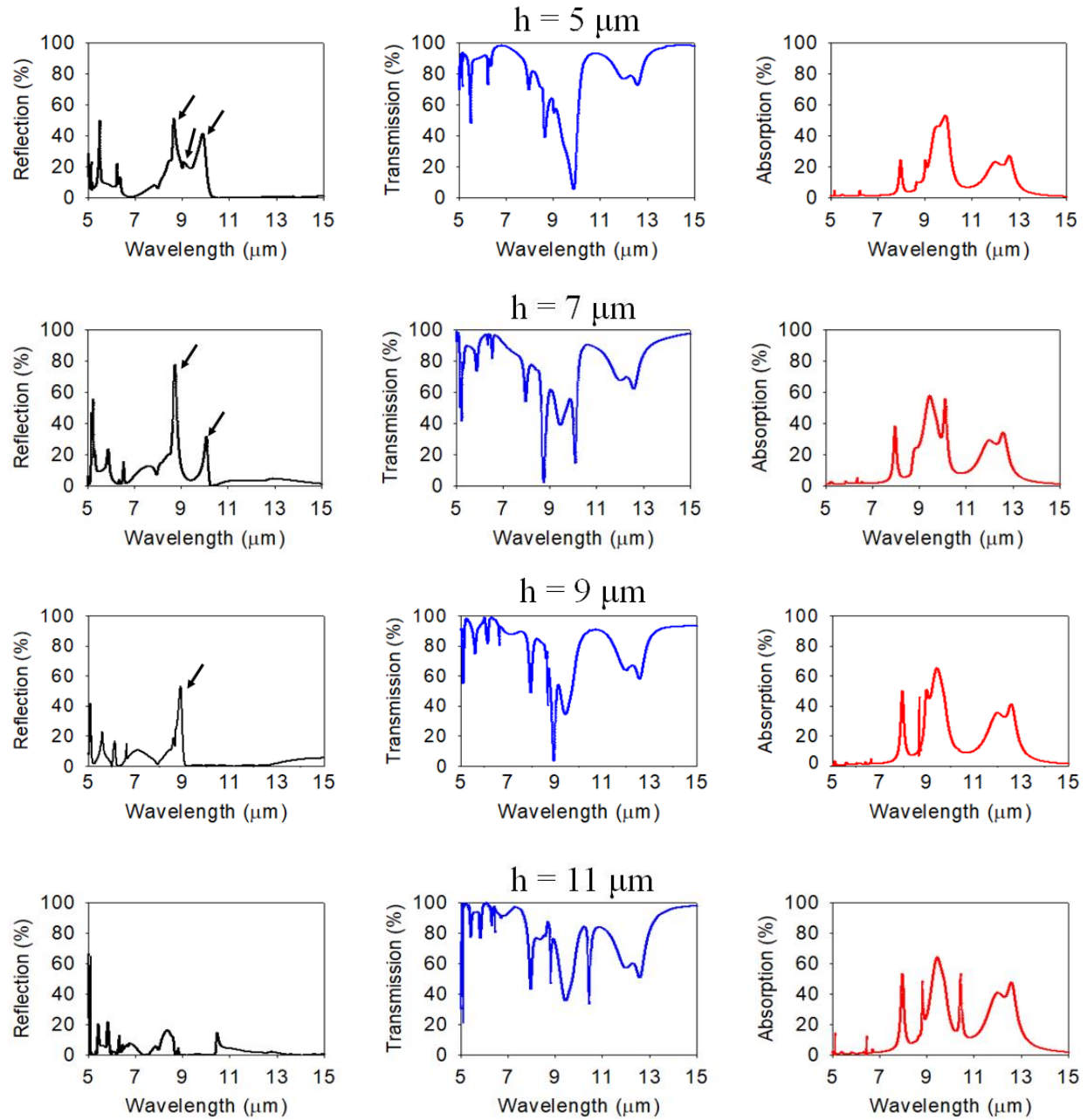


Figure 3.11: Evolution of the reflection, transmission and absorption spectra of the structured membrane versus the thickness (h) of the membrane in the range [5, 15] μm , keeping constant the period $P = 10 \mu\text{m}$ and the hole diameter $D = 7.9 \mu\text{m}$.

For thin membranes ($h = 3 \mu\text{m}$), the reflection is low, except for a peak around 10 μm associated to the structuration of the membrane. Then the reflection coefficient increases for thicknesses $h = 5 - 7 \mu\text{m}$ with the appearance of the peaks **a**, **b** and **c** (black arrows), before disappearing again when $h > 9 \mu\text{m}$.

For $h = 11 \mu\text{m}$, the peaks **a**, **b** and **c** which belong to the structuration do not appear anymore in the reflection spectrum, while they appear now in the absorption spectrum. Note that the effect of the structuration on the transmission spectrum appears lower in this case.

Figure 3.12 represents the behavior of the efficiency coefficient as a function of the thickness of the membrane. One can see that $h = 5 \mu\text{m}$ and $11 \mu\text{m}$ correspond to the same level of transmission. However, for $h = 5 \mu\text{m}$, the decrease in transmission is associated to both reflection and absorption at the same level of response. On the contrary, for $h = 11 \mu\text{m}$, the drop in transmission is almost completely compensated by an absorption while the response in reflection appears to be almost zero.

Finally, the minimum of transmission is obtained when the reflection is maximum, *e.g.* for $h = 5.7 \mu\text{m}$. It also corresponds to the higher difference with a regular non-structured membrane.

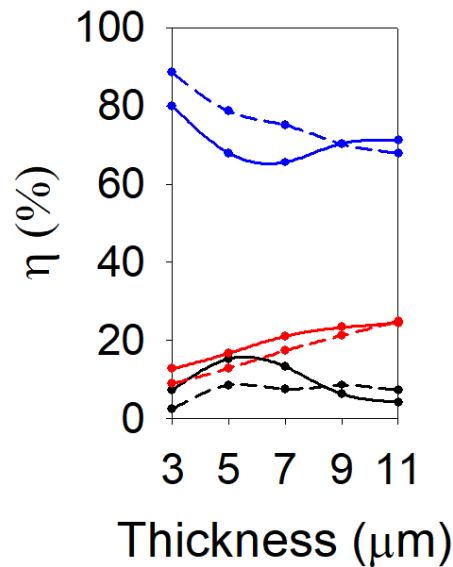


Figure 3.12: Evolution of the reflection (black), transmission (blue), and absorption (red) efficiency coefficient η in the range $[7.5 - 11.5] \mu\text{m}$, as a function of the thickness of the structured (solid lines) and unstructured membrane (dashed lines) for $P = 10 \mu\text{m}$, $D = 7.9 \mu\text{m}$.

In conclusion, one can propose two different photonic membranes with the same lattice of air holes that represents either an increment of its reflection or of its absorption:

- a) Membrane with equal reflection and absorption ($h = 5 \mu\text{m}$).

b) Membrane with low reflection and absorption ($h = 11 \mu\text{m}$).

The thermal behavior of these two membranes while be studied thereafter in order to decouple the influence of the reflection / absorption on the temperature of the membrane.

III.3.3.4 Influence of incident angle

We have investigated, for the scaling factor α_4 ($P = 10 \mu\text{m}$; $D = 7.9 \mu\text{m}$; $h = 5.7 \mu\text{m}$), the effect of the angle of incidence θ of the human body emissivity for TE (solid line) and TM (dashed line) polarization. The figure 3.13 shows the reflection spectra for an incident angle of 10° for both polarizations.

One can see clearly that TE and TM incident wave polarizations induce now two different spectra.

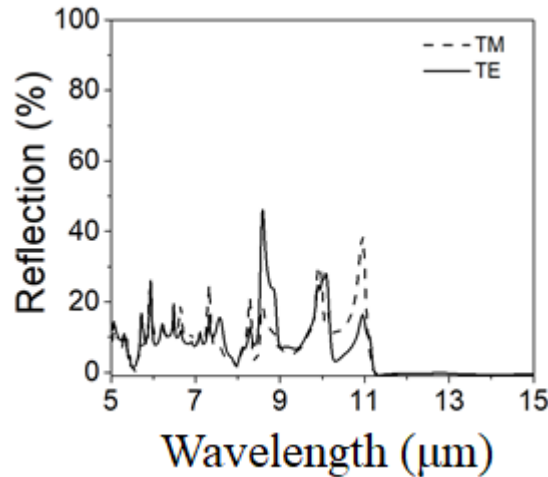


Figure 3.13: Reflection spectra for an incident angle of 10° for both polarizations TE (solid line) and TM (dashed line).

Therefore, the reflection spectra under the incident angles 0° , 10° and 20° (Figure 3.14 (a)) are calculated considering the average of the TE and TM polarization. When $\theta = 0^\circ$, we recognize the peaks **a**, **b** and **c**. When θ increases, to 10° then 20° , these reflective peaks widen and shift toward the high wavelength.

The Figure 3.14 (b) shows the efficiency factor as a function of the incident angle. The calculation reveals a robustness of the transmission as long as the incident angle is lower than 10° . Over 10° , the transmission increases meaning the incident radiation is less captured or reflected by the

structured membrane. This means that the surface must remain almost flat to have an efficient scattering response.

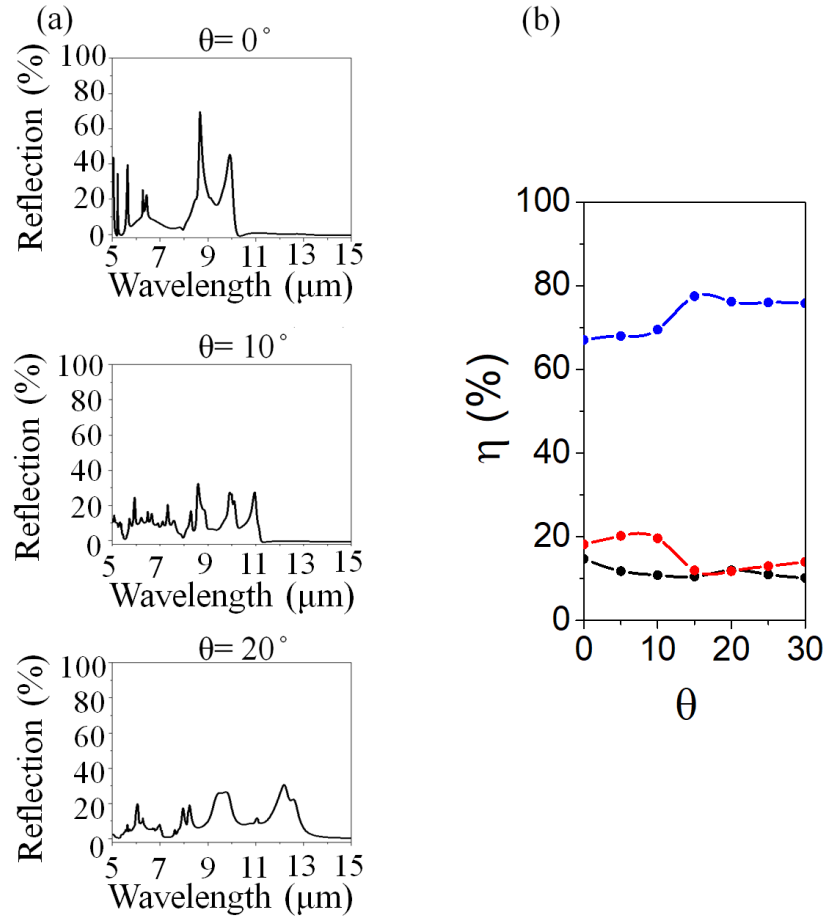


Figure 3.14: (a) Evolution of the reflection spectrum for the perforated membrane for three incidence angles θ in the range $[5, 15]$ μm for the scaling factor α_4 . (b) Evolution of the corresponding reflection (black), transmission (blue), and absorption (red) efficiency coefficient η , as a function of the incident angle θ .

III.3.3.5 Variation of the refractive index of the microclimate

As seen in chapter I, moisture transfer is one of the main mechanisms for thermal regulation. In this study, humidity is addressed from an optical point of view. In order to take perspiration into account, we considered a variation of the refractive index of the air medium distributed both inside the microclimate (MC) and the holes.

The calculations have been performed for the structured membrane of scaling factor α_4 . To characterize the effect of the moisture, we have modified progressively the refractive index inside the microclimate (MC) and the holes. Figure 3.15 (a) reports the evolution of the reflection,

transmission and absorption spectra for $n' = 1.0$ (n_{air}), 1.1, 1.2 and 1.3 (n_{water}). As far as n' approaches the index of refraction of water, the effect of scattering vanishes and the membrane becomes more and more transparent. One can see that both the reflection and the absorption coefficients decrease, converging toward the non-structured membrane spectra. This behavior comes from the decreasing of the contrast index between the photonic crystal components, *i.e.* the holes and the matrix.

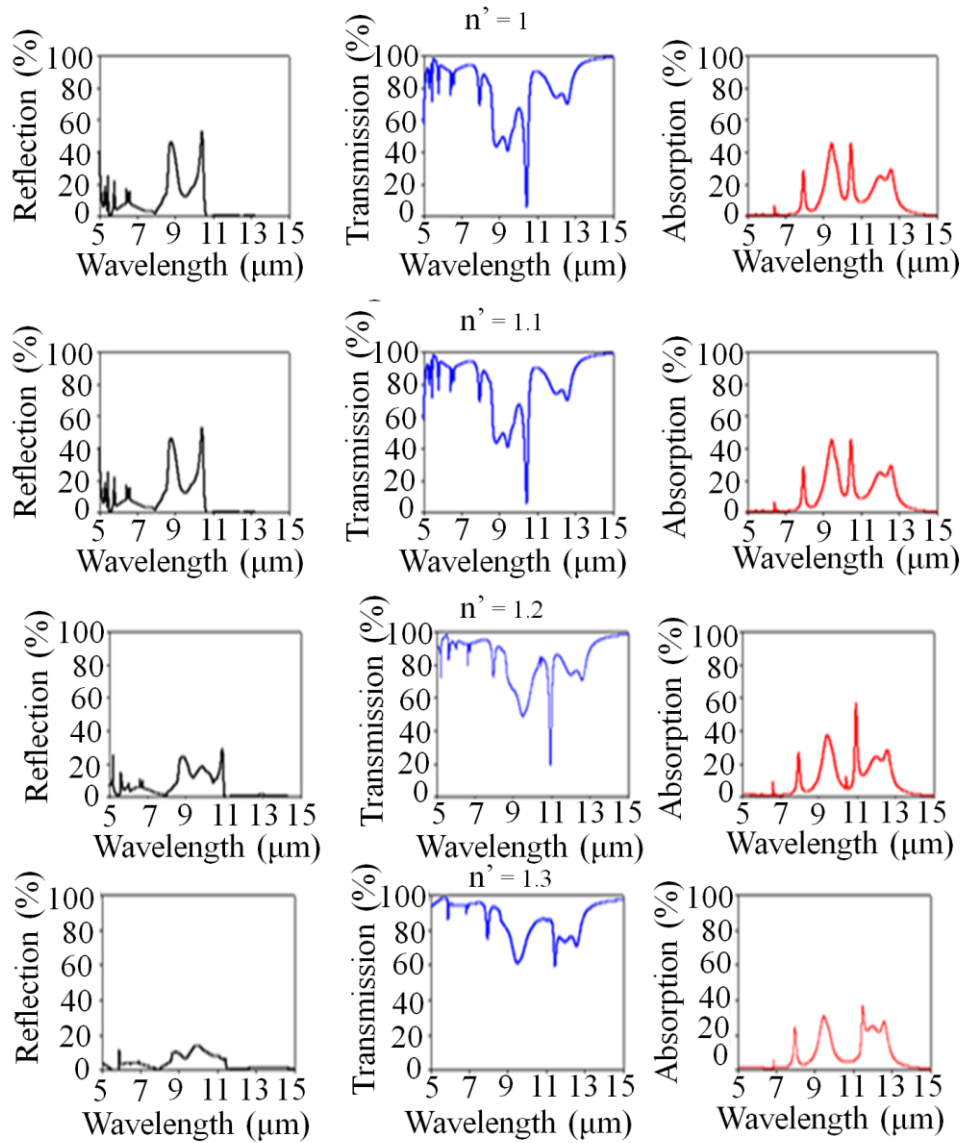


Figure 3.15: Evolution of the reflection, transmission and absorption spectra of the perforated membrane (scaling factor α_4) versus the refractive index of both the microclimate and the holes.

Figure 3.16 summarizes this behavior through the efficiency coefficient representation as a function of the refractive index of the microclimate and holes media. This situation will be considered in the next section, dealing with the thermal management.

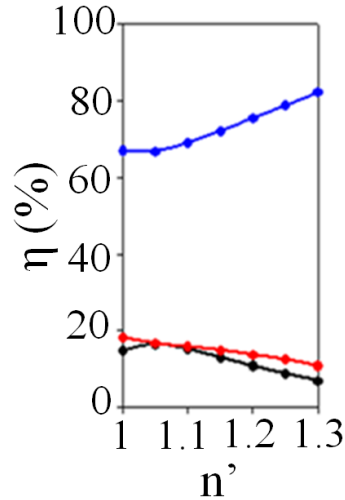


Figure 3.16: Evolution of the corresponding reflection (black), transmission (blue), and absorption (red) efficiency coefficient η , as a function of n' .

III.3.4 Conclusion on the impact of the optical properties

As a summary, we have studied the behavior of a polymer based photonic membrane in the mid-infrared. We have shown that, according to the structure of the membrane, it was possible to modify the reflection, transmission and absorption properties in the mid-infrared. We found that, by scaling the geometrical parameters of the crystal, the transmission can be modulated up to 28% of the human body emissivity in the wavelength range $[7.5, 11.5] \mu\text{m}$. Moreover, this tunability is also supported by a variation of one geometrical parameter (D, h) independently. According to the thickness of the membrane, the decreasing of the transmission can be managed in two ways: (i) an increase of the reflection when the thickness is thin ($h = 5 \mu\text{m}$) or (ii) an increase of the absorption when the thickness is thick ($h = 11 \mu\text{m}$). Besides, we found that the perspiration decreases the scattering effects.

III.4 Heat transfer analysis

The objective of this section is to investigate the effects of optical properties, described previously, on the thermal flows between the human body and the surrounding environment. The main objective is to control and regulate the temperature of the membrane based on the modulations of the optical radiations in the mid-infrared.

III.4.1 Thermal balance model

To evaluate the impact of our system on the personal thermoregulation, we used a one-dimensional steady-state heat transfer model analysis, illustrated in figure 3.17. The thermal analysis is done considering radiative, conductive, and convective heat transfer. The following sections provide a summary of the assumptions, input parameters, and analytical formula used in our study. Throughout this work, as already explained in chapter I, we limit ourselves to a functionality of the membrane for everyday use, assuming that the human body is in a sedentary state, inside a room. As a consequence, uniform skin temperature and heat generation from the human body are considered. The air flow between the skin and the polymer membrane is assumed to be stationary, meaning that convective heat transfer will be neglected in this region. In the model, both skin and environment are assumed to be an ideal blackbody emitter and absorber respectively. The membrane will then partially reflect, transmit and absorb the incoming optical radiations, in support of the optical results obtained in section III.3.3. We used Kirchhoff's law and define the emissivity $\varepsilon_m(\lambda)$ of the membrane throughout its absorption coefficient, as (eq. III.5):

$$\varepsilon_m(\lambda) = A = 1 - R - T \quad \text{III.5}$$

Where A , R and T are respectively the absorbance, reflectance and transmittance of the polymer membrane calculated in section III.2.

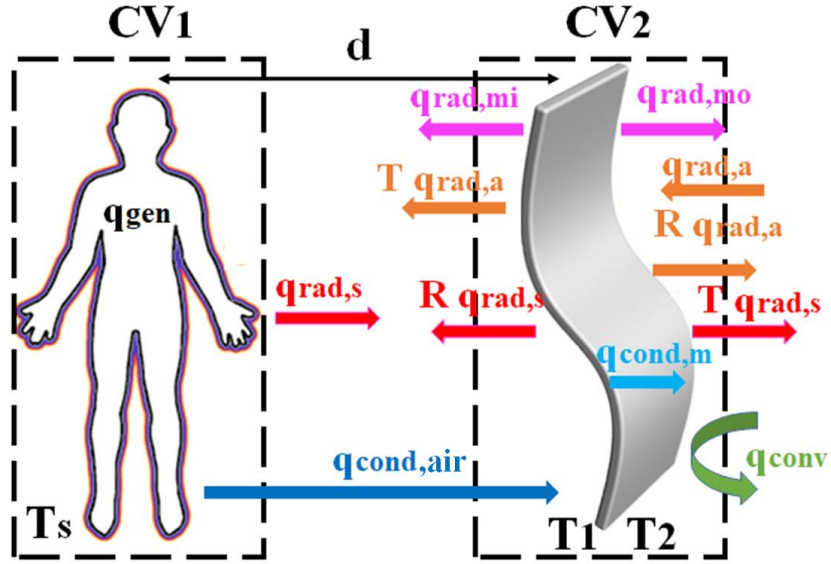


Figure 3.17: Schematic representation of the heat transfer model of the clothed human body to the surrounding environment, considering all radiative (*rad.*), conductive (*cond.*) and convective (*conv.*) mechanisms. The indices *s*, *a*, *mo* and *mi* respectively mean skin, ambient air, membrane inner and membrane outer surfaces. *d* is the distance between the human body and the membrane.

The conductive, convective, and radiative heat flux terms follow respectively the Fourier, Newton, and Stefan-Boltzmann laws and take the following expressions:

$$q_{rad,s} = \sigma T_s^4 \quad \text{III.6}$$

$$q_{rad,e} = \sigma T_e^4 \quad \text{III.7}$$

$$q_{rad,po} = A \cdot \sigma T_2^4 \quad \text{III.8}$$

$$q_{rad,mi} = A \cdot \sigma T_1^4 \quad \text{III.9}$$

$$q_{cond,air} = k_{air} \frac{T_s - T_1}{d} \quad \text{III.10}$$

$$q_{conv} = h(T_2 - T_a) \quad \text{III.11}$$

Where

- $q_{rad,s}$ is the radiative heat flux from the skin,
- $q_{rad,a}$ is the radiative heat flux from the ambient air,
- $q_{rad,mi}$ is the radiative heat flux from the polymer membrane inner surface,
- $q_{rad,mo}$ is the radiative heat flux from the polymer membrane outer surface,
- $q_{cond,air}$ is the conductive heat flux in the air gap between the skin and the textile,
- q_{conv} is the convective heat flux from the membrane to the ambient air,
- T_S is the temperature of the skin ($T_S = 34\text{ }^{\circ}\text{C}$), T_a is the temperature of the ambient air, T_1 and T_2 are the temperatures of the inner and outer surfaces of the membrane respectively,
- k_{air} is the thermal conductivity of air ($k_{air} = 0.027\text{ W.m}^{-1}.\text{K}^{-1}$), h_c is the convective heat transfer coefficient ($h_c = 3.0\text{ W.m}^{-2}.\text{K}^{-1}$), and σ is the Stefan-Boltzmann constant ($\sigma = 5.6710^{-8}\text{ W.m}^{-2}.\text{K}^{-4}$).

Note that the conductive heat transfer coefficient h_c can be adapted to simulate different environmental conditions as, for example, the air circulation within the room (not considered here).

Additionally, the air gap thickness, d , has been fixed to $d = 2\text{ mm}$ as a reference.

Table 3.3 shows a list of the input parameters used in this study.

Parameter name	Value
Heat generation rate, q_{gen} [2]	73 w.m^{-2}
Skin temperature, T_s	$34\text{ }^{\circ}\text{C}$
Thermal conductivity of air, k_{air}	$0.027\text{ w.m}^{-1}.\text{K}^{-1}$
Thermal conductivity of the BCB polymer, k_{BCB}	$0.2\text{ w.m}^{-1}.\text{K}^{-1}$
Membrane thickness	$[3 - 9]\text{ }\mu\text{m}$
Holes diameter, D	$[4-12]\text{ }\mu\text{m}$
Period of triangular lattice, P	$[5-15]\text{ }\mu\text{m}$
Total emittance of skin	1
Total emittance of environment	1
Convective heat flux, h	3 w.m^{-2}
Air gap thickness, d	2 mm
Membrane reflectance, R	[0-1]

Parameter name	Value
Membrane transmittance, T	[0-1]
Membrane absorbance, A	[0-1]

Table 3.3: Input parameters for heat transfer model analysis

In the following, we will study the thermal balance analysis in two ways. In the first one, the membrane temperature is calculated for different ambient air temperatures, regulated from 20 °C to 40 °C, by neglecting the thermal conduction ($q_{cond,m}$) within the membrane. In this case, the membrane will be considered thermally insulated. In the second one, more realistic, the BCB membrane and the ambient temperatures are calculated considering the heat conduction through the membrane.

III.4.2 Non-thermally conductive Benzocyclobutene membrane

The overall goal of this part is to determine the temperature of a thermally isolated membrane, as a function of the polymer optical properties and its geometrical parameters, for different room temperatures. In this first approach, we neglected the thermal conduction ($q_{cond,m}$) within the membrane from the heat transfer model.

As shown in figure 3.15, we have considered two control volumes [3]: $CV1$ is defined around the human body and $CV2$ integrates the totality of the membrane. All the incoming flows passing through these control volumes get a positive sign, while the outgoing flows get a negative one. When applying the energy balance around $CV1$ and $CV2$, we found the two equations, respectively:

at the control volume ($CV1$),

$$q_{gen} - q_{rad,s}(1 - R) - q_{cond,air} + T \cdot q_{rad,a} + q_{rad,mi} = 0 \quad \text{III.12}$$

and at the control volume ($CV2$):

$$q_{cond,air} + A \cdot q_{rad,s} + A \cdot q_{rad,a} - [q_{rad,mi} + q_{rad,mo} + q_{conv}] = 0 \quad \text{III.13}$$

By fixing the skin temperature at 34 °C, the unknown variables are the temperature T_1 and T_2 of the inner and outer face of the membrane.

The resolution of the two fundamental equations (III.12) and (III.13) allows the determination of the inner and outer temperature of the membrane (T_1 and T_2). We finally define the average temperature of the BCB membrane, T_{BCB} , as:

$$T_{BCB} = \frac{T_1 + T_2}{2} \quad \text{III.14}$$

III.4.2.1 Temperature of the non-thermally conductive unstructured membrane

We study in the following sections, the effect of the structure of the membrane on the thermal balance.

We first present, as a reference, the evolution of the temperature of the unstructured membrane, T_{BCB} , as a function of the membrane thickness h , for two room temperatures, $T_a = 20^\circ\text{C}$ and $T_a = 40^\circ\text{C}$ (Figure 3.18). For a room temperature of $T_a = 20^\circ\text{C}$, when the membrane thickness increases, the temperature of the unstructured membrane increases from 26.3°C to 28°C . On the contrary, when the room temperature is $T_a = 40^\circ\text{C}$, the temperature of the membrane decreases from 47.8°C to 43.3°C when the thickness of the membrane increases.

This means that the thickness of the unstructured membrane modulates its temperature. As we have seen in figure 3.13, the membrane absorbs more when it is thicker. So the absorption allows to regulate the temperature of the membrane. For a low (resp. high) ambient temperature, the increase of the absorption leads to an increase (resp. decrease) of the temperature of the membrane.

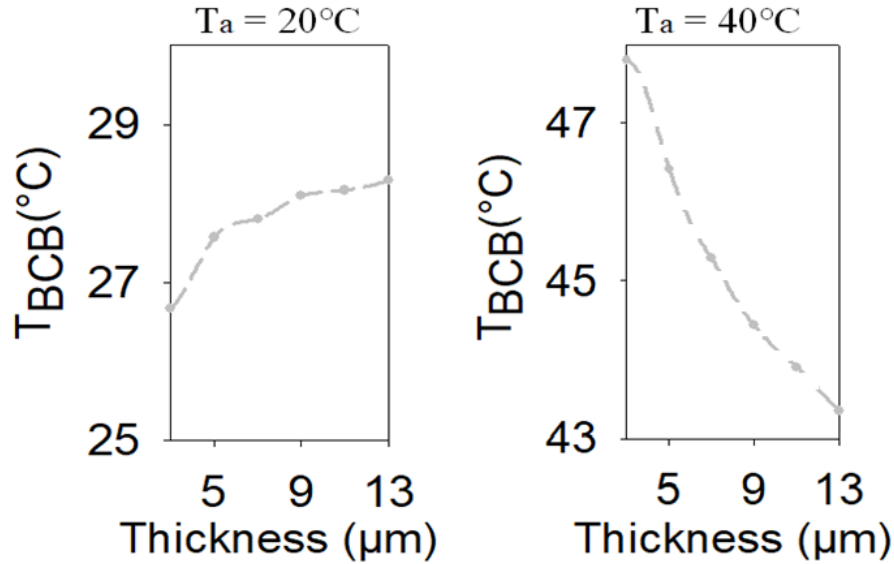


Figure 3.18: Evolution of the unstructured membrane's temperature, T_{BCB} , as a function of the membrane thickness h , for a room indoor temperature of $T_a = 20^\circ\text{C}$ (left) and $T_a = 40^\circ\text{C}$ (right).

We now turn to the structuration of the membrane. As explained in the optical part, the structuration produces scattering effects which introduce both supplementary absorption and reflection of the incident wave. The goal is to understand the effect of this scattering and to discuss the roles of absorption and reflection on thermal responses.

III.4.2.2 Effect of the structuration of the non-thermally conductive membrane

In section III.3.3.2, we have shown the evolution of the optical efficiency coefficient η as a function of the scaling factors α_i . As a reminder, α_i is associated to the homothetic variation of the geometrical parameters of the photonic crystal membrane, *e.g.* the period P_i , the diameter of the holes D_i , and the thickness of the plate h_i (see table 3.2). We have shown that, when increasing α_0 to α_3 , the transmission drops by 28% to the benefit of the reflection and the absorption, which increase respectively by 16% and 12%. The efficient coefficient is then almost constant until the geometrical parameters reach α_6 where the transmission increases again.

In figure 3.19(a) we report the evolution of the temperature of the membrane, T_{BCB} , as a function of the scaling factor α_i , for a room temperature of $T_a = 20^\circ\text{C}$ (solid line). To estimate the impact of the structuration, we compared the temperature of the structured membrane with the non-structured one (dashed line in figure 3.19 (a)). When the scaling factor increases, the temperature

membrane jumps from 26.5 °C to 28.5 °C before decreasing. This increase of temperature results from the decrease in transmission to the benefit of both the reflection and the absorption of the membrane that cross the wavelength range [7.5µm-11.5µm], as reported in section III.3.3.1 (see for instance figure 3.8 (a)). If we consider the geometrical parameters of the membrane associated to α_5 , ($P = 11 \mu\text{m}$, $D = 8.6 \mu\text{m}$, $h = 6.3 \mu\text{m}$) one can see that the temperature of the membrane increased by 1°C compared to a non-structured membrane of equivalent thickness. This means that, when the indoor temperature of the room is 20 °C, the photonic crystal membrane acts as a heating element.

Figure 3.19 (b) shows the evolution of the temperature of the membrane when the ambient temperature is 28 °C. One can see that the general level of the membrane temperature increases to 34 °C. The structured membrane has the same temperature than the non-structured one, meaning that 28 °C corresponds to a working point for which the structuration of the membrane is not active. Figure 3.19 (c) presents the evolution of the temperature when the ambient temperature is 40 °C. When the scaling factor increases, the temperature of the membrane drops from 49 °C to 45 °C before slightly increasing. Again, this rough decrease of temperature comes from the structuration of the membrane which modulates the transmission for the benefit of both the reflection and absorption. Considering the geometrical parameters of the membrane associated to α_5 , ($P = 11 \mu\text{m}$, $D = 8.6 \mu\text{m}$, $h = 6.3 \mu\text{m}$) the temperature of the membrane is now decreasing by 1 °C than the non-structured membrane of equivalent thickness. This means that, when the indoor temperature of the room is 40 °C, the photonic crystal membrane acts as a cooling element.

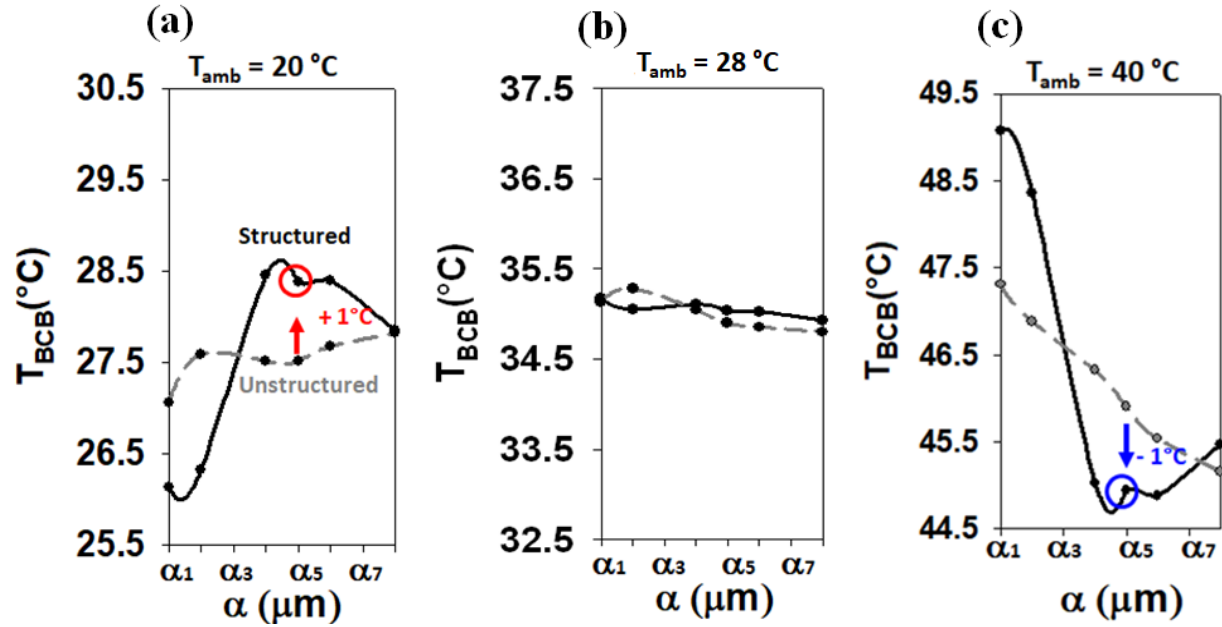


Figure 3.19: Evolution of the temperature of the membrane T_{BCB} , as a function of the scaling factor α_i for a structured (solid lines) and non-structured (dashed lines) membrane at three different room temperatures: (a) $T_{amb} = 20\text{ °C}$, (b) $T_{amb} = 28\text{ °C}$, and (c) $T_{amb} = 40\text{ °C}$.

We have reported the temperature of the membrane (structured and unstructured) for α_4 at different ambient temperatures (from 18 °C to 40 °C). The intersection of these two lines, at the ambient temperature of 28 °C , corresponds to the working point of the polymer BCB (Figure 3.20).

As a summary, non-thermally conductive photonic crystal membrane can behave dynamically as a heater or a cooler depending on the environmental temperature.

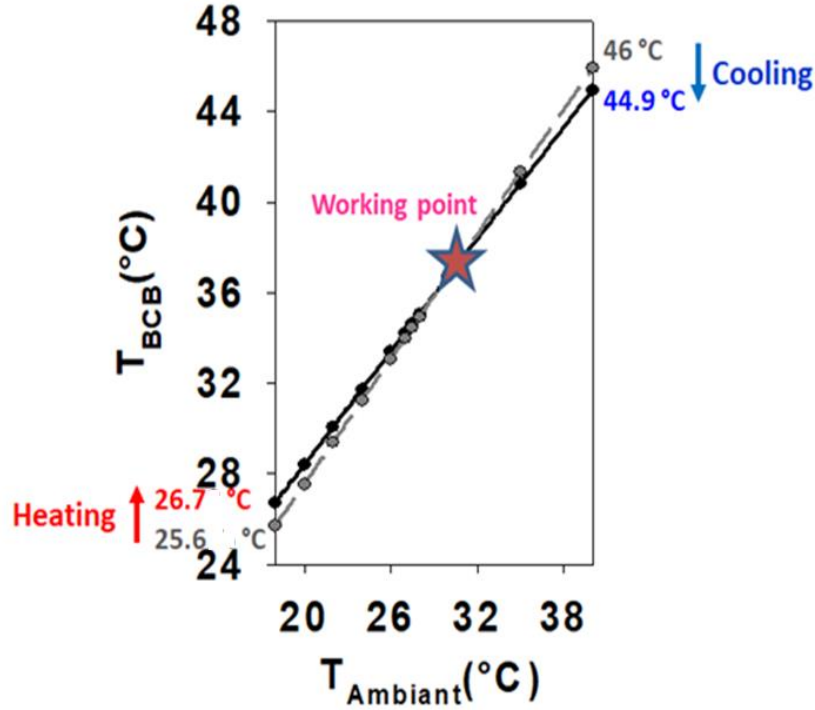


Figure 3.20: Evolution of the membrane BCB temperature T_{BCB} , as a function of the ambient temperature for a non-structured (grey lines) and structured (black lines) BCB membrane α_4 .

III.4.2.3 Effect of hole diameter of the non-thermally conductive membrane

In section III.3.3.2, we have studied the evolution of the optical efficiency coefficient η as a function of the hole diameters, keeping constant $P = 10 \mu\text{m}$ and $h = 5.7 \mu\text{m}$. We concluded that the transmittance of the membrane decreases when the diameter increases in favor of absorption and/or reflection. For a diameter $D = 7.8 \mu\text{m}$, corresponding to the scaling factor α_4 , we recover a decrease of the transmission down to 66%. We now complete the study by the evolution of the temperature varying the diameter from 1 to 8 μm (Figure 3.21).

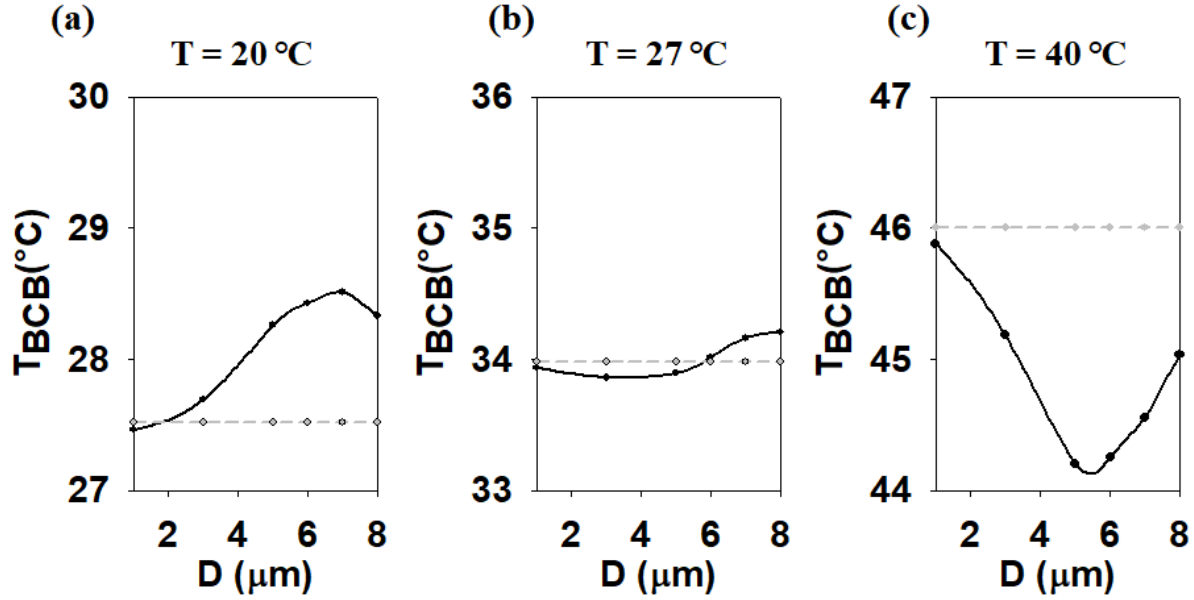


Figure 3.21: Evolution of the temperature of the membrane T_{BCB} , as a function of the holes diameter for a structured (solid lines) with $P = 10\text{ μm}$, $h = 5.7\text{ μm}$ and non-structured (dashed lines) membrane at three different room temperatures: (a) $T_{amb} = 20\text{ °C}$, (b) $T_{amb} = 27\text{ °C}$, and (c) $T_{amb} = 40\text{ °C}$.

In figure 3.21(a) we report the evolution of the temperature of the membrane, T_{BCB} , as a function of the diameter, for a room indoor temperature of $T_a = 20\text{ °C}$ (solid line). We compared the temperature of the structured membrane with the non-structured one (dashed line). When the diameter increases, the temperature jumps from 27.5 °C to 28.5 °C. Since there is an increase in the reflectance and absorbance, the transmittance decreases, which leads to a progressive increase in the membrane temperature. For $D = 7\text{ μm}$, the membrane temperature is 1 °C more compared to a non-structured membrane of equivalent thickness. Therefore, the photonic crystal membrane acts as a heating element.

When the ambient temperature reaches 28 °C (figure 3.21(b)), one can see that the structured membrane has the same temperature than the non-structured one.

On the contrary, for an ambient temperature of 40 °C (figure 3.21 (c)), the temperature of the membrane drops from 45.9 °C to 44.2 °C before slightly increasing with the increment of the hole diameter. Considering the geometrical parameters of the membrane $P = 10\text{ μm}$, $h = 5.7\text{ μm}$ and $D = 7\text{ μm}$, the membrane temperature is 1 °C less compared to a non-structured membrane of equivalent thickness. Thus, the non-thermally conductive photonic crystal membrane acts as a cooling element.

III.4.2.4 Effect of the membrane thickness of the non-thermally conductive membrane

Two specific cases have been highlighted with the variation of the membrane thickness for the scaling factor α_4 , *e.g.* one for $h \leq 7\mu\text{m}$ and the other for $h \geq 7\mu\text{m}$. In both cases, the transmission through the membrane decreases (Figure 3.12). But in the first case, it corresponds to an increase of the reflection ($R=19\%$) while in the second case, it comes from an increase of the absorption ($A=30\%$). In figure 3.22 (a), we have reported the evolution of the temperature of the membrane, T_{BCB} , as a function of the thickness h , for a room temperature of $T_a = 20^\circ\text{C}$ (solid line). When the thickness is lower than $7\mu\text{m}$, the temperature of the structured membrane is 1°C more than a non-structured one. When h is larger than $7\mu\text{m}$, the two temperatures are almost the same. For an ambient temperature of $T_a = 40^\circ\text{C}$ (Figure 3.22 (b)), the temperature is 1°C less for the structured membrane as long as the thickness of the membrane remains lower or equal to $7\mu\text{m}$. Therefore, it is essential to keep a membrane thinner than $7\mu\text{m}$ to preserve the diffusion in reflection and activate the thermoregulatory properties of the photonic membrane. When the membrane is thicker, the maximum of absorption is achieved, independently of the structuration.

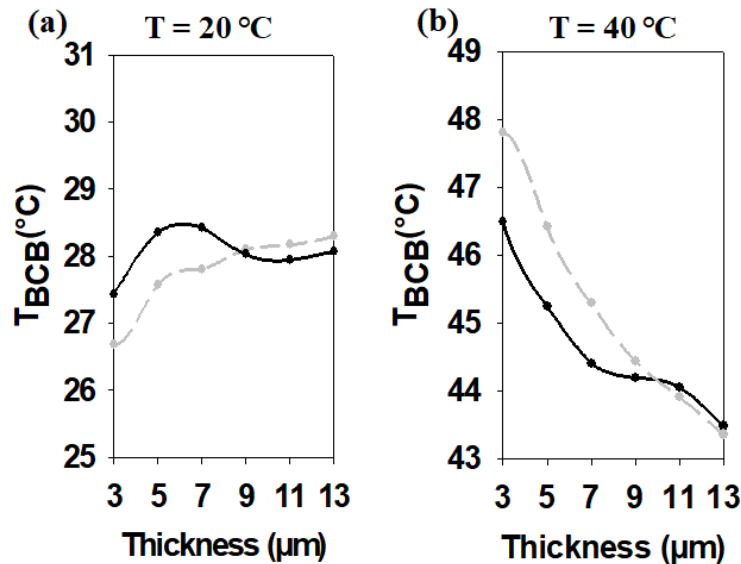


Figure 3.22: Evolution of T_{BCB} as a function of the thickness of a non-structured (grey lines) and structured (black lines) BCB membrane at the room temperature (a) $T_{amb} = 20^\circ\text{C}$, and (b) $T_{amb} = 40^\circ\text{C}$.

III.4.2.5 Effect of the moisture of the non-thermally conductive membrane

We have seen in section III.3.3.5 that the reflection vanishes as far as the microclimate (MC) and the hole refractive indexes approach the refractive index of water ($n_{\text{water}} = 1.3$). The calculations have been performed with a structured membrane of scaling factor α_4 . We investigate here the thermal response associated to a moisture effect. In figure 3.24, we report the evolution of the membrane temperature, T_{BCB} , as a function of the refractive index n' of the microclimate and holes media, for an ambient temperature going from $T_a = 20^\circ\text{C}$ to $T_a = 32^\circ\text{C}$.

For an ambient temperature $T_a < 28^\circ\text{C}$, the temperature of the membrane decreases. One can suppose that the resentment of sultriness can be partially compensated. On the contrary, when the room temperature becomes higher than $T_a > 28^\circ\text{C}$, the temperature increases with n' , and the reactivity of the structured membrane will be counterproductive.

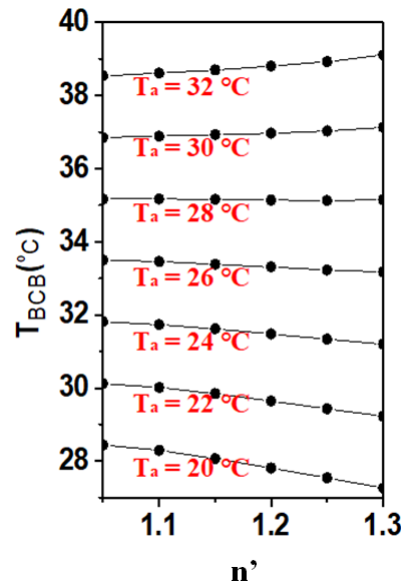


Figure 3.24: Evolution of the membrane temperature, T_{BCB} , as a function of the microclimate and hole refractive index, n' , for an ambient temperature going from $T_a = 20^\circ\text{C}$ to $T_a = 32^\circ\text{C}$.

In this section, for the thermal balance analysis, both the skin temperature and ambient temperature were fixed to calculate the temperature of the inner/outer surface. We found that the inner and outer temperature of the membrane (T_1 and T_2) were not similar, despite the extremely thinness of the membrane. The temperature of the membrane T_{BCB} was calculated by taking the average value of these two temperatures. It means that in this model, there is a lack in the relationship that

connects the inner temperature T_I with the outer one, T_2 . An additional equation is required in order to complete the model. The remaining equation will describe the heat transfer within the membrane itself, as seen in the next section.

III.4.3 Thermally conductive membrane

In this part, we now consider the heat conduction inside the membrane in the heat transfer analysis. Following the temperature profile within the membrane developed in [3], we have been able to get a relation between the temperatures T_I and T_2 respectively at the inner and outer faces of the membrane as:

$$T_2 = \frac{h}{2k_m} \{ \epsilon_m \sigma (T_1)^4 + \epsilon_m \sigma (T_2)^4 - \epsilon_m \sigma T_s^4 - \epsilon_m \sigma T_a^4 \} - \frac{k_{air} h}{k_m d} (T_s - T_1) + T_1 \quad \text{III.15}$$

Where $k_m = 0.2 \text{ W.m}^{-1}.\text{K}^{-1}$ is the BCB thermal conductivity [4], h is the thickness of the membrane, T_a is the ambient temperature, T_s is the skin temperature and d is the thickness of the microclimate. Therefore, with equations (III.12), (III.13) and (III.15), we have a complete set of equations to describe the full heat transfer from a human body to the ambient environment.

Now, the overall goal is to determine the efficiency of the structuration by representing the ambient temperature that can be sustained while maintaining a person's thermal comfort, as a function of the geometrical parameters of the membrane.

III.4.3.1 Temperatures evolution using a thermally conductive non-structured membrane

The effect of the membrane is demonstrated by fixing the temperature of the skin, typically $T_s = 34 \text{ }^\circ\text{C}$, and by determining the unknown temperatures T_I , T_2 , and T_a from the resolution of equations (III.12), (III.13) and (III.15).

We first present in table 3.4 the temperatures (T_1 , T_2 , T_a), calculated for different unstructured membrane thicknesses h at $T_s = 34 \text{ }^\circ\text{C}$.

Thickness h (μm)	3	5	7	9	11
T_1 ($^{\circ}\text{C}$)	32.11	31.91	31.83	31.74	31.67
T_2 ($^{\circ}\text{C}$)	32.11	31.91	31.83	31.74	31.67
T_a ($^{\circ}\text{C}$)	25.28	24.75	24.7	24.54	24.52

Table 3.4: Reports the temperatures (T_1 , T_2 , T_a) calculated from eq. (III.12), (III.13) and (III.15) for unstructured membrane thickness h at $T_s = 34$ $^{\circ}\text{C}$.

One can notice that the inner and outer temperatures of the membrane are exactly the same. So, T_1 and T_2 will be reported as T_{BCB} in the following.

Then we show, as a reference, the evolution of the thermally conductive non-structured BCB membrane and the ambient temperatures (T_{BCB} and T_a) as a function of the membrane thickness h (Figure 3.25).

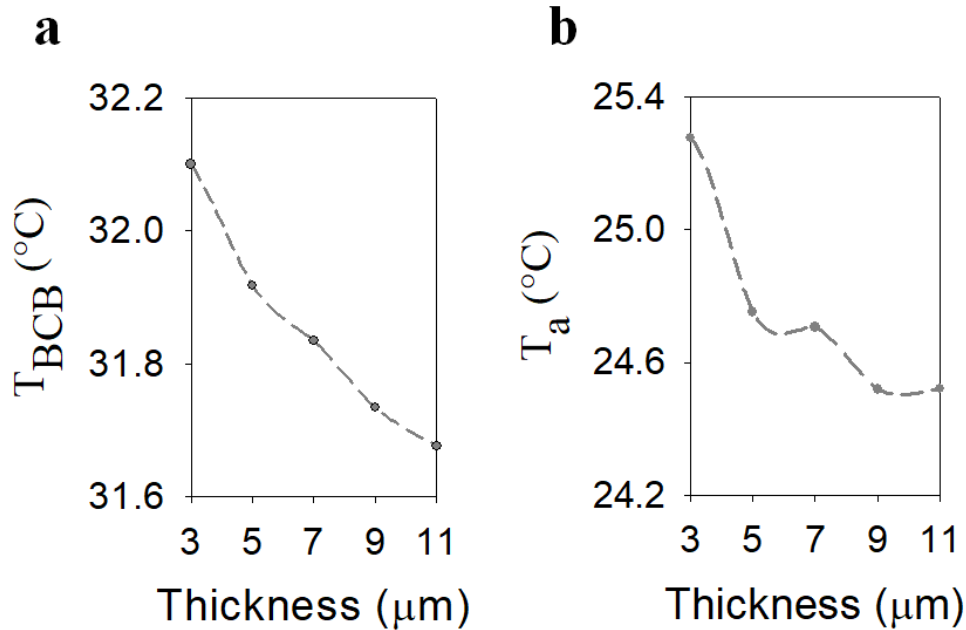


Figure 3.25: Evolution of (a) the temperature of the membrane $T_{BCB} = T_1 = T_2$ and (b) the ambient temperature as a function of the thickness h for a non-structured membrane (dashed lines).

When the thickness increases from $h = 3$ μm to $h = 11$ μm , the temperature T_{BCB} decreases from 32.1 $^{\circ}\text{C}$ to 31.6 $^{\circ}\text{C}$ (Figure 3.25a). The calculated room temperature also decreases from 25.27 $^{\circ}\text{C}$ to 24.52 $^{\circ}\text{C}$ (Figure 3.25b). It means that, to keep the skin temperature at 34 $^{\circ}\text{C}$, the room temperature needs to be almost 0.8 $^{\circ}\text{C}$ less when the membrane is thick. From the optical point of

view, as shown in figure 3.13, section III.3.3.3, when the thickness increased, the absorption increased as well. Therefore, the increase of the absorption is in favor of energy consumption. We will now see how the structuration of the membrane will support this conclusion in a complementary manner.

III.4.3.2 Effect of the structuration of the thermally conductive membrane

In figure 3.26 (a) and (b), we show the evolution of the temperatures, T_{BCB} and T_a as a function of the scaling factor α_i . To estimate the effect of the structuration of the membrane, we compare the results (solid lines in figure 3.26) with those of the non-structured membrane of equivalent thickness (dashed lines). When the scaling factor increases, the temperature of the membrane varies, from 32.4 °C to 31.75 °C, reaching a minimum for $\alpha_i = \alpha_5$. This modulation of temperature is directly related to the variation in transmission (see figure 3.9 (a)) occurring in benefit of the reflection and absorption of the membrane. Finally, if we consider the geometrical parameters of the membrane associated to α_5 , one can see that the temperature is lower in the structured membrane as compared to a non-structured membrane of equivalent thickness by about 0.25 °C. As before, to keep the skin at the comfort temperature of 34 °C, a lower temperature of the membrane is needed in the structured membrane as compared to the unstructured one.

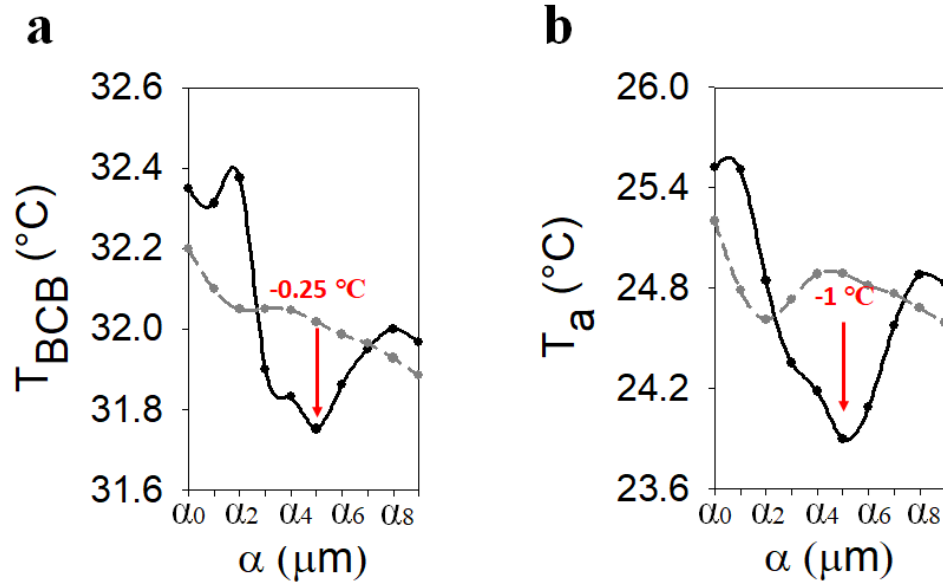


Figure 3.26: Evolution, for a fixed skin temperature $T_s = 34^{\circ}\text{C}$, of (a) the temperature of the membrane $T_{BCB} = T_1 = T_2$ and (b) the ambient temperature as a function of the scaling factor α_i for a structured (solid lines) and non-structured (dashed lines) membrane.

Another way to demonstrate the efficiency of the structuration is to represent the ambient temperature as a function of the scaling factor (Figure 3.26 (b)). This representation allows to compare the necessary temperature of the room to keep the thermal comfort of the human body. For the design α_5 , the calculated ambient temperature can be up to 1°C lower for the structured membrane as compared to the non-structured one. This property offers the opportunity of maintaining the individual comfort while reducing the external energy supply of the room. Therefore, a lower ambient temperature will be sufficient to provide the same comfort.

We also calculated the set of temperatures (T_1 , T_2 , T_a) for different skin temperatures lower than 34°C (see table 3.5).

T_s ($^{\circ}\text{C}$)	30		32		34	
(Membrane)	(unstruct.)	(struct.)	(unstruct.)	(struct.)	(unstruct.)	(struct.)
T_1 ($^{\circ}\text{C}$)	27.9	27.7	29.9	29.7	32.0	31.7
T_2 ($^{\circ}\text{C}$)	27.9	27.7	29.9	29.7	32.0	31.7
T_a ($^{\circ}\text{C}$)	20.6	19.6	22.7	21.7	24.8	23.8

Table 3.5: Calculated temperatures (T_1 , T_2 , T_a) for different skin temperature, lower than 34°C , for the unstructured (unstruct.) and structured (struct.) membranes associated to α_5 ($P = 11\text{ }\mu\text{m}$, $D = 8.6\text{ }\mu\text{m}$ and $h = 6.3\text{ }\mu\text{m}$).

The data of table 3.5 have been reported on figure 3.27 which shows the evolution of the skin temperature as a function of the ambient temperature for the structured and unstructured membrane. One can clearly see that the temperature of the skin is systematically almost 1°C higher when the human body is clothed with the structured membrane. It demonstrates the heating capacity of the photonic membrane. A variation of 1°C would thus lead to a significant reduction in energy consumption, which represents a positive impact, both economically and in terms of environment.

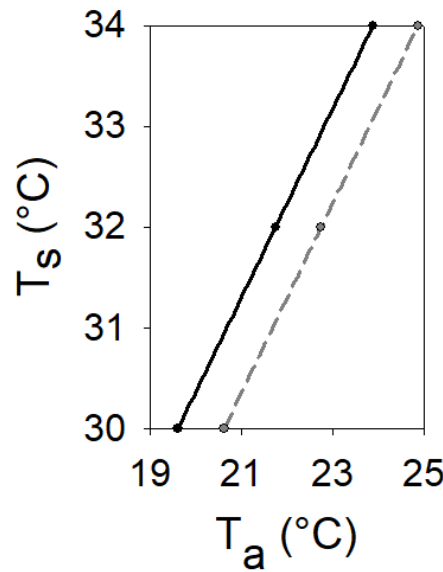


Figure 3.27: Evolution of the skin temperature as a function of the ambient temperature for the structured (solid line) and unstructured (dashed line) membrane associated to α_5 ($P = 11 \mu\text{m}$, $D = 8.6 \mu\text{m}$ and $h = 6.3 \mu\text{m}$).

III.4.3.2 Effect of the thickness on the thermally conductive structured membrane

Figure 3.28 shows the temperature progression of T_{BCB} and T_a , starting from the scaling factor α_4 ($D = 7.9 \mu\text{m}$, $P = 10 \mu\text{m}$ and $h = 5.7 \mu\text{m}$), as a function of the thickness of the membrane, ranging from $3 \mu\text{m}$ to $11 \mu\text{m}$. One can see that, for a fixed skin temperature $T_s = 34^{\circ}\text{C}$, the minimum of both the membrane and the ambient temperatures occurs for thicknesses between 5 and $7 \mu\text{m}$.

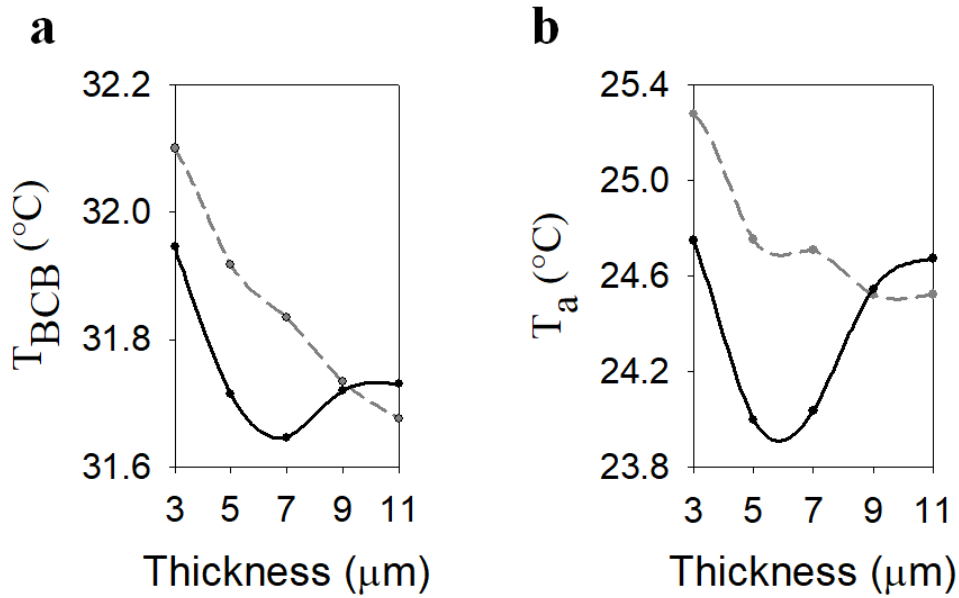


Figure 3.28: Temperature progression, for a fixed skin temperature $T_s = 34^{\circ}\text{C}$, of (a) the membrane $T_{BCB} = T_1 = T_2$ and (b) the ambient temperature T_a as a function of the thickness for a structured (solid lines) and non-structured (dashed lines) membrane.

III.4.3.4 Effect of holes diameter for the thermally conductive BCB membrane

In figure 3.29 (a) and (b), we report the temperature progression T_{BCB} and T_a as a function of the diameter of the holes, for $P = 10 \mu\text{m}$ and $h = 5.7 \mu\text{m}$. We compared the temperature of the structured membrane (solid line) with the non-structured one (dashed line). When the diameter increases from $D = 1 \mu\text{m}$ to $D = 8 \mu\text{m}$, the temperature drops, from 31.9°C to 31.7°C for T_{BCB} and drops from 24.7°C to 24°C for T_a , before increasing. There is a diameter D of $7 \mu\text{m}$ which allows a minimum ambient temperature value. This value is different from that of α_4 . Thus, for a fixed skin temperature $T_s = 34^{\circ}\text{C}$, we can have a lower T_a , value by using a hole diameter of $7 \mu\text{m}$ instead of $7.9 \mu\text{m}$.

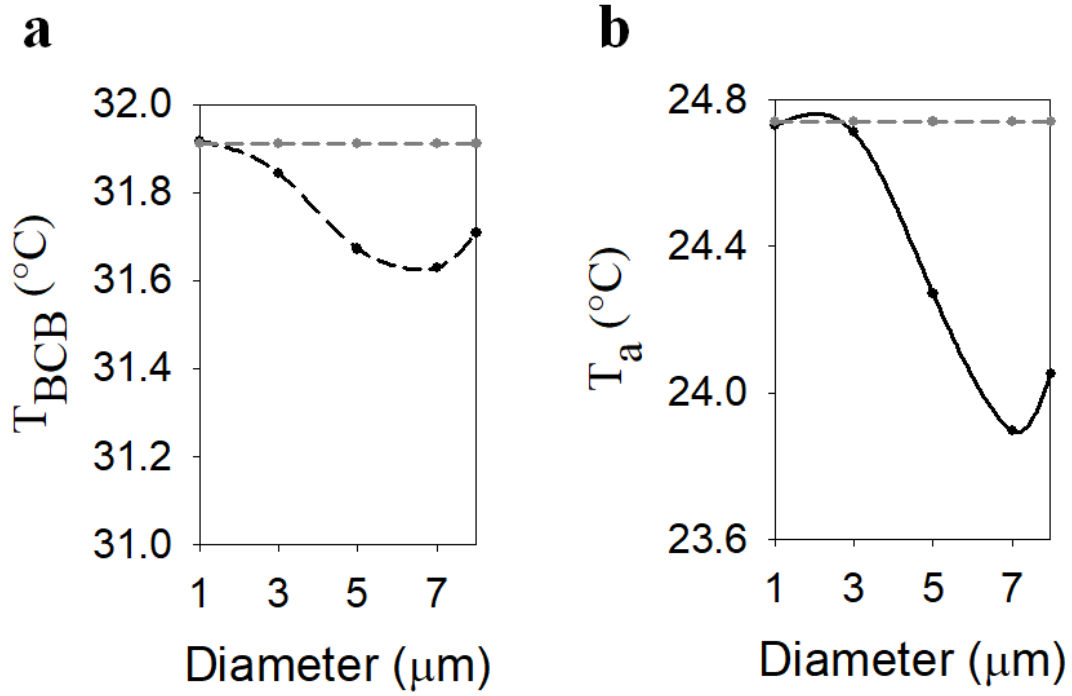


Figure 3.29: Temperature of (a) the membrane T_{BCB} and (b) the ambient temperature T_a as a function of the diameter D with $P = 10 \mu\text{m}$, $h = 5.7 \mu\text{m}$ for a structured (solid lines) and non-structured (dashed lines) membrane (for a fixed skin temperature $T_s = 34 \text{ }^\circ\text{C}$).

III.4.3 Effect of moisture on the thermally conductive BCB membrane

Finally, to complete our study of the thermally conductive membrane, we evaluate the effect of humidity on the thermal response of the membrane, for a set of geometrical parameters ($P = 10 \mu\text{m}$, $D = 7.9 \mu\text{m}$, $h = 5.7 \mu\text{m}$).

Figure 3.30 presents the evolution of the temperatures, T_{BCB} and T_a as a function of the refractive index of the microclimate and holes media n' by fixing the temperature of the skin at $T_s = 34 \text{ }^\circ\text{C}$.

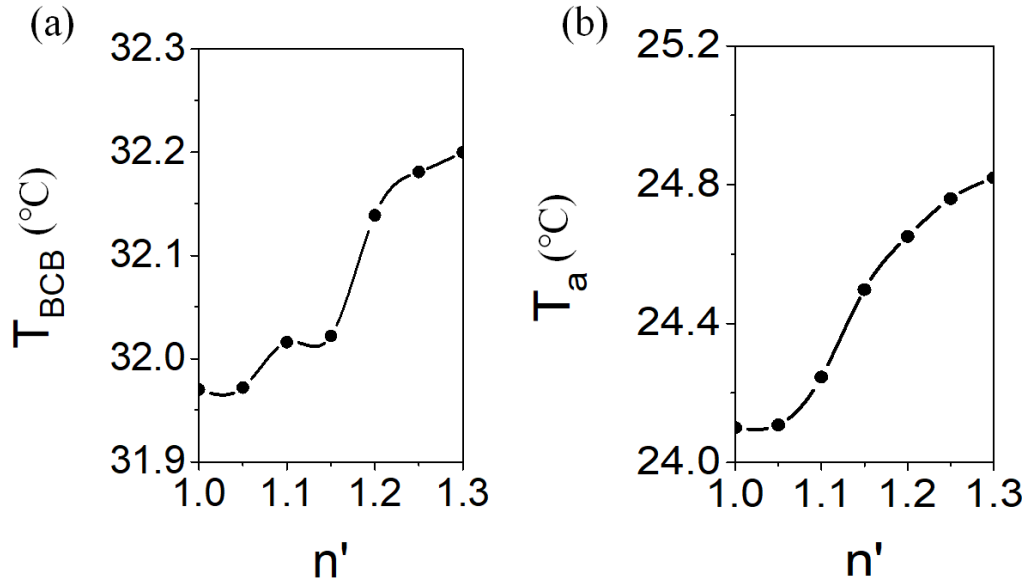


Figure 3.30: Temperature of (a) the membrane T_{BCB} and (b) the ambient temperature T_a as a function of the refractive index of the microclimate and holes media n' .

When the index n' increases, the calculated membrane and ambient temperature increase as well. It means that the presence of humidity decreases the efficiency of the membrane.

III.5 First experimental demonstration

The first experimental demonstration was carried out by Maud Viallon during her thesis, where Benzocyclobutene (BCB) polymer was used for membranes fabrication [5]. The process for the fabrication of the structured membrane and the encountered difficulties are briefly summarized as follows. First, a layer of BCB is deposited on a silicon substrate using spin coating before being transferred on the thermal plate for curing. Then, a second run is completed to structure the membrane into a network of holes using UV photolithography, followed by reactive ion etching (RIE). It appears to be too difficult to release the membrane and also to obtain a network with the good dimensions by etching the BCB on 10 μm thickness, so the thickness of the BCB membrane was reduced to 4 μm . During the release of the membrane, it has been observed a detachment at the edges of the structured zones of the sample, which may be due to the relaxation of the intrinsic stresses of the membrane. This detachment (from the silicon substrate) makes manipulation of the membrane difficult. Maud Viallon concluded that the BCB did not appear to be the appropriate polymer, but in principle, her work validated the effect of structuring on optical properties in the

mid-infrared [5]. We have taken up this finding and developed it further to extend to thermal effects, as discussed in the previous chapter.

Conclusion

In this chapter, we studied a polymer membrane made of Benzocyclobutene (BCB), based on the first experimental demonstration done by Maud Viallon during her PhD thesis [5].

Numerically, we started with the study of the transmission, reflection and absorption properties of the BCB polymer membrane in the mid-infrared domain. The BCB membrane presents both an absorbance and sufficient refractive-index contrast with air to deal with the photonic crystal properties, following a triangular array of air holes. Then we introduced a quantitative coefficient to estimate the transmission efficiency of human body emissivity through the photonic membrane. We found that membrane structuration leads to new features in spectral reflection, transmission and absorption spectra that have been identified as guided and localized modes of the photonic crystal membrane. We found that, by scaling the geometrical parameters of the crystal, transmission can be modulated by up to 28% of human body emissivity in the wavelength range $[7.5, 11.5] \mu\text{m}$. Also, we decoupled the different geometrical effects and discuss them by an independent variation of the geometrical parameters (D, h). We have seen that the transmittance of the membrane decreases with the diameter and the thickness of the membrane, in favor of absorption and/or reflection. Finally, we have presented the incidence angle and the perspiration effects on the spectra R, T and A .

Then, we investigated the optical properties on thermal balance analysis, applied between the human body and the surrounding environment, through the structured membrane. We worked on two cases (non-thermally and thermally conductive membranes). For the case of a non-conductive membrane, we found a difference between the inner and outer temperatures, despite the relative thinness of the membrane. We found that for a set of geometrical parameters ($P = 10 \mu\text{m}$, $D = 7.9 \mu\text{m}$, $h = 5.7 \mu\text{m}$) the non-conductive membrane behaves as a thermoregulator of the human body. Compared to a non-structured regular membrane of equivalent thickness, when the temperature of the room is low (20°C) the membrane behaves as a heater, increasing the temperature up to $+1^\circ\text{C}$. On the contrary, when the ambient temperature is high (40°C), it behaves as a cooler and decreases the temperature by -1°C . The equilibrium is obtained when the temperature is 28°C , which represents the working point of the photonic crystal membrane. Also,

it was essential to have a membrane smaller than $7\text{ }\mu\text{m}$ to preserve the diffusion properties for reflection and activate the thermoregulatory properties of the photonic membrane. In addition, we have concluded that the thermoregulation of the non-conductive photonic membrane was deactivated by the presence of moisture in the microclimate.

To propose a more realistic model, we introduced the conductivity of the membrane. Due to the thinness of the membrane, we found that the inner and outer temperatures were the same. We found that, for a set of geometrical parameters ($P = 11\text{ }\mu\text{m}$, $D = 8.6\text{ }\mu\text{m}$, $h = 6.3\text{ }\mu\text{m}$), compared to a non-structured regular conductive membrane of equivalent thickness, the temperature of the room needs to be systematically almost 1°C less when the human body is clothed with the structured membrane in order to get the same thermal comfort ($T_s = 34^{\circ}\text{C}$).

To support production of such polymer membranes for textile applications, thermal and optical properties of several types of polymers will be studied in the next chapter. Our goal will be to choose the optimal polymer for the fabrication of a photonic polymer membrane in a cleanroom setting.

References

1. Zhou D, Pennec Y, Djafari-Rouhani B, Cristini-Robbe O, Xu T, Lambert Y, et al. Optimization of the optical properties of nanostructured silicon surfaces for solar cell applications. *J Appl Phys.* 2014; 115:134304.
2. Oğulata RT. The effect of thermal insulation of clothing on human thermal comfort. *Fibres & Textiles in Eastern Europe*, 2007 ;15: 61.
3. Tong JK, Boriskina S. Cambridge, MA (US) @ (72) Inventors: Gang Chen, Carlisle ,MA (US); :49.
4. Pinel S, Marty A, Tasselli J, Bailbe J-P, Beyne E, Van Hoof R, et al. Thermal modeling and management in ultrathin chip stack technology. *IEEE Trans Compon Packag Technol.* 2002; 25:244–53.
5. Viallon M. Réalisation et caractérisation de membranes polymères microstructurées capables de moduler leurs propriétés de réflexion dans le domaine du moyen infrarouge : application aux textiles pour le confort thermique (Doctoral dissertation, Lille 1). 2017.

Chapter IV:

Ideal polymer for personal thermoregulation

Introduction:

In the previous chapter, we have theoretically investigated the effect of reflection, transmission and absorption of a BCB polymer-based photonic membrane on human body emissivity at 34 °C (i.e. in the mid-infrared range). We were able to demonstrate the thermoregulation effects of the photonic crystal membrane using the results of thermal balance analysis. In this chapter, we will introduce and address two new main issues.

The first is to quantitatively analyze a set of different polymers, chosen for their compatibility with textile applications (i.e. membranes of a few tens of microns which can be produced as textiles, possibly through structuration and textile lamination) and discuss the effect of their nature on their optical and thermal properties. We will study numerically the influence of the geometry of unstructured and structured membranes of four regular polymers (PDMS, PI, PE and PET) on the reflection, transmission and absorption spectra. To accomplish this, we will couple the polymer's optical properties with the thermal balance analysis applied between the human body and the surrounding environment.

The second focus of this chapter is an initial approach to experimentally implementing one of the four polymer materials previously detailed. The experimental work for membrane fabrication will be done in the IEMN clean room and tested with FT-IR measurements at the engineering school HEI.

The objective of this chapter is to identify the impact of the optical properties (especially the absorption) of different photonic membranes in polymers and their benefit on personal thermoregulation, in order to establish their viability for use in textiles.

IV.1 Optical analysis of usual polymers in textile

As mentioned in conclusion of chapter 3, since we faced difficulties in releasing and manipulating the BCB membrane, this polymer did not appear to be the appropriate candidate for an experimental proof of concept for textile applications. Therefore, we are looking to replace BCB polymer with a more appropriate polymer for experimental demonstration of personal thermoregulation utility.

To analyze the impact of the optical properties of polymers we propose to study the influence of the geometry of an unstructured and a structured membrane of four usual polymers (PDMS, PI, PE and PET) on the reflection, transmission and absorption spectra.

IV.1.1 Choice of polymers

The selected polymers can be classified into two groups, the first being polymers frequently used in clean room manufacturing (microfabrication) and including PDMS and PI, and the second being polymers currently used in the field of textiles (including PET and PE). Collectively, these polymers cover a wide range of optical properties (more or less absorbent) in the mid-infrared.

IV.1.1.1 Polydimethylsiloxane (PDMS)

PDMS polymer is widely used in microfabrication and particularly recommended for its low cost, its extreme flexibility and its hydrophobicity. Even if this polymer is not directly used by the textile industry, it could be used to obtain a proof of concept for our application by developing self-supporting membranes or laminated to textiles. Indeed, it can be coated to membranes of thickness from few to several hundreds of micrometers. It can also be molded and shaped by photolithography [1]. This polymer is commonly used in the BioMems group at IEMN, especially in the applications related to:

- Microfluidic system for the electrical detection of parasites [2],
- Flexible microsystems and electronics [3],
- Superomniphobic surfaces [4].

IV.1.1.2 Polyimide (PI)

In technology processes, polyimide (PI) membranes have already been used for a long time and in a wide variety of applications. PI is an excellent polymer to prepare membranes because of its outstanding heat resistance and good mechanical strength, as well as its chemical resistance to many solvents. More recently, the concept of crosslinking PI membranes has become very popular [5]. This polymer is used by the MITEC group at IEMN, especially in applications related to its thermoelectric properties [6,7].

The challenge with using this polymer will be to find a method for developing a self-supporting membrane that validates our study.

IV.1.1.3 Polyethylene (PE)

Nowadays, one of the most widely used polymer in the industry and the simplest synthetic polymers is the Polyethylene (PE). Repeating Ethylene monomer, with a total length that can vary relying on the molecular weight, forms the chemical structure of polyethylene. Woven polyethylene fabrics are often used in tarpaulins, geotextiles and taps for textile applications [8]. Nevertheless, manufacturing PE is not so obvious. The structuration will need solvent with high boiling point (160°) like toluene, xylene, trichlo, decaline. The solutions must be dispensed on a hot substrate during the spin-coating.

IV.1.1.4 Polyethylene terephthalate (PET)

A great deal of attention has been attracted to Polyethylene terephthalate PET for its use in numerous applications and industrial fields, such as data storage, in food and pharmaceutical packing, high performance polarization optics, sutures, artificial vascular grafts, recording media and optoelectronic devices, and as well in artificial heart valves [9,10].

PET is used in the production of flexible electronic devices by large scale manufacturing processes, such as solar cells and flexible displays [11,12]. This polymer is not available in our lab but can be provided by the University of Mons, partner in the Interreg PHOTONITEX project.

We will start with a comparison of the real and imaginary parts of the refractive index of the selected polymers.

IV.1.2 Refractive index of polymers

For PDMS polymer, we retrieved the oscillator parameters in the mid-infrared from the work of A. Srinivasan et al. [13]. We then used the Lorentz-Drude model (described in Chapter II) with 15 oscillators, and reported the results in table 4.1 to define the real and complex variations of the refractive index of PDMS polymer in the mid-infrared.

$\varepsilon_{\infty} = 2.276$			
i^{th} oscillator	$\nu_{pi} \text{ (rad/s)} \times \sqrt{10^{11}}$	$\nu_{oi} \text{ (rad/s)} \times 10^{14}$	$\Gamma_i \text{ (rad/s)} \times 10^{12}$
1	$\sqrt{2.35}$	1.1197	2.36
2	$\sqrt{3.6}$	1.24	1.82.
3	$\sqrt{3.95}$	1.28	3.9
4	$\sqrt{1.87}$	1.32	5.98
5	$\sqrt{2.99}$	1.42	1.38
6	$\sqrt{1.37}$	1.5	3.59
7	$\sqrt{2.78}$	1.58	2.92
8	$\sqrt{2.24}$	1.63	2.24
9	$\sqrt{5.59}$	1.94	2.95
10	$\sqrt{2.4}$	2.04	7.67
11	$\sqrt{2.06}$	2.37	1.446
12	$\sqrt{1.32}$	2.65	2.7
13	$\sqrt{1.3610^{11}}$	2.73	6.88
14	$\sqrt{2}$	5.51	2.89
15	$\sqrt{3.34}$	5.57	2.78

Table 4.1: Physical parameters of the PDMS photonic membrane

For PI, PE and PET, we used the variations of the real and the imaginary part of the refractive index in the wavelength range between [5-15] μm , found in the work of Z.M. Zhang *et al.* JK Tong *et al* and A. Laskarakis *et al.* [14,15,16].

Figure 4.1 below shows the refractive index components of the usual polymers PE, PI, PET and PDMS respectively (real (n_{PE} , n_{PI} , n_{PET} , n_{PDMS}) and imaginary (k_{PE} , k_{PI} , k_{PET} , k_{PDMS}) parts) as a function of the wavelength.

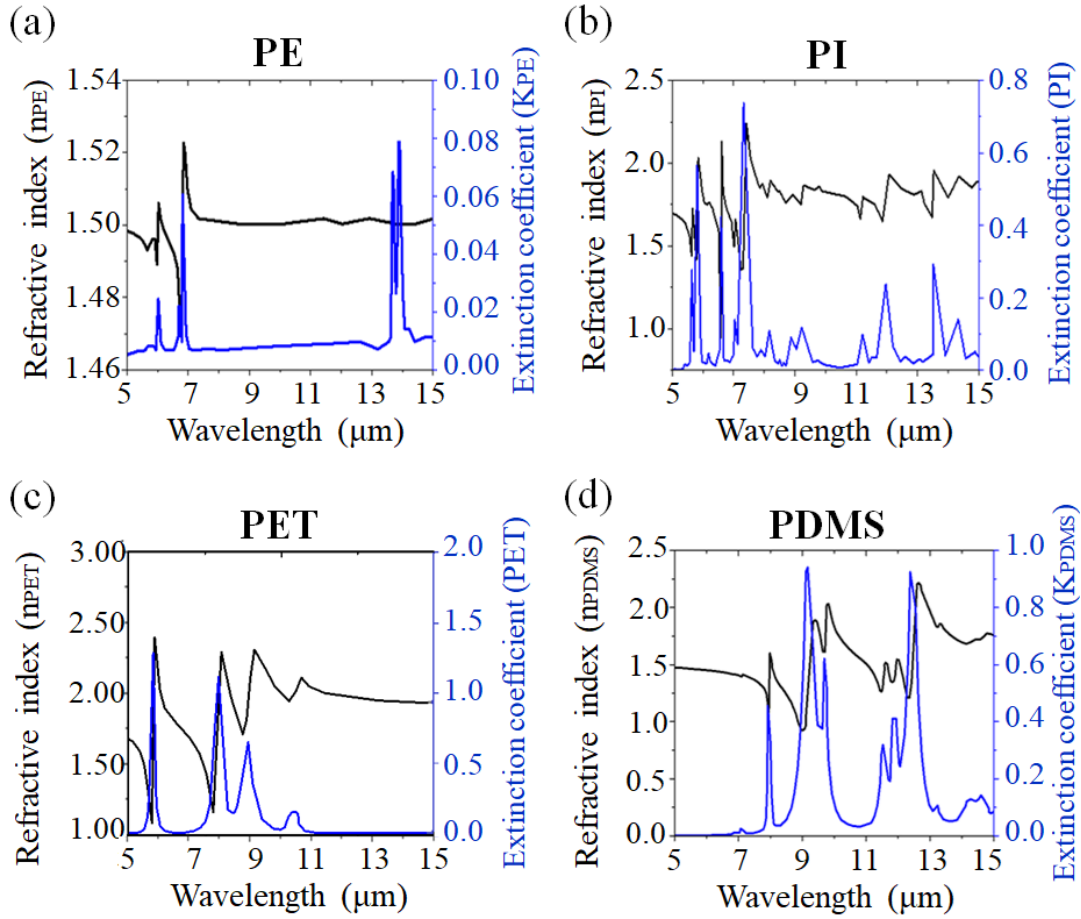


Figure 4.1: Representation of the refractive index components of (a) polyethylene (PE), (b) polyimide (PI), (c) polyethylene terephthalate (PET) and (d) polydimethylsiloxane PDMS polymer (real (n_{PE} , n_{PI} , n_{PET} , n_{PDMS}) and imaginary (k_{PE} , k_{PI} , k_{PET} , k_{PDMS}) parts) as a function of the wavelength in the MIR range.

The average of the real part of the refractive index is around $n_{PE} \sim 1.5$ for PE and $n_{PDMS} \sim 1.54$ for PDMS, close to the BCB ($n_{BCB} \sim 1.56$). PI and PET have higher values, around ~ 1.76 and ~ 1.9 respectively.

For PE, the average extinction coefficient is very low ($k_{PE} \sim 0.01$), especially in the range [7.5-11.5] μm. PI has a high extinction coefficient for wavelengths lower than 7.7 μm, which becomes low for higher wavelength, typically around ($k_{PI} \sim 0.04$). For PDMS, k_{PDMS} presents a high value (~ 0.2) between [7.5-11.5] μm. Finally, for the PET, k_{PET} is high (~ 0.3) between [7.5-11.5] μm.

Table 4.2 summarizes the characteristics of each polymer regarding our application: average of the real part of the refractive index, absorption capacity, suitability for textiles, and feasibility of manufacturing the polymer in a cleanroom.












	Real refractive index In MIR	Absorption capacity In MIR	Feasibility of manufacturing	Suitability for textiles
PE	Low	Lower		 
PI	High	Low		
PDMS	Low	High	 	
PET	Higher	Higher		 

Table 4.2 : Summary of PE, PI, PDMS, PET characteristics: real refractive index, absorption capacity, suitability for textiles, and feasibility of manufacturing.

These four polymers offer a large diversity of optical characteristics, providing a great opportunity to analyze the relation between the refractive index, the optical responses and the thermal behaviors.

IV.1.3 Study of polymer membranes

IV.1.3.1 Optical spectra

In this section, we study the influence of the geometry of an unstructured and structured membrane of the four selected polymers on the reflection (R), transmission (T) and absorption (A) spectra.

Figure 4.2 presents the effect of the structuration of PE, PI, PET and PDMS membranes following the scaling factors α_i . The calculated reflection, transmission and absorption spectra of these four polymer membranes, with three scaling factors α_1 ($P = 7 \mu\text{m}$, $D = 5.5 \mu\text{m}$, $h = 4 \mu\text{m}$), α_5 ($P = 11 \mu\text{m}$, $D = 8.6 \mu\text{m}$, $h = 6.3 \mu\text{m}$) and α_7 ($P = 13 \mu\text{m}$, $D = 10.2 \mu\text{m}$, $h = 7.4 \mu\text{m}$), are shown in figure 4.2.

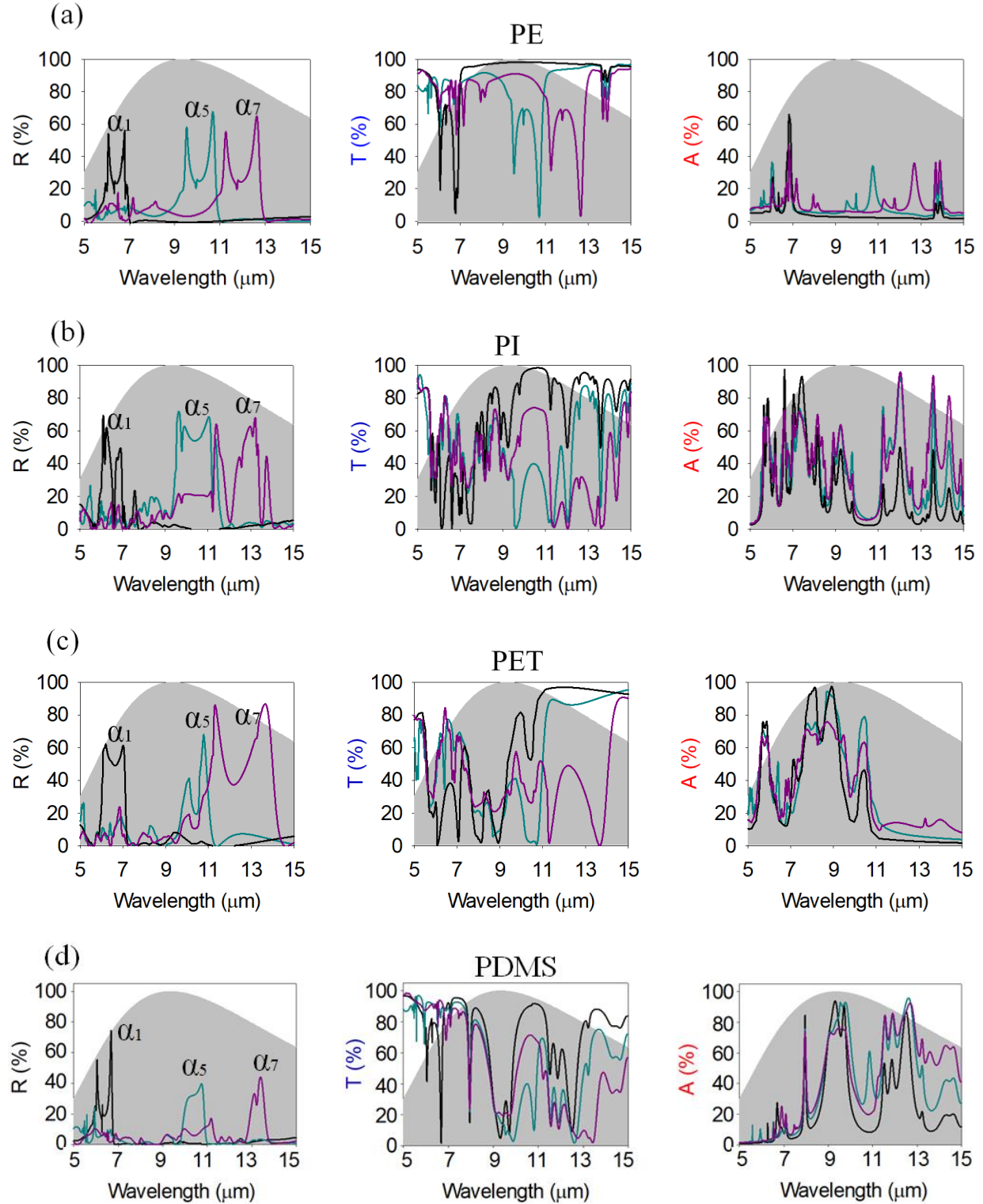


Figure 4.2: Evolution of the reflection (R), transmission (T), and absorption (A) coefficients as a function of the wavelength in the mid-infrared for four photonic polymer membranes (a) PE, (b) PI (c) PET and (d) PDMS, designed following the scaling factor α_1 , α_5 and α_7 .

For PE (Figure 4.2 (a)), the reflection spectrum shows that, as for BCB (chapter III), the structuration of the membrane introduces double reflection peaks that shift to high wavelength when increasing the size of the geometrical parameters. In the transmission spectra, one can follow their signatures corresponding to the different dips. The double transmission dips cross the human body emissivity toward the high wavelength when α_i increases, thus altering deeply the transmission of the incident wave. From the point of view of the absorption, the situation is not so obvious. Nevertheless, one can observe that the peaks of absorption varies in amplitude as a function of α_i .

For PI (Figure 4.2 (b)) and PET (Figure 4.2 (c)), one can see from the reflection spectrum, that the double peaks also appear, with different level of amplitudes. From the transmission spectra, the main effect of the α_i coefficient appears in the wavelength range [9, 11] μm (PI) and [9, 15] μm (PET). It means that the structuration also clearly affects the transmission for these two polymers. From the absorption spectra, the effects are again not so obvious.

For PDMS (Figure 4.2 (d)), the amplitude of the peaks of reflection for the scaling α_5 and α_7 , decreases drastically compared to the previous polymers. This main be due to the presence of significant absorption peaks in the corresponding wavelength area.

Comparing all spectra, one can keep in mind that a local modulation of both the reflection and the transmission is efficient as far as the absorption is not important.

IV.1.3.2 Efficiency coefficient

To complete the analysis, we report in figure 4.3 the evolution of the efficiency coefficient η in reflection R (black line), transmission T (blue line) and absorption A (red line) as a function of the scaling factors α_i . Looking at the dashed lines representing the non-structured membrane of equivalent thickness, one can see that the average level of the transmission is around 87.5% for PE, 60% for PI, 29.5% for PET and 56% for PDMS. In parallel, the average level of the absorption (red dashed lines) is respectively 6% (PE), 26% (PI) 56% (PET) and 48.3% (PDMS) while the reflection is around 6.5% (PE), 13% (PI) 14.5% (PET) and 6 % (PDMS). With respect to the refractive index of the involved materials, one can remark that such evolution is in close agreement

with the variation of the refractive index. The reflection follows the real part of the refractive index while the absorption depends on its imaginary part.

In the previous chapter, we have seen that the structuration of the BCB membrane, compared to the non-structured one, offers the possibility to modulate the optical properties. Now, if we fix the geometrical parameters of the photonic crystal to α_5 , we can modulate the transmission curves (see the variation between the solid and the dashed lines) (Figure 4.3). The amplitude of this modulation depends clearly on the properties of the polymer. When the polymer is weakly absorbent with a low refractive index (*e.g.* PE, $n_{PE} \sim 1.5$) the decrease in transmission is caused solely by reflection. The transmission coefficient drops from 88.6% to 77.3%, representing a small variation of 11.3% when compared to a non-structured membrane with the same thickness. When we introduce some absorption with a high refractive index (*e.g.* PI, $n_{PI} \sim 1.76$), the decrease in transmission comes from both absorption and reflection. This leads to a large transmission variation of 21.5%. Finally, in cases where the polymer is highly absorbent (*e.g.* PET and PDMS), the modulation effect of structuration on the transmission level is weak in comparison to the other polymers. The four polymers can be characterized by the following absorption efficiency coefficient, reported for α_5 :

$$\eta_A(PE) = 10\%;$$

$$\eta_A(PI) = 30\%;$$

$$\eta_A(PDMS) = 51\%$$

$$\eta_A(PET) = 60\%$$

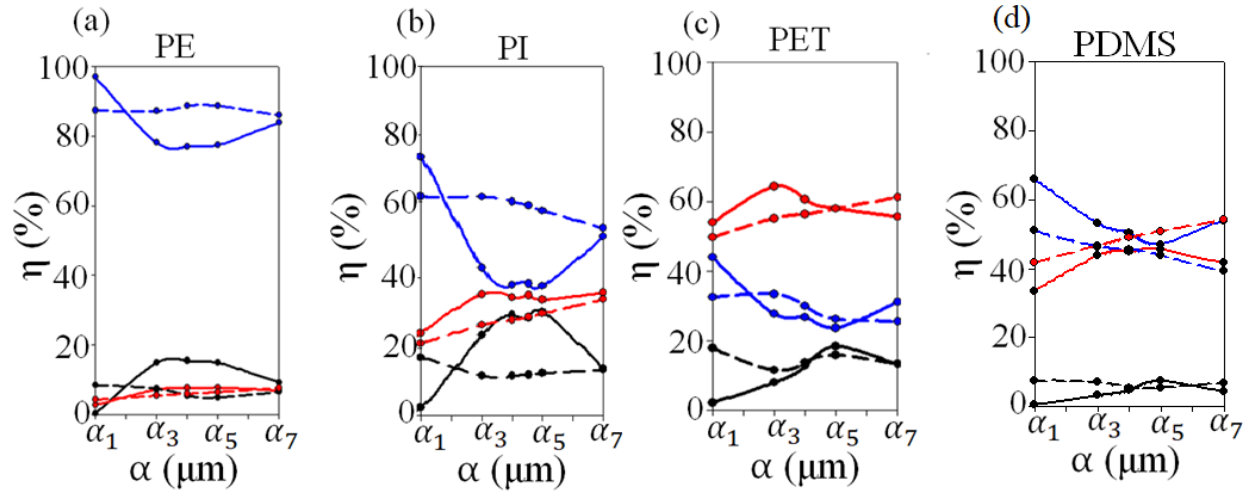


Figure 4.3: Evolution of the efficiency coefficient η , associated to the reflection (black), transmission (blue), absorption (red) responses of the non-structured (dashed lines) and structured (solid lines) (a) PE, (b) PI, (c) PET and (d) PDMS membrane as a function of the scaling factor α_i .

As a first conclusion, for membrane structuration to have its maximum effect, it is necessary to choose a polymer with optical properties including a high refractive index so that it has low absorption in the mid-infrared domain.

IV.2 Thermal response of the polymers

We now turn to the analysis of the thermal behavior of the four selected polymers. The investigation is based on the thermal balance equations, considering the heat conduction through the membrane (eq. (III.12), (III.13) and (III.15), chapter III).

Before examining the structured membrane, we first calculate the temperatures of unstructured PE, PI, PET and PDMS membranes (dashed lines, figure 4.4) and the indoor room (dashed lines, figure 4.5) as a function of membrane thickness. Those temperatures have been calculated to keep the skin temperature at $T_s = 34^\circ\text{C}$, corresponding to the thermal comfort temperature for the human body (see table 4.3). The thicknesses have been associated to the scaling factor α_i .

		PE		PI		PDMS		PET	
α_i	h (μm)	T_{PE} ($^{\circ}\text{C}$)	T_a ($^{\circ}\text{C}$)	T_{PI} ($^{\circ}\text{C}$)	T_a ($^{\circ}\text{C}$)	T_{PDMS} ($^{\circ}\text{C}$)	T_a ($^{\circ}\text{C}$)	T_{PET} ($^{\circ}\text{C}$)	T_a ($^{\circ}\text{C}$)
$\alpha_1 = 1.0$	4.0	32.1	24.8	31.7	23.9	31.4	24.0	30.8	22.5
$\alpha_3 = 1.28$	5.1	32.1	24.9	31.7	24.2	31.3	23.9	30.8	22.9
$\alpha_4 = 1.42$	5.7	32.1	25.0	31.6	24	31.3	23.9	30.8	22.6
$\alpha_5 = 1.56$	6.3	32.1	25.0	31.6	23.8	31.2	23.9	30.6	22.3
$\alpha_7 = 1.56$	7.4	32	24.9	31.5	24.1	31.1	23.6	30.6	22.5

Table 4.3: Calculated membrane and ambient temperatures for PE,PI,PDMS and PET non-structure membranes for different thicknesses at skin temperature $T_s = 34^{\circ}\text{C}$.

The average temperature depends on the polymer and one can observe that the temperature is negatively correlated with the absorption coefficients. Indeed, the average ambient temperature can be classified as:

$$T_a(PE) = 24.9^{\circ}\text{C} > T_a(PI) = 24^{\circ}\text{C} > T_a(PDMS) = 23.8^{\circ}\text{C} > T_a(PET) = 22.5^{\circ}\text{C}$$

And, as reported before for α_5 :

$$\eta_A(PE) = 10\% < \eta_A(PI) = 30\% < \eta_A(PDMS) = 51\% < \eta_A(PET) = 60\%$$

This means that the more absorbent the membrane is, the lower the ambient temperature can be while still maintaining thermal comfort at 34°C body temperature.

Moving now to the structured membrane, the solid lines in Figures 4.4 and 4.5 represent the evolution of the temperatures as a function of α_i . For PE and PI, the structuration decreases the temperatures in comparison with the unstructured membranes. For PET, the temperatures are almost the same while for PDMS, the temperatures of the structured membrane are higher than the unstructured one.

In perspective of decreasing the room temperature, the PE and PI offer the more efficient result. With the scaling factor α_5 the ambient temperatures decreases, by (-0.77°C) for PE and by (-2°C) for PI. It means that the PE and PI structured membranes are advantageous, as they provide thermal comfort ($T_s = 34^{\circ}\text{C}$) at lower ambient temperatures.

Looking at the trend between PE, PI, PET and PDMS, it appears that the relationship between the ambient temperature and the optical properties of the polymers is not obvious, depending on both the real and imaginary parts of the refractive index. A more in-depth and systematic study on the relationship between these two physical parameters should be carried out. This work is actually on going.

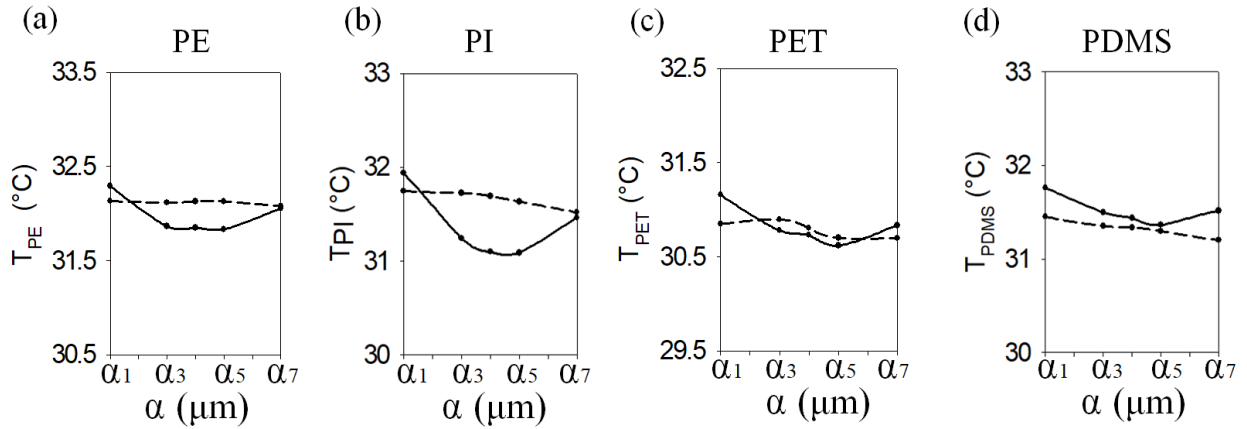


Figure 4.4: Evolution of the temperature of the membrane for (a) PE, (b) PI, (c) PET and (d) PDMS as a function of the scaling factor α_i for a structured (solid lines) and non-structured (dashed lines) membrane, to keep the skin temperature at 34°C .

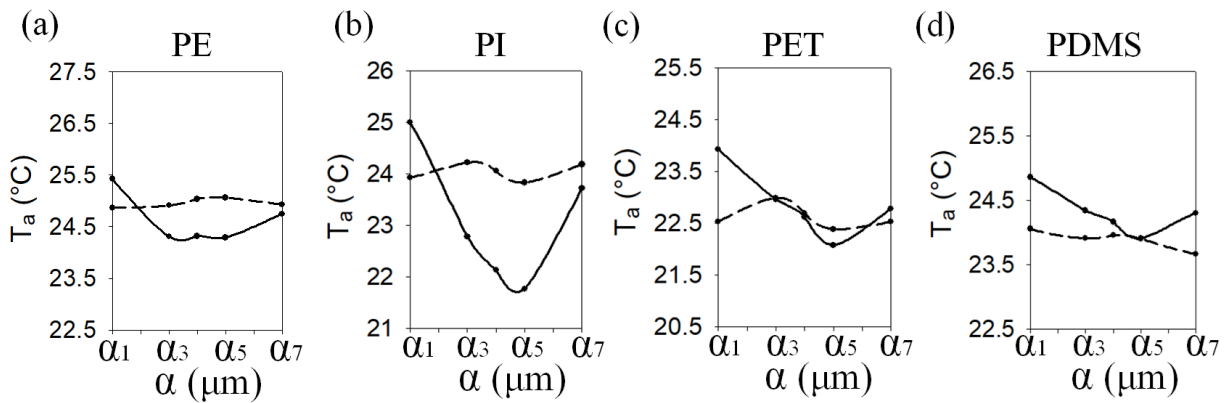


Figure 4.5: Evolution of the ambient temperature as a function of the scaling factor α_i for a structured (solid lines) and non-structured (dashed lines) membrane for (a) PE, (b) PI, (c) PET and (d) PDMS to keep the skin temperature at 34°C .

To emphasize the latter results, the figure 4.6 shows the progression of skin temperature as a function of the ambient temperature for the PE, PI, PET and PDMS. These calculations are performed for the scaling factor α_5 . For PE (resp. PI) one can clearly see the 0.77°C (resp. 2°C) temperature shift between the structured and unstructured membranes. Looking at PI, if the ambient temperature is 22°C, the structured membrane will produce a thermal comfort of 34°C while the non-structured membrane will need an ambient temperature of 24°C to get the same thermal comfort. On the other hand, for an ambient temperature of 22°C, the structured membrane will produce a thermal comfort with $T_s = 34^\circ\text{C}$ while the non-structured one will deliver a cold discomfort with a $T_s = 32^\circ\text{C}$.

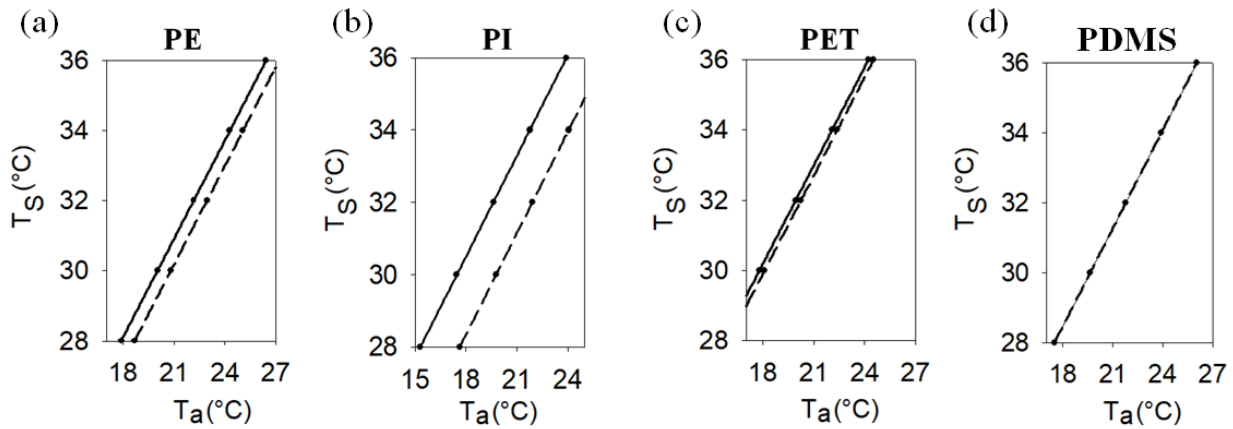


Figure 4.6: Evolution of the skin temperature as a function of the ambient temperature for the structured (solid line) and unstructured (dashed line) membranes for PE, PI, PET and PDMS.

Then, we have represented figure 4.7 the progression of skin temperature as a function of the ambient temperature for the scaling factors α_1 to highlight the effect of structuration for the PDMS membrane. One can see that, for a given ambient temperature, the skin temperature for the structured membrane is systematically almost 1°C lower than the non-structured one. This demonstrates that the structuration is effective when the outside temperature is hot as it reduced the temperature of the skin.

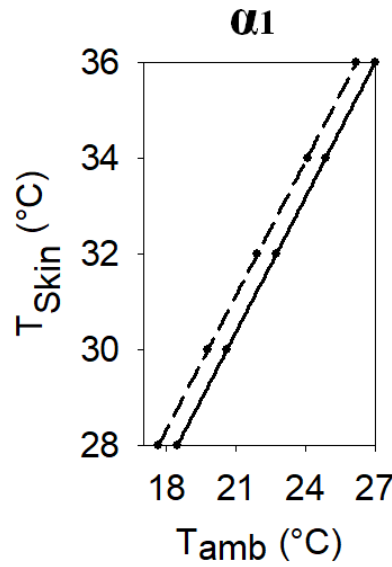


Figure 4.7: Evolution of the skin temperature as a function of the ambient temperature for the structured (solid line) and unstructured (dashed line) membrane for α_1 .

Therefore, conversely to PI, the structuration of the PDMS can be used to reduce energy consumption for cooling applications.

Figure 4.8 summarizes the skin temperature regarding the room temperature for all polymers studied through the manuscript. In this figure, we report the behavior of the unstructured membrane. We also report the behavior of the structured PI membrane for a set of geometrical parameters ($P = 11 \mu\text{m}$, $D = 8.6 \mu\text{m}$, $h = 6.3 \mu\text{m}$). It appears that the PI offers the most amplitude of variation, from non-structured to structured membrane and cover the larger field of possibilities in the (T_s, T_a) diagram.

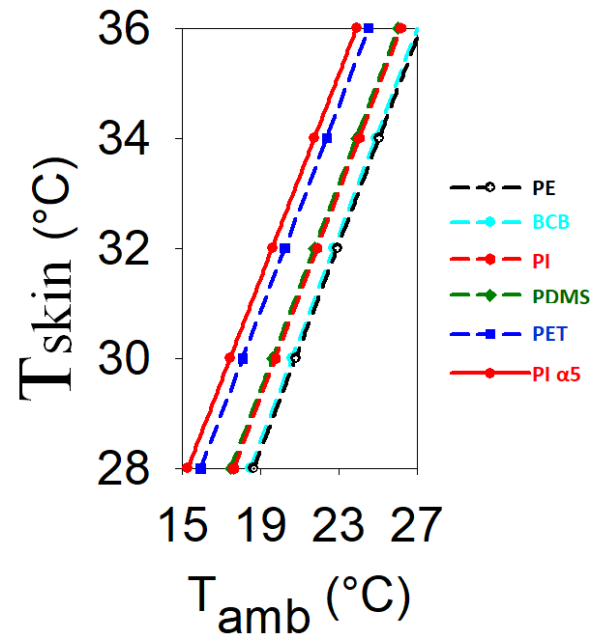


Figure 4.8: Evolution of the skin temperature as a function of the ambient temperature for the structured (PIs) (solid line) and unstructured membrane of BCB, PE, PI, PDMS and PET (dashed line).

We can conclude that the structured photonic membrane with the highest effect of structuration leads to the greatest temperature variation when compared with a non-structured polymer such as PI.

IV.3 Fabrication of PDMS polymer membrane

We are interested in testing a method to release a polymer membrane and perform its characterization by FT-IR spectroscopy in the mid- infrared in order to compare with the optical numerical calculations.

PDMS was one of the polymers available and easy to manufacture in the BioMems group. So the quickest solution to do this manipulation and to release a polymer membrane was through the PDMS.

IV.3.1 Method of manufacturing a thin PDMS membrane

It is not possible to manipulate a membrane of micrometric thickness, so it is necessary to have a physical support. The simplest method is to prepare a rigid and thick support manufactured in PDMS. Once the support is prepared, we then hollow out its center so that we can deposit a thin PDMS membrane which covers the hole.

All fabrication processes and measurements were performed in an ISO 5/7 cleanroom. PDMS samples were prepared using a commercially available kit (Sylgard 184, Dow Corning). The base and curing agent were mixed to a mass ratio of 10:1. Then the mixture was left in the vacuum box for half an hour until almost all the bubbles have disappeared from the solution. A hydrosilylation reaction makes it possible to form the PDMS solution (Figure 4.9 (a) and (b)).

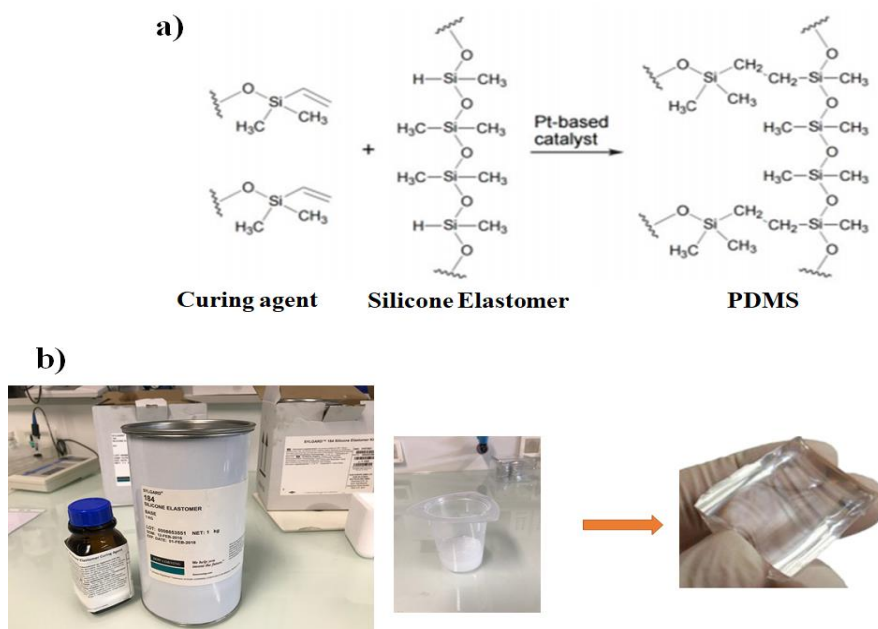


Figure 4.9: (a) Overall reaction of the PDMS synthesis. (b) Schematic process presenting the silicon elastomer mixed with the curing agent, to finally obtain a layer of PDMS after baking.

Figure 4.10 describes the different steps in the process to release the membrane. The numbering from {1} to {5} represents the steps of the following figure.

first, we prepared a hydrophobic silicon substrate which makes it possible to reduce the adhesion of the thin layer of PDMS on the substrate {1}. Then we deposit the PDMS solution on the hydrophobic substrate by spin coating followed by a curing treatment {2}. In parallel, we prepare a thick and rigid layer of PDMS as a support (the PDMS solution were left in the oven to become solid for 120 minutes at 70°C). Thereafter, we hollowed out in its center.

An oxidization by Corona treatment (type of atmospheric plasma surface treatment) is then carried out in order to increase the adhesion between the thin layer of PDMS and the rigid support of PDMS {3}. These latter were bonded and heated at 100°C during 30 minutes before removing the thin PDMS layer from the hydrophobic Si substrate {4}. Finally, the thin membrane layer covered the hole of the rigid support of PDMS {5}.

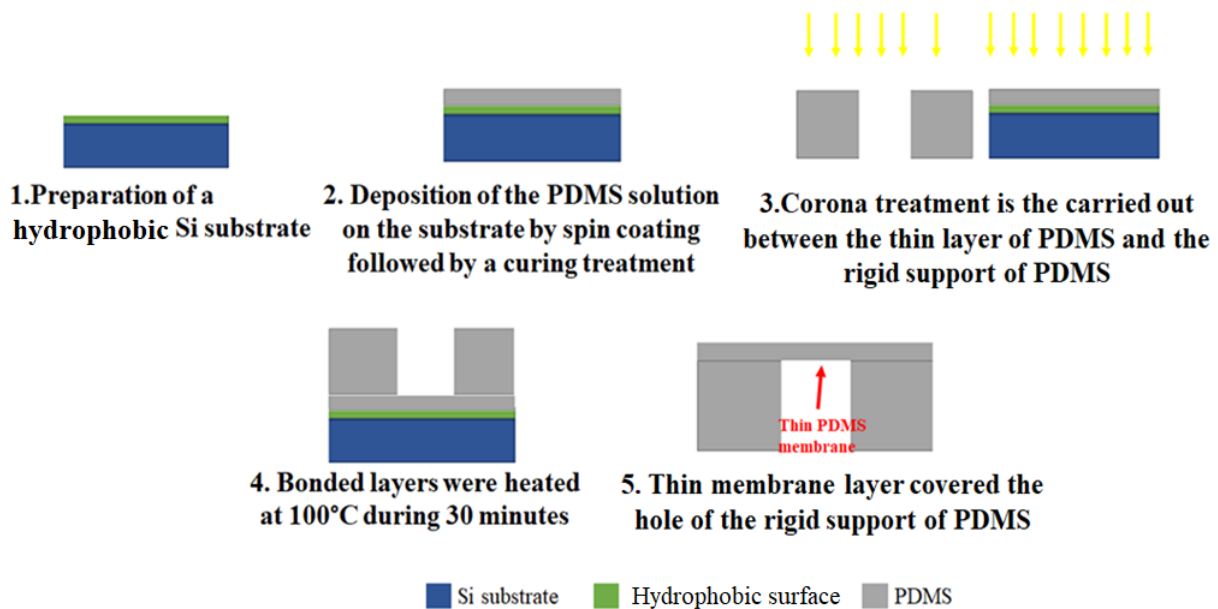


Figure 4.10: Schematic representation of the process for releasing a thin PDMS membrane.

Membranes of different thicknesses were fabricated, having a circular geometric shape with diameters of 1 and 2.5 cm. The thicknesses were measured with a reflectometer. The larger dimension is more suitable for characterization at the FT-IR (entrance port diameter of 2.3 cm described in chapter II) but they are more difficult to obtain for thin membrane thickness.

We have released three thin PDMS membranes of thicknesses 6 μm , 9 μm , and 12 μm .

The parameters used to obtain the different thicknesses of the PDMS are reported in table 4.4:

Parameters	Sample 1	Sample 2	Sample 3
Speed (RPM)	5000	3750	2500
Time (s)	300	300	300
Thickness (μm)	6	9	12

Table 4.4: Parameters of PDMS deposition for different thicknesses.

The PDMS membrane of thicknesses $6\ \mu\text{m}$ after release is shown in figure 4.11.

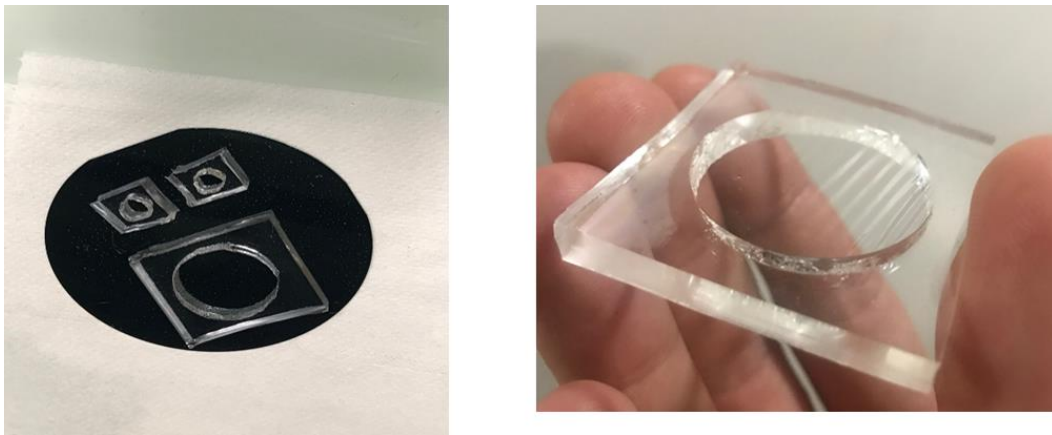


Figure 4.11: Image of the PDMS membrane after release.

IV.3.2 Comparaison of the FT-IR measurement and the simulation

Following the previous manufacturing process, we have released three thin PDMS membranes of thicknesses $6\ \mu\text{m}$, $9\ \mu\text{m}$, and $12\ \mu\text{m}$. The transmitted spectra measured using FT-IR spectroscopy are reported in figure 4.12 (solid lines) together with the theoretical calculation (dashed lines). We get a good agreement between the experimental and the theoretical calculations. We find zero

transmission dips in the wavelengths range between $[7.9-8.1] \mu\text{m}$, $[8.6-10.1] \mu\text{m}$ and $[11.2-13] \mu\text{m}$ (red arrows) which correspond to the absorption of the PDMS according to the extinction coefficients (see figure 4.1 (d)). However, some discrepancies exist, especially around $10 \mu\text{m}$. To have a better correspondence with the experiment, it would be necessary to modify the parameters of the oscillators describing the absorption and reported table 4.1 from the literature.

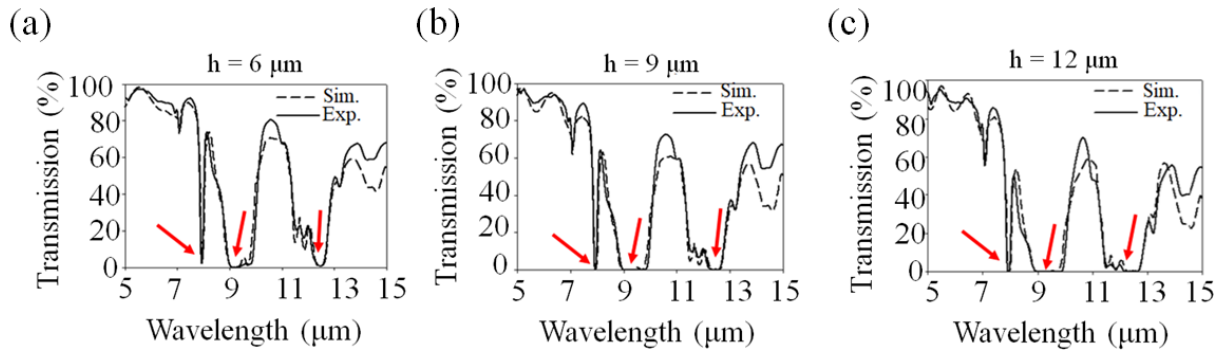


Figure 4.12: FT-IR (solid line) and simulation (dashed line) transmission spectra under for an unstructured PDMS membrane of thickness (a) $h = 6 \mu\text{m}$, (b) $9 \mu\text{m}$, and (c) $12 \mu\text{m}$.

IV.4 Conclusion about the ideal polymer

In order to determine the ideal thermoregulating polymer, we have integrated table 4.5 the results obtained from the optical and thermal calculations for all polymers studied through the manuscript, considering the scaling factor α_5 and taking as an objective a comfort temperature $T_{\text{skin}} = 34 \text{ }^\circ\text{C}$.

In MIR	n_{poly}	k_{poly}	η_A	$T_{a,ns}$	ΔT_a
PE	1.5	≈ 0	10 %	$25 \text{ }^\circ\text{C}$	$0.77 \text{ }^\circ\text{C}$
BCB	1.56	≈ 0.01	15 %	$24.9 \text{ }^\circ\text{C}$	$1 \text{ }^\circ\text{C}$
PI	1.75	0.1	30 %	$24 \text{ }^\circ\text{C}$	$2 \text{ }^\circ\text{C}$
PDMS	1.5	0.2	51 %	$23.9 \text{ }^\circ\text{C}$	$\approx 0 \text{ }^\circ\text{C}$
PET	1.9	0.3	60 %	$22.5 \text{ }^\circ\text{C}$	$\approx 0 \text{ }^\circ\text{C}$

Table 4.5: Summary of optical and thermal behaviors for PE, BCB, PI, PDMS and PET for the scaling factor α_5 , taking into consideration the comfort temperature ($T_{\text{skin}} = 34 \text{ }^\circ\text{C}$).

Where n_{poly} and k_{poly} are the real and imaginary part of the mean refractive index, η_A is the absorption coefficients for a non-structured membrane, $T_{a,ns}$ is the ambient temperature for a non-structured membrane and ΔT_a is the difference of ambient temperature between the structured and non-structured membrane for the scaling factor α_5 .

Following this table, PI can be chosen as the polymer to be fabricated as it presents a high difference in temperature between the structured and the unstructured membrane ($\Delta T_a = 2^\circ\text{C}$). PI polymer is readily available in our lab and can be useful for experimentation and to validate numerical calculations in the short term. The weak point comes is that the PI is not textile compatible as the other polymers, as PE for instance. But one of the constraints on the usage of PE polymer is that the structuration requires a solvent with a high boiling point (around 160°C) such as xylene, decaline, toluene, and trichlo. This limits the feasibility of fabrication in our cleanroom.

Conclusion

This chapter is devoted to the optical and thermal properties of several types of polymer in order to select one as a candidate for experimental fabrication and demonstration.

We have quantitatively analyzed the effect of structuration for different polymer membranes (PDMS, PE, PET and PI). The PDMS is a well-known and currently used polymer in our research group for microfluidic systems. In addition, we have successfully fabricated and released a thin PDMS membrane. The numerical study of the thermal balance between the human body and the membrane showed that the PDMS has a cooling effect. Considering these factors, PDMS is a promising candidate for demonstrating cooling functionality. To focus on heating properties, we numerically studied a set of several other polymers such as PE, PET and PI, which are all regularly used in microelectronic and / or textile industries.

Structuration of the PET membrane had a weak structuration effect in comparison to the effects observed with other polymers. From a theoretical point of view, a PE membrane could be selected, but manufacturing the PE would be challenging due to the constraints of fabrication in a cleanroom. Considering the drawbacks of the PE and PET membranes discussed above, the PI membrane is the most suitable candidate. We have clearly seen that the temperature of the skin is

systematically 2°C higher when the human body is clothed with a structured PI membrane, so PE effectively demonstrates the heating capacity of a photonic membrane. A variation of 2°C would lead to a significant reduction in energy consumption, which offers a positive impact both economically and in terms of the environment. Furthermore, PI polymer is readily available in our lab. Even though this polymer is not currently compatible with textiles, we are continuing to improve our method for developing self-supporting membranes to validate our theoretical results.

References

1. Xia Y, Whitesides GM. Soft Lithography. *Angew Chem Int Ed*. 1998;37:550–75.
2. Dibao-Dina A, Follet J, Ibrahim M, Vlandas A, Senez V. Electrical impedance sensor for quantitative monitoring of infection processes on HCT-8 cells by the waterborne parasite *Cryptosporidium*. *Biosens Bioelectron*. 2015;66:69–76.
3. Baëtens T, Pallecchi E, Thomy V, Arscott S. Cracking effects in squashable and stretchable thin metal films on PDMS for flexible microsystems and electronics. *Sci Rep* [Internet]. 2018 [cited 2020 Mar 8];8. Available from: <http://www.nature.com/articles/s41598-018-27798-z>
4. Dufour R, Brunet P, Harnois M, Boukherroub R, Thomy V, Senez V. Zipping Effect on Omniphobic Surfaces for Controlled Deposition of Minute Amounts of Fluid or Colloids. *Small*. 2012; 8:1229–36.
5. Vandezande P, Gevers LEM, Vankelecom IFJ. Solvent resistant nanofiltration: separating on a molecular level. *Chem Soc Rev*. 2008; 37:365–405.
6. Yuan Z, Ziouche K, Bougrioua Z, Lejeune P, Lasri T, Leclercq D. A planar micro thermoelectric generator with high thermal resistance. *Sens Actuators Phys*. 2015; 221:67–76.
7. Boutchich M, Ziouche K, Yala MA-H, Godts P, Leclercq D. Package-free infrared micro sensor using polysilicon thermopile. *Sens Actuators Phys*. 2005 ;121 :52–8.
8. Ugbolue SC. Polyolefin fibres: industrial and medical applications. Elsevier. Ed. 2009.
9. Gould SAC, Schiraldi DA, Occelli ML. Analysis of poly(ethylene terephthalate) (PET) films by atomic force microscopy. :7.
10. Gioti M, Laskarakis A, Logothetidis S. IR–FUV ellipsometry studies on the optical, electronic and vibrational properties of polymeric membranes. *Thin Solid Films*. 2004;455–456:283–7.
11. Nomura K, Ohta H, Takagi A, Kamiya T, Hirano M, Hosono H. Room-temperature fabrication of transparent flexible thin-film transistors using amorphous oxide semiconductors. *Nature*. 2004;432:488–92.
12. Hamers RJ. Flexible electronic futures. *Nature*. 2001;412:489–90.

13. Fodil K, Denoual M, Dolabdjian C, Treizebre A, Senez V. In-flow detection of ultra-small magnetic particles by an integrated giant magnetic impedance sensor. *Appl Phys Lett*. 2016; 108:173701.
14. Zhang ZM, Lefever-Button G, Powell FR. Infrared Refractive Index and Extinction Coefficient of Polyimide Films. :12.
15. Tong JK, Huang X, Boriskina SV, Loomis J, Xu Y, Chen G. Infrared-Transparent Visible-Opaque Fabrics for Wearable Personal Thermal Management. *ACS Photonics*. 2015; 2:769–78.
16. Laskarakis A, Logothetidis S. Study of the electronic and vibrational properties of poly(ethylene terephthalate) and poly(ethylene naphthalate) films. *J Appl Phys*. 2007; 101:053503.

Conclusion

For the past ten years, photonic nanostructures have represented a new paradigm for the control of thermal radiation, offering a panoply of exciting properties for energy management applications. Because of their abilities to control and manage electromagnetic waves in the mid-Infrared (MIR) wavelength scale, photonic nanostructures provide a drastically different way to manage thermal radiations from conventional thermal emitters. The modification of Planck blackbody radiation by photonic band gap materials has been discussed, based on either simple photonic multilayered structures or more complex 1D, 2D and 3D ones, thus demonstrating the enhancement, suppression and selectivity of thermal emission based on the properties of the photonic crystal selected. These fundamental advances in controlling thermal radiation led to different applications in the energy domain as thermo-photovoltaic devices or through the concept of daytime radiative cooling to passively decrease the temperature of terrestrial structures.

Recently, another field of application has appeared in the thermal radiation control, with the introduction of photonic nanostructures in textiles for personal thermoregulation. The main motivation for this work is the reduction of building energy consumption for Heating, Ventilation and Air-Conditioning (HVAC) systems by locally providing heating or cooling in the environment around the human body. To this end, personal thermoregulation photonic textiles have been proposed with the objective to obtain specific spectral properties. Personal thermoregulation is an exciting scientific challenge to investigate, especially in the energy efficiency context. However, a tremendous effort is still necessary to develop smart wearable thermo regulating textiles to meet user demand for better thermal comfort. The goal of this thesis is to study different passive photonic membranes that modulate the optical radiation of the human body in the MIR for personal thermoregulation.

The work presented in this manuscript shows theoretically and experimentally the link between the structural properties of a polymer membrane and its optical and thermal properties in the mid-infrared.

In the first chapter of this thesis, we have seen that the notion of thermal comfort is a subjective, purely qualitative and complex notion involving many physiological and psychological factors. There are different aspects of comfort: psychological comfort, sensory comfort, ergonomic comfort and thermal comfort. Within the framework of this project, we were only interested in thermal comfort. This latter parameter is very sensitive to the physiology (metabolism) of the

individual as well as to its environmental conditions. Maintenance of thermal comfort is also sensitive to the balance between heat gains (thermogenesis) and heat losses (thermolysis) induced by the individual. Under these conditions, the textile will act on heat and moisture transfers at the skin-textile interface (microclimate) in order to maintain thermal comfort. By offering this functionality, the textile is then qualified as smart textiles. Indeed, it acts on the heat and moisture transfers occurring by convection, conduction, evaporation and radiation. The latter, radiation, was the center of our focus since it represents 50% of the heat losses induced by the human body. The polymer membrane incorporated to a textile has to be able to reflect this thermal radiation towards the human body in order to limit the thermal losses and to maintain comfort. A study of the scientific literature in the field (with recent articles published in high impact factor journals) shows that photonic structures can be associated to smart textile to reach this objective. Thus, considering the thermal radiation of the human body in the range of the mid-infrared (MIR), the goal of my thesis has been to make a polymer photonic membrane capable of controlling MIR radiation.

In the second chapter, we described the FEM method used to perform calculation of our structures. The principle and the requirements of the method were stated. For technological realization capabilities, the choice of (poly)silicon has been made prior to the start of my work. Thus, since silicon is non-absorbent in the infrared domain, we have studied the evolution of the reflective properties of two photonic crystal membranes, showing either 1D or 2D periodicity in the mid-infrared range (5-15 μm) versus their geometric features. We have found that the interactions of an incident wave with ridges or holes in a slab modified the reflective spectrum in a similar way to a thin full plate PolySi layer. For both geometries, we have been able to highlight the occurrence of at least one specific dip in the reflection spectrum, due to the structuration of the membrane. We showed that in the ridge structure, the mode is confined inside the ridges while in the drilled layer, the mode is spread over the whole membrane. For this latter case, we demonstrated the robustness of the results regarding polarization. Two types of periodic lattices based on polycrystalline silicon (PolySi) and SiO_2 , previously fabricated by Maude Viallon, were characterized experimentally: a lattice of PolySi ridges and a triangular lattice of air holes in a PolySi layer. We compared the spectra obtained by simulation with those found by FT-IR measurement and obtained a good agreement between the experimental and the numerical curves.

Nevertheless, to target our final application, we had to translate the results obtained in silicon materials into polymers to facilitate textile integration.

In the third chapter, the silicon material has been replaced by Benzocyclobutene (BCB) polymer. Here again, this choice has been made prior to the start of my work and for technological realization capabilities. We theoretically arranged a BCB photonic membrane into triangular arrays of air holes because this structure was insensitive to the polarization of a normal incident wave. We have established the thermoregulation effects of a photonic crystal membrane, based on modulation of human body optical radiations in the mid-infrared range. We have studied the transmission, reflection and absorption properties of a BCB membrane in the mid-infrared domain. We found that the structuration of the BCB membrane leads to new features in the spectral reflection, transmission and absorption spectra that have been identified as guided and localized modes of the photonic crystal membrane. Furthermore, by scaling the geometrical parameters of the crystal, the transmission can be modulated up to 28% in wavelength range $[7.5, 11.5] \mu\text{m}$ representing the typical human body emissivity. Additionally, we decoupled the different geometrical effects and discussed them as an independent variation of the geometrical parameters (D, h). We found that the transmittance of the membrane decreases with the diameter and the thickness of the membrane, to favor absorption and/or reflection. We finally presented the effect of the angle of incidence and the effect of perspiration on the spectra R, T and A . This theoretical study was followed by a first optical experimental demonstration which was carried out in collaboration with Maud Viallon who fabricated BCB membranes during her thesis. Besides, we explored the optical effects on thermal balance analysis, applied between the human body and the surrounding environment, through the structured membrane. The two cases we worked on were done on a non-thermally conductive and a thermally conductive membrane. For the case of a non-conductive membrane, there appeared to be a difference between the inner and outer temperatures, despite the relative thinness of the membrane. We observed that for a set of geometrical parameters ($P = 10 \mu\text{m}, D = 7.9 \mu\text{m}, h = 5.7 \mu\text{m}$) the non-conductive membrane acts as a thermoregulator of the human body. Compared to a non-structured regular membrane of equivalent thickness, when the temperature of the room is low (20°C) the membrane acts as a heater, and increases the temperature up to $+1^\circ\text{C}$. In contrast, when the ambient temperature is high (40°C), it acts as a cooler and adjusts the temperature by -1°C . The equilibrium is obtained when the temperature is

28 °C, which represents the working point of the photonic crystal membrane (in that case the structuration of the membrane is not active). We found that it was essential to have a membrane smaller than 7 μm to preserve the diffusion properties by reflection and activate the thermoregulatory properties of the photonic membrane. In addition, we concluded that the presence of moisture in the microclimate deactivates the thermoregulation effect of the non-conductive photonic membrane. For more realistic considerations, we introduced the conductivity of the membrane. Because of the thinness of the membrane, we found that the inner and outer temperatures were the same. We found that the temperature of the room needs to be systematically 1°C less when the human body is clothed with the structured membrane to obtain the same thermal comfort ($T_s = 34$ °C).

In the last chapter, we are looking to replace BCB polymer with more suitable ones. We investigated a set of different polymers (PDMS, PE, PET and PI). Collectively, these polymers cover a wide range of optical properties (more or less absorbent) in the mid-infrared. First, we completed a quantitative analysis on the effect of structuration on the reflection, transmission and absorption spectra of these polymers. We have seen that, for a maximum effect of a membrane structuration, it is necessary to choose a polymer with optical properties including a high refractive index so that it has low absorption in the mid-infrared domain. Next, we studied the thermal behavior of the four selected polymers. The temperature calculation for an unstructured membrane showed that the temperature of the membrane, as well as the ambient temperature, depends on the polymer selected. Thus, room temperature and absorption are inversely proportional for a fixed skin temperature. To focus on heating properties, the PI polymer is the most suitable. We have clearly seen that the temperature of the skin is systematically 2°C higher when the human body is clothed with a structured PI membrane. It demonstrates the heating capacity of the photonic membrane. Finally, we used easily processable PDMS polymer to fabricate a membrane in order to validate our optical model. With this approach, we were able to fabricate and study three thin non-structured PDMS membranes of thicknesses 6 μm , 9 μm , and 12 μm , and observed good alignment between the experimental optical results and the theoretical calculations for this membrane.

Perspectives

Many efforts remain to be made to improve the efficiency of the proposed membranes and to obtain a large-scale transferable photonic textile.

The short-term perspective that follows the last chapter is to fabricate a structured polymer membrane in the IEMN cleaning room. For the PI, the first issue is to find the right manufacturing processes to fabricate the demonstrator. The goal will be to improve the manufacturing method for developing self-supporting membranes and release the membranes after fabrication. This phase requires another technique, as deposit the PI liquid on a substrate compatible with chemical etching and choosing the right solution to remove the support. Even though this polymer is not compatible with textiles, it will still allow us to validate our work and compare our findings from simulations with experimental results. Once we finish this study, one can apply the manufacturing approach to polymers such as PE that are more compatible with textile applications.

The fabricated membrane will then be optically tested experimentally using FT-IR and compared to the numerical results. The experimental characterization of the thermal properties of the membranes is still not available at the moment while representing a real challenge for the final validation of the work. Within the PHOTONITEX project, the HEI partner is actually developing the experimental set up that will be used to characterize our photonic membranes.

In Chapter III and IV of this thesis, we identified the impact of optical properties of photonic membranes in polymers (particularly absorption) and their benefit on personal thermoregulation. We have shown that structuring the membranes allows to change the optical spectra of the polymer. The medium- and long-term opportunities for the continuation of this thesis work can be pursued through to two main issues:

First, on-going research looks at modifying the optical properties by adding charges to the membrane (PhD Mohamed Boutghatin). To achieve this, we add mineral microparticles (e.g. TiO_2 , SiO_2 , etc.) or carbon nanotubes to the polymer matrix. Experimentally, one main difficulty will lie in controlling the distribution of charges in order to obtain / guarantee a homogeneous and regular dispersion throughout the membrane. It will also be necessary to determine the minimum and maximum charge rates to obtain a significant effect on the optical properties of the membrane, keeping the flexibility of the membrane.

Second, research should be conducted to examine the dynamic aspect of the modulation of the optical spectra. We have studied a static polymer, with constant geometry according to external conditions. Our ultimate goal for smart textiles is to have a system that dynamically adapts to temperature and humidity and modulate the emission of radiation emitted by the human body and regulate the temperature of the microclimate between the textile and the body. Within the framework of the PHOTONITEX project, partners of the University of Mons are offering shape memory polymers that depend on temperature and humidity, which could be used for this area of research.

Abstract

For the past ten years, photonic nanostructures have represented a paradigm for the control of thermal radiations, offering a panel of exciting properties for energy applications. Because of their abilities to control and manage electromagnetic waves at the mid-infrared (MIR) wavelength scale, photonic nanostructures demonstrate their ability to manage thermal radiations properties in a way drastically different from conventional thermal emitters. The fundamental advances in controlling thermal radiation led to different applications in the energy domain, as thermo photovoltaic devices or through the concept of daytime radiative cooling to passively decrease the temperature of terrestrial structures. Recently, another field of application has appeared in the thermal radiation control, with the introduction of photonic nanostructures in textiles for personal thermoregulation.

The goal of the thesis is to study different passive photonic membranes that modulate the human body optical radiations in the MIR for personal thermoregulation. We have investigated the optical properties of different polymer membranes, considering the effect of their structuration. We showed that a photonic crystal membrane is able to modulate the transmission coefficient by 28% in benefit or deficit of both the absorption and reflection. We analyzed the thermal balance between the human body and the indoor environment through the photonic membrane, considering the radiation, convection and conduction mechanisms. We found that the temperature of the skin is almost 2°C higher when the human body is clothed with a structured membrane. The study was carried out on analytical calculations and numerical simulation with the help of the finite element method (FEM). The numerical study was supported by experiments in fabrication in the IEMN cleaning room and in characterization by infrared spectroscopy (FT-IR) at the HEI engineering school.

Keywords:

Photonic membrane; Optical properties; Thermal balance; MIR; Polymer; Personal thermoregulation; Finite Element Method.

Résumé

Au cours des dix dernières années, les nanostructures photoniques ont représenté un paradigme pour le contrôle des radiations thermiques, offrant un panel de propriétés passionnantes pour les applications énergétiques. En raison de leurs capacités à contrôler et à gérer les ondes électromagnétiques à l'échelle de la longueur d'onde dans l'infrarouge moyen (MIR), les nanostructures photoniques ont démontré leur capacité à gérer les propriétés des radiations thermiques d'une manière radicalement différente des émetteurs thermiques conventionnels. Les progrès fondamentaux du contrôle du rayonnement thermique ont conduit à différentes applications dans le domaine de l'énergie, comme les dispositifs thermo-photovoltaïques ou à travers le concept de refroidissement radiatif diurne pour diminuer passivement la température des installations terrestres. Récemment, un autre domaine d'application est apparu dans le contrôle du rayonnement thermique, avec l'introduction de nanostructures photoniques dans les textiles.

Le but de la thèse est d'étudier différentes membranes photoniques passives qui modulent le rayonnement optique du corps humain dans l'IR moyen pour assurer la thermorégulation individuelle. Pour cela, nous avons étudié les propriétés optiques de membranes polymères, en fonction de leur structuration. Nous avons montré que la membrane photonique est capable de moduler l'amplitude de transmission de 28% au profit ou au dépend de l'absorption et de la réflexion. Nous avons déterminé le bilan thermique entre le corps humain et le milieu environnant à travers la membrane photonique, en tenant compte des mécanismes de rayonnement, de convection et de conduction. Nous avons trouvé que la température de la peau est supérieure de presque 2 °C lorsque le corps humain est revêtu d'une membrane photonique structurée. Cette étude a été réalisée à partir de calculs analytiques et de codes de simulation numérique par la méthode des éléments finis (FEM). L'étude numérique a été accompagnée par des expériences de fabrication en salle blanche à l'IEMN et de caractérisation par spectroscopie infra rouge (FT-IR) à l'école d'ingénieur HEI.

Mots clés:

Membrane photonique ; Propriétés optiques ; Bilan thermique ; MIR ; Polymère ; Thermoregulation personnelle ; Méthode des éléments finis.